

Quantum Information Processing in Rare Earth Ion Doped Insulators

Jevon Joseph Longdell

A thesis
submitted for the degree
of
Doctor of Philosophy
of the
Australian National University



The Australian National University
April 2003

Statement of authorship

This thesis contains no material which has been accepted for the award of any other degree or diploma in any university. To the best of the author's knowledge and belief, it contains no material previously published or written by another person, except where due reference is made in the text.

Jevon Longdell
November 29, 2003

For Poppa.

Acknowledgements

Firstly I would like to thank my primary supervisor Matt Sellars. I have very good reason to be grateful for his talent, his continual and intense interest in this work, and for his friendship and support throughout.

Secondly I'd like to thank Neil Manson who in his role as my supervisor and the head of our group provided substantial support and wise advice.

This PhD is a very different one to that which I started in the Applied Maths department. I have to thank my original supervisor Stephen Hyde for the enjoyment that only comes from working alongside a talented and passionate individual. I also must thank Stephen for his understanding when I decided to change tack and his friendship then and now.

I am grateful to all the members of the Applied Maths department for the fantastic environment that Applied Maths provides. I would especially like to thank Mathias Boström and Barry Ninham for the work we did together.

I'd like to also thank the technical staff of the Laser Physics Centre, Ian McRae, John Bottega, Craig Macleod, Mike Pennington and Anita Smith, both for their skills and their willingness to use them in the aid of this project.

To all of the students I have shared an office or a lab with, Gerd, Elliot, Joanne, Darryl, Elena, Annabel, thank you for providing such an enjoyable and productive working environment.

I have had a rich life during my stay in Canberra, for this I must thank all my friends, be they my fellow students at the RSPHysSE, fellow outdoors freaks from the ANUMC, or people I have met along the way. I must make special mention of Glen who took on the job of my running coach without being asked, 4:02:12, I couldn't have done it without you.

I have to thank my family, I didn't get to see enough of any of you in the last three years, but you never felt far away.

I am unable to sufficiently repay my to proof readers, Katherine Lilly and Susie Longdell, for the many hours of service they willingly provided.

Finally I thank you Kat, for being the only thing that really matters.

*Jevon Longdell
April 2003*

Abstract

A great deal of theoretical activity has resulted from blending the fields of computer science and quantum mechanics. Out of this work has come the concept of a quantum computer, which promises to solve problems currently intractable for classical computers. This promise has, in turn, generated a large amount of effort directed toward investigating quantum computing experimentally.

Quantum computing is difficult because fragile quantum superposition states of the computer's register must be protected from the environment. This is made more difficult by the need to manipulate and measure these states.

This thesis describes work that was carried out both to investigate and to demonstrate the utility of rare earth ion dopants for quantum computation. Dopants in solids are seen by many as a potential means of achieving scalable quantum computing. Rare earth ion dopants are an obvious choice for investigating such quantum computation. Long coherence times for both optical and nuclear spin transitions have been observed as well as optical manipulation of the spin states. The advantage that the scheme developed here has over nearly all of its competitors is that no complex nano-fabrication is required. The advantages of avoiding nano-fabrication are two fold. Firstly, coherence times are likely to be adversely effected by the “damage” to the crystal structure that this manufacture represents. Secondly, the nano-fabrication presents a very serious difficulty in itself.

Because of these advantages it was possible to perform two-qubit operations between independent qubits. This is the first time that such operations have been performed and presents a milestone in quantum computation using dopants in solids. It is only the second time two-qubit operations have been demonstrated in a solid.

The experiments performed in this thesis were in two main areas: The first was the characterisation of hyperfine interactions in rare earth ion dopants; the second, simple demonstrations directly related to quantum computation.

The first experiments that were carried out were to characterise the hyper-

fine interactions in $\text{Pr}^{3+}:\text{Y}_2\text{SiO}_5$. The characterisation was the first carried out for the dopants in a site of such low symmetry. The resulting information about oscillator strengths and transition frequencies should prove indispensable when using such a system for quantum computation. It has already enabled an increase in the coherence times of nuclear spin transitions by two orders of magnitudes.

The experiments directly related to the demonstration of quantum computation were all carried out using ensembles. The presence of a significant distribution of resonant frequencies, or inhomogeneous broadening, meant that many different sub-ensembles could be addressed, based on their resonant frequencies. Furthermore, the properties of the sub-ensembles could be engineered by optically pumping unwanted members to different hyperfine states away from resonance with the laser.

A previously demonstrated technique for realising ensembles that could be used as single qubits was investigated and improved. Also, experiments were carried out to demonstrate the resulting ensembles' utility as qubits. Further to this, ions from one of the ensembles were selected out, based on their interaction with the ions of another. Elementary two qubit operations were then demonstrated using these ensembles.

Contents

Acknowledgements	v
Abstract	vii
Outline	1
1 Introduction to quantum computing	3
1.1 Computer science goes quantum	3
1.2 The requirements for experimental quantum computing	7
1.3 Bloch spheres and Rabi frequencies	8
1.3.1 Qubit dynamics and the Bloch sphere	11
1.3.2 Damping and the Bloch sphere	13
1.4 Efforts toward experimental quantum computing	15
1.4.1 Liquid state NMR	16
1.4.2 Superconducting qubits	20
1.4.3 Ion traps	22
1.4.4 Linear optics quantum computing	23
1.5 Error correction	25
1.6 Type-II quantum computing	26
1.7 Quantum state tomography	27
1.8 Quantum process tomography	29
2 Rare earth ion spectroscopy	30
2.1 Homogeneous and inhomogeneous broadening	30
2.2 Chemistry and occurrence of the rare earths	31
2.3 Energy levels of the $4f$ states	33
2.4 Theory of hyperfine splittings	36
2.5 The linewidths of rare earth spectra	37
2.5.1 Optical transitions	37
2.5.2 Hyperfine transitions	38
2.6 Techniques that probe inside the inhomogeneous line	38

2.6.1	Spectral holeburning	38
2.6.2	Optical free induction decay and photon echoes	39
3	Hyperfine splittings in rare earth ion dopants	45
3.1	Hyperfine interaction in praseodymium doped Y_2SiO_5	46
3.1.1	Background	46
3.1.2	Experiment	48
3.1.3	Solving the inverse problem	51
3.1.4	Model parameters and the misfit metric	56
3.1.5	Sensitivity of the spectra to the Hamiltonian	59
3.1.6	Implementation of algorithm	62
3.1.7	Results	63
3.1.8	The future	74
3.2	Hyperfine interaction in europium doped Y_2SiO_5	76
3.2.1	Experimental setup and procedure	76
3.2.2	Results	80
3.2.3	Discussion	80
3.2.4	Conclusions	81
4	Optical Quantum Computing in Solids	84
4.1	Interaction between rare earth ions' optical transitions	86
4.1.1	Electric dipole-dipole interactions	87
4.1.2	The resonance interaction	91
4.1.3	Dephasing by non-equilibrium phonons	92
4.2	Previous schemes	93
4.2.1	Ensembles and instance identification	94
4.3	The direction pursued in this thesis	96
4.4	NMR-like measurements for ensembles	97
4.5	CNOT with refocusing	99
4.6	Inhomogeneity in the interaction strength and scaling	104
4.6.1	Solid state "molecules"	105
4.6.2	Single dopant detection	106
4.7	Cyclic transitions in rare earth systems	107
4.8	Conclusion	109
5	Quantum computing using rare earths — Experiment	111
5.1	The sample	111
5.2	Experimental setup	114
5.2.1	Ultra-high resolution laser	116
5.3	Generating and characterising single qubits	118

5.3.1	Zero area pulses	120
5.3.2	Burning back anti-holes	123
5.3.3	Nutations	127
5.4	Quantum state tomography	128
5.5	A four level system for type-II quantum computing	132
5.6	Characterisation of dipole-dipole interactions	135
5.6.1	Instantaneous spectral diffusion on an anti-hole	136
5.6.2	Dependence of the first pulse length	138
5.6.3	Echo demolition	140
5.6.4	Perturbing pulse position dependence	140
5.6.5	Perturbing pulse length dependence	145
5.6.6	Rephasing of the interaction induced decoherence	146
5.7	Conditional phase shifts	149
5.7.1	Limiting factors	152
5.7.2	Realising larger conditional phase shifts	152
5.7.3	Tomography	156
5.8	The future	157
6	Summary	158
	Appendices	161
A	Rotation conventions used in creating M and Q tensors	162
B	Algorithm for assigning observed spectral lines.	164
C	Publications	170
	Bibliography	173

Outline

The thesis begins with two introductory chapters, describing relevant details from the fields of quantum computation and rare earth spectroscopy respectively.

The first experiments carried out in the course of this work were to characterise the hyperfine structure in praseodymium doped yttrium orthosilicate ($\text{Pr}^{3+}:\text{Y}_2\text{SiO}_5$). This characterisation was the first to be successful in a site with such low symmetry. These and an attempt to gain similar information for europium dopants in the same host are described in Chapter 3.

It was initially envisioned that the characterisation of the $\text{Pr}^{3+}:\text{Y}_2\text{SiO}_5$ system would be used to improve the demonstrations of slow and stopped light in the material. However, the first time these results were used was in a technique to extend this material's coherence times for hyperfine transitions by over two orders of magnitude. This represented a very significant result for rare earth quantum computing because it is these transitions that would be used for the long term storage of quantum information.

In Chapter 4 a review is made, with the emphasis on rare earth ion dopants, of the mechanisms that cause interactions between optical centres in solids. Following this, the previously published schemes for achieving quantum computation in such materials are evaluated. The general plan for quantum computation pursued in this thesis is then presented. This plan consists of two areas of endeavour. The first is the demonstration, using ensembles, of quantum logic operations for a small number of qubits. As part of this, a practical method that was developed for achieving two qubit operations is presented. The second area of endeavour is the study of methods for scaling to a large number of qubits. Various possibilities for scaling are discussed.

Chapter 5 describes the experimental work that was directly aimed at carrying out quantum computing operations. Ensembles that can act as qubits (anti-holes) have been demonstrated previously. Here the improvements made are discussed. Also, the utility of the resulting ensembles as qubits was demonstrated using single qubit quantum state tomography ex-

periments.

Following this, various experiments with two of these anti-holes were carried out. These were used to both characterise the strength of the interaction between the ions and demonstrate its suitability for multi-qubit operations.

This was followed by the application of some of the techniques described theoretically in Chapter 4. Using these techniques, a phase shift in the state of one qubit, that was conditional on the state of another qubit, was demonstrated. This represents the most elementary two qubit operation. Various simple ways in which the experiment could be improved to significantly increase the fidelity of the operation are discussed.

The thesis finishes with a summary of the results achieved. The future for quantum computing that is based on optical centres, and rare earth ion dopants in particular, is discussed.

Chapter 1

Introduction to quantum computing

1.1 Computer science goes quantum

Modern computer science was founded in 1936 by Alan Turing [1]. He did this by developing the notion of *Turing Machines*, machines that follow algorithmic processes. Further to this, Turing gave an example of a *universal Turing machine* which could simulate any other Turing machine. By investigating his universal Turing machine he showed various things are and others are not possible using Turing machines.

In his view, any physical machine which performed a task in an algorithmic manner was a Turing machine. This led to the assertion that any algorithmic process could be simulated with a Turing Machine. This assertion is known as the *Church-Turing principle* [2], in honour of the work of both Turing and Alonzo Church, another early computer scientist.

Since the time of Church and Turing the field of computing has of course exploded, with computer hardware performance improving like no other class of tools previously. In 1965 [3] Gordon Moore, then at Fairchild Camera and Instrument Corp., noticed that the number of components in an integrated circuit (then about 50) had doubled yearly for the past three years. He pointed out that if this continued, chips would have typically on the order of 50,000 components by 1975. Following this people started using the term “Moore’s Law” to describe the idea that performance per cost would double every year or so. Since 1965 Moore’s Law has more or less held true, giving us the amazing computational power that we now have readily available to us.

In the years following 1936 computing has become more of a practical

concern than a purely mathematical one, making the relative performance of various forms of computation important. To a computer scientist it is just as important to know whether your computer can tell you the answer in a timely manner, as it is to know whether any conceivable computer can, given any length of time.

A general rule developed which separated ‘efficient’ methods of computation from ‘inefficient’ ones. As the size of a problem increases so does the resources required to solve it. Here resources could represent a number of things such as the number of computational steps, or information storage required. The problem is deemed efficient if the increase in resources can be bounded by a polynomial in the problem size. If it cannot it is deemed inefficient. This is a very practical definition. Generally we solve problems on computers where the performance can be described by taking the limit of large problem size. In this limit the ‘efficient’ methods outperform the ‘inefficient’ ones. Furthermore the definition is a very simple one which appeals to theorists in their search for deep results.

A strengthened version of the Church-Turing principle was put forward, with this in mind. This version said that any algorithmic process could not only be simulated on a Turing machine, but could be done so *efficiently*.

However, in the mid 1970’s, not long after this strengthened form was put forward, stochastic algorithms were developed that solved problems more efficiently than any current deterministic algorithms can. While there is a finite probability of failure on each run through such an algorithm, such methods will always be much faster than their deterministic counterparts¹. This led to a modification of the strong Church-Turing principle, which replaced the words ‘Turing machine’ with ‘probabilistic Turing machine’ [4].

In the mid 1980’s, David Deutsch began investigating whether it was possible to come up with something like a strong Church-Turing principle with its basis in physical laws, rather than speculative arguments.

In his search for a physical system that could simulate any other system efficiently, Deutsch came up with the notion of a “Universal Quantum Computer” [5]. Instead of being a collection of classical two state systems, the register of such a computer would be a collection of two state quantum systems known as ‘qubits’. The basis in which the qubit is read out is known as the *computational* basis, with basis states $|0\rangle$ and $|1\rangle$.

The computation would proceed as follows. First the register would be initialised, for example, all to the ground state $|0\rangle$. Then various different unitary operations would be performed to the register, either to one or more

¹Unless you are exceedingly unlucky.

than one qubit at a time. Finally the states of the qubits would be measured and you would (hopefully) have your answer.

To model a N -qubit computer you would need a Hilbert space of dimension 2^N . As the size of a quantum computer is increased, its simulation by a classical computer requires exponentially more resources. Thus Deutsch produced a hypothetical system which provided a violation of the Church-Turing principle.

Following on from this Deutsch introduced the idea of *quantum parallelism*. He argued that the potential power of a quantum computer could be understood by thinking of it as a massively parallel classical computer, with the possibility that each of the 2^N possible computational basis states go through the calculation at the same time. However you can only make N measurements at the end of the calculation.

With these two factors in mind, Deutsch gave a trivial example of a task where a quantum computer could out-perform a classical one. Suppose you have a function that maps a member of the set $\{0, 1\}$ to a member of the same set. Such functions — there are of course four of them — can be classed as either constant ($f(x) = f(\neg x)$) or balanced ($f(x) = \neg f(\neg x)$)². Suppose you were given a rule for calculating such a function and had to find out whether it was constant or balanced. On a classical computer you would calculate $f(0)$ and $f(1)$ and compare them. However with a 2-qubit quantum computer one can achieve the same with only one evaluation of f by making use of quantum parallelism. Deutsch and Josza [6] extended this idea to show that with a $n + 1$ qubit quantum computer you can distinguish between a constant or balanced function that takes $\{0, 1\}^n$ to $\{0, 1\}$ with just one evaluation of the function. Such a function is said to be balanced if it returns 1 for half of its 2^n possible input states.

Perhaps the most obvious situation where a quantum computer could out-perform a classical one is in the simulation of quantum mechanical systems. Feynman [7] pointed this out in his early contribution to quantum computing. Following on from this idea, quantum algorithms have been found for studying various quantum mechanical problems on a universal quantum computer. These include simulating many-body fermionic systems [8] and finding eigenvalues and eigenvectors of atomic Hamiltonians [9, 10].

It could be argued that the above examples are not of particularly wide interest. However, in 1994, Peter Shor [11] showed that it is possible for a quantum computer to efficiently solve a problem of great importance. The problem was finding two large prime numbers when given their product. No

²Here \neg represents the logical *not* operation.

corresponding efficient classical algorithm is known and this fact forms the basis of the security of RSA public key encryption.

Public key cryptography is a process by which two parties can communicate securely with all of their correspondence public. It is hard to overstate the importance this has had in commerce and the internet. The idea behind the protocol is that each party has a public key and a corresponding private key. If Alice wants to send a sensitive message to Bob, she asks Bob for his public key and uses this to scramble the message in such a way that Bob's private key is needed to unscramble it.

Bob's public key is analogous to an open padlock and Bob's private key to the padlock's key. Bob sends Alice his padlock open, Alice uses this to lock a box containing the message, then sends it to Bob knowing that only he can open the lock.

The details of a method for public key cryptography were first made public following the work of Ronald Rivest, Adi Shamir and Leonard Aldeman [12].

In their scheme, which is by far the most practical available today, the public key contains the product of two large primes and the private key can easily be found from the two primes. This method is secure as long as no one is able to find the two primes from their product. There is no known algorithm which allows classical computers to solve this problem efficiently (where the resources required are polynomial in problem size). This means that with the current level of computation available it is possible to choose a size for the primes such that the encryption and the decryption with the private key takes moments whereas to find the two factors and so decrypt the message without the private key would require a prohibitively long time. Shor's algorithm would allow a sufficiently large quantum computer to efficiently find the two primes from their product and thus render RSA encryption insecure.

Lov Grover, a colleague of Shor at Bell Labs discovered another use for a quantum computer. Grover's algorithm [13] was related to finding a particular member in an unstructured database. Suppose you have a function $f(x)$ that maps the integers $\{1, 2, 3, \dots, N\}$ to the set $\{0, 1\}$ and has the value of 0 for all but one member of its domain. Finding the value of x for which $f(x) = 1$ on a classical computer takes $\mathcal{O}(N)$ function evaluations, because you can't really do any better than going through $\{1, 2, 3, \dots, N\}$ one by one. Grover gave a quantum mechanical algorithm that takes $\mathcal{O}(\sqrt{N})$ function evaluations. The intrinsic benefit of using a quantum computer in this case is smaller than with Shor's algorithm — large sub-primes cannot be factored with classical computers whereas large databases can be searched.

While quantum computers have the potential to dramatically out-perform

classical computers for certain tasks, it appears to be very hard to write algorithms that make use of this power. Until more algorithms are found, Shor's algorithm is the only immediate use to which a practical quantum computer would be put.

1.2 The requirements for experimental quantum computing

With Shor's algorithm came increased interest in achieving practical quantum computing. Many, many proposals have been put forward. It would be close to the truth to say that almost every type of system for which a coherent effect can be demonstrated has been proposed for quantum computing.

David DiVincenzo [14] put forward five requirements a system must meet in order for it to be useful as the basis for a quantum computer. The criteria constitute a set of criteria against which potential quantum computers can be judged.

The requirements he gave are:

1. A scalable physical system with well characterised qubits.
2. The ability to initialise the state of the qubits to a simple starting state, such as $|000\dots\rangle$.
3. Very long coherence times relative to the time required for quantum gates.
4. A “universal” set of quantum gates.
5. A qubit-specific measurement capability.

The “quantum gates” are unitary transformations of the state of the computer, and because of inspiration from classical computers, they are generally simple operations that only affect the state of a small number of qubits. A set of quantum gates is said to be “universal” if any unitary transformation of the state of the computer's register can be achieved by repeated application of members of such gates. In 1995, DiVincenzo et al. [15] showed that single qubit operations and the CNOT operation between two qubits are universal. The CNOT or conditional-not gate inverts the “target” qubit conditional on the state of a “control” qubit. In the basis $\{|00\rangle, |01\rangle, |10\rangle, |11\rangle\}$ this has

the matrix representation

$$\begin{bmatrix} 1 & 0 & 0 & 0 \\ 0 & 1 & 0 & 0 \\ 0 & 0 & 0 & 1 \\ 0 & 0 & 1 & 0 \end{bmatrix} \quad (1.1)$$

Quantum computing proposals generally choose the CNOT and single qubit operations to show that they can achieve a universal set of gates. As far as universality is concerned there is nothing particularly special about the CNOT, it has been shown [16, 17] that ‘almost any quantum logic gate is universal’. Work along with a similar theme has shown that any fixed entangling gate along with single qubit operations is also universal [18, 19].

DiVincenzo’s requirements highlight the fundamental difficulty in achieving quantum computing. On the one hand, the qubits must be made to interact both with themselves and some sort of measuring apparatus. At the same time they must be well isolated from everything so their coherence times are long.

1.3 Bloch spheres and Rabi frequencies

Before reviewing a number of current experimental demonstrations relevant to quantum computing, it is helpful to present the Bloch formalism for describing a single qubit system. In this formalism it is very easy to understand the dynamics of such systems when influenced under coherent driving and dissipation and this is presented also.

In understanding the dynamics of single qubits, the formal equivalence between a spin half system and any other two state quantum system is very useful. We treat the state $|0\rangle$ as the $z = -1/2$ state and $|1\rangle$ as the $z = +1/2$ state of our fictitious spin-half particle. In the z basis our two states are³

$$|0\rangle = \begin{bmatrix} 0 \\ 1 \end{bmatrix}, \quad |1\rangle = \begin{bmatrix} 1 \\ 0 \end{bmatrix} \quad (1.2)$$

For an arbitrary initial state $|\psi\rangle$ we define a position vector

$$\mathbf{r}_\psi = (\langle\psi|X|\psi\rangle, \langle\psi|Y|\psi\rangle, \langle\psi|Z|\psi\rangle) \quad (1.3)$$

³Many people do the opposite of this and have the $|0\rangle$ along the positive z axis on the Bloch sphere. Presumably this is so the state $|0\rangle$ can have the vector representation $[1; 0]$ rather than $[0; 1]$.

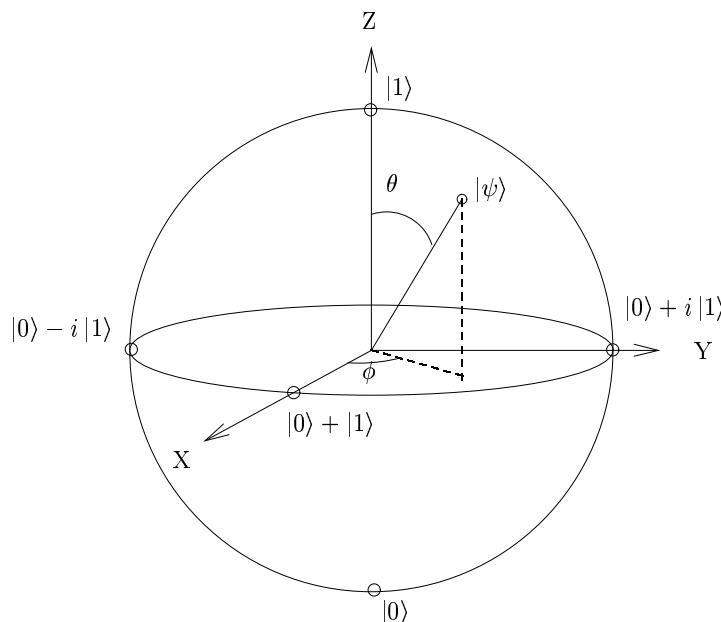


Figure 1.1: Bloch sphere with the state given in Eq. 1.5 shown.

where X , Y and Z are the Pauli operators:

$$X = \begin{bmatrix} 0 & 1 \\ 1 & 0 \end{bmatrix}, \quad Y = \begin{bmatrix} 0 & -i \\ i & 0 \end{bmatrix}, \quad Z = \begin{bmatrix} 1 & 0 \\ 0 & -1 \end{bmatrix} \quad (1.4)$$

As can be seen by direct substitution, for all states $|\phi\rangle$, \mathbf{r}_ϕ will be a unit vector. Further if one considers the arbitrary state

$$|\psi\rangle = \sin \theta |0\rangle + e^{i\phi} \cos \theta |1\rangle \quad (1.5)$$

which gets mapped to (see Fig. 1.1)

$$\mathbf{r} = (\cos \phi \sin \theta, \sin \phi \sin \theta, \cos \theta) \quad (1.6)$$

One can see that the mapping is one to one with the z co-ordinate given by the population difference between the two states. The angle the projection of the state onto the x, y plane makes with the x axis (ϕ) shows the phase of the superposition. The position of a state on the Bloch sphere is unchanged by the transformation $|\psi\rangle \rightarrow e^{i\alpha} |\psi\rangle$. However, for a single two state system this global phase factor is irrelevant physically.

The density matrix, conventionally denoted ρ [21], is useful to describe *mixed* states, that is states where there is classical uncertainty about which quantum state the system is located in. Mixed states are distinct from *pure* states. Pure states are those where there is certainty about which quantum

state the system is in.

Suppose the system could be in one of a set of states $|\psi_i\rangle$ ⁴ and the probabilities for each state are given by p_i . The density matrix in this situation is given by:

$$\rho = \sum_i p_i |\psi_i\rangle \langle \psi_i| \quad (1.7)$$

From the definition it is easy to verify that the expectation value for a given quantity associated with a given operator M is

$$\langle M \rangle = \text{Tr}(\rho M) \quad (1.8)$$

where Tr denotes the trace. Again from the definition, one can verify that the time evolution of the density matrix under the action of the Hamiltonian H is given by ($\hbar = 1$)

$$\dot{\rho}(t) = -i[H, \rho(t)] \quad (1.9)$$

Another property of the density matrix is that it has a trace of one. This can be seen by considering the expectation value of the identity operator. Further to this, because the eigenvalues are real and positive, we have $\det(\rho) \geq 0$.

For a mixed state, one can define a Bloch vector in the same manner as for a pure state.

$$\mathbf{r}_\rho = (\text{Tr}(\rho X), \text{Tr}(\rho Y), \text{Tr}(\rho Z)) \quad (1.10)$$

In fact, the following identity, which is valid for all 2×2 Hermitian matrices,

$$\rho = \frac{1}{2} (\text{Tr}(\rho)I + \text{Tr}(\rho X)X + \text{Tr}(\rho Y)Y + \text{Tr}(\rho Z)Z) \quad (1.11)$$

shows that again there is a one to one mapping between the state of the system ρ and a 3-vector. This time however the result $|\mathbf{r}| = 1$ which was true for pure states, gets replaced with $|\mathbf{r}| \leq 1$. This can be seen from

$$\det \rho = 1 - X^2 - Y^2 - Z^2 \geq 0 \quad (1.12)$$

$$\Rightarrow X^2 + Y^2 + Z^2 \leq 1 \quad (1.13)$$

Thus we have the situation in which an arbitrary mixed state gets mapped onto the unit ball. Two measures of the degree to which a state is a mixed

⁴Here we will assume that the $|\psi_i\rangle$ are orthogonal to one another. This assumption doesn't need to be made but makes the argument simpler. If the $|\psi_i\rangle$ weren't orthogonal the resulting density matrix could be diagonalised and the new eigenvalues p'_i and eigenstates $|\psi'_i\rangle$ used instead

state, $\text{Tr}(\rho^2)$ (which is the sum of the squares of the probabilities for orthogonal $|\psi_i\rangle$) and $|\mathbf{r}|^2$, are related by the following.

$$\text{Tr}(\rho^2) = \frac{1 + |\mathbf{r}|^2}{2} \quad (1.14)$$

1.3.1 Qubit dynamics and the Bloch sphere

The real power of the Bloch sphere formalism comes through its use in understanding the dynamics of single qubit systems. The dynamics of states under the action of a time independent Hamiltonian, H , can be described simply as a spinning about a particular axis on the Bloch sphere.

Consider the Hamiltonian

$$H = \omega_0 |0\rangle \langle 0| + \omega_1 |1\rangle \langle 1| \quad (1.15)$$

This can be rewritten

$$H = \frac{\omega_1 - \omega_0}{2} Z + \frac{\omega_1 + \omega_0}{2} \quad (1.16)$$

The term $(\omega_1 + \omega_0)/2$ can be safely ignored for a single qubit as it only causes irrelevant global phase shifts. The second term on the Bloch vectors can most easily be seen in the Heisenberg picture. In this case the Heisenberg equations of motion are

$$\dot{X} = -\delta Y \quad (1.17)$$

$$\dot{Y} = \delta X \quad (1.18)$$

$$\dot{Z} = 0 \quad (1.19)$$

These have the solution

$$X(t) = X_0 \cos(\delta t) - Y_0 \sin(\delta t) \quad (1.20)$$

$$Y(t) = Y_0 \cos(\delta t) + X_0 \sin(\delta t) \quad (1.21)$$

$$Z(t) = Z_0 \quad (1.22)$$

Thus the initial state just precesses about the z -axis with angular frequency $\delta = \omega_1 - \omega_0$. For a spin-half system in a magnetic field, this is called Larmor precession [22] and is analogous to the classical precession of a gyroscope.

The above can be generalised to an arbitrary Hamiltonian with the help of Eq. 1.11. A Hamiltonian H , will cause the rotation of states on the Bloch

sphere with an angular frequency given by the generalised Rabi frequency

$$\Omega_g = \sqrt{\text{Tr}(HX)^2 + \text{Tr}(HY)^2 + \text{Tr}(HZ)^2} \quad (1.23)$$

about the axis

$$\frac{(\text{Tr}(HX), \text{Tr}(HY), \text{Tr}(HZ))}{\Omega_g}. \quad (1.24)$$

A very common situation is where there is an energy gap between the two states $|0\rangle$ and $|1\rangle$ and you are driving the system with a time-dependent perturbation with a frequency approximately commensurate with the energy difference. For example, when driving an optical transition of an atom coherently, one has the following Hamiltonian [23]

$$H = \hbar\omega_e |e\rangle \langle e| + \hbar\omega_g |g\rangle \langle g| - E \cos(\zeta t)(P |g\rangle \langle e| + P^* |e\rangle \langle g|) \quad (1.25)$$

Here P is the transition dipole moment. For a single electron atom this is equal to $e \langle g|x|e\rangle$, where e is the electron charge and x is the position operator for the electron. Without loss of generality P can be assumed to be real. Here x is assumed to be in the same direction as the applied electric field E . Another example of a two level system driven close to resonance is in a magnetic resonance experiment. A large DC magnetic field is applied along the z axis and a much smaller AC field applied in a perpendicular direction. The Hamiltonian in this case is given by

$$H = \frac{\mu(B_0 Z + B_1 \cos(\zeta t)X)}{2} \quad (1.26)$$

The two situations are formally equivalent. Both the Hamiltonians can be written in the form

$$H/\hbar = \frac{\Delta}{2} Z + \frac{\Omega}{2} \cos(\zeta t)X \quad (1.27)$$

Here the *Rabi frequency* Ω is given by PE/\hbar for the optical case and $\mu B_1/\hbar$ for the magnetic case. In the parameter regime $\Delta \gg \Omega$ (which is always the case for optical systems) the perturbation caused by the second term in Eq. 1.27 will be small, except when $\zeta \approx \Delta$. On the Bloch sphere the term $\frac{\Delta}{2}Z$ causes a fast rotation about the Z axis, the term $\Omega \cos(\zeta t)X$ will oscillate between causing positive and negative rotations about the X axis of the Bloch sphere. If the rate of this oscillation is the same as the rate at which the state is spinning around the Z axis the effects of this perturbation will combine constructively during each trip round the Bloch sphere. This can be seen mathematically in the interaction picture where the evolution due to $\hbar\zeta/2 Z$ is taken out of the states. This is equivalent to looking at

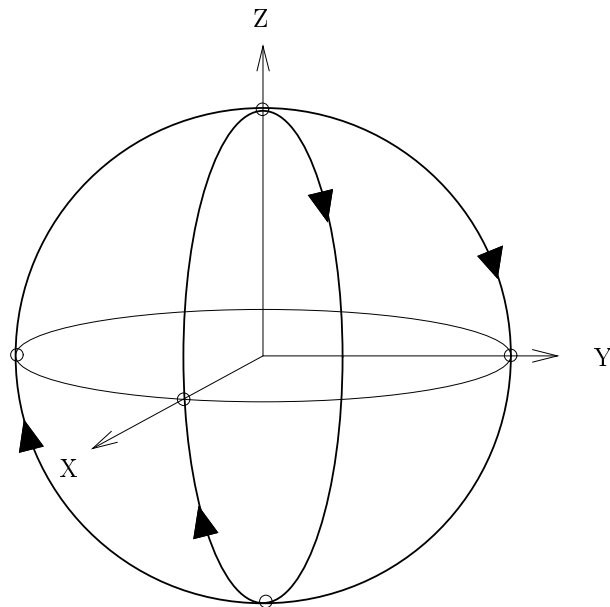


Figure 1.2: The trajectories on the Bloch sphere of the ground state, for two resonant driving fields with the phases differing by 90° .

the state of the Bloch vector in a co-ordinate frame rotating about the Z axis with angular frequency ζ . After the *rotating wave approximation*, that neglects the terms that are now oscillating at a frequency 2ζ , the Hamiltonian becomes

$$H = \frac{\delta}{2}Z + \frac{\Omega}{2}X \quad (1.28)$$

Here $\delta = \Delta - \zeta$. If you consider the case of resonant excitation ($\delta = 0$) you can see from Eqns. 1.23 and 1.24 that the dynamics will be a rotation about the X axis at frequency Ω . This is the well known Rabi flopping phenomenon. If the phase of the driving field was shifted by ϕ , the axis about which the states were precessing would be shifted by ϕ along the equator. The effect of the detuning is to cause the rotation axis to move off the equator and the rate at which the state precesses is given by the *generalised* Rabi frequency $\sqrt{\delta^2 + \Omega^2}$.

1.3.2 Damping and the Bloch sphere

In the above, all coupling of the qubit to the environment, apart from that due to the coherent driving, has been ignored. Consequently, the results are only valid for times short compared to times over which the system interacts with the environment. Here we shall introduce a description of the damping process which simplifies the dynamics down to two variables T_1 and T_2 . This model was first put forward by Bloch when introducing his now ubiquitous

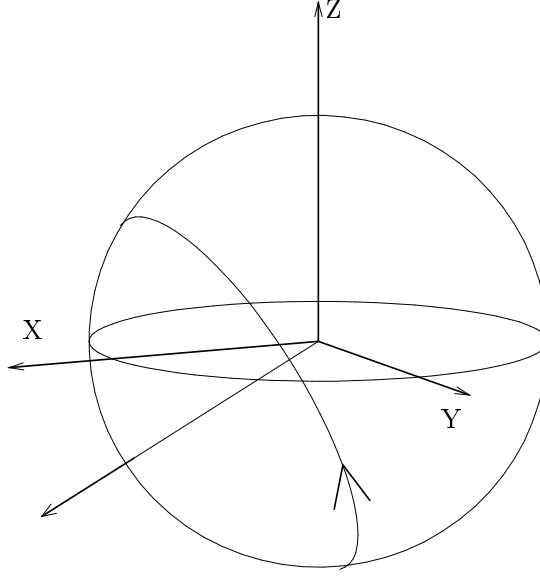


Figure 1.3: The trajectory on the Bloch sphere of the ground state being driven off resonance, in this case $\delta/\Omega = 0.5$

Bloch equations [24]. While for many situations describing the damping by T_1 and T_2 is very useful, in solids often gross approximations must be made regarding the dynamics of the environment of the qubit and the nature of the coupling. For a formal approach to the damping of quantum mechanical systems see [25, 26].

In the T_1 , T_2 approximation the equations describing a damped Bloch vector are:

$$\langle \dot{X} \rangle = -\frac{1}{T_2} \langle X \rangle \quad (1.29)$$

$$\langle \dot{Y} \rangle = -\frac{1}{T_2} \langle Y \rangle \quad (1.30)$$

$$\langle \dot{Z} \rangle = -\frac{1}{T_1} (\langle Z \rangle - Z_0) \quad (1.31)$$

Here Z_0 is the Z value at thermal equilibrium. Because of their roots in magnetic resonance T_1 and T_2 are known as the *longitudinal* and *transverse* relaxation times respectively.

As an example, we now consider damping of our qubit analogous to spontaneous emission in an atom. This gives an equation of motion for the density matrix of the form[26]

$$\begin{aligned} \dot{\rho} = & \frac{\gamma}{2}(N+1)(2\sigma_- \rho \sigma_+ - \sigma_+ \sigma_- \rho - \rho \sigma_+ \sigma_-) \\ & + \frac{\gamma}{2}N(2\sigma_+ \rho \sigma_- - \sigma_- \sigma_+ \rho - \rho \sigma_- \sigma_+) \end{aligned} \quad (1.32)$$

Here $N = (\exp(\hbar\omega/kT) - 1)^{-1}$ describes the temperature of the system's surroundings, $\sigma_+ = |0\rangle\langle 1|$ is the raising operator and $\sigma_- = \sigma_+^\dagger$ is the lowering operator.

This gives the following equations of motion for the Bloch vector.

$$\langle \dot{X} \rangle = -\frac{1}{2T_1} \langle X \rangle \quad (1.33)$$

$$\langle \dot{Y} \rangle = -\frac{1}{2T_1} \langle Y \rangle \quad (1.34)$$

$$\langle \dot{Z} \rangle = -\frac{1}{T_1} \left(\langle Z \rangle + \frac{1}{2N+1} \right) \quad (1.35)$$

where $1/T_1 = \gamma(2N+1)$ and $-1/(2N+1)$ is the Z value at thermal equilibrium. You can see that associated with population decay you have a decay in the coherence — in this situation $T_2 = 2T_1$. It is true in general that population decay always causes phase decay of this magnitude and as a result we have the inequality

$$T_2 \leq 2T_1 \quad (1.36)$$

The transverse relaxation time can be shorter than twice T_1 because of processes that cause a loss of coherence only. These can be thought of as being due to fluctuations in the frequency splitting between the ground and excited states, which in turn cause fluctuations in the speed of the precession around Z . This causes a loss of information about the phase of any superposition state without any population damping.

1.4 Efforts toward experimental quantum computing

Many proposals for realising experimental quantum computing have been put forward⁵ and the list discussed here is by no means exhaustive. Indeed in the author's opinion the field is characterised to some extent by high profile proposals that have only been investigated to the level of “back of the envelope calculations” before being published. The schemes discussed here are those the author believes have the most well established fundamentals.

⁵Rare-earth and other optically based quantum computing schemes in solids will be discussed in Chapter 4.

1.4.1 Liquid state NMR

Liquid state NMR has provided the most successful demonstrations of quantum computing to date, although there are fundamental difficulties in scaling to large numbers of qubits. Currently about 5 qubits is the state of the art [29]. Furthermore NMR quantum computing has direct parallels with the quantum computing attempts described in this thesis. For these two reasons NMR quantum computing will be described in the most detail of all the quantum computing proposals described here.

To investigate NMR the sample is placed in a large, steady and homogeneous magnetic field. A set of smaller coils are placed perpendicular to the large DC coils both to provide RF driving fields and for detection. By convention, the strong magnetic field is applied in the Z direction and the field from the driving/detection coils placed perpendicular to that, leading to a Hamiltonian of the form

$$H = \mu(B_0 Z + B_1(t)X) \quad (1.37)$$

where X and Z are Pauli spin operators and B_0 and $B_1(t)$ are the large static and smaller driving magnetic fields respectively.

The detection is based on the bulk magnetisation of the sample. Due to the small magnetic moment of the nuclei this magnetisation is very small. The component of the magnetisation parallel to the Z axis would be very difficult to observe over the large DC field. However, under the action of the $\mu B_0 Z$ term, the magnetisation components perpendicular to the Z axis precess around the Z axis at the angular frequency $\mu B/\hbar$. This small voltage induced in the driving/detection coils can be detected easily.

The steady magnetic field should be made as large as possible. This large magnetic field is important for a number of reasons. Even for the largest fields, the energy difference between spin states $\approx \mu_N B$ is much smaller than $k_B T$. Because the signal extractable is proportional to the population difference, the stronger B the bigger the signal. Large fields also improve spectral resolution. The coherence times and therefore linewidths are only weakly dependent on the magnetic field strengths, whereas splittings between the resonant frequencies of different nuclei increase linearly with field.

Nuclear spin states in liquids are an ideal place to store quantum information, with coherence times generally being measured in seconds or minutes. The robust nature of the nuclear states in such a chaotic environment as a liquid is due to differing time-scales. The orientation of molecules in a liquid is changing rapidly compared to the resonant frequencies of the nuclear

spin transitions, so the effect of the fluctuating magnetic field from outside a given molecule averages out. Indeed, if the sample is frozen, the spectral lines become much broader. This is due to a marked increase in both the homogeneous and inhomogeneous broadening in the system. The homogeneous linewidth, or the linewidth of each individual nucleus, becomes much broader because couplings to nuclei outside the molecule now become important. The relative orientations of all the nuclei are now more or less fixed, allowing cross relaxation and similar effects to take place. Furthermore because no crystal is ever perfect, each nuclei now exists in a slightly different environment. This leads to a spread in resonant frequencies or inhomogeneous broadening.

However, even in a liquid the magnetic fields that have their origin within a molecule do not average to zero, this can be seen as frequency shifts in the spectra of liquids. Shifts in the spectral lines due to differences in the chemical environments (*chemical shifts*) of nuclei within a molecule are generally in the range of tens to hundreds of kilohertz. These shifts are much larger than the linewidths and allow inequivalent nuclei/qubits in a molecule/computer to be addressed individually based on their resonant frequency. The linewidths are indeed small enough for the frequency shift due to the change in the spin state of another nucleus within the molecule to be resolvable. It is this interaction between the two nuclei that allows one to perform two qubit gates. These interactions come in part from simple magnetic dipole-dipole interactions and in part from *J-coupling* where the interaction is mediated by shared electrons in a chemical bond.

Because the spin-spin interactions and the chemical shifts provide a wealth of information about the molecule being studied, techniques for studying them were very advanced before interest arose in quantum computing [30].

For simplicity we shall now restrict our attention to a molecule containing two spin-1/2 nuclei. In this case the Hamilton describing our system can be written ($\hbar = 1$):

$$H = \sum_{i=1,2} \frac{\omega_i}{2} Z_i + \frac{\alpha}{2} Z_1 Z_2 + H_{\text{RF}} + H_{\text{env}} \quad (1.38)$$

Here ω_i are the resonant frequency for each of our two nuclei and are due to the splitting produced by the magnetic field and chemical shifts. The term $\frac{\alpha}{2} Z_1 Z_2$ describes the coupling between the two nuclei. H_{RF} describes the action of driving fields and H_{env} describes the unwanted coupling to the environment which leads to dissipation. Z_i is the Pauli Z operator for the i th spin.

The steady state of such a system when coupled to a bath of temperature

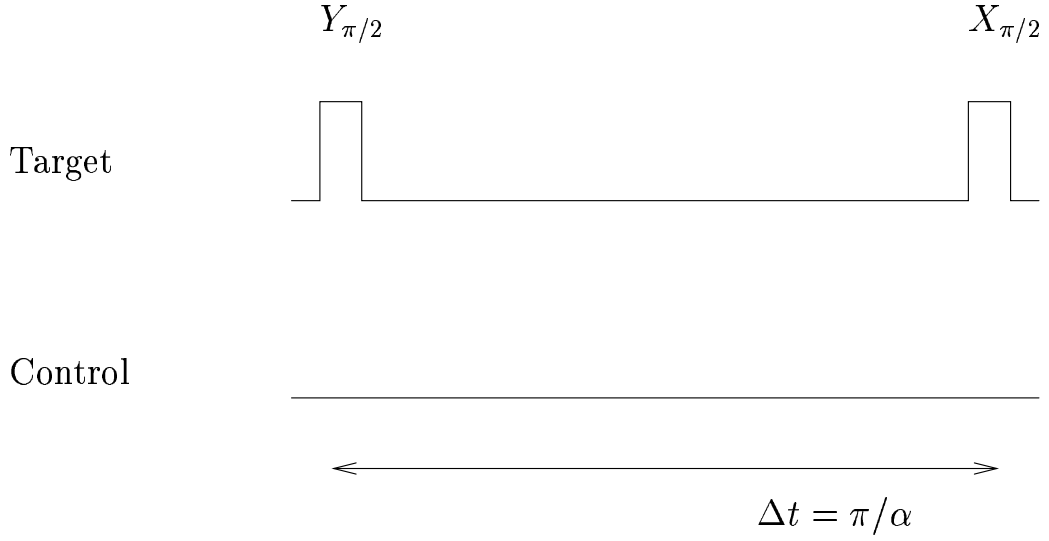


Figure 1.4: Pulse sequence used to achieve CNOT in NMR quantum computing

T is dominated by the first term $\sum_{i=1,2} \frac{\omega_i}{2} Z_i$ and because we are dealing with the situation $k_B T \gg \hbar \omega_i$ the thermal state is highly mixed.

The terms $\frac{\omega_i}{2} Z_i$ can be removed by moving to the appropriate interaction picture. We shall neglect dissipation by assuming that the terms in H_{env} are small enough to be ignored for the time over which the computation takes place. It shall also be assumed that both the frequency difference between the two nuclei and the Rabi frequencies available from the driving fields are much bigger than the interaction strength α . The fact that this approximation can be made means that by applying pulses of the right frequency, phase, intensity, and length the driving fields can cause instantaneous, arbitrary single qubit operations.

In order to show that we can apply a universal set of gates, it suffices to show that, in addition to single qubit rotations, a CNOT gate is possible.

Now the coupling term $\frac{\alpha}{2} Z_1 Z_2$ in the Hamiltonian of Eq. 1.38 can be seen as causing a rotation of the state of one qubit on the Bloch sphere at an angular velocity of $\pm\alpha$ conditional on whether the other is the excited state or not. Of course such a description is valid only if the other qubit is in the ground or excited state and not some other linear combination. However, such a description is sufficient to describe the action of the pulse sequence on the member of the computational basis $\{|00\rangle, |01\rangle, |10\rangle, |11\rangle\}$. If the target nucleus is initially in the ground state, then the first pulse, which provides a rotation of $\pi/2$ about the Y axis, moves the state to being along the X axis. Under the action of the coupling term this state vector precesses around the equator and at a time π/α later is either pointing along

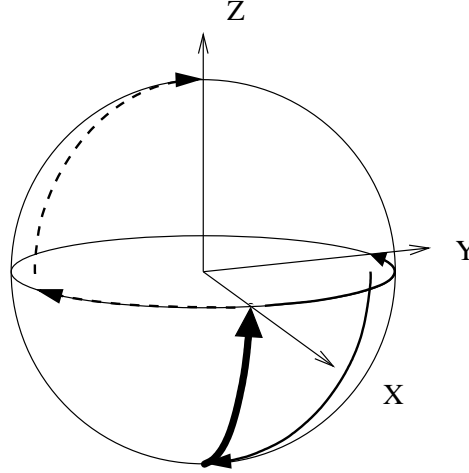


Figure 1.5: The trajectories on the Bloch sphere for the target qubit during CNOT operation. The target starts off in the ground state and the two trajectories correspond to the control being either in the ground state or the excited state.

the positive or negative Y axis. The actual direction is of course conditional on which direction the state was precessing, which in turn was conditional on whether the control qubit was in the ground or excited state. The second pulse rotates the state vector $\pi/2$ around the Y , which takes the qubits either to the ground or excited state. These two trajectories are shown in Fig. 1.5. The control qubit is either in the ground or excited state for the whole operation and thus is insensitive to the interaction.

The problem with liquid state NMR quantum computing is DiVincenzo's requirement number two (see Sec. 1.2), namely to be able to initialise the system in a particular state. As already mentioned, the current experiments have been done with the temperature large compared to the transition frequency resulting in highly mixed states. In order for a pure initial state the ratio between scaled temperature and scaled transition frequency would ideally be large compared to one, instead it is

$$\frac{\hbar\omega}{kT} \approx 10^{-6}. \quad (1.39)$$

There is no way of avoiding this highly-mixed initial state. Reducing the temperature helps but it cannot be reduced very far or the sample will freeze. Increasing the Zeeman splitting in order to make the ratio of Eq. 1.39 more respectable is not fruitful either. Modern NMR spectrometers work with fields similar to the highest static fields available — further increasing $\hbar\omega$ by the many orders of magnitude that would be required is not currently possible.

There are two techniques for getting round the problem of state initial-

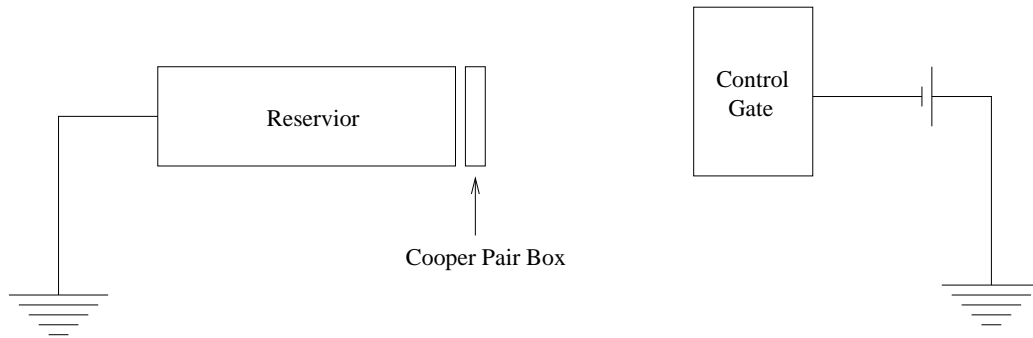


Figure 1.6: Simplified view of a Cooper-pair-box based qubit. The reservoir and Cooper-pair-box are made of superconducting material and separated by a Josephson junction. The two computation basis states in such a qubit would be whether an excess Cooper pair is in the Cooper pair box or on the reservoir. By changing the field on the control gate the energy differences between the two computational basis states can be tuned.

isation. These are *logical labelling* and *temporal labelling*[31]. They both provide a method for extracting a signal proportional to what would have resulted if the system was initially in a pure state. The problem they and all of their variants share is that the strength of this signal decreases exponentially as the number of qubits increases. This means that it is not possible to scale to a large number of qubits.⁶

Another, perhaps less severe, problem for NMR quantum computing is that the interaction is on all the time. This means you have to employ refocusing pulses in order to turn off all but the wanted interactions for each computational step. There are methods for achieving this refocusing with an overhead that goes up polynomially in the number of qubits. [33]

1.4.2 Superconducting qubits

Electrons are great for classical computing and people are now very good at manufacturing small electronic devices. With the nano-fabrication techniques available, one can routinely make conductors sufficiently small for the increase in potential caused by adding one electron to be significant. This leads to the classical effect known as Coulomb-blockade [34] in which movement of an electron onto a conducting region can be blocked by the excess of one electronic charge. Single electron transistors (SET) [35, 36] that are based on this effect can measure with good fidelity the movements of single charges. What stops single electrons being useful in implementing single

⁶It should be mentioned that there are actually schemes for state labelling that don't have a exponential signal decrease [32]. However such schemes are not practical with the very small polarisations that are present in liquid state NMR.

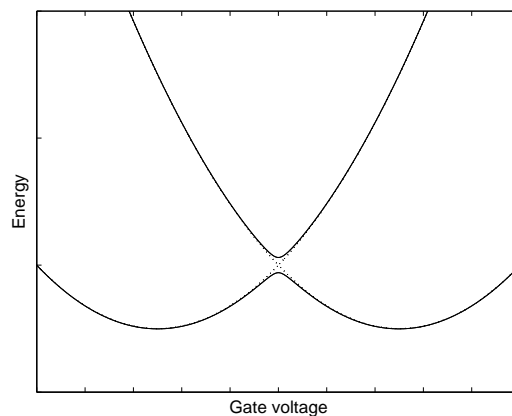


Figure 1.7: Energy level diagram for stationary states of the Cooper pair box as a function of control gate voltage. The left minima corresponds to N Cooper pairs in the box and the right to $N + 1$ Cooper pairs. The dotted line represents the absence of Josephson tunnelling. Only the N and $N + 1$ states are shown here. In reality the figure should be periodic along the x -axis with minima corresponding to $\{\dots N - 1, N, N + 1, N + 2 \dots\}$ in the Cooper-pair box.

qubits is their very short coherence times. These are hundreds of picoseconds at best [31]. Because of their charge, electrons strongly interact with everything, especially the ions of the host lattice. One way of improving this situation dramatically is using superconducting materials. In these materials, at temperatures below their transition temperature, the electrons pair up into *Cooper pairs*. These electrons that make up these Cooper pairs are bound by their interaction. The net interactions of a pair and the lattice are much smaller than those of single electrons. As a result the coherence times for qubits based on Cooper pairs can be much larger — typically nanoseconds.

A simplified description of such a qubit is shown in Fig. 1.6. The diagonal terms of the Hamiltonian for the qubit are determined by the potential difference between the box and the reservoir. This depends both on the self capacitive charging energy for the box and on the effect of the control gate, which is capacitively coupled to the box. The off-diagonal terms of the Hamiltonian are constant and are given by the tunnelling rates through the Josephson junctions. In experiments, the readout is effected by having the Cooper pair box weakly coupled to a “probe” via an incoherent tunnel junction. The presence of an excess Cooper pair on the box will cause a current through this probe when it jumps off.

Nakamura and his coworkers at NEC in 1997 [37] showed an effect similar to Rabi flopping with such a system. They set the control gate so that they were operating at, for example, the left minima of Fig. 1.7. After sufficient time for the system to fall into the ground state the voltage was ramped

quickly to the anti-crossing. Ideally this would be done much quicker than any other of the system dynamics and the *sudden approximation* [38] could be made.

The eigenstates for the system at the anti-crossing are linear combinations of those states with definite numbers of pairs. An initial state with a definite pair number will undergo a nutation between N and $N + 1$ Cooper pairs on the box. After waiting for a chosen length (Δt) of time, the voltage is quickly ramped back away from the anti-crossing. By looking for an excess Cooper-pair tunnelling through the probe junction, the probability of finding the qubit in the excited state can be measured. The probe current shows a sinusoidal variation as the length of time at the anti-crossing (Δt) is varied.

Very recently, the same group at NEC has shown similar oscillations for two Cooper pair boxes capacitively coupled together [39]. They infer from their measurements that the two qubits were at some part of the process entangled, although no direct measurements were made.

Many of the problems encountered while carrying out these experiments came from the extreme timescales involved. While the coupling can be made large enough for the coherence time to be large compared to the interaction, other factors are also important. The coherence time of ≈ 10 ns [39] was estimated. The Josephson coupling terms were of the order of 10 GHz. This means that rise times much quicker than 100 ps would be required to make the sudden approximation strictly valid. This pushes the limits of available technology and rise times of approximately 35 ps were estimated for the experiment.

In these experiments the coupling between the Cooper-pair box and the probe was constant. In order that the decoherence caused by this coupling be kept to a reasonable level the coupling must be weak. Given this situation it would be difficult to imagine that the near perfect readout that can be achieved with ion traps could be attained.

1.4.3 Ion traps

In contrast to superconducting qubits, qubits based on the hyperfine structure levels of trapped ions are very robust. Coherence times in excess of 10 minutes have been realised [40]. For this reason they have found applications in time and frequency standards. Also the state of qubits based on single ions can be read out with very close to unit fidelity.

In 1995 Cirac and Zoller [41] proposed a method for achieving the one remaining piece of the puzzle, qubit-qubit interactions. They proposed using a harmonic trap that provided tight confinement in two dimensions and looser



Figure 1.8: In the Cirac-Zoller scheme the qubits would be stored in a chain of ions in a linear trap. Interactions would be effected using the motion of the atoms along the weaker axis of the trap.

confinement in the third. The confinement in each direction would need to be sufficiently large so that in the motional ground state the atom would be trapped within a wavelength of the light used to probe the ions. In this “Lamb-Dicke limit”, the vibrational structure on the optical spectra can be resolved.

It was envisioned that the trap would be loaded with a handful of ions and that they would be cooled to their motional ground states by sideband cooling. Because of coulomb repulsion between the ions, they would form a string of ions lined up along the weaker axis of the trap as shown schematically in Fig. 1.8. The separation between the ions would be a few micrometres allowing the ions to be addressed individually with a focused laser beam. The qubits would be stored in the ground state structure of the ions. Addressing one of the ions with a laser one could deterministically affect the collective motion of the whole group, because the vibrational structure is resolvable optically. In this manner interactions between the qubits could be effected.

When compared against the DiVincenzo criteria, trapped ion quantum computing measures up very well. There are however serious obstacles that need to be overcome before the approach can be extended from the currently small number of qubits.

A review of the issues involved in implementing this scheme experimentally can be found in Ref. [42]. Currently operations have been achieved on a small number of ions, including the entanglement of four ions [43]. The main problem to be overcome is to avoid the heating of the ions’ motion caused to the time varying trapping potential, the mechanism for this heating is poorly understood.

1.4.4 Linear optics quantum computing

Photons make ideal qubits, with it possible to encode the quantum information in a number of ways. One possibility is in polarisation, where the $|1\rangle$ state is represented by one particular polarisation and the $|0\rangle$ state by an orthogonal polarisation [44]. Another possibility is using photon number states. Single qubit operations can be done easily using standard optical elements such as beam-splitters and wave plates. Single photon detectors now

have quantum efficiencies approaching unity and ever decreasing dark count rates. In addition to this, two qubit entangled states are easily produced using pair generation.

The problem with using photons for quantum computation is performing two-qubit operations. Nonlinear materials provide a mechanism for interaction between photons and have been suggested as a mechanism for two-qubit gates [45, 46]. The problem with such an approach is achieving a high enough nonlinearity such that there is an appreciable effect for just one photon while keeping losses low. Such effects can be seen, with great difficulty, using high finesse optical cavities [47].

A ingenious scheme for doing photon based quantum computation with only linear elements, feed-forwards and photon detectors was put forward by Knill, Laflamme and Milburn [48]. The details are particularly complicated and, for someone that doesn't like aligning one interferometer, the resources needed are breathtaking. However Knill et al. conclude that they have an efficient (in the sense that the required resources grow linearly with the number of qubits and gates) scheme that is robust against errors from photon loss and detector inefficiency.

The scheme achieves conditional phase shifts using auxiliary entangled pairs which are combined to be incident on various ports of an interferometer. Measurements are made on some of the output ports of the interferometer. Depending on the results of the measurement it can be concluded that the measurement induced back action has either caused the gate operation to be a success or a failure. If the gate operation was a success then the photons can be allowed to propagate to the next step in the calculation, if not then the feed-forwards must take appropriate action to send the inputs through the gate again.

One advantage that this scheme has is the simplicity of the physical elements used. While the scheme itself could be described as complex one can make very realistic predictions about how well each element should behave.

Other than keeping a complex array of optics stable enough other technical difficulties in realising this scheme would be in implementing the feed-forwards required and creating a suitable single photon source. Light travels at 1 foot/ns which means that a combination of long lengths of optical fibre and fast switching optical elements will be required. Currently the best single photon sources use parametric down conversion sources. By detecting its twin you know when a photon comes out of such a source with very high fidelity. However you can't trigger the source and you get no warning as to when a photon is coming. In order not to make the feed-forward require-

ments unrealistically stringent, a trigger-able single photon source would be required. Such devices have been proposed [49, 50] but not yet realised.

1.5 Error correction

A remarkable feature of classical computation is how reliable with respect to errors it can be made⁷. While this is due in part to the very low error rates in many of the devices used, error prone devices can also be used effectively without adversely affecting system performance. In general for classical processes these devices are involved in either transmission or storage of data. For example consider the situation where you have a noisy communication channel and you want to tell the person at the other end either ‘yes’ (1) or ‘no’ (0). One way would be to encode yes as 11111 and no as 00000. Suppose that the errors are independent, and the probability of them occurring p , is small enough that things with probability p^3 could be neglected. Now the receiving party would take your transmission and if it consisted of a majority of ones then it would assume that the message was ‘yes’ and ‘no’ if it got a majority of zeros. More sophisticated classical codes for error correcting and checking exist [51]. An example is CD-ROMs, which are used to store large amounts of data in situations where bit errors cannot be tolerated. It does this using a physical format that has a reasonably high error rate while still storing close to the same amount of data as raw encoding.

As well as schemes to overcome the errors in transmission and storage of data, there are methods for performing all of classical computation in a fault tolerant manner [52, 53]. However, due to the very low error rates of electronic logic devices such schemes are only used in specialised circumstances.

When trying to apply similar ideas to quantum computers, three rather formidable difficulties arise [31]:

- It is not possible to clone the quantum state of a physical system/qubit [54, 55].
- A continuum of different errors can affect a qubit.
- Measurement destroys quantum information.

A great deal of theoretical investigation has been carried out into the area of fault tolerant quantum computing.

A chapter in [31] is devoted to the subject and provides an excellent review. Perhaps the most profound result is the so-called threshold theorem.

⁷This thesis was written using Emacs and L^AT_EX on a Dell laptop running GNU/Linux.

The threshold theorem for quantum computation:

Provided the error rate on individual quantum gates is below a certain threshold, it is possible to efficiently perform an arbitrarily large quantum computation.

The most optimistic value of the threshold is of the order of one part in 10^4 [31] which is beyond the fidelity of most current experiments. However, in the absence of dephasing this threshold is not as high as it might appear. If the gate operation was carried out by turning some sort of unitary evolution on for a given length of time the precision in the time which this evolution turned on for need only be 1 part in 10^2 .

1.6 Type-II quantum computing

By anyone's measure, it will be difficult to make a standard (or 'type-I') quantum computer with a large enough number of qubits to be useful. In 2001 Yezpez [56] proposed a hybrid classical-quantum computer or type-II quantum computer. Such a computer would consist of a large number of nodes, each of which consisted of a quantum computer with a small number of qubits. The communication channels between these nodes would be classical. Modelling of the diffusion equation has been proposed [57] and demonstrated using NMR style quantum computing with gradient fields [58]. A large type-II quantum computer is a lot easier to construct,⁸ than a standard quantum computer. However such a computer wouldn't have the advantage over a classical computer that a large (type-I) quantum computer would. As there is only classical interaction between each node, for such a computer to make sense each node must be able to out perform the best classical process. Because of the inherent difficulty in making these little quantum computers it could easily be assumed that such a computer would operate slower than the best classical device. Thus, one is left with the situation that the number of qubits in each node must be large enough for the exponential speedup of quantum parallelism to push you past the best classical computer. This is the same situation as for standard quantum computers.

⁸The author would like to be the first to suggest making a world-wide type-II quantum computer using NMR spectrometers connected via the internet.

1.7 Quantum state tomography

Quantum state tomography will be important in the diagnosis of any quantum computer. Given one instance of a quantum system in an unknown state, quantum mechanics tells us it is impossible to completely determine the state of the system. Quantum state tomography is the method by which the state of the system, ρ , can be determined from measurements of a collection of systems in such a state. These collections can either be an ensemble of systems such as in NMR quantum computing, or a number of “shots” of a single quantum system, such as with single-photon based experiments.

Quantum state tomography was first proposed for continuous variable systems [59] but we will restrict ourselves to the much simpler case of finite dimensional systems, in particular those comprising of a few qubits.

Quantum state tomography is best understood by treating the operators of a Hilbert space as another inner-product space [60]. We will call the space of quantum states the Hilbert space and the space of operators the inner-product space so that they can be distinguished although mathematically they are both Hilbert spaces and both inner-product spaces.

The inner product used is the Hilbert-Schmidt inner product [31], and the inner product between two operators A and B , is given by

$$(A, B) = \text{Tr}(A^\dagger B) \quad (1.40)$$

For a Hilbert space of dimension N , this inner product space has dimension N^2 and an orthonormal basis given by the N^2 operators E_i . The matrix representation of each E_i consists of all zeros except one member which is a one.

Given a set of operators $\{A_1, A_2, \dots\}$ and their expectation values for a particular state $\{a_1, a_2, \dots\}$ we have the following relationship.

$$a_i = \text{Tr}(A_i \rho) \quad (1.41)$$

$$= (A_i, \rho) \quad (1.42)$$

$$= \sum_{j=1}^{N^2} (A_i, E_j)(E_j, \rho) \quad (1.43)$$

In the situation where there are N^2 linearly independent operators A , the density matrix can easily be found from the measurements. Defining

$M_{ij} = (A_i, E_j)$ we have

$$(E_i, \rho) = \sum_{j=1}^{N^2} (M^{-1})_{ij} a_j \quad (1.44)$$

$$\Rightarrow \quad \rho = \sum_{i=1}^{N^2} \sum_{j=1}^{N^2} (M^{-1})_{ij} a_j E_i \quad (1.45)$$

In many situations, the set of measurements made will not have exactly N^2 members and perhaps will not be linearly independent. In particular when the measurements over-determine the density matrix the Morse-Penrose pseudo-inverse [61] can be used. In this situation M^{-1} is replaced with $(M^\dagger M)^{-1} M^\dagger$. The reconstructed density matrix is a least squares fit (in terms of the norm associated with the Hilbert-Schmidt inner product) to the density matrix. In cases where the measurements under-determine the density matrix or other cases where the problem of determining ρ is “ill-posed”, regularisation methods used in the field of inverse problems [61] are useful.

Quantum state tomography is particularly simple for one qubit. In that case four operators that form an orthonormal basis of the inner-product space are the Pauli operators $\{I, X, Y, Z\}$. Of course $\text{Tr}(\rho I) = 1$ so the only measurements that need to be made are of $\{X, Y, Z\}$, which confirms what we already know from Section 1.3.

For more than multi-qubit systems, one orthonormal basis of the inner-product is made of the operators of the form

$$\Theta_1 \otimes \Theta_2 \otimes \Theta_3 \otimes \dots \quad (1.46)$$

where each Θ independently takes on the values $\{I, X, Y, Z\}$. In particular for a two qubit system, the following operators provide an orthonormal basis

$$\begin{array}{cccc} I_1 \otimes I_2 & I_1 \otimes X_2 & I_1 \otimes Y_2 & I_1 \otimes Z_2 \\ X_1 \otimes I_2 & X_1 \otimes X_2 & X_1 \otimes Y_2 & X_1 \otimes Z_2 \\ Y_1 \otimes I_2 & Y_1 \otimes X_2 & Y_1 \otimes Y_2 & Y_1 \otimes Z_2 \\ Z_1 \otimes I_2 & Z_1 \otimes X_2 & Z_1 \otimes Y_2 & Z_1 \otimes Z_2 \end{array} \quad (1.47)$$

One can see that the number of measurements required to completely characterise a system increases rapidly with the number dimensionality of the Hilbert space. In particular totally describing the state of an N qubit system requires the measurement of $2^{2N} - 1$ real valued parameters.

1.8 Quantum process tomography

Quantum process tomography [62, 63] is an extension of the ideas introduced in quantum state tomography. In this case it is not the state of the system that we are trying to determine but the effect some process has on the system. The measurements that need to be carried out are quantum state tomography on each of the output states corresponding to a complete set of d^2 input states. Here d is the dimensionality of the Hilbert space, and the set of states must be complete in terms of the inner product (1.40) when the states are expressed as density matrices.

Chapter 2

Rare earth ion spectroscopy

Rare earth ions are characterised by partially full $4f$ orbitals and their spectroscopy is dominated by $4f^n \rightarrow 4f^n$ transitions. The electrons involved in these transitions are inside filled $5s$ and $5p$ orbitals, which screen them from perturbations caused by the lattice. The narrow lines caused by this screening have fascinated spectroscopists for a long time. In the days before tunable laser sources huge spectrometers were used to get the required resolution in order that the lines not be instrumentally broadened [65]. The tunable laser sources developed in the 1970s made the resolution required to study *inhomogeneously* broadened aspects of these transitions more accessible. Further to this the holeburning and time-domain techniques that could then be used allowed one to probe the *homogeneously* broadened nature of these transitions. These homogeneous linewidths are up to 10^7 times narrower than the inhomogeneous ones. To date linewidths of around 100 Hz [66] for a transition in the visible and approximately 50 Hz for a transition in the infrared [67] have been reported.

2.1 Homogeneous and inhomogeneous broadening

The processes which broaden the transitions in rare-earth doped solids can be broken up into two categories. These are those that cause *inhomogeneous* broadening and those that cause *homogeneous* broadening. It is the homogeneous linewidth that one would measure if measurements could be made of a single system rather than of an ensemble. The absolute narrowest this can be is determined by the population decay rate. In modern materials such as Y_2SiO_5 which provide a quiet environment this limit has been approached [66] but for most systems magnetic interactions with other spins in the lattice

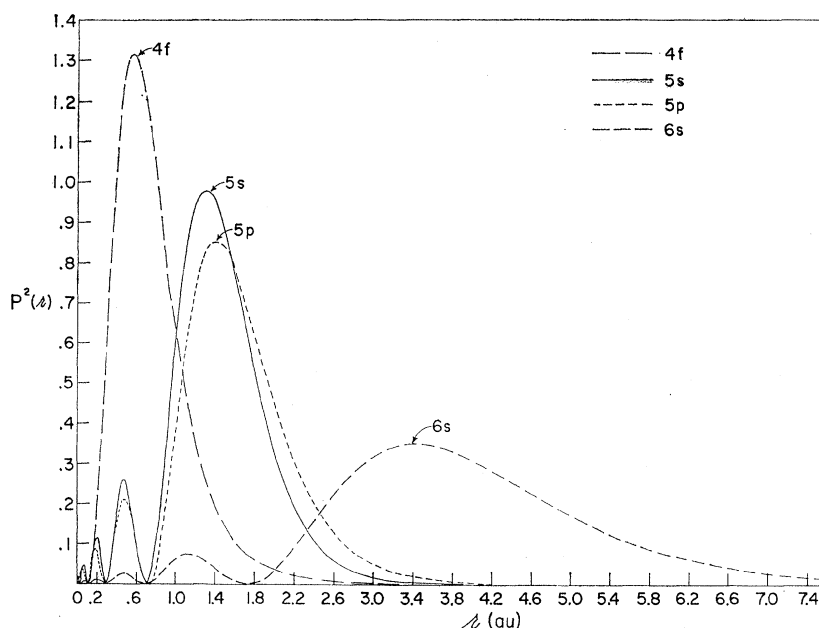


Figure 2.1: Radial distribution functions for rare earth orbitals. The screening caused by the 5s and the 5p orbitals effectively shields the 4f electrons from perturbation. The figure here was drawn for Gd^+ . It was taken from [64].

cause significant excess dephasing.

Crystal strain and similar effects alter the immediate environment around each dopant making each slightly different, resulting in a spread of the resonant frequencies in an ensemble of ions. For the transitions we are interested in this inhomogeneous broadening is generally much larger than the homogeneous broadening and the transitions are called *inhomogeneously broadened*. A large ratio of inhomogeneous to homogeneous broadening is desirable for classical information processing. Transitions where the inhomogeneous broadening is insignificant, compared to the homogeneous broadening, are called *homogeneously broadened*.

2.2 Chemistry and occurrence of the rare earths

The rare earth elements also known as the Lanthanides are the 15 elements between Lanthanum ($Z = 57$) and Lutetium ($Z = 71$) on the periodic table and correspond with the filling of the 4f orbitals.¹ The elements are all strongly electro-positive and their bonding can, to a good approximation, be considered purely ionic. The chemistry of the rare earths is dominated by

¹The are differing views about whether either or both of the two elements on the ends should be included [68].

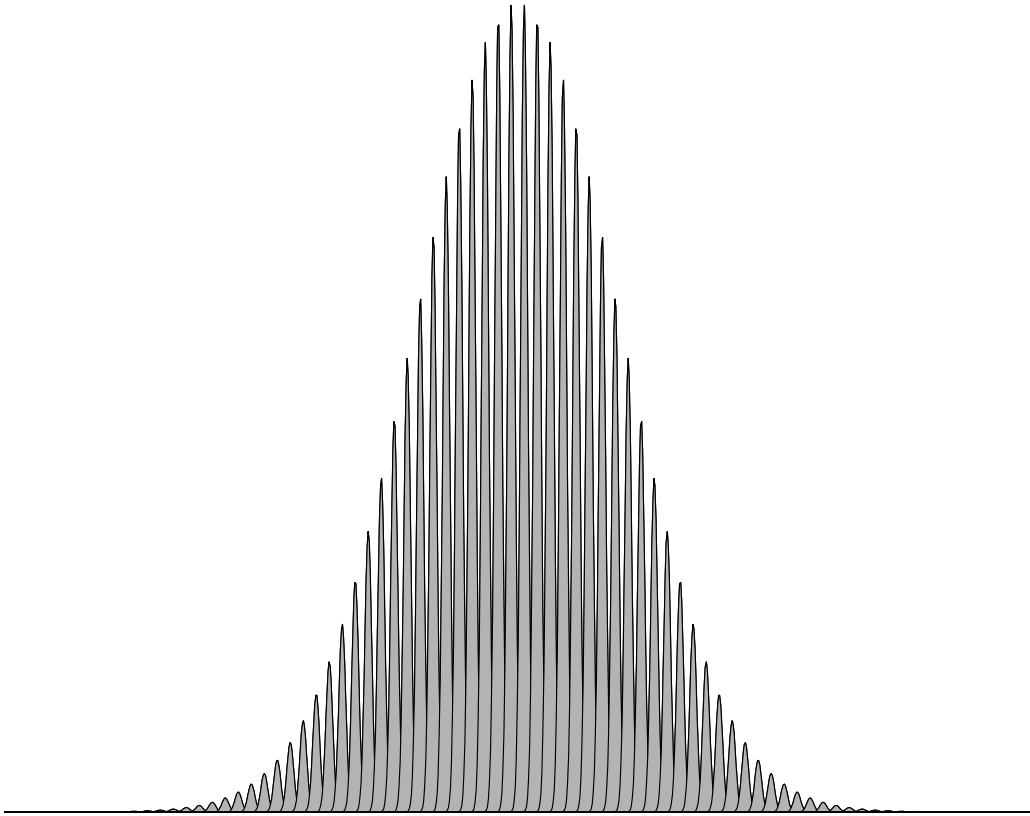


Figure 2.2: Shows the relationship between inhomogeneous and homogeneous broadening. The inhomogeneous line is made up of a continuum of homogeneously broadened packets. The diagram is not to scale, the ratio of inhomogeneous to homogeneous broadening is much smaller than the ratio encountered in physical systems where it can be as high as 10^7 [67].

a single oxidation state (M^{3+}) to an extent unparalleled in the transition metals or the actinides. The most stable M^{2+} and M^{4+} oxidation states are those of Eu^{2+} , Yb^{2+} , Ce^{4+} and Tb^{4+} . These correspond to full, empty or half filled f orbitals ($4f^0$, $4f^7$ and $4f^{14}$) but are not as stable as the elements' 3+ oxidation state. Yttrium has similar chemical properties to the rare earths because of its similar size and 3+ oxidation state. It is often included in discussions of rare earth chemistry.

As the prevalent oxidation states of the rare earths are all the same, the main feature that distinguishes between the elements chemically is ionic size. The ionic radii of the elements steadily and uniformly decrease across the series, an effect known as the *lanthanide contraction*.

The term “rare earth” is a bit of a misnomer. It came about because they were initially discovered in small quantities in oxide mixtures. These were once called “earth” mixtures. The only rare-earth that you would describe as rare is promethium which is radioactive and occurs naturally only in trace amounts associated with uranium [69]. The rarest stable rare earth is thulium and has a similar crustal abundance to iodine [70]. With its abundance of $\approx 2 \times 10^{-5}$ wt. % it is more common than arsenic, mercury, cadmium or selenium, none of which is usually considered rare [71].

2.3 Energy levels of the 4f states

A sketch of the energies of the 4f states to differing levels of approximation is shown in Fig. 2.3. In a coulombic potential, all the f states are degenerate as indicated in Fig. 2.3(a). Spin orbit coupling is large in rare earths due to their low position on the periodic table and this splits the f states into different manifolds as shown in Fig. 2.3(b). As the total angular momentum J is conserved by the spin orbit coupling, J can be treated as a good quantum number and label for the manifolds. It is the spin orbit interaction that primarily determines the frequencies of the transitions. The host dependent interactions can be treated as perturbations. The classic “Dieke” diagram [72, 73] showing the spin orbit levels in lanthanum trichloride is shown in Fig. 2.4.

Fig. 2.3(c) depicts the action of the crystal field on the spin-orbit split manifolds. As already stated the crystal field splittings are much smaller than the spin orbit coupling, generally $\mathcal{O}(100\text{cm}^{-1})$. The crystal field perturbation splits the J manifolds into at most $2J + 1$ components. An important exception to the validity of this is Eu^{3+} where there is a low lying spin orbit level close to the ground state and the small energy gap allows significant

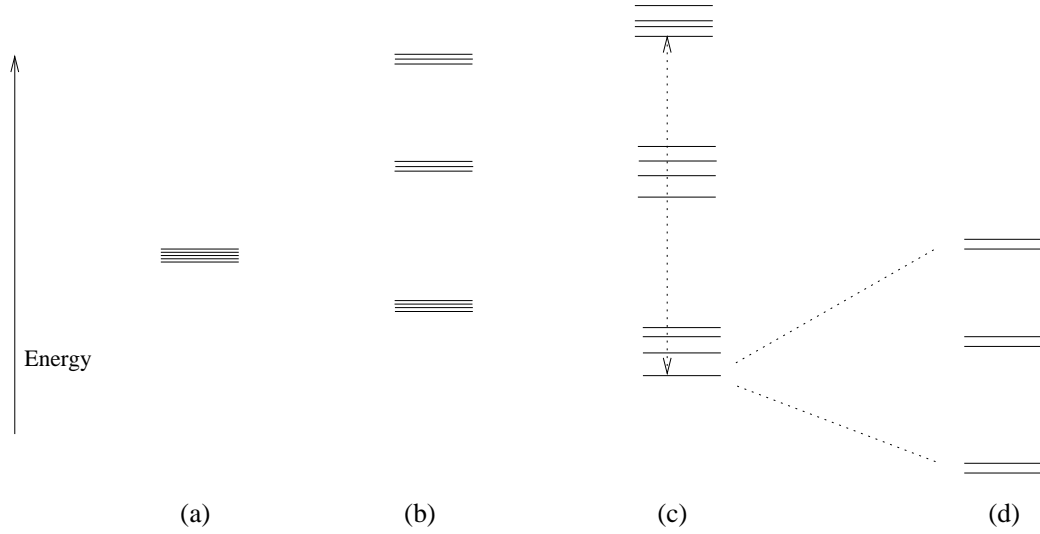


Figure 2.3: Energy levels of the f states of rare earth ions to different levels of approximation. It is drawn for an ion/host system which shows no electronic Zeeman effects to first order, as is the case for both europium and praseodymium in Y_2SiO_5 . The dotted line in (c) represents a “lowest to lowest” transition

mixing between the two manifolds.

When it comes to the magnetic properties of rare earth ions, it is useful to treat ions with an odd number of f electrons differently from those with an even number. Because of the unpaired electron rare earth ions with an odd number of f electrons have ground states that are magnetic doublets (Kramers doublets) with a magnetic moment about that of the Bohr magneton. Both the species studied in this work (Pr^{3+} , Eu^{3+}) have an even number of electrons and therefore no magnetic moment due to electron spin. For sites of axial symmetry or higher, it is possible for the ground state to be a magnetic doublet due to non-zero orbital angular momentum around the symmetry axis (non-Kramers doublet). In sites with less than axial symmetry, such angular momentum is said to be “quenched”. All the states have zero angular momentum because the Hamiltonian no longer commutes with an angular momentum operator for any direction. In such situations the degeneracy in the J manifolds is completely lifted and the states are all electronic singlets.

If we restrict ourselves to non-Kramers ions in low symmetry hosts the next level of detail in the level structure beyond crystal field splitting comes from a range of sources. Electronic Zeeman, nuclear Zeeman, hyperfine and quadrupole interactions tend to be of similar strength and all appear at the level of second order perturbations to the crystal field split lines. The one natural occurring praseodymium isotope ^{141}Pr and the two europium

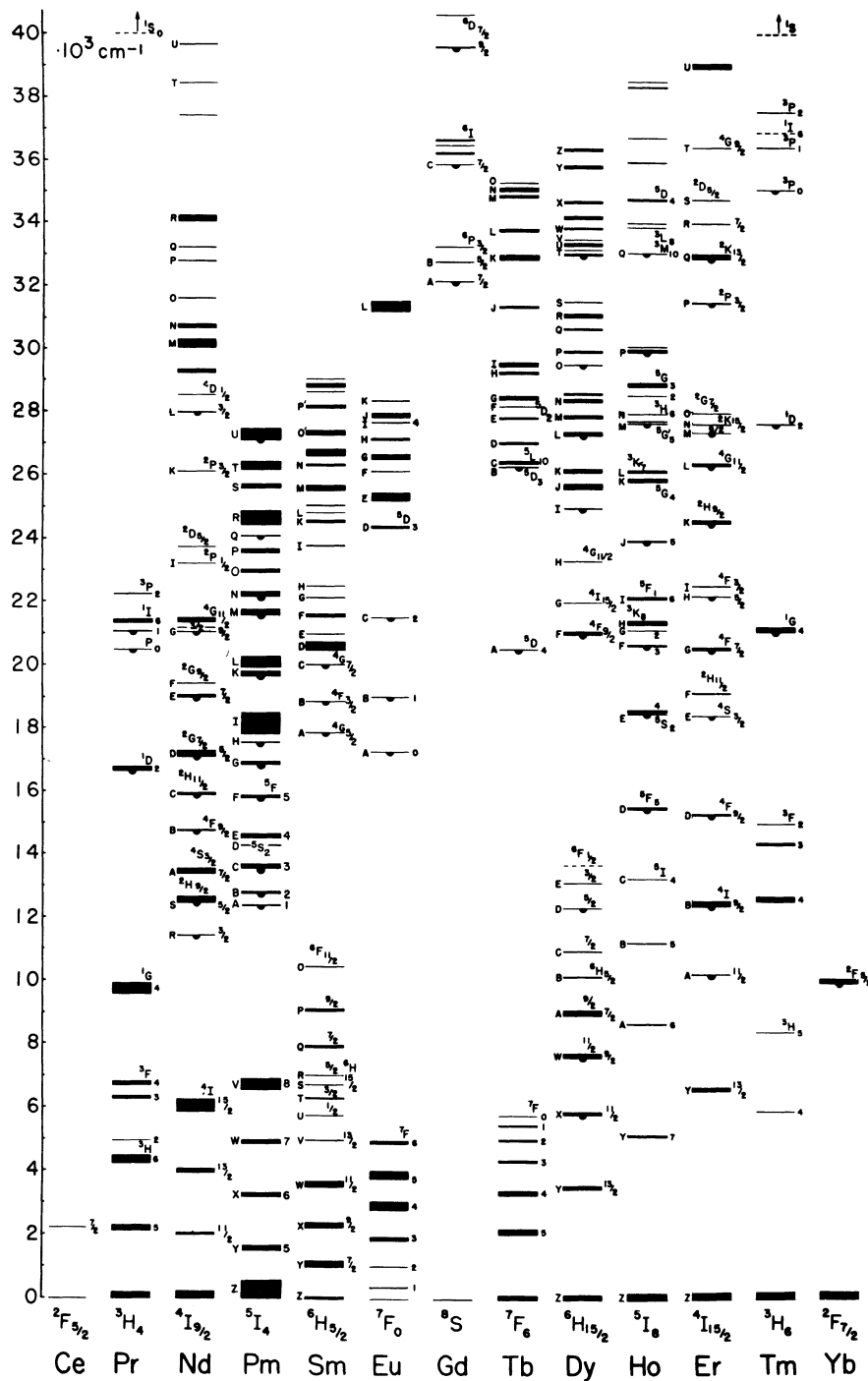


Figure 2.4: The classic Dieke diagram, the energy levels of triply ionised rare earths in LaCl_3 [72, 73]. Because the energy levels are determined predominantly by the spin-orbit interaction rather than the crystal field interaction the energy levels are similar for other hosts. The two transitions of interest to this thesis are from the ground ($^3\text{H}_4$) state to the $^1\text{D}_2$ state of praseodymium and from the ground ($^7\text{F}_0$) state to the $^5\text{D}_0$ of europium. Both of these transitions occur at about $17 \times 10^3 \text{ cm}^{-1}$. This image was scanned from [74].

isotopes ^{151}Eu and ^{153}Eu all have nuclear spin $\frac{5}{2}$ and in zero magnetic field each crystal field split level is broken into three doublets. For the three nuclei we are interested in this splitting is $\mathcal{O}(10\text{MHz})$.

2.4 Theory of hyperfine splittings

An overview of the theory of hyperfine splittings in rare earth ions where the unperturbed states are electronic singlets follows. To describe the dynamics of the f -electrons and nucleus we start with the following Hamiltonian

$$H = \{H_{\text{FI}} + H_{\text{CF}}\} + \{H_{\text{HF}} + H_{\text{Q}} + H_{\text{z}} + H_{\text{Z}}\} \quad (2.1)$$

The six terms on the right represent the free ion, crystal field, hyperfine, nuclear quadrupole, electronic Zeeman and nuclear Zeeman Hamiltonians respectively. The first group of terms are much larger than the second and are what determine the electronic energy levels.

The perturbation caused by the second group of terms is what determines the electronic levels' hyperfine structure. As mentioned above for both the systems studied in this thesis the energy eigenstates of $H_{\text{FI}} + H_{\text{CF}}$ are orbital singlets. Due to this “quenching” of the electronic angular momentum there is no first order perturbation due to hyperfine and the electronic Zeeman. Second order hyperfine and electronic Zeeman and the nuclear Zeeman and quadrupole effects are generally of similar size.

Applying second order perturbation theory gives, for a particular hyperfine manifold, the following effective spin Hamiltonian [75]

$$\begin{aligned} H = & \mathbf{B} \cdot (g_J^2 \mu_B^2 \mathbf{\Lambda}) \cdot \mathbf{B} + \mathbf{B} \cdot (\gamma_N \mathbf{E} + 2A_J g_J \mu_B \mathbf{\Lambda}) \cdot \mathbf{I} \\ & + \mathbf{I} \cdot (A_J^2 \mathbf{\Lambda} + \mathbf{T}_Q) \cdot \mathbf{I} \end{aligned} \quad (2.2)$$

The tensor $\mathbf{\Lambda}$ is given by

$$\Lambda_{\alpha\beta} = \sum_{n=2}^{2J+1} \frac{\langle 1 | J_{\alpha} | n \rangle \langle n | J_{\beta} | 1 \rangle}{\Delta E_{n,1}} \quad (2.3)$$

where the sum is over all the members of the J manifold except for the one labelled $|1\rangle$ for which the spin Hamiltonian applies. Generally we are only interested in the lowest energy level in the J manifold as it is insensitive to spontaneous phonon processes.

Also \mathbf{E} is the 3×3 identity matrix, \mathbf{B} is the magnetic field and \mathbf{I} is the vector of nuclear spin operators, while g_J is the Landé g-value, γ_N is the

nuclear gyro-magnetic ratio and A_J is the hyperfine interaction parameter. $\Delta E_{n,1}$ is the difference between the unperturbed energy eigenstates for the energy levels n and 1.

The term $\mathbf{I} \cdot \mathbf{T}_Q \cdot \mathbf{I}$ describes the nuclear electric quadrupole interaction. The term $A_J^2 \mathbf{I} \cdot \mathbf{\Lambda} \cdot \mathbf{I}$ which has the same form is due to the second order magnetic hyperfine, also known as the pseudo-quadrupole interaction [76].

The term $\mathbf{B} \cdot (g_J^2 \mu_B^2 \mathbf{\Lambda}) \cdot \mathbf{B}$ is due to the second order magnetic hyperfine interaction and is known as the quadratic Zeeman interaction. For the work on Pr:Y₂SiO₅ it was neglected, because it makes no changes to the hyperfine splittings and has only a small effect on the optical frequency for the small magnetic field values used. For the work on Eu:Y₂SiO₅ the technique used was just as sensitive to changes in the optical frequency as to the hyperfine splittings and this term was important.

2.5 The linewidths of rare earth spectra

2.5.1 Optical transitions

The lowest levels in each crystal field split J manifold are much longer lived than the other members. This is because the energy gap from the lowest state of a J manifold down to the next available level is large and it cannot be bridged by spontaneous phonon processes. The transitions that link these lowest members are correspondingly narrow. Such a “lowest to lowest” transition is indicated by the dotted line in Fig. 2.3(c).

In the absence of thermal phonons the only vibrational mechanism causing decoherence of this transition comes from weak population decay due to multi-phonon emission. The combination of this and radiative decay result in long population lifetimes. The corresponding minimum homogeneous linewidths are generally small, somewhere in the region of 10 Hz to 10 MHz. At low temperatures (compared to the Debye temperature), the effect of these thermal phonon processes rapidly decrease with further decreases in temperature. At liquid helium temperatures these thermally induced effects are often entirely negligible.

At such low temperatures, the lowest to lowest transitions are inhomogeneously broadened by the effects of crystal strain — typically by a few gigahertz. The homogeneous linewidths are very narrow yet generally slightly wider than the lifetime limit. The bulk of this excess dephasing comes from magnetic spins in the lattice, although with very quiet hosts like Y₂SiO₅ these effects can be very small. At higher temperatures, the homogeneous

linewidth is broadened by the effects of thermal phonons and the homogeneous linewidth approaches that of the inhomogeneous broadening.

The transitions that involve levels other than the lowest in each crystal field manifold are homogeneously broadened at essentially all temperatures. The spontaneous phonon processes determine the linewidths with values in the region of 10-100 GHz common.

2.5.2 Hyperfine transitions

The spin-lattice relaxation times for the hyperfine transitions are very long and linewidths are limited by other factors. The hyperfine transitions are inhomogeneously broadened to tens of kilohertz for the same reason as the optical transitions. The homogeneous linewidths are dominated by spin-spin interactions with other ions in the lattice. Recently, it has been shown that the dephasing effect of these interactions can be alleviated at a particular magnetic field value allowing for much larger coherence times, see Sec. 3.1.8.

2.6 Techniques that probe inside the inhomogeneous line

With the advent of tunable laser sources in the 1970's, a range of methods for probing inside the inhomogeneous linewidth became possible. Two of these methods are described here. The concepts introduced by these techniques form the basis for the quantum computing demonstrations described in Chapter 5. These and other 'non-linear' spectroscopic techniques are discussed in [77].

2.6.1 Spectral holeburning

The population of the ions is initially spread throughout the different ground state levels. When a laser is applied with its frequency somewhere inside the inhomogeneous line, a certain set of the ions will have an optical transition close to the laser. As the ions get excited and fall back down to the ground states, the population gets optically pumped into ground state levels from which there is no transition resonant with the laser. The ions that have been optically pumped away no longer interact with the laser. The mechanism for this is shown in Fig. 2.5. Fig. 2.5(b) is a crude approximation of the absorption pattern only; in reality a complex pattern of holes and anti-holes (corresponding to enhancement of population in some hyperfine levels) ap-

pear around the hole. The narrowest holes that can be burned depend on the homogeneous linewidth of the transitions. However, burning narrow holes is an inaccurate way to measure homogeneous linewidths. These measurements are very susceptible to laser jitter and for all but the most stable laser systems the holes will be limited by this. With such narrow features power broadening and saturation phenomena are also hard to avoid.

2.6.2 Optical free induction decay and photon echoes

Photon echoes and measuring free induction decays are part of a range of *coherent transient* techniques that can be applied to the study of rare earth systems. These techniques are directly analogous techniques used in magnetic resonance experiments. With them instead of a RF driving field, a laser is used to excite the ions. In magnetic resonance the transverse magnetisation (ensemble averages of the X and Y components of the Bloch sphere) is measured using the AC voltage induced in the same driving coils. Analogous measurements can be made in the rare earth system using the coherent spontaneous emission described in Section 4.4.

Suppose that one was able to align the optical Bloch vectors for a group of the ions at a particular point on the equator of the Bloch sphere. This would initially result in a strong coherent emission in a way fully analogous to a similar magnetic system. As time progresses this coherent emission will decay as the ensemble decoheres. The resulting signal is called an optical free induction decay (FID) because of its similarity to the analogous situation in magnetic resonance.

In rare earth systems, the timescale over which the free induction decays is generally given by the spectral width of the excited ensemble rather than the homogeneous linewidth which is narrower. Indeed the Fourier transform of the FID signal gives the spectra of the excited ions. This fact is used extensively in the optical memory and signal processing applications using rare earths [78]. It was also used to extract the spectra in Section 3.2

The excitation of spectrally narrow ensembles is helpful in observing optical FIDs. The length of time that the signal lasts is inversely proportional to the spectral width, meaning that the FIDs from wide spectral features are hard to distinguish from transients in the detection system due to the exciting pulses. There are various ways these spectrally narrow packets can be achieved, perhaps the simplest of these is by a long weak pulse. Alternatively a short pulse can be applied to a narrow feature.

Measuring FIDs offers one a better way of characterising sharp spectral features that have been prepared in the inhomogeneous line using hole-

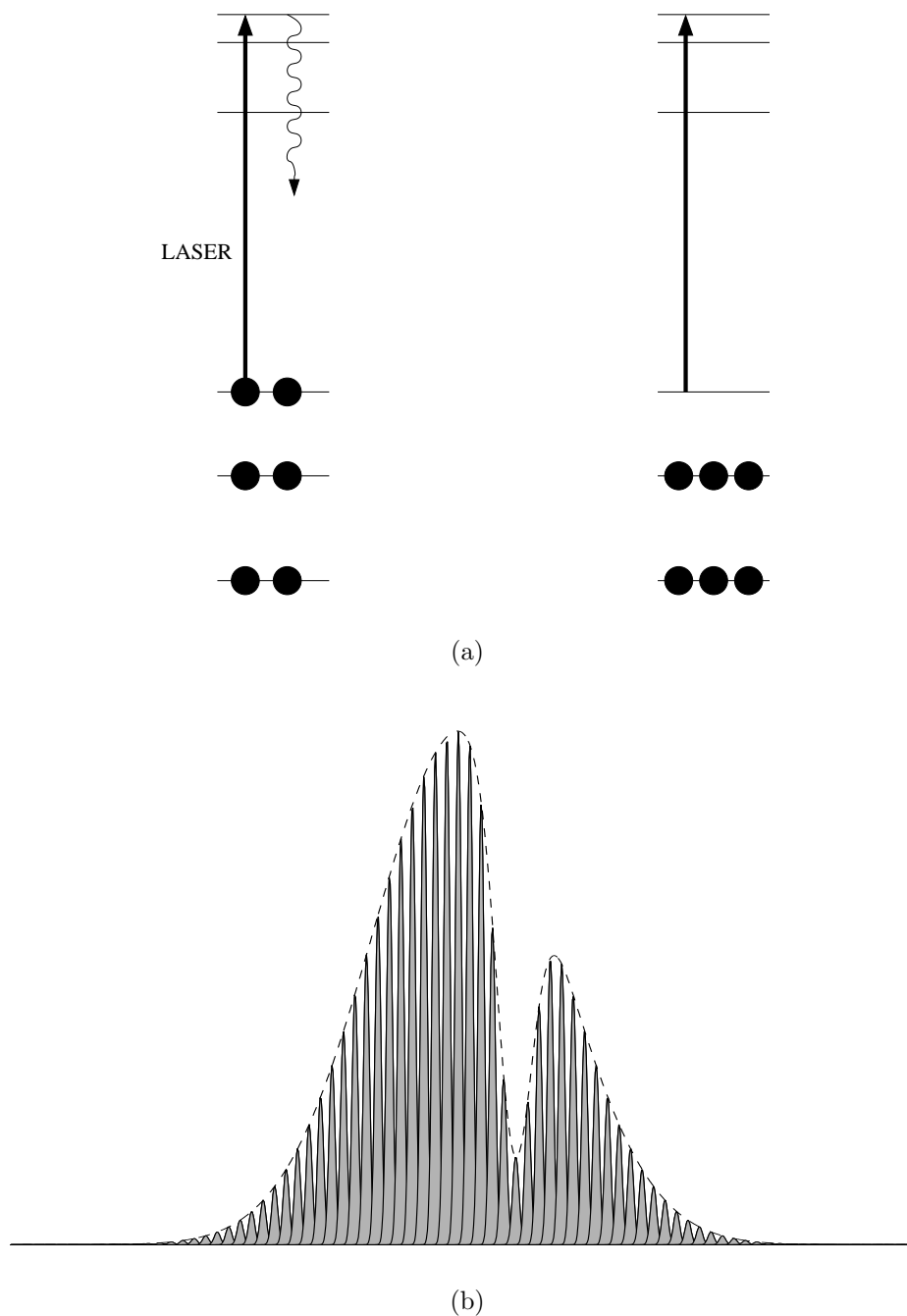


Figure 2.5: The spectral holeburning mechanism. (a) Illustrates how an ion which has a transition resonant with the laser gets optically pumped to another hyperfine level. This means that the homogeneous packets that would absorb at the laser frequency will now have a lot of their members in different hyperfine levels. This results in a “hole” in the absorption spectrum, as shown in (b). This lower figure is a crude approximation of the true absorption, see text.

burning techniques than sweeping the laser frequency and measuring absorption. They do not however provide a way of measuring homogeneous linewidths that is insensitive to laser stability and saturation. Photon echoes, however, provide a means of measuring homogeneous linewidths in a manner which is much less sensitive to laser frequency stability. Photon echoes are named after ‘spin echoes’ [79], the corresponding phenomenon in spin systems. An ideal photon echo sequence is to apply $\pi/2$ pulse, and then after a wait of Δt , a π pulse. After a further wait of Δt the sample produces a pulse of light in the same spatial mode as the driving laser.

To make the explanation simpler we shall assume that the phase of the laser is such that it causes rotations about the Y axis of the Bloch sphere. Further to this we shall assume that the pulses are short compared to the inverse spectral width of the feature. As discussed below, neither of these restrictions are necessary in order for photon echoes to give a measure of the coherence time for the transition T_2 . The states of the ions in the ensemble after the first $\pi/2$ pulse has been applied are shown in Fig. 2.6(a). The result of a $\pi/2$ rotation about the Y axis has moved the ensemble from the ground state to along the X axis. In the time that follows this pulse, each ion in the ensemble precesses around the Bloch sphere at a rate given by its detuning from the laser. For an atom with detuning δ the angle from the X axis at time t is simply δt . At the time $t = \Delta t$, a π pulse is applied, which rotates all the Bloch vectors π about the Y axis. Before the π pulse an ion with detuning δ is at an angle of $\delta \Delta t$ from the X axis and afterwards it is at an angle of $\pi - \delta \Delta t$.

The states before the π pulse are depicted in Fig. 2.6(b). Fig. 2.6(c) shows the states after the π pulse. Usually this second pulse is applied long after the coherence of the ensemble has decayed; here it has been applied before the states are too spread out in order that each individual homogeneous packet can be followed more easily. In the time period after the π pulse the states evolve in exactly the same manner as they did before. The angle a state makes with the X axis is therefore given by

$$\pi - \delta \Delta t + \delta(t - \Delta t)$$

Thus at a time $t = 2\Delta t$ all the ions, regardless of their detuning, will have their states aligned along the negative X axis. This is shown in Fig. 2.6(d).

The evolution on the Bloch diagrams is shown for pulses with ideal hard pulses and a perfectly stable laser. These criteria do not need to be satisfied in order to observe a photon echo or even for photon echoes to be useful. Photon echoes can be obtained from features much broader than the Rabi

frequency of the pulses. In this situation it is the duration of the pulses that determines the duration of the echo rather than the width of the feature.

While the description above has been for ideal $\pi/2$ and π pulses the process that produces the echo is very robust to changes in the pulse areas. Often, sometimes for reasons of simplicity in the experimental setup or otherwise, photon echo sequences with two equal pulse lengths are used.

The homogeneous linewidth is determined by varying the delay between the driving pulses and recording the echo intensity. For the amplitude of an echo to be reproducible there are only two conditions that need to be met regarding the frequency stability of the laser. Firstly it must be phase stable over the length of the pulses. Secondly the frequency must not change by more than the inverse of the length of the pulses in the time between the pulses. The much more stringent stability criterion of phase stability between the pulses is not required. A drift in the phase of the laser in the time between shots will cause the π rotation of the second pulse to be applied about an axis different to the Y axis. As a result the ensemble will still rephase in exactly the same way except now at a different point on the equator.

It is by a combination of spectral holeburning to the use of coherent transients that enabled the quantum computation demonstrations in this thesis. The techniques used can be considered an extension of those used by Pryde et al. [80]. In that work ensembles with a narrow spectral width were produced using holeburning techniques. The width of those ensembles were less than the available Rabi frequency which allowed pulses of accurate area to be applied for the first time. A photon echo sequence applied to such an ensemble is shown in Fig. 2.7. The use of such ensembles is discussed in Chapters 4 and 5.

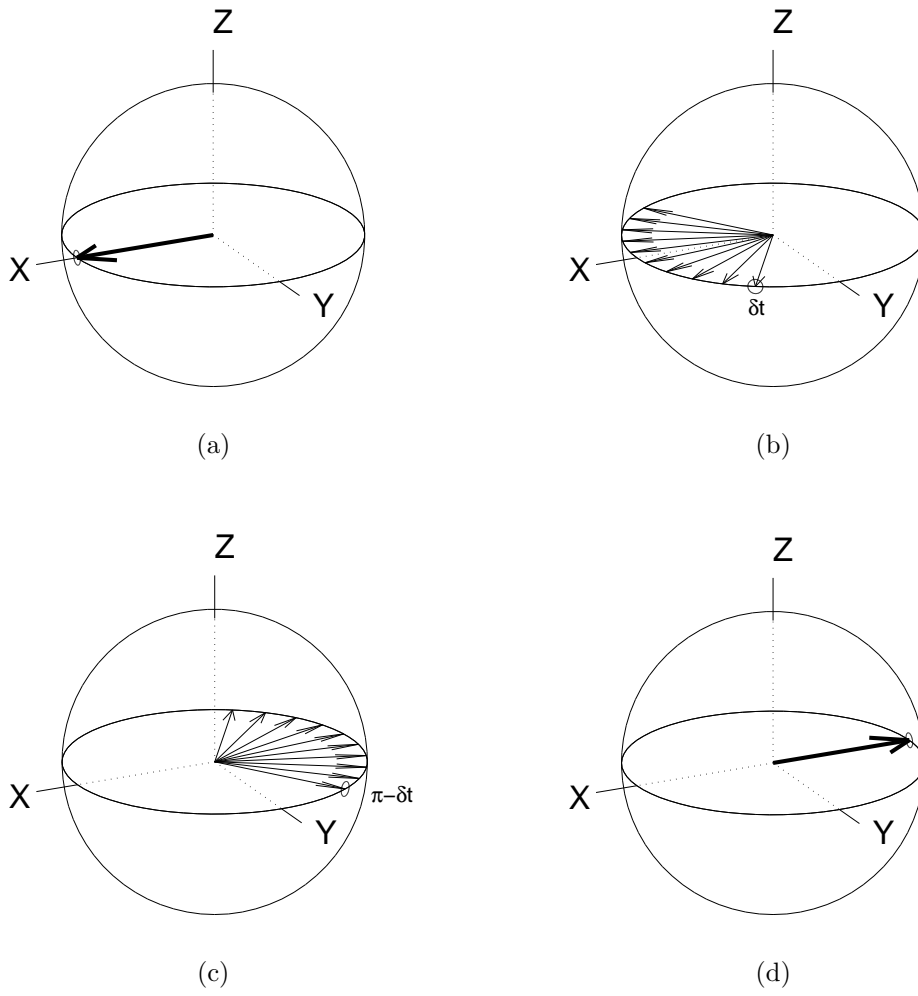


Figure 2.6: The positions of the Bloch vectors of a group of ions during an ideal photon echo sequence.

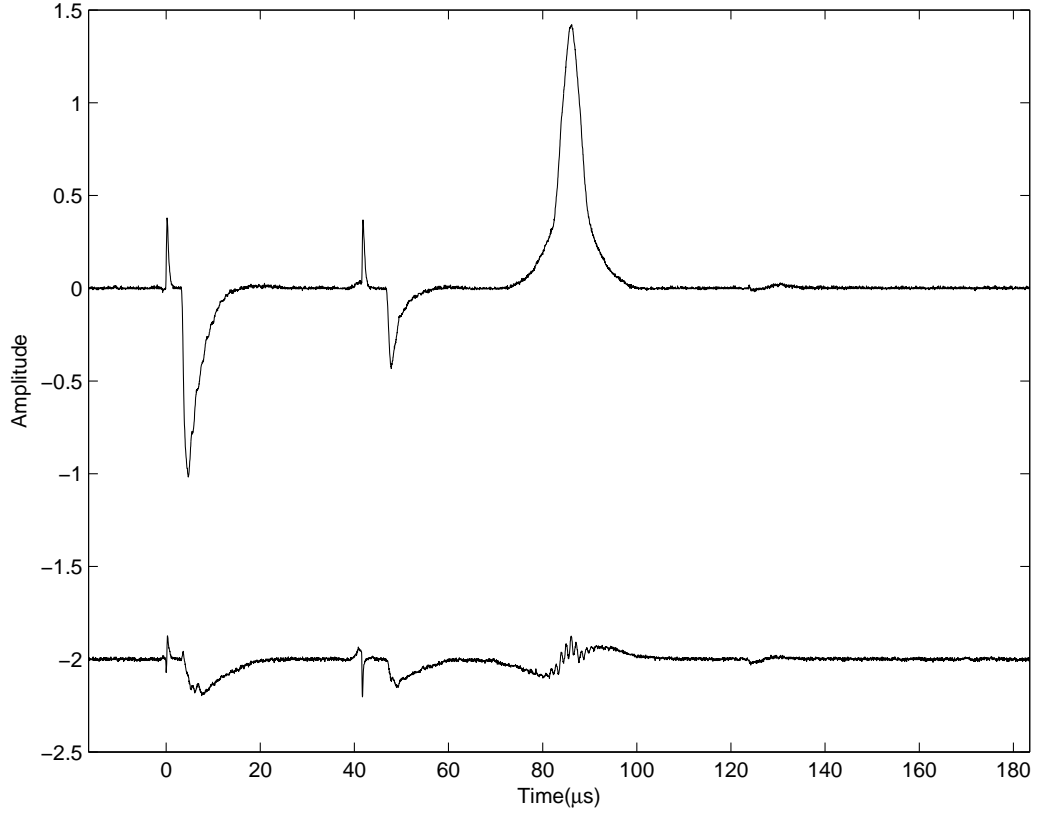


Figure 2.7: An experimental trace of an echo applied to an anti-hole. The upper and lower traces show the coherent emission produced in phase and in quadrature with the laser respectively. A pulse of approximately $3 \mu s$ in length is applied at $t = 0 \mu s$. This length was chosen to roughly correspond to a $\pi/2$ pulse. The pulses are about 30 db more intense than the coherent emission and saturate the detection system. The pulses appear in the trace as a sharp transient followed by a flat area where the detection system is saturated. Following the first pulse there is a free induction decay with a decay constant of about $20 \mu s$. This corresponds to the $\mathcal{O}(50 \text{ kHz})$ width of the anti-hole. The π at $t = 40 \mu s$ should result in no coherence in the sample, but because the ions in the anti-hole are spread throughout the laser beam, it will not be an ideal π pulse for all of the ions. This variation in the Rabi frequencies means that accurate pulses cannot be applied to the ensemble. Selecting the ions in the anti-hole based on their Rabi-frequency, as well as their detuning, can overcome this problem. At $t = 80 \mu s$ the echo forms and if the π pulse was ideal this would consist of two back to back versions of the first echo flipped in phase. The fact that the echo is pretty much out of phase with initial FID shows that the phase of the laser remained fairly stable throughout the shot. The slight dispersive nature of the echo and the FIDs suggests a small detuning between the laser and the centre of the anti-hole.

Chapter 3

Hyperfine splittings in rare earth ion dopants

This chapter investigates the characterisation of the hyperfine structure for trivalent praseodymium and europium dopants in yttrium orthosilicate (Y_2SiO_5). This characterisation has already provided the foundation for an elegant technique used to extend the hyperfine coherence times in rare earth ion dopants [81]. Information about oscillator strengths and transition frequencies will be of importance in any quantum information processing applications in which these materials are used.

While such a characterisation would have limited usefulness with other hosts, yttrium orthosilicate is an ideal host for rare earth ions with a lattice that provides a very quiet environment for rare earth ions.

The demonstration of slow light in a solid [82] and the narrowest observed optical resonance in a solid [66] both used dopants in this host, the dopants being praseodymium and europium respectively.

The rare earth ions substitute for yttrium. The yttrium carries a charge of +3 allowing trivalent rare earth ions to be substituted without charge compensation effects. Yttrium is also of a similar size to the dopants and that means comparatively little strain is introduced by the substitution. Further to these, the Y_2SiO_5 provides only small perturbations from spins within the lattice. There are no unpaired electron spins in the lattice — oxygen provides no nuclear moment and silicon only provides a small nuclear moment from a minor isotope. This leaves the yttrium nuclei with their small magnetic moments as the dominant unwanted spin. Handling Y_2SiO_5 samples is made much simpler because of its stability. It has melting temperature of 1980°C and against most reagents it can be considered inert. It is even under investigation for a coating to protect against oxidation in high temperature materials [83].

Yttrium orthosilicate has symmetry given by the C_{2h}^6 space group [84] with two formula units of Y_2SiO_5 per translational unit (four per conventional unit cell) [85, 86]. This gives four different sites at which the praseodymium can substitute for yttrium. The four sites can be divided into two pairs, with the members of each pair related to each other by the crystal's C_2 axis. These two pairs have different crystal field splittings and hence different optical transition frequencies.

The yttrium sites in Y_2SiO_5 have C_1 (no) site symmetry, which makes interpretation of the spectra difficult. To the author's knowledge the work presented here on $Pr:Y_2SiO_5$ is the first time that such information has been obtained for such a low symmetry site. Powerful inverse problem techniques and not insubstantial (especially compared to the simplicity of the system) computing resources were needed to arrive at the parameters for the spin Hamiltonian. Such a lack of symmetry does, however, remove any requirement of learning group theory which should always be seen as positive.

In the case of $Pr:Y_2SiO_5$ Raman-heterodyne spectroscopy (see Sec. 3.1.2) gave good signals and was used to obtain hyperfine spectra as a function of the magnetic field vector. For $Eu:Y_2SiO_5$ Raman-heterodyne spectroscopy gave barely visible signals in some conditions and these were not enough to be useful for characterising the hyperfine interaction. Instead a technique based on spectral holeburning was used. This didn't provide data as readily as Raman-heterodyne spectroscopy and (unlike for $Pr:Y_2SiO_5$) it hasn't proved possible yet to extract a total characterisation of the parameters of the spin Hamiltonian.

3.1 Hyperfine interaction in praseodymium doped Y_2SiO_5

3.1.1 Background

The two cryptographically distinct sites in the crystal pairs have different crystal field environments. Here we are only concerned with "site 1", for which the optical transition between the lowest energy components of the 3H_4 and 1D_2 multiplets is at 605.7 nm.

The crystal on which the measurements were performed consisted of 0.05% praseodymium, which has only one naturally occurring isotope (Pr^{141} , $I = 5/2$).

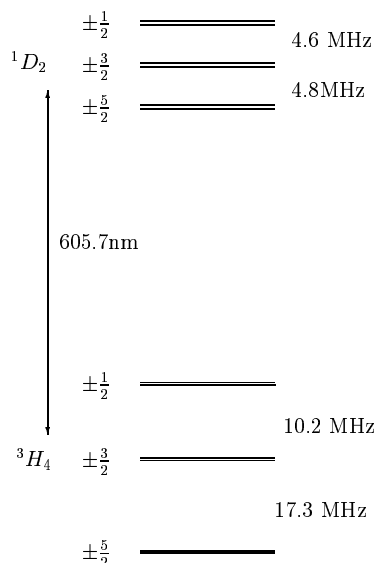


Figure 3.1: Zero field energy level diagram for $\text{Pr}:\text{Y}_2\text{SiO}_5$ as given in the work of Ham et al. [87, 88, 89, 82]

The spin Hamiltonian, Eq. 2.2, for our purposes can be rewritten:

$$H = \mathbf{B} \cdot \mathbf{M} \cdot \mathbf{I} + \mathbf{I} \cdot \mathbf{Q} \cdot \mathbf{I} \quad (3.1)$$

The $\mathbf{M}(= \gamma_N \mathbf{E} + 2A_J g_J \mu_B \mathbf{\Lambda})$ and $\mathbf{Q}(= A_J^2 \mathbf{\Lambda} + \mathbf{T}_Q)$ are the two (tensor valued) parameters that we wish to determine. The quadratic Zeeman term has been ignored for the praseodymium work. It has the effect of moving the whole hyperfine manifold up or down in energy and as such it does not contribute to the hyperfine splittings.

The zero field energy level diagram for $\text{Pr}:\text{Y}_2\text{SiO}_5$ in “site 1” is shown in Fig. 3.1, where each of the six membered hyperfine manifolds are split into three degenerate pairs by the term $\mathbf{I} \cdot \mathbf{Q} \cdot \mathbf{I}$. By convention, these states are labelled $\pm 1/2$, $\pm 3/2$ and $\pm 5/2$ even though they are only very approximately angular momentum eigenstates. Using the coordinate system (x', y', z') which diagonalises \mathbf{Q} the Hamiltonian becomes

$$H = E(I_{x'}^2 - I_{y'}^2) + DI_{z'}^2 \quad (3.2)$$

For axial sites $E = 0$ leading to a Hamiltonian $DI_{z'}^2$, which in turn leads to $I_{z'}$ eigenstates for the stationary states. For non-axial sites in which we are interested, the term $E(I_{x'}^2 - I_{y'}^2)$ causes significant mixing among the $I_{z'}$ eigenstates. The energy levels are still doubly degenerate because of inversion symmetry. Zero magnetic field Raman heterodyne signals can be seen at 10.2,

17.3, 4.6 and 4.8 MHz. Smaller signals can be seen at 17.3 and 9.4 MHz, due to the $\pm 1/2 \leftrightarrow \pm 5/2$ transitions because the mixing allows violation of the $\Delta I = 1$ selection rule.

The application of a magnetic field splits the degenerate pairs, and for a 40 Gauss magnetic field the splitting is of order of 1 MHz. For each orientation of “site 1” in the crystal, each of the above Raman heterodyne lines would split into four. The line splits into eight, in general, because of the two possible orientations of “site 1”.

3.1.2 Experiment

A diagram of the experimental setup is shown in Fig. 3.2.

The sample was mounted in a set of small superconducting XYZ -coils which enabled a field of about 40 Gauss to be generated from currents of in the region of 3 A. These coils were calibrated using an simple magnetometer made from the 3516 Linear Hall Effect Sensor chip [90] of Allegro Microsystems. The current was supplied with a purpose-made three channel current supply. The sample and XYZ coils were placed in a glass cryostat and immersed in liquid helium. The measurements were carried out with the sample below the lambda point (2.2 K).

To obtain Raman-heterodyne [91, 92] spectra, light from a frequency-stabilised (1MHz) dye laser was incident on the sample. The laser was tuned so it was resonant with the transition from the lowest level of the 3H_4 multiplet to the lowest level of the 1D_2 . The frequency of the laser was slowly swept within the ($^3H_4 \rightarrow ^1D_2$) inhomogeneous line to prevent holeburning processes.

A swept radio-frequency (RF) field was applied to the sample using a 6 turn coil wrapped around the sample. When the RF field was resonant with a hyperfine transition a coherence was produced between the hyperfine levels. This coherence, along with that induced by the laser, creates another optical field with the same mode characteristics as the laser but with a frequency shifted by the frequency of the RF driving field. See Fig. 3.4. This optical field is detected as a beat on the transmitted light. An example of a Raman-heterodyne spectrum is shown in Fig. 3.3.

The task of generating the RF signal and analysing the signal was carried out using a RF network/spectrum analyser. The signal was averaged on a digital oscilloscope and then stored on a PC. Along with a computer-controlled current supply for the XYZ coils this enabled autonomous collection of the data.

For the ground state the spectra were recorded as the magnetic field was

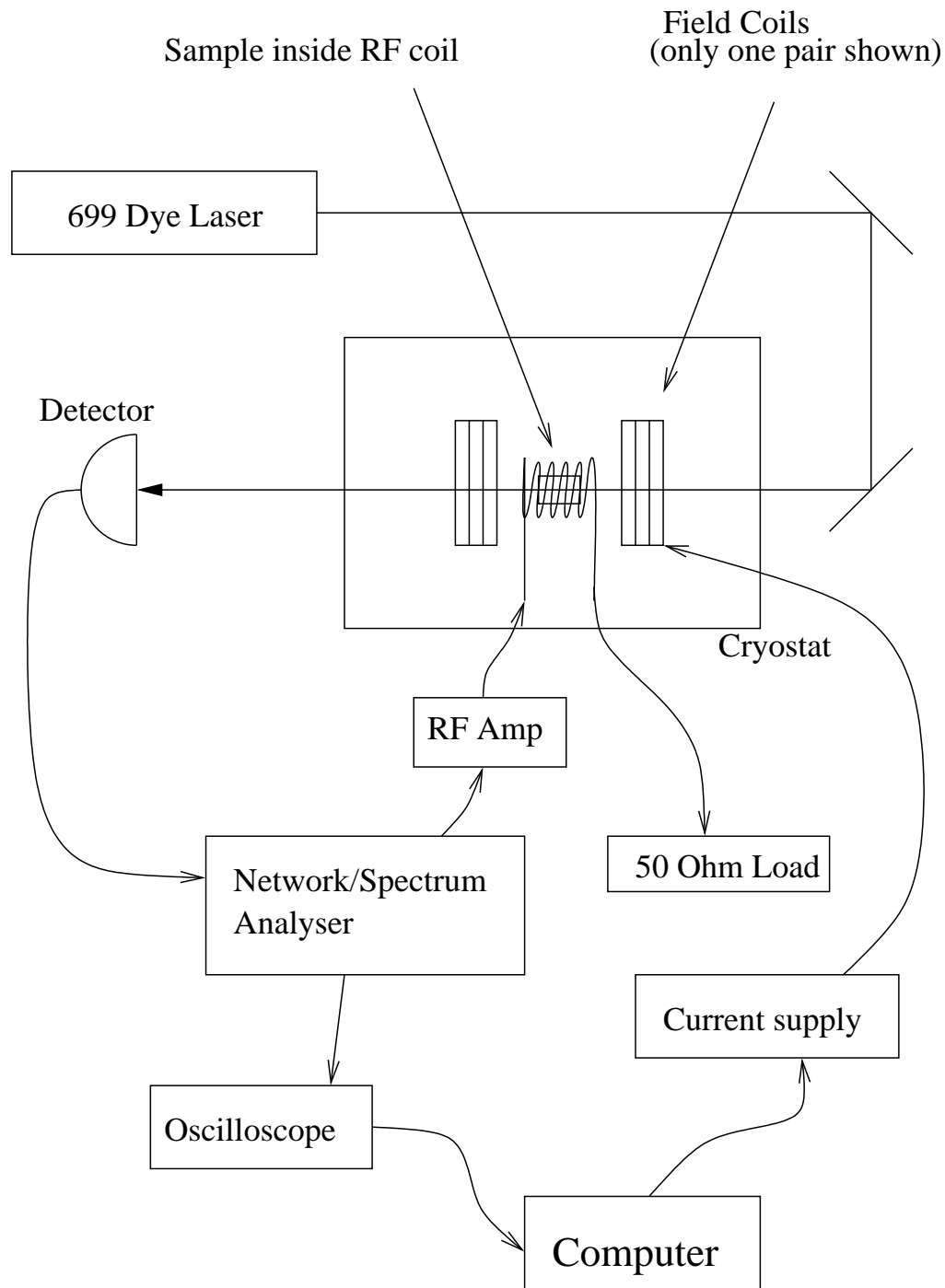


Figure 3.2: Experimental setup for collecting the $\text{Pr}:\text{Y}_2\text{SiO}_5$ Raman-heterodyne data.

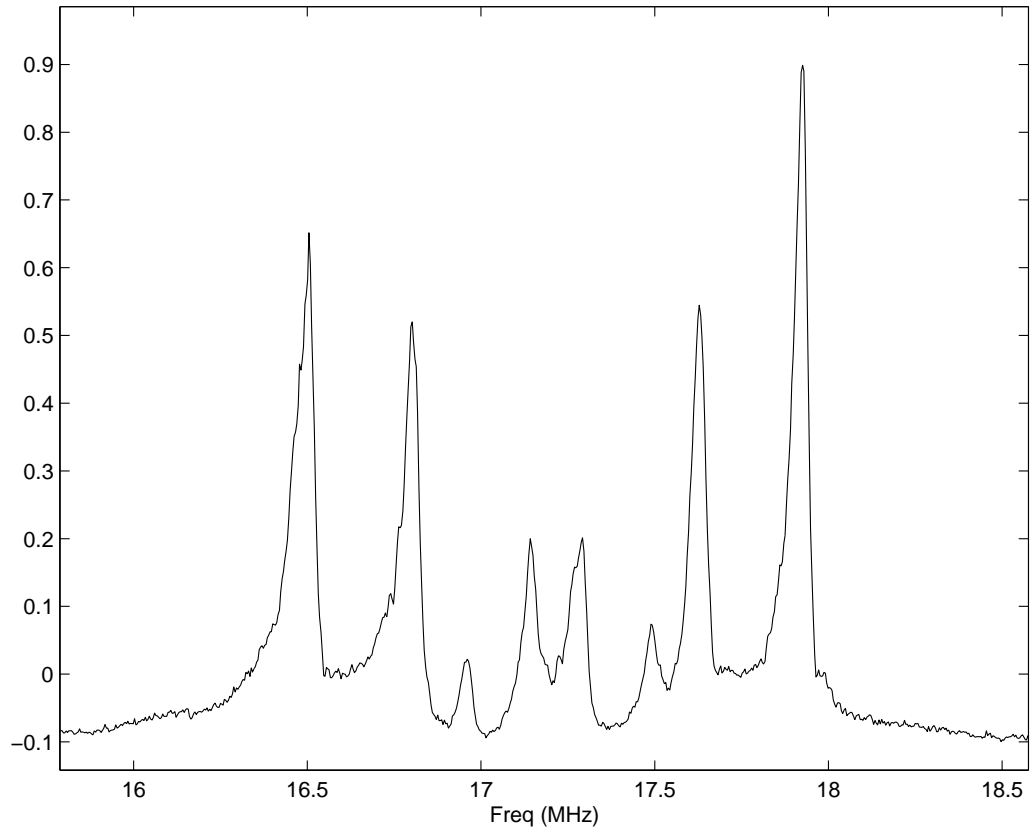


Figure 3.3: An example Raman-heterodyne spectrum. The frequency is plotted against the signal (in arbitrary units).

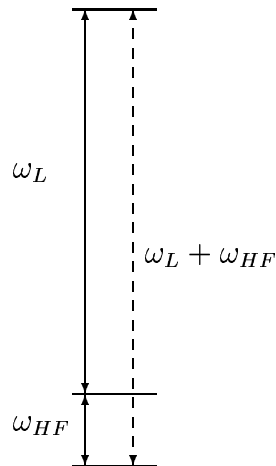


Figure 3.4: Energy levels involved in the Raman Heterodyne detection. The applied optical and RF fields are ω_L and ω_{HF} respectively. The Raman field produced at $\omega_L + \omega_{HF}$ gives a beat with the transmitted laser beam at ω_L .

rotated in a spiral (see Fig. 3.5) of the form

$$\mathbf{B} = \begin{bmatrix} B_0\sqrt{1-t^2}\cos 6\pi t \\ B_0\sqrt{1-t^2}\sin 6\pi t \\ B_0t \end{bmatrix}, \quad t \in [-1, 1] \quad (3.3)$$

The ground state spectral lines were in two bands a couple of MHz wide, one centred around 10.2 MHz ($\pm 1/2 \leftrightarrow \pm 3/2$) and the other 17.3 MHz ($\pm 3/2 \leftrightarrow \pm 5/2$). Sweeping the entire range from 9 through to 19 MHz would mean that a lot of time would be spent scanning the 12 – 15 MHz region where no spectral lines were present. Considering the relatively short hold time of the cryostat used (a couple of hours), it was desirable to make the data collection process as time efficient as possible. For this reason, and because they were available, two spectrum/network analysers were used — one to look at the region around 10.2 MHz and the other for the region around 17.3 MHz. The simultaneous collection of two spectra in this manner had no adverse effects on the measurements and may have slightly improved signal levels due to suppression of holeburning processes.

For the excited state, the magnetic field was rotated in cones (see Fig. 3.6) about each axis. This was because it was desirable to have larger fields for the excited state to help resolve all the lines present. This was most easily achieved by having a larger non-computer-controlled current supply on one of the three channels.

The positions of all the visible peaks in the 100 ground state and 135 excited state spectra were recorded. These positions were determined by the manual inspection of the spectra and were recorded using a computer by clicking on spectra. Out of the total of 1600 ($= 16 \times 100$) ground state peaks, 1223 positions were recorded. For the excited state the frequencies of 1503 out of a total of 2160 peaks were determined. The 25 per cent of peaks that didn't have their positions recorded were either too weak to be seen above the noise or were obscured by an overlapping peak. These sets of peak positions and their corresponding magnetic field values were the datasets used in reconstruction of the spin Hamiltonians.

3.1.3 Solving the inverse problem

Given the spin Hamiltonian parameters \mathbf{M} and \mathbf{Q} and the magnetic field \mathbf{B} the calculation of the hyperfine transition frequencies is straightforward. The Hamiltonian given by Eq. 3.1 is constructed and its eigenvalues found, then the frequency differences between these eigenvalues give the spectral lines.

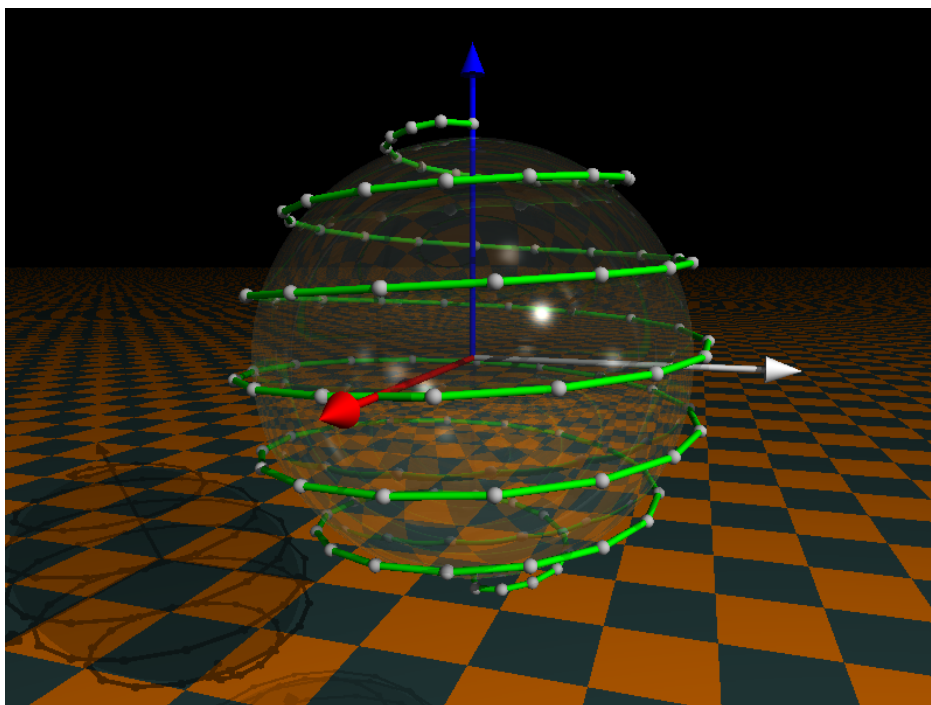
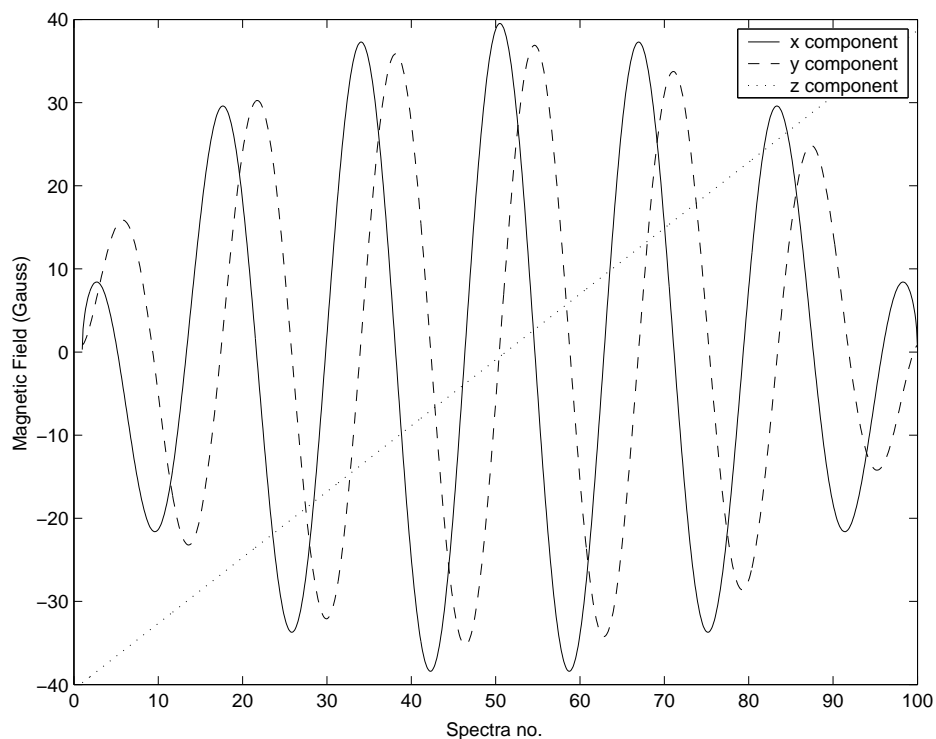


Figure 3.5: Magnetic field values used to obtain ground state hyperfine spectra. The x , y and z axes are coloured red, white and blue respectively.

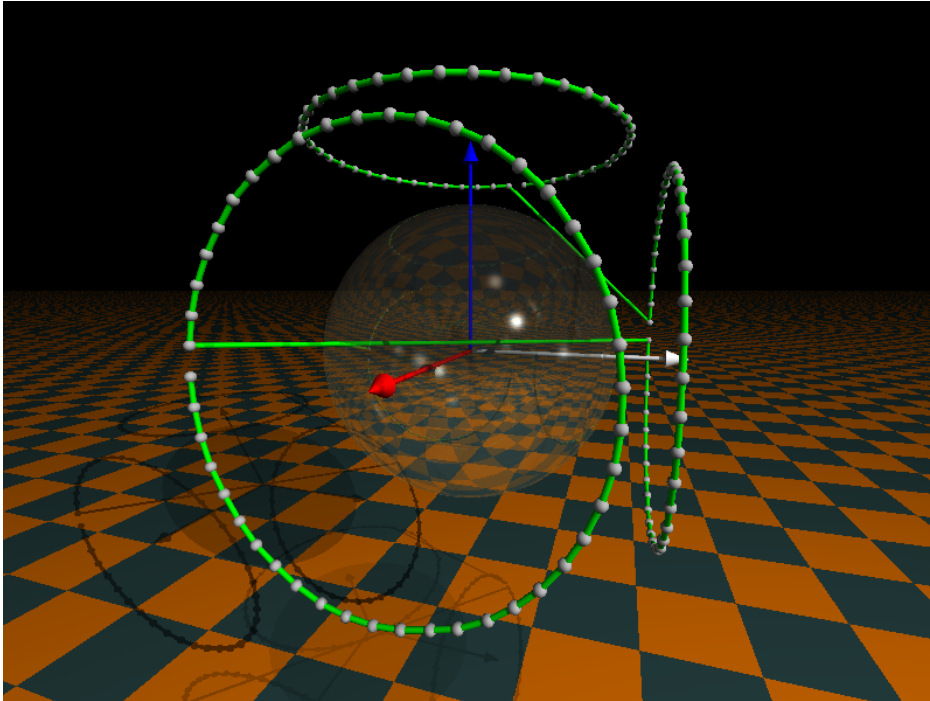
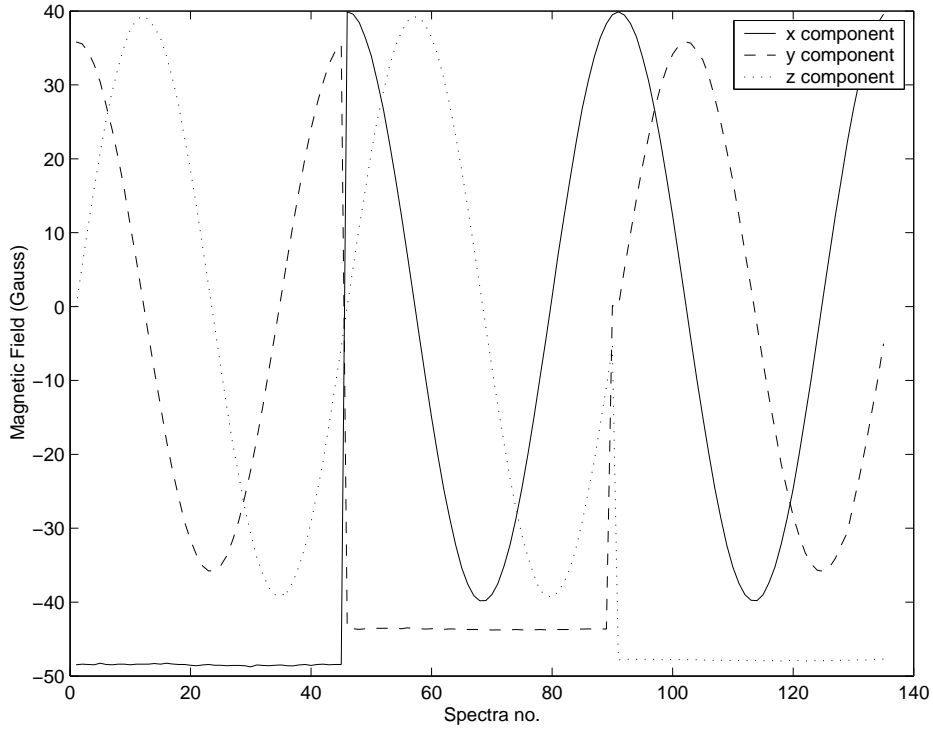


Figure 3.6: Magnetic field values used to obtain excited state hyperfine spectra. The x , y and z axes are coloured red, white and blue respectively.

The techniques used for solving the inverse problem are outlined below. As the problem is nonlinear and there are a large number of unknowns, the only available techniques are those based on the stochastic sampling of the posterior probability distribution function.

Given two binary random variables x and d we have the following identity

$$p(x, d) = p(x|d)p(d) = p(d|x)p(x) \quad (3.4)$$

Here $p(x, d)$ is the probability that both x and d are true, while $p(x)$ is the probability that x is true and $p(x|d)$ is the conditional probability that x is true given that d is known to be true.

The above can be rearranged to give Bayes theorem

$$p(x|d) = \frac{1}{p(d)}p(d|x)p(x) \quad (3.5)$$

Such an argument is equally valid for the p 's as probability distribution functions rather than just probabilities. We will assume that we are trying to infer the value of x (the unknown) from the value of a measurement of d (the data). If we treat the probability distribution $p(x)$ as our “state of knowledge” of the value of x before the measurement Eq. 3.5 provides a method for determining $p(x|d)$, which is our “state of knowledge” of x following the measurement. All that is required in updating our state of knowledge is $p(d|x)$, which is the probability that one would obtain a certain value for the measurement of d if, hypothetically, the model parameters which we are trying to determine had value x . The term $1/p(x)$ can be treated as a normalisation constant. We shall call $p(x)$ the *prior* probability distribution and $p(x|d)$ the *posterior* probability distribution.

Using Bayes theorem it is no more difficult to calculate the probability distribution relevant to the inverse problem $p(x|d)$ than the one relevant to the forward problem $p(d|x)$. The difficulty comes in obtaining something useful from the probability distribution. In our particular problem the number of unknowns N is of order 10, (for example 5 or 6 for each of the two tensors \mathbf{M} and \mathbf{Q} and two for the directions of the crystal's C_2 axis). Obtaining statistics, such as a mean, from such a distribution requires a N dimensional integration. Conventional quadrature techniques are useless for such a high number of dimensions. Calculating the mode of the posterior probability distribution function, or the most-likely value of the model parameters, requires finding the global maximum within N dimensional space. This is a difficult problem because of the large number of local maxima in which the algorithm may get stuck. In order to overcome these problems in this situation it was

necessary to use stochastic methods. The success of these techniques relies on efficient solution of the forward problem because its solution is required many many times in the execution of the algorithms. In this situation solving the forward problem for the dataset involves creating and diagonalising of the order of 100 6×6 Hamiltonians. The two million steps used in the annealing took approximately 8 hours on a 933 MHz Pentium III PC.

The technique used for this work was based on the work of Metropolis et al. [93]. They devised a scheme for stochastically jumping around the configuration space of a given model system in such a way as to sample the Boltzmann distribution. Hastings provided a generalisation [94] that allowed the sampling of arbitrary distributions. However, for this and many other inverse problems, the posterior probability can be made to coincide with the Boltzmann distribution. If we assume no prior information and if the uncertainty can be effectively modelled by the addition of uncorrelated Gaussian noise to the peak positions then one has

$$p(x|d) = p(d|x) = \frac{1}{Z} \exp \left(\sum_i \frac{-(\omega_i - d_i)^2}{2\sigma^2} \right) \quad (3.6)$$

Here Z is the normalisation constant, ω_i is the theoretical frequency for the spectral line i , which is based on the model parameters x . The corresponding observed frequency is given by d_i . Such a distribution is the same as the $\exp(-E/kT)$, but with the energy replaced by the misfit between experimental results and theory, $E = \sum_i (\omega_i - d_i)^2$, and temperature replaced with the uncertainty in the measurements, $kT = 2\sigma^2$.

Because of its simplicity Eq. 3.6 was used when solving the inverse problem. However, it should be noted that the experimental uncertainty cannot be modelled so simply. As a result of this the uncertainties in the various spin Hamiltonian parameters determined using it should be viewed with caution. This is discussed further in the results section.

The Metropolis algorithm is as follows:

- (i) Record the system state a
- (ii) Randomly choose a trial state a' based on a
- (iii) Chose a randomly distributed number r between 0 and 1.
If $\exp \left(\frac{E(a) - E(a')}{kT} \right) < r$ then replace a with a' otherwise leave a unchanged.
- (iv) Goto Step (i).

Here $E(a)$ is the energy of the system when in state a and kT is Boltzmann's constant times the temperature. The states of a at step 1 sample the Boltzmann distribution representatively. For $E(a) > E(a')$ the algorithm always accepts the trial state, that is, it always accepts a step down in energy. Sometimes, it also accepts steps for which $E(a) < E(a')$. When the energy difference is small compared to kT this is likely; when the energy difference is large compared to kT this is unlikely.

In many situations it would be enough to loop through the Metropolis algorithm a large number of times. The statistics collected from the set of the values of a at step (i) approximate the statistics of the posterior probability distribution function. The difficulty in many situations, including this one, is that the Metropolis algorithm can require a prohibitively large number of steps to come to equilibrium. The initial state will, no doubt, be one of high energy (low probability) and it can take a prohibitively large number of steps to reach equilibrium. This is similar to the situation in some physical systems where a system can get stuck in a metastable high energy state, even though there exist much lower energy states. A physical example of such a situation is where a melt ends in an amorphous state and stays there for a long time at low temperatures, despite the existence of a lower energy crystalline state. In order to achieve such a crystalline state physically the melt must be cooled slowly. Using this slow cooling for numerical minimisation, or *simulated annealing*, was pioneered by Kirkpatrick and co-workers [95]

3.1.4 Model parameters and the misfit metric

Along with the orientation of the principal axes there are two parameters required to determine the pseudo-quadrupole tensors. For this work the following parameterisation was used

$$\mathbf{Q} = R(\alpha, \beta, \gamma) \begin{bmatrix} E & 0 & 0 \\ 0 & -E & 0 \\ 0 & 0 & D \end{bmatrix} R^T(\alpha, \beta, \gamma) \quad (3.7)$$

where $R(\alpha, \beta, \gamma)$ is the rotation matrix defined by the three Euler angles (α, β, γ) [96]. For the Zeeman tensor there are six independent parameters and the following parameterisation was used

$$\mathbf{M} = R(\alpha, \beta, \gamma) \begin{bmatrix} g_x & 0 & 0 \\ 0 & g_y & 0 \\ 0 & 0 & g_z \end{bmatrix} R^T(\alpha, \beta, \gamma) \quad (3.8)$$

There is the potential for a great deal of confusion when dealing with Euler angles, many different conventions are used. For this reason the convention used to convert the parameters in Eq. 3.7 and 3.8 into the \mathbf{M} and \mathbf{Q} tensors is given in Appendix A.

In the case of a system with no true quadrupole interaction, it can be easily seen from (2.2) that the principal axes of the two tensors \mathbf{M} and \mathbf{Q} will be aligned. Further to this the parameters apart from \mathbf{A} are all known, and so there are only three independent parameters in addition to the orientation of the tensors. The absolute values of the parameters D and E can be determined from zero-field quadrupole splittings which would help greatly in determining these. Because of this three different models were used to try and fit the data, one where it was assumed that there was no real quadrupole interaction, one where the tensors \mathbf{M} and \mathbf{Q} were taken to share the same axes but the principal values were allowed to vary freely and one where no relationship was assumed between the two tensors.

The position of the C_2 axis was nominally along the y -axis but was included as a parameter because of the small misalignment between the coils and the sample. The parameters D and E were allowed to vary from their values determined by the zero field splittings because the zero-field lines were broader than those that had been split by the magnetic field. This was a result of a small background magnetic field.

The data containing all the peak positions was then fed into a computer program that used simulated annealing to minimise the difference between the experimental values and what would be expected from a pair of systems, one with a Hamiltonian

$$H = \mathbf{B} \cdot \mathbf{M}_1 \cdot \mathbf{I} + \mathbf{I} \cdot \mathbf{Q}_1 \cdot \mathbf{I} \quad (3.9)$$

and the other with a Hamiltonian

$$H = \mathbf{B} \cdot \mathbf{M}_2 \cdot \mathbf{I} + \mathbf{I} \cdot \mathbf{Q}_2 \cdot \mathbf{I} \quad (3.10)$$

Here each \mathbf{X}_1 and \mathbf{X}_2 are related to each other via the C_2 axis.

The misfit metric which is used for the “energy” in the simulated annealing process was the sum of the squares of the differences between the calculated and measured frequency values. The difficulty of assigning theoretical peaks to experimental ones, especially when each spectral line is not always visible added complications. You never see *more* experimental peaks than theoretical peaks, so the number of experimental peaks is always less than or equal to the number of theoretical ones. In early attempts it was

assumed that each experimental peak corresponded with the closest theoretical one. However with this strategy the algorithm tended to get stuck in unrealistic situations in which one theoretical peak was used to explain a number of distinct experimental peaks.

To counteract this tendency it was decided to use the mapping from the set of experimental peaks X to the set of theoretical peaks Y such that

$$\mathcal{M}(f) = \sum_{x \in X} (f(x) - x)^2 \quad (3.11)$$

is minimised — with the restriction that each member of Y gets mapped to at most once.

Such a minimum mapping has to be an increasing function.¹ Suppose that f is the minimum of \mathcal{M} , $x_1 > x_2$ and $f(x_1) < f(x_2)$. Then by considering the function $g : X \rightarrow Y$, which is identical to f except that $g(x_1) = f(x_2)$ and $g(x_2) = f(x_1)$, we have the following contradiction,

$$\begin{aligned} \mathcal{M}(f) - \mathcal{M}(g) &= (f(x_1) - x_1)^2 + (f(x_2) - x_2)^2 \\ &\quad - (g(x_1) - x_1)^2 - (g(x_2) - x_2)^2 \end{aligned} \quad (3.12)$$

$$= f(x_1)x_2 + f(x_2)x_1 - f(x_2)x_2 - f(x_1)x_1 \quad (3.13)$$

$$= (f(x_2) - f(x_1))(x_1 - x_2) \quad (3.14)$$

$$> 0 \quad (3.15)$$

With the set of possible mappings reduced to increasing functions we have a set of $\binom{n}{m}$ candidates, where n is the number of theoretical peaks and m is the number observed. You can specify the mapping by just deciding which m theoretical peaks will get mapped to.

For the case of 8 theoretical lines, as is the case for each of the set of lines about 10 MHz and 17 MHz in the ground state, the largest this can be is $\binom{8}{4} = 70$. For the excited state where each experimental peak could be assigned to any one of 16 theoretical peaks the worst case blows out to $\binom{16}{8} = 12,870$. Exhaustively searching through 70 possible combinations is possible, but 12,870 makes the algorithm prohibitively slow. Keeping in mind of course that this procedure has to be done for each of the ~ 100 or so spectra in the dataset at each of the ~ 2 million steps of the simulated annealing algorithm. For the ground state the hyperfine parameters were first found by searching exhaustively for the minimum. For the excited state a more

¹For practical purposes we can assume that the sets X and Y are non-degenerate. This can be arranged by adding an insignificantly small amount of either experimental or numerical “error”.

sophisticated algorithm was developed. The source code and a description is given in Appendix B.

3.1.5 Sensitivity of the spectra to the Hamiltonian

An important question to ask when determining Hamiltonian parameters from spectra is whether more than one Hamiltonian can lead to the same spectra. The answer is yes, as can be seen by considering the transformation $H \rightarrow -H$. The energies of the eigenvalues of the new Hamiltonian will be minus those of the old one, but the transition frequencies will be the same. At sufficiently low temperatures the two situations could be distinguished but for a 10 MHz transition ΔE doesn't equal kT until a temperature of 0.5 mK.

In zero magnetic field, the ambiguity $H \rightarrow -H$ in our system presents itself as the ambiguity $Q \rightarrow -Q$. In our case the spectra would have been indistinguishable for the reasons mentioned above. It should be noted however that experiments that measure the optical transition strengths and frequencies, such as spectral holeburning, will be sensitive to the 'sign' of Q .

Holliday and his co-workers [97] reported negative signs for both D and E (see Eq. 3.7) in the ground state and positive signs in the excited state. This determination was made by comparing spectral holeburning patterns with those calculated from the transition strengths. As pointed out in their paper this method is not entirely robust and has led to false conclusions with Pr:LaF₃ [98, 99]. While it is not made clear, in their paper it appears that Holliday et al. took the principal axes to be overlapped. If this was the case it would make sense to report the sign of E . In general however exactly the same tensor Q (see Eq. 3.7) could be made by flipping the sign of E if a different rotation matrix was used. This is because flipping the sign of E is exactly the same as swapping the roles of x' and y' in the quadrupolar Hamiltonian

$$H_Q = D (I_{z'}^2 - I(I+1)/3) + E (I_{x'}^2 - I_{y'}^2) \quad (3.16)$$

The orientations of the pseudo-quadrupole tensors were found during the work undertaken for this thesis and the relative orientations for the principal axes are shown in Fig. 3.15. It can be seen there that the principal axes with principal values D are close to each other for the two tensors, whereas the other principal axes are not.

Another insight into the relative signs of the D is in the work of Ham and co-workers who have investigated electromagnetically induced transparency

phenomena (EIT) in this material [87, 88, 89, 82]. While they give the work of Holliday [97] as its source, in their papers they report an energy level diagram as shown in Fig. 3.1. This energy level diagram would be the result of choosing a negative sign for D for both the ground and excited states. As the EIT work carried out by Ham and his coworkers is both extensive and sensitive to this technicality, one must assume that this is the correct situation.

As already mentioned above, the work carried out for this thesis was insensitive to $Q \rightarrow -Q$ and in analysing the data the D and E parameters (see Eq. 3.7) were positive for each of the electronic states. In order for these results to coincide with Ham's energy level diagram, the substitution $Q \rightarrow -Q$ should be made for both the ground and optically excited state tensors. This substitution is done when reporting the results in Tables 3.1 and 3.2.

For our problem we must also consider the following:

Given a coordinate transformation \mathbf{P} ($\mathbf{P}^\dagger \mathbf{P} = \mathbf{E}$) with the property that $\mathbf{P} \mathbf{Q} \mathbf{P}^\dagger = \mathbf{Q}$ the two Hamiltonians (Eq. 3.1) $H = \mathbf{B} \cdot \mathbf{M} \cdot \mathbf{I} + \mathbf{I} \cdot \mathbf{Q} \cdot \mathbf{I}$ and $H' = \mathbf{B} \cdot \mathbf{M} \mathbf{P} \cdot \mathbf{I} + \mathbf{I} \cdot \mathbf{Q} \cdot \mathbf{I}$ give the same hyperfine spectra and oscillator strengths.

This can be seen by considering the following

$$H = \mathbf{B} \cdot \mathbf{M} \cdot \mathbf{I} + \mathbf{I} \cdot \mathbf{Q} \cdot \mathbf{I} \quad (3.17)$$

$$= \mathbf{B} \cdot \mathbf{M} \mathbf{P} \mathbf{P}^\dagger \cdot \mathbf{I} + \mathbf{I} \cdot \mathbf{P} \mathbf{P}^\dagger \mathbf{Q} \mathbf{P} \mathbf{P}^\dagger \cdot \mathbf{I} \quad (3.18)$$

$$= \mathbf{B} \cdot \mathbf{M} \mathbf{P} \cdot (\mathbf{P}^\dagger \mathbf{I}) + (\mathbf{P}^\dagger \mathbf{I}) \cdot \mathbf{Q} \cdot (\mathbf{P}^\dagger \mathbf{I}) \quad (3.19)$$

The three operators $(\mathbf{P}^\dagger \mathbf{I})_{x,y,z}$ are simply the three angular momentum operators for a different set of axes and have the same algebra as the angular momentum operators for the initial basis.² This leads to the same eigenvalues for both cases, with the eigenstates differing only in their representation. Oscillator strengths for transitions between these eigenstates are calculated by considering the matrix elements of operators corresponding to magnetic field perturbations. These are also unchanged. To understand this consider an oscillating magnetic field pointed along the $\hat{\mathbf{n}}$ direction. The relevant operator when calculating the transition strength between two states $|\alpha\rangle$

²If \mathbf{P} involves a change in the handedness of the coordinate system, $\det(\mathbf{P}) = -1$, the commutation relations change from $[I_i, I_j] = i\hbar\epsilon_{ijk}I_k$ to $[(\mathbf{P}^\dagger \mathbf{I})_i, (\mathbf{P}^\dagger \mathbf{I})_j] = -i\hbar\epsilon_{ijk}(\mathbf{P}^\dagger \mathbf{I})_k$. This doesn't affect the argument.

and $|\beta\rangle$ is

$$\langle\alpha|\hat{\mathbf{n}}\cdot\mathbf{M}\cdot\mathbf{I}|\beta\rangle \quad (3.20)$$

$$= \langle\alpha|\hat{\mathbf{n}}\cdot\mathbf{M}\mathbf{P}\cdot(\mathbf{P}^\dagger\mathbf{I})|\beta\rangle \quad (3.21)$$

$$= \langle\alpha'|\hat{\mathbf{n}}\cdot\mathbf{M}\mathbf{P}\cdot\mathbf{I}'|\beta'\rangle \quad (3.22)$$

$$(3.23)$$

Here $|\alpha'\rangle$ is the same as $|\alpha\rangle$ but written in terms of, for example, the I'_z eigenstates rather than the eigenstates for I_z .

The eight coordinate transformations that have the property $\mathbf{P}\mathbf{Q}\mathbf{P}^\dagger = \mathbf{Q}$ form a representation of the D_{2h} point group. The operations which make up this group are: rotations of π about the principal axes of \mathbf{Q} ; reflections in the planes whose normals are the principal axes; inversion and the identity.

Explicitly the operations are

$$\mathbf{P} = \mathbf{U} \begin{bmatrix} \pm 1 & 0 & 0 \\ 0 & \pm 1 & 0 \\ 0 & 0 & \pm 1 \end{bmatrix} \mathbf{U}^\dagger \quad (3.24)$$

where \mathbf{U} rotates the coordinate frame onto the principal axes of \mathbf{Q} .

Taking the limit of no quadrupolar term in the Hamiltonian one finds that \mathbf{M} can be right multiplied by any coordinate transformation \mathbf{P} without affecting the observables inferred from the spin Hamiltonian. In this case all that is important is $\mathbf{M}\mathbf{M}^\dagger = \mathbf{M}\mathbf{P}\mathbf{P}^\dagger\mathbf{M}^\dagger$, for example the splittings are proportional to:

$$\|\mathbf{B}\cdot\mathbf{M}\| = \sqrt{\mathbf{B}^\dagger\mathbf{M}\mathbf{M}^\dagger\mathbf{B}} \quad (3.25)$$

However if we make the restriction that \mathbf{M} be symmetric then the number of \mathbf{M} s that lead to the same physical results drop dramatically.

To see this, suppose we have a symmetric \mathbf{M} , then:

$$\mathbf{M}\mathbf{P} \text{ is symmetric} \iff \mathbf{M}\mathbf{P} = \mathbf{P}^\dagger\mathbf{M}^\dagger \quad (3.26)$$

$$\iff \mathbf{M}\mathbf{P} = \mathbf{P}^\dagger\mathbf{M} \quad (3.27)$$

$$\iff \mathbf{M}\mathbf{P} - \mathbf{P}^\dagger\mathbf{M} = 0 \quad (3.28)$$

$$\iff \mathbf{P}^\dagger(\mathbf{M}\mathbf{P} - \mathbf{P}^\dagger\mathbf{M}) = 0 \quad (3.29)$$

$$\iff \mathbf{P}^\dagger\mathbf{M}\mathbf{P} = \mathbf{P}^\dagger\mathbf{P}^\dagger\mathbf{M} \quad (3.30)$$

The inference between line 3.28 and 3.29 is in both directions. Because $\det \mathbf{P} \neq 0$ we have $\mathbf{P}\mathbf{X} = 0 \iff \mathbf{X} = 0$.

As we are only interested in coordinate transforms \mathbf{P} that leave the

quadrupole tensor invariant (given by Eq. 3.24) we have $\mathbf{P}^\dagger \mathbf{P}^\dagger = \mathbf{E}$. This leads to the result that $\mathbf{M}\mathbf{P}$ is symmetric if and only if

$$\mathbf{P}\mathbf{M}\mathbf{P}^\dagger = \mathbf{M} \quad (3.31)$$

So ultimately we have the following situation: For sites of axial or higher symmetry or when the principal axes for the tensors overlap, all the \mathbf{P} given by Eq. 3.24 satisfy Eq. 3.31. The transformations $\mathbf{M} \rightarrow \mathbf{M}\mathbf{P}$ simply flip the signs of the principal values of the Zeeman tensor (the g -values). In such a situation we can conclude that the signs of the principal axes of the Zeeman tensor are unable to be inferred from the hyperfine spectra. Indeed they have no relevance until situations involving transitions between hyperfine manifolds are considered. An example of this would be when determining oscillator strengths for optical transitions.

When the principal axes do not overlap, the only transformation $\mathbf{M} \rightarrow \mathbf{M}\mathbf{P}$ that keeps the Zeeman tensor symmetric is inversion. In this situation we can conclude that spectra observed *are* sensitive to the signs of the g -values. The spectra are only insensitive to a simultaneous flip of all the signs of the g -values.

3.1.6 Implementation of algorithm

Simulated annealing was used to solve the inverse problems in this work. In order to obtain some idea of the uncertainties in the inferred values, the Metropolis algorithm was run at a temperature corresponding to the uncertainties in the spectral lines. As mentioned above, this can be shown to be rigorous if all the uncertainty in the experiment is due to independent Gaussian noise added to the true positions of the spectral lines as they are measured. In such a case, the posterior probability distribution and the “pretend” Boltzmann distribution we are sampling are the same.

The model parameters chosen were:

- The values of the parameters describing the pseudo-quadrupole and Zeeman tensors. E , D , g_x , g_y , g_z , α_Q , β_Q , γ_Q , α_M , β_M and γ_M , see Eqns. 3.7 and 3.8.
- The azimuthal angle and elevation angle that describe the position of the C_2 axis.
- The background magnetic field (B_x, B_y, B_z) .

For each magnetic field value in the data set a Hamiltonian was constructed and theoretical positions for the spectral lines calculated. The misfit between the theoretical and experimental values was calculated with the help of the algorithm for assigning peaks described above. The misfit was the dominant contribution to the “energy” but small contributions were added to reflect the prior knowledge of the position of the C_2 .

When implementing such an algorithm there is freedom in choosing two things — how you lower the “temperature” and how you choose the proposed state. When analysing the data collected for this thesis, in order to find the solution that minimised the error the initial temperature was chosen at a level corresponding to an uncertainty in the spectral lines of about 1 MHz. It was then lowered exponentially to 1 kHz over two million jumps, at which point it was no longer changing. This was repeated several times with different initial conditions and random number seeds to confirm that the true minimum had been found. For the evolution step one of the system parameters was chosen at random and a random variable with a Lorentzian distribution was added to it. The initial width (it has infinite variance) of this distribution was chosen to be about five degrees for angles and 10% of the expected results for other quantities. These were also reduced exponentially but three times slower than the temperature.

3.1.7 Results

The spectra, along with the best theoretical fit, are shown in Figs. 3.7 and 3.8. The RMS deviation between the measured and fitted lines was 23 kHz for the ground state and 7 kHz for the excited state.

In order to find the uncertainties in the determined parameters, a further two million time-steps of the Metropolis procedure were carried out after the annealing. This was with a constant nonzero “temperature”, corresponding to the uncertainties in the measured peak positions. As has been mentioned earlier, such a method can be shown to be rigorous if all the uncertainty was due to independent Gaussian noise in the peak positions. The frequencies of a large number of spectral lines were used in determining parameters and if the uncertainties in the positions of each of them were perfectly uncorrelated this would lead to small uncertainties in the inferred parameters. In this situation however this assumption was not strictly valid, leading to what is probably an underestimate of the uncertainties.

The other important consideration is inhomogeneous broadening of the hyperfine parameters. Each ion is sitting in a slightly different environment leading to a distribution of hyperfine parameters among the ensemble.

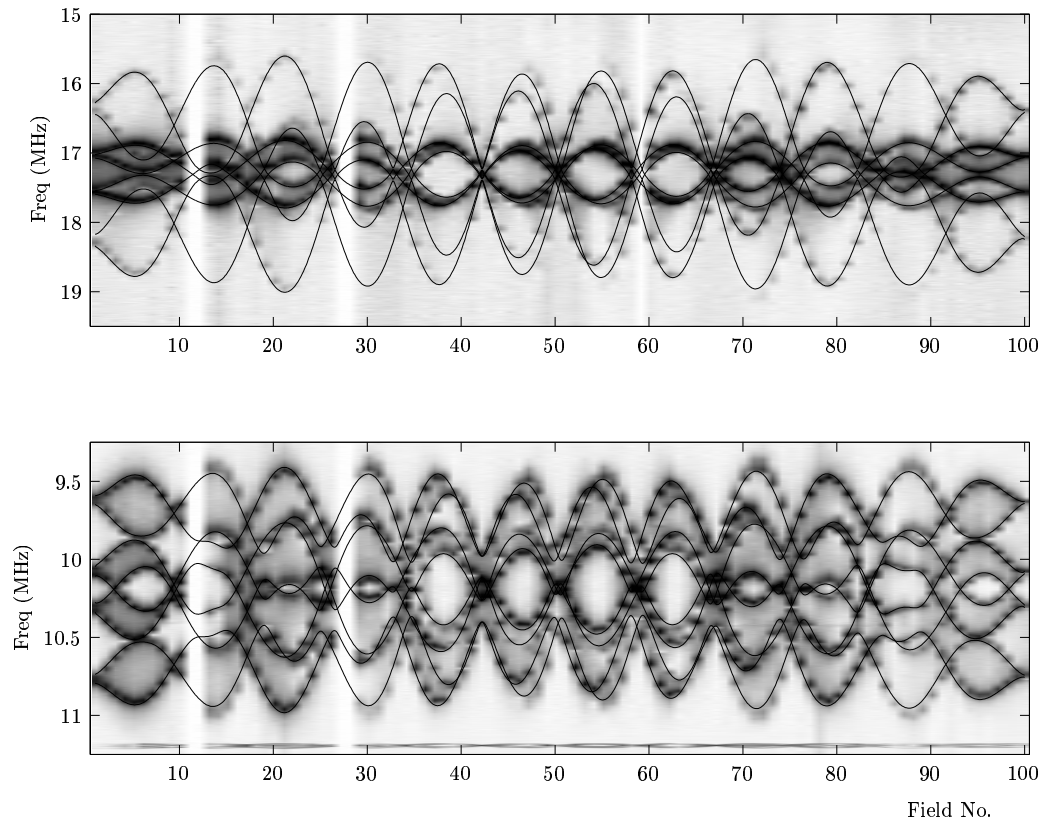


Figure 3.7: The hyperfine spectra obtained for the ground state. Each vertical slice is one spectrum with darkness indicating intensity of Raman heterodyne signal. The field was varied along the horizontal axis as described in the text.

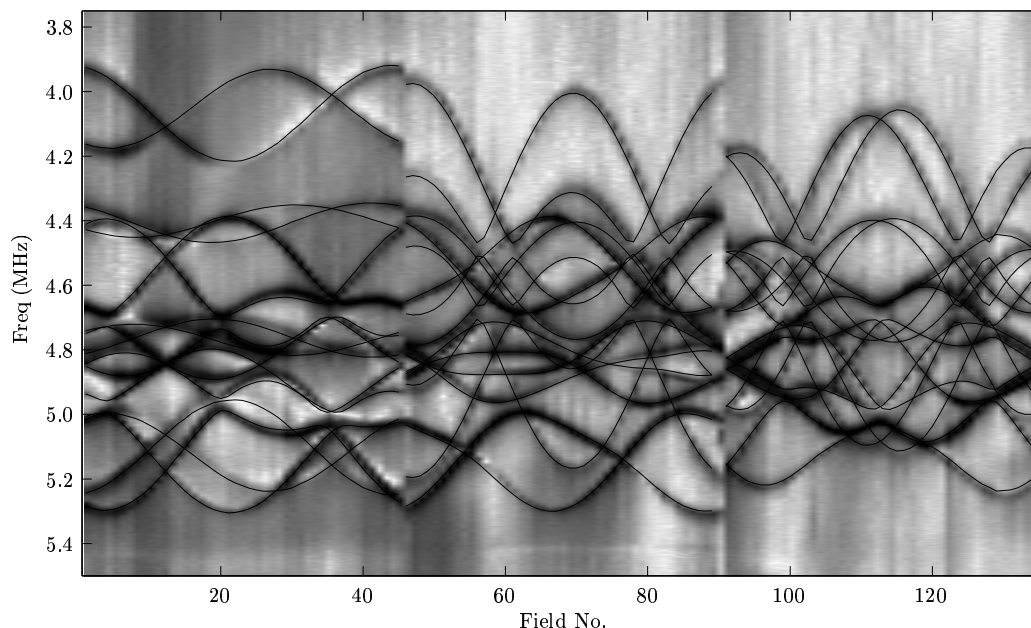


Figure 3.8: The hyperfine spectra obtained for the optically excited state. Each vertical slice is one spectrum with darkness indicating intensity of Raman heterodyne signal. The field was varied along the horizontal axis as described in the text.

Characterising these distributions using, for example, the line-shapes of the observed spectral lines was not attempted.

To work out the uncertainties in the hyperfine parameters the “temperature” was chosen to correspond with the standard deviation of the errors in peak positions for the best fit (23 kHz for the ground state and 7 kHz for the excited state). The best values for the hyperfine parameters are shown in Tables 3.1 and 3.2.

The total uncertainty is a more conservative estimate that includes various systematic errors. These include the systematic errors in the measurement of the frequencies due to slightly dispersive line-shapes and imperfections in the XYZ coils but do not include uncertainty due to misalignment of the crystal and the calibration of the magnetometer. While the chip used for the calibrations of the XYZ coils was very precise its absolute calibration was only guaranteed to be good to 10% [90]. The alignment of the crystal was done by eye and was the greatest source of uncertainty in the orientations, being of the order of 5° .

The position of the C_2 axes were in both cases close to the y -axis. The difference between the C_2 and the y -axis represents how well the crystal was aligned in the XYZ coils. The crystal was taken out and remounted between the collection of the ground and excited state data. Because of how

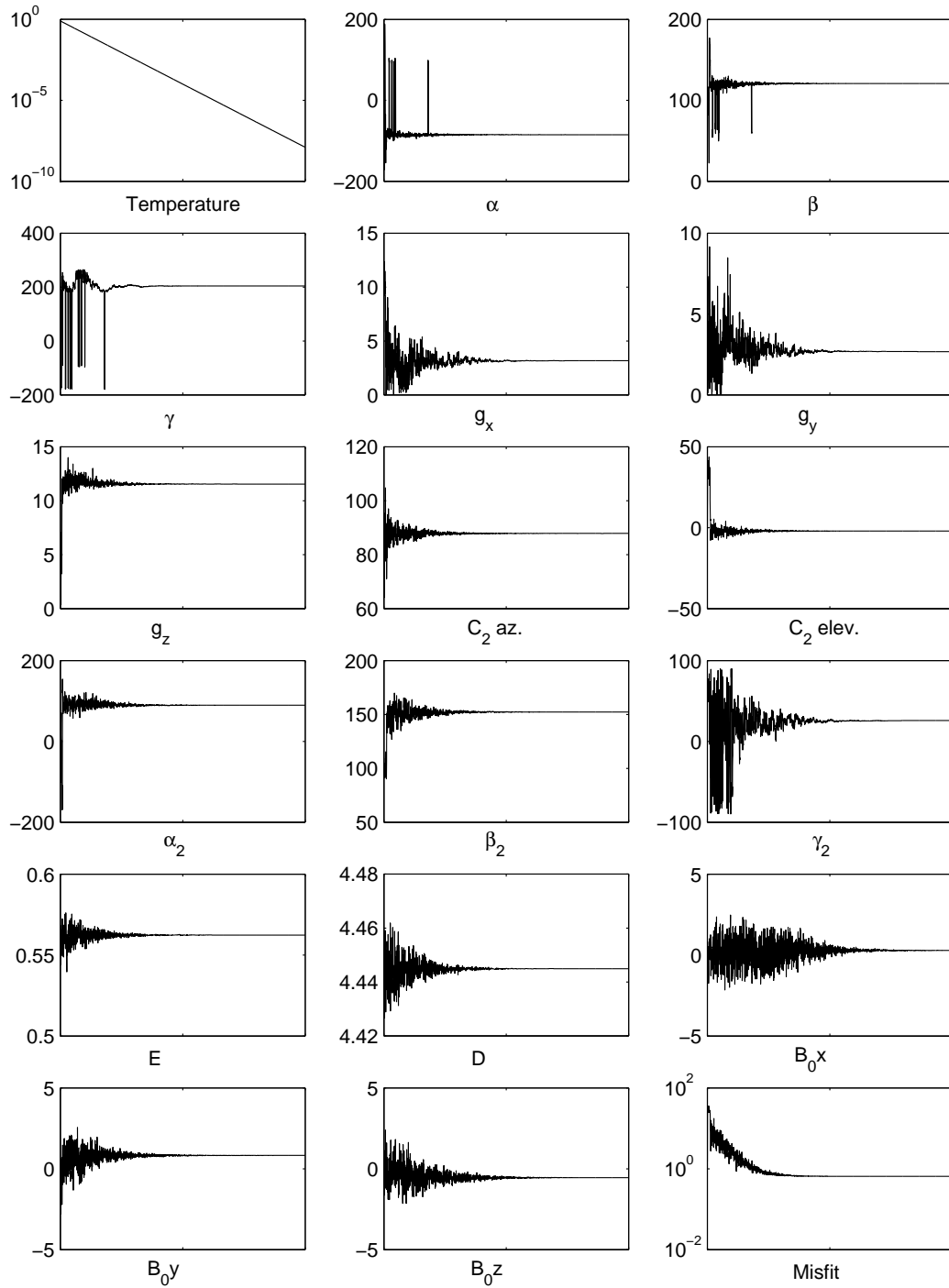


Figure 3.9: Program output for fitting of the ground state. This shows the values of the program parameters during an annealing run. The program lasted for 2 million time steps with values for the parameters recorded every 1000 points. All angles are in degrees, the g values in kHz/Gauss and the pseudo-quadrupole parameters D and E are in MHz. The components of the background field B_0 are in Gauss. The misfit and ‘temperature’ are in MHz^2

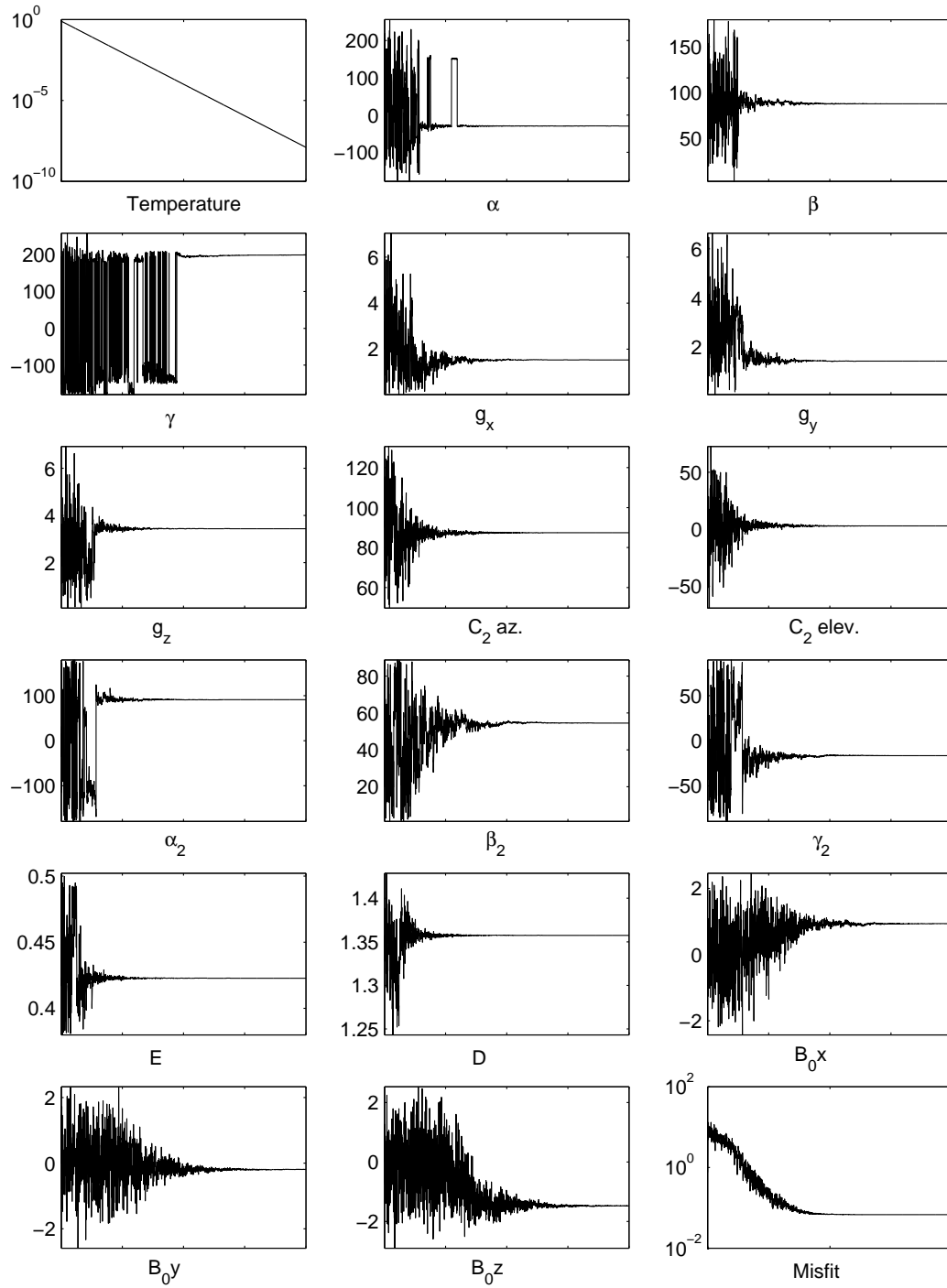


Figure 3.10: Program output for fitting of the excited state. This shows the values of the program parameters during an annealing run. The program lasted for 2 million time steps with values for the parameters recorded every 1000 points. Units used for the parameters are the same as for Fig 3.9.

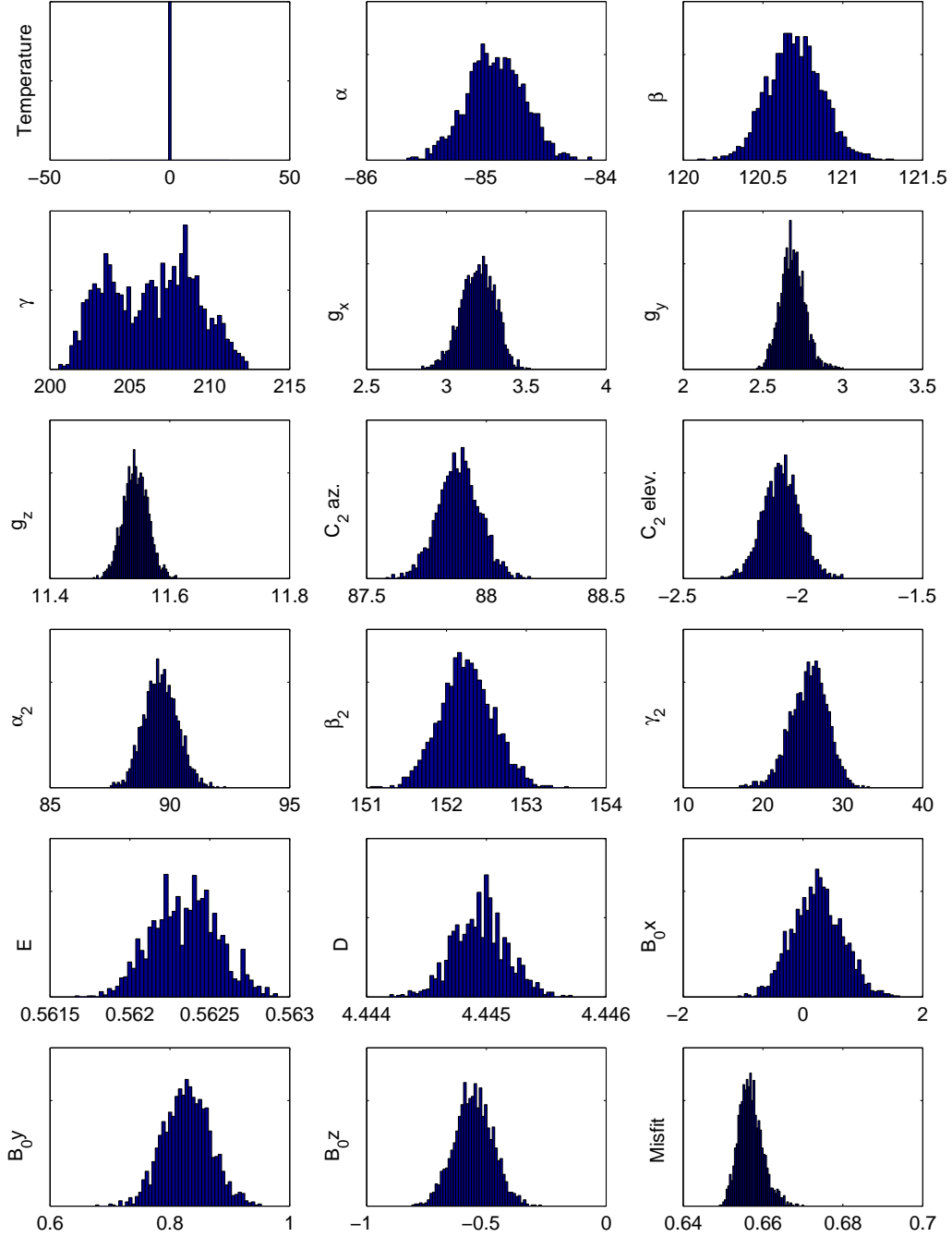


Figure 3.11: Ground state results. Histograms of program parameters with the program run at constant temperature. The histograms represent approximations to the posterior probability distribution for the parameters. Units used for the parameters are the same as for Fig 3.9.

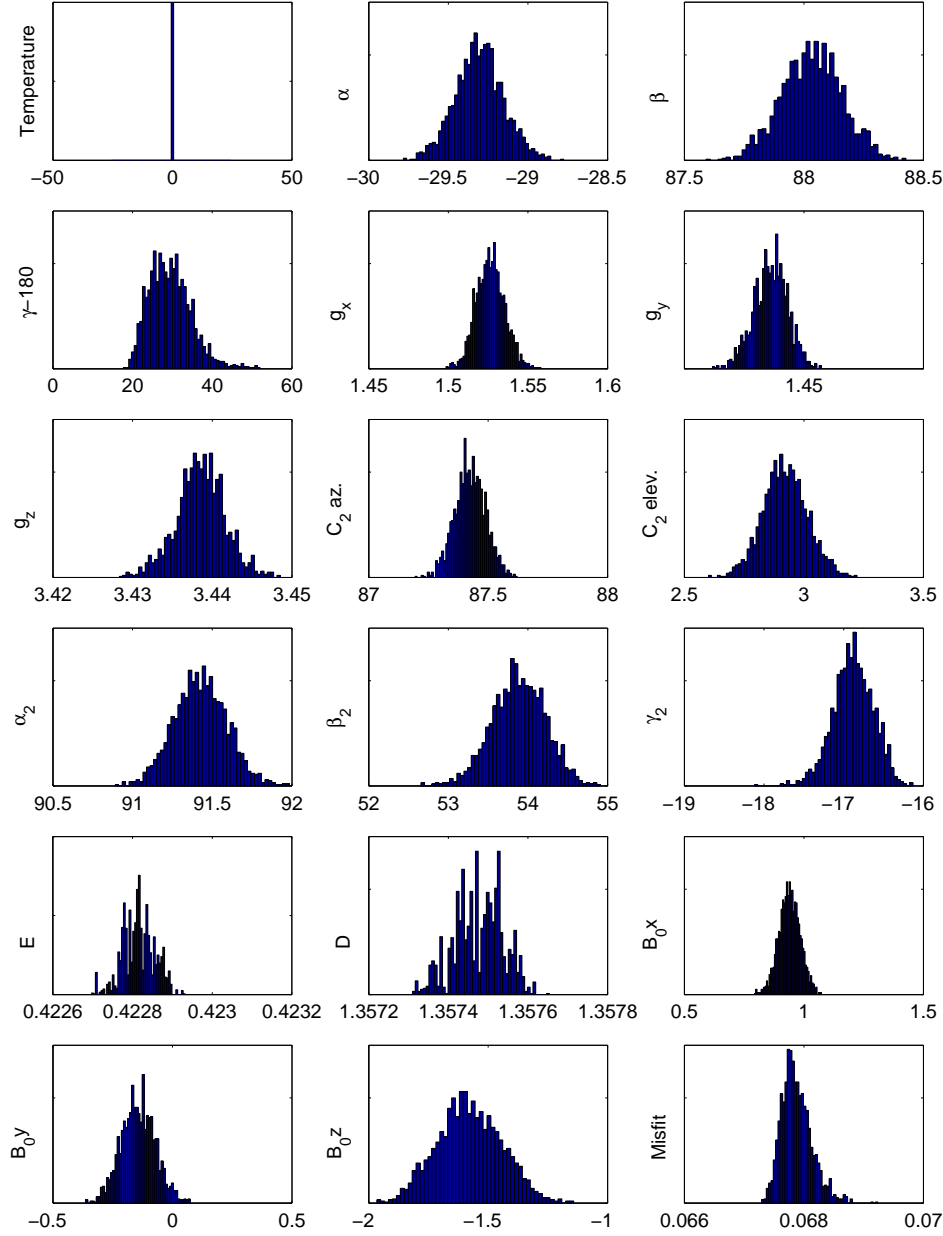


Figure 3.12: Excited state results. Histograms of program parameters with the program run at constant temperature. The histograms represent approximations to the posterior probability distribution for the parameters. $\gamma - 180^\circ$ (modulo 360°) is plotted rather than γ to avoid problems with the angles wrapping around the circle. Units used for the parameters are the same as for Fig 3.9.

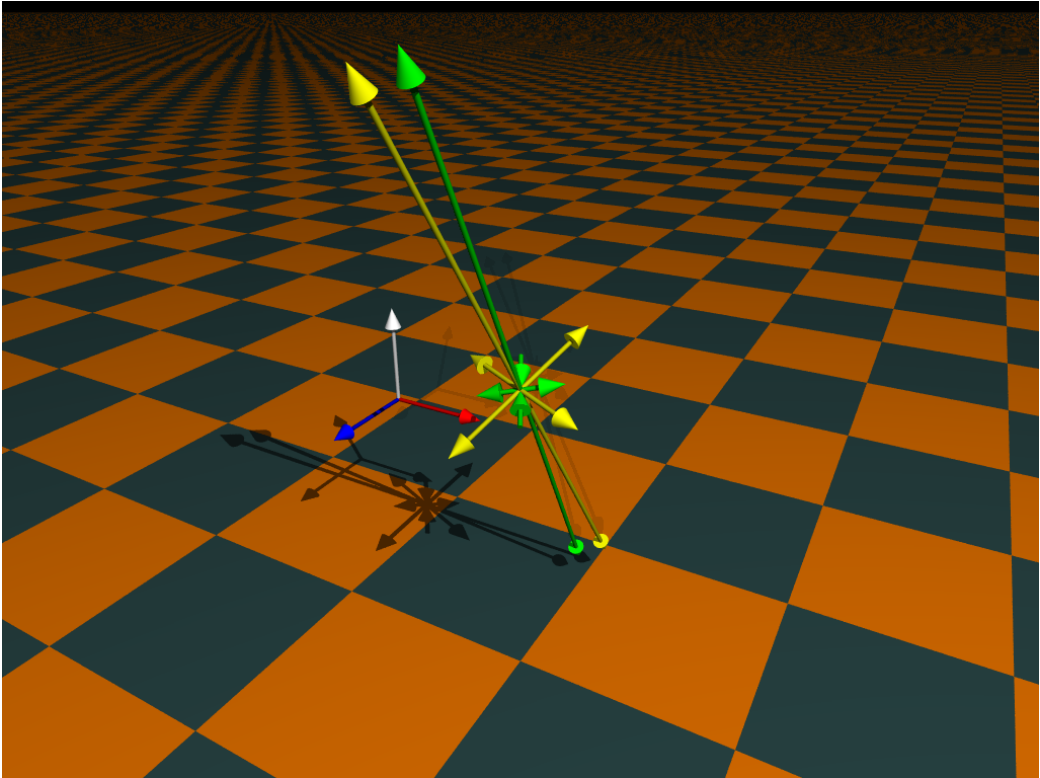


Figure 3.13: An “artist’s impression” of the ground state tensors. The green vectors represent the principal axes of the pseudo-quadrupole tensor with lengths proportional to the principal values. The yellow vectors represent the Zeeman tensor. Negative principal values are depicted by inward pointing vectors. Only one of the two orientations is shown. The tensors have been scaled so the length of the vector corresponding to the principal axis with the largest principal value is the same for both tensors.

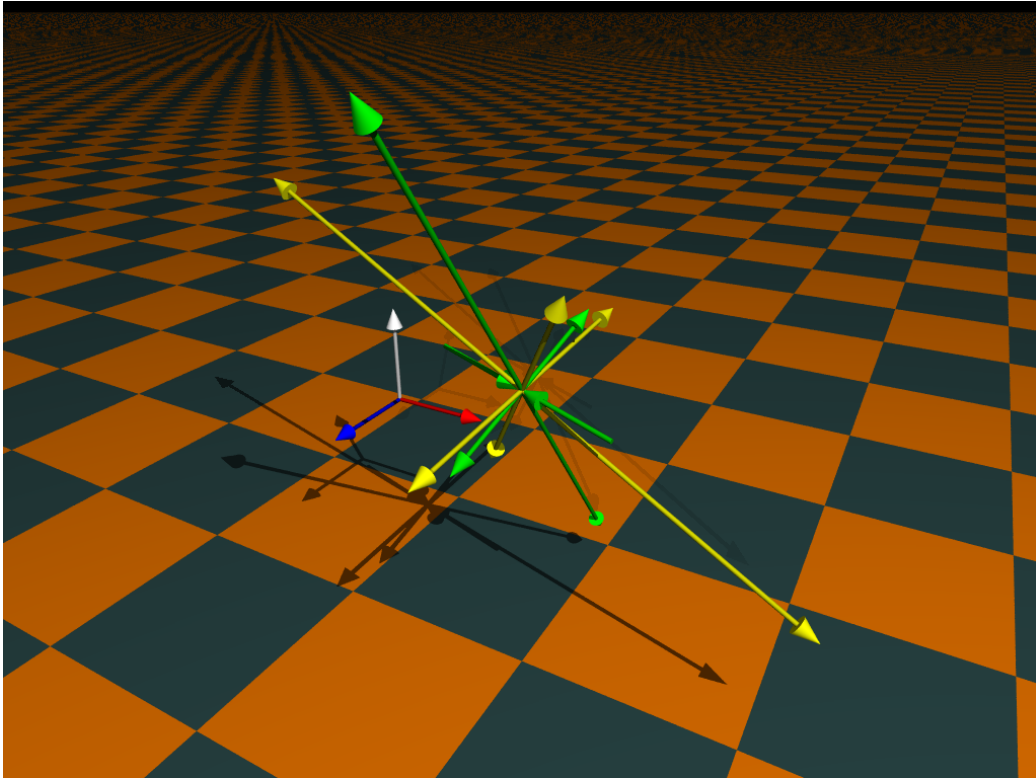


Figure 3.14: An “artist’s impression” of the excited state tensors. The green vectors represent the principal axes of the pseudo-quadrupole tensor with lengths proportional to the principal values. The yellow vectors represent the Zeeman tensor. Negative principal values are depicted by inward pointing vectors. Only one of the two orientations is shown. The tensors have been scaled so the length of the vector corresponding to the principal axis with the largest principal value is the same for both tensors.

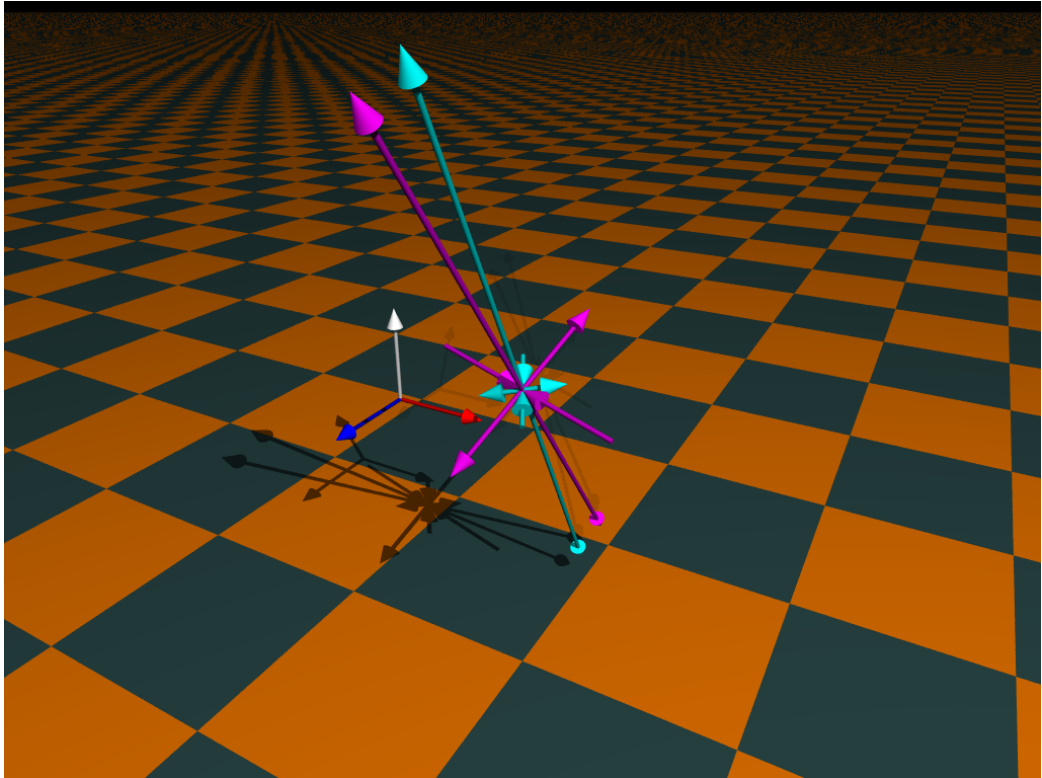


Figure 3.15: An “artist’s impression” of the two quadrupole tensors. The cyan vectors represent the ground state and the magenta the excited state. The vectors show the principal axes with lengths proportional to the principal values. Negative principal values are depicted by inward pointing vectors. Only one of the two orientations is shown. The tensors have been scaled so the length of the vector corresponding to the principal axis with the largest principal value is the same for both tensors.

Table 3.1: Results for fitting of the ground state. The uncertainties stated are those from the Metropolis algorithm, see the text for a discussion. The substitutions $D \rightarrow -D$ and $E \rightarrow -E$ have been made so the results agree with the energy level diagrams of Hemmer et al. (see Sec. 3.1.5)

Quantity	Value	Uncertainty	Units
E	-0.5623	0.0002	MHz
D	-4.4449	0.0003	MHz
g_x	3.20	0.11	kHz/G
g_y	2.69	0.08	kHz/G
g_z	11.54	0.02	kHz/G
α_M	-84.9	0.2	deg.
β_M	120.7	0.2	deg.
γ_M	206	3	deg.
α_Q	89.6	0.7	deg.
β_Q	152.3	0.3	deg.
γ_Q	26	2	deg.
C_2 az.	87.8	0.1	deg.
C_2 elev.	-2.1	0.1	deg.

Table 3.2: Results of fitting of the excited state. The uncertainties stated are those from the Metropolis algorithm, see the text for a discussion. The substitutions $D \rightarrow -D$ and $E \rightarrow -E$ have been made so the results agree with the energy level diagrams of Hemmer et al. (see Sec. 3.1.5)

Quantity	Value	Uncertainty	Units
E	-0.4228	0.0001	MHz
D	-1.3575	0.0002	MHz
g_x	1.526	0.009	kHz/G
g_y	1.441	0.004	kHz/G
g_z	3.439	0.003	kHz/G
α_M	-29.3	0.2	deg.
β_M	88.0	0.1	deg.
γ_M	210	5	deg.
α_Q	91.4	0.2	deg.
β_Q	53.8	0.2	deg.
γ_Q	-16.8	0.3	deg.
C_2 az.	87.4	0.1	deg.
C_2 elev.	2.9	0.1	deg.

the crystal was mounted the azimuthal angle of C_2 axis should be much more reproducible than the elevation. This is seen in the results — the azimuthal angle differs only 0.4° between the ground and excited state experiments. The elevation of the C_2 axes differs by about 5° .

For the ground state, while the difference between the principal axes of the Zeeman and pseudo-quadrupole tensors was resolved, the difference was small ($< 5^\circ$). This would be expected if the pseudo-quadrupole was much greater than the real quadrupole interaction. However the data could not be at all well explained by a model where the real quadrupole contribution was neglected.

For the excited state, the Zeeman and pseudo-quadrupole tensors are not aligned, however the pseudo-quadrupole tensors for both the ground and excited state are aligned.

It must be recognised that working with such a low symmetry system increases the chance that the fit might be fortuitous. However, the author is confident in the results presented here because of the range of magnetic field directions used and the robust nature of simulated annealing. Values for some of the parameters were known independently of the fitting procedure (quadrupole parameters and position of the C_2 axis) and the fitted and a priori values agreed with each other within the respective uncertainties.

Furthermore, measurements were made with larger field strengths, with the large magnet used changing the direction of the magnetic field was not attempted, instead spectra were taken only as a function of field magnitude. The measurements are shown in Fig. 3.16 along with the theoretical values calculated using the spin Hamiltonian derived in this work. The spin Hamiltonian parameters derived here were also used successfully in the work of Alexander [100].

While one can be confident in the ability of the parameters found here to reproduce the spectra for an arbitrary magnetic field, it should be remembered (as discussed in Sec. 3.1.5) that such spectra are not sensitive to all aspects of the Hamiltonian. So rather than finding the ‘true’ spin Hamiltonian we have found a small class of Hamiltonians. This class of Hamiltonians contains the true spin Hamiltonian and all the members give the same spectra.

3.1.8 The future

We have characterised the hyperfine manifolds for both the ground and one optically excited state of praseodymium dopants in Y_2SiO_5 . This enables one to find both the transition frequencies and oscillator strengths for any

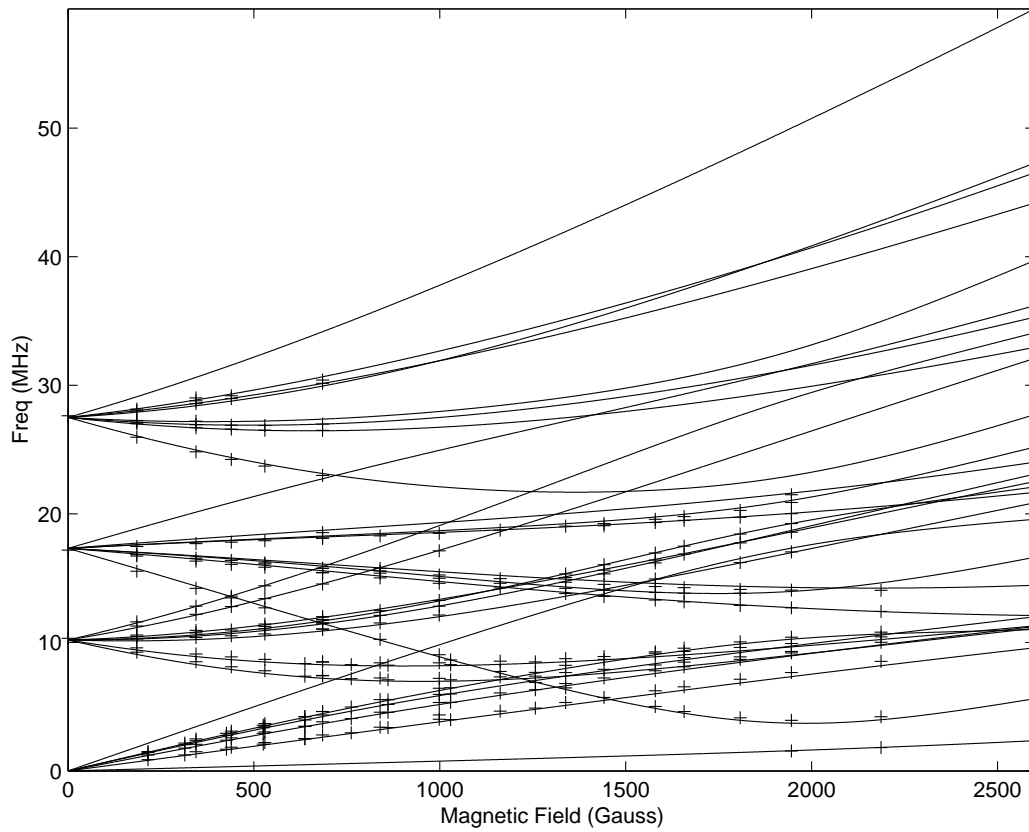


Figure 3.16: A test of the spin Hamiltonian parameters at higher field values. The graph shows experimental and calculated frequencies of spectral lines as the magnetic field was increased along a particular direction, nominally the x -axis. The direction used in the calculation was allowed to move slightly off the x -axis to allow for errors in alignment. The data for this graph was collected with Elliot Fraval.

transition between or within the manifolds for an arbitrary applied magnetic field.

The initial motivation behind this work was to enable EIT experiments to be performed in a magnetic field, because knowledge of the energies of the hyperfine levels would be required to apply the re-pumping beams (see [87, 88, 89]). However the most exciting use of these results so far is in the work of Fraval et al. [81].

They have used the information gained to significantly extend the coherence times of a hyperfine transition. The coherence time for hyperfine transitions that has appeared in the literature for Pr:Y₂SiO₅ is 500 μ s [101]. This has been attributed to the fluctuating magnetic field from the yttrium nuclei. These fluctuations can be reduced by the application of a magnetic field and the coherence time can be increased correspondingly. However with the knowledge of the hyperfine splittings that this work has made available it has been possible to find a magnetic field value where the frequency of a hyperfine transition was insensitive to magnetic field.

The transition frequency of the transition undergoes a turning point as the magnetic field is increased in two orthogonal directions and a point of inflection in the third. At this point, to first order, the fluctuating magnetic field causes no Zeeman shift in the transition, and thus the dephasing due to these random Zeeman shifts is greatly reduced. Fig. 3.17 shows T_2 measurements made by Fraval at this critical point. Coherence times as long as 80 ms were observed. In a rare earth quantum computer, it is envisioned that these hyperfine transitions will be used for long term storage of the quantum information. Thus, for the field of rare earth quantum computation, this is a very significant result.

3.2 Hyperfine interaction in europium doped Y₂SiO₅

After the Pr:Y₂SiO₅ hyperfine characterisation proved to be very useful and because the attempts reported in Section 5.5 were thwarted by lack of adequate oscillator strengths for all the required transitions, it was decided to attempt the characterisation for Eu:Y₂SiO₅.

3.2.1 Experimental setup and procedure

As mentioned in the introduction to this chapter this task was made difficult by the lack of Raman-heterodyne signals. In an attempt to collect enough

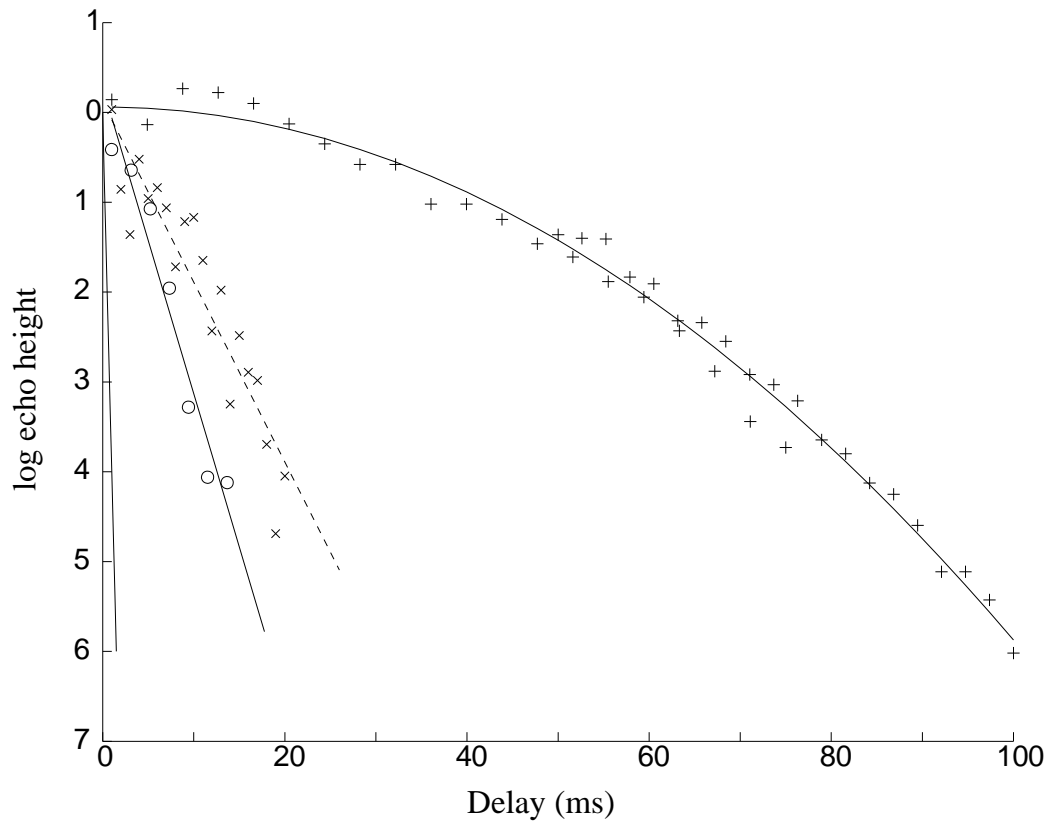


Figure 3.17: A figure taken from [81] showing spin echo amplitude verses time interval between the driving pulses. The pluses show the echo decay behaviour for the insensitive transition. The crosses and circles show the echo decay behaviour for transitions at the same magnetic field but where the gradient of transition frequency with respect to magnetic field does not vanish. A line corresponding to the $T_2 = 500 \mu\text{s}$ for zero magnetic field is shown for comparison.

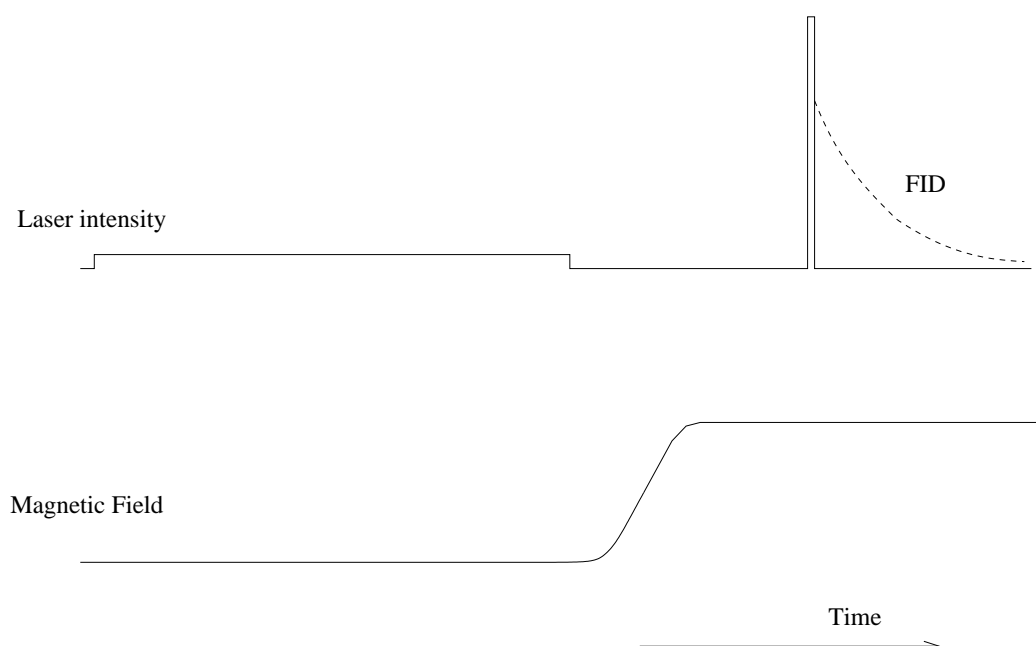


Figure 3.18: The sequence events used to take each experimental shot.

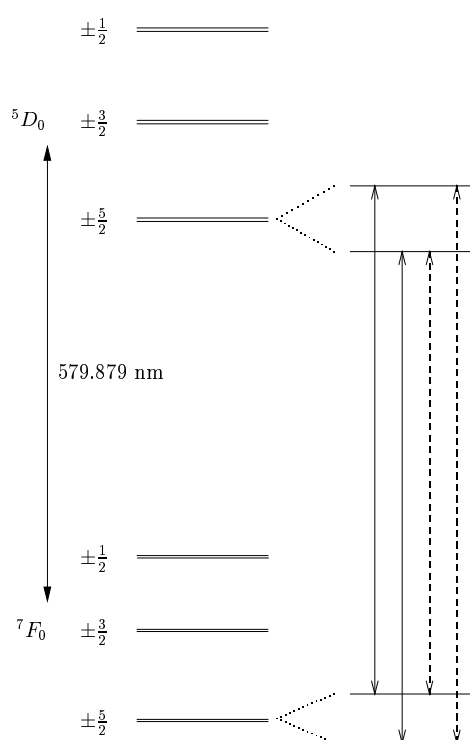


Figure 3.19: Europium energy level diagram showing the transitions involved in the holeburning spectra. The splitting of the $\pm 5/2$ energy levels due to the magnetic field is exaggerated. The hyperfine splittings are of the order of 50 MHz (see Fig. 5.1 on page 112) and the Zeeman splittings were of the order of 500 kHz. The four transitions that might be expected to be seen in the spectra taken are shown. The transitions represented by dotted lines were not observed.

data to infer the hyperfine parameters, a holeburning technique was used. The sequence of events in each experimental shot is shown in Fig. 3.18. First a long weak pulse (≈ 160 ms) was applied to the sample to burn a narrow hole in the sample. The transition was then split by the application of an applied magnetic field, and a time of 500 ms was allowed for the supplies to reach the appropriate currents. The spectra of the resulting feature was then read out with a short intense pulse (≈ 0.6 μs). The resulting free induction decay was Fourier transformed to obtain the spectra. The experimental setup used was essentially the same as described in Sec. 5.2.

Just as in the case of Praseodymium dopants, there are four different crystallographic positions at which the europium can substitute yttrium. The four positions can be divided into two pairs with the members of each pair related to each other by the crystal's C_2 axis. These two pairs have different crystal field splittings and hence different optical transition frequencies. Unlike praseodymium which has only one stable isotope, europium has two stable isotopes of approximately equal abundance, ^{151}Eu and ^{153}Eu . These two isotopes have the same transition optical frequencies but different hyperfine transition frequencies. The experiments of this thesis were carried out on the ^{151}Eu isotope at “site 1” [102]. In order to simplify the spectra, the procedure was applied to a broad anti-hole that had been prepared in a manner similar to that described in Sec. 5.3.2. Although other measurements were made, all the results presented here were for the $\pm 5/2 \rightarrow \pm 5/2$ transition as shown on Fig. 3.19.

The magnetic field was supplied by a set of custom made superconducting XYZ coils. These were newer than those used for the praseodymium work and had a larger number of turns. The X and Y coils had sensitivities of 70 G/A and the Z , 50 G/A.

In order to better distinguish between the quadratic Zeeman effect and laser drifts, it was decided to take spectra while increasing the magnetic field along a discrete set of directions.

The crystal was delivered cut with faces perpendicular to the crystallographic axes and the faces marked as such, using an a , b or c . The sample was placed in the XYZ coils with X axis parallel to the b (which is the C_2) axis and the normal of the face marked c pointing along the Z direction. The laser beam was directed along the X axis and polarised in the vertical plane. The optical transition was somewhat polarised with maximum absorption occurring for this vertical polarisation.

3.2.2 Results

From each of the two orientations of “site 1” up to four spectral lines were expected. Thus, in general, eight spectral lines could be expected for an arbitrary field and four when the field was applied along or perpendicular to the C_2 axis. Instead, either four lines or two lines were observed.

The spectra as a function of magnetic field for two field directions are shown in Figs. 3.20 and 3.21. Measurements were taken for the field changing along 13 directions. These were approximately the directions³ $[abc]$ where each of a , b and c took on the values $\{0, 1, \bar{1}\}$.

For Fig. 3.20, the applied magnetic field was along the C_2 axis and two transitions can be seen, as well as a number of what could be weaker lines. One serious weakness in the method used is that it is not possible to tell if these are due to weakly allowed transitions or to signals from other subgroups of ions, for example, from the other isotope or a packet that is resonant with the laser due to some other transition. The spectral lines split at approximately 1 kHz/G and the line traced out by the peaks of the spectra is gently curved due to the quadratic Zeeman. The magnetic field values used are shown in Fig. 3.22(a).

For Fig. 3.21 the field was ramped along a direction close to the $[\bar{1}11]$. Because this direction was not perpendicular to or parallel with the C_2 axis, four spectral lines can be seen, two for each of the orientations of the site. The quadratic Zeeman splitting was among the highest seen for all the directions measured and was of the order of 4 Hz/G². The magnetic field values used are shown in Fig. 3.2.4.

3.2.3 Discussion

It might be expected that the $\pm 5/2 \rightarrow \mp 5/2$ transitions would be weak because they only occur due to the mixing between the $+5/2$ and $-5/2$ states and for these two states the mixing would be small. However, the situation was similar for the $\pm 1/2 \rightarrow \mp 1/2$, in this case the hyperfine ratio of the hyperfine splittings suggests that the mixing of these states should be large [103]. Reflecting on these results led to the ‘discovery’ of the cyclic transition (see Sec. 4.7). It should be noted that Silversmith [103] used the same property of the Hamiltonian in order to more simply arrive at analytic expressions for the Hamiltonian eigenvalues.

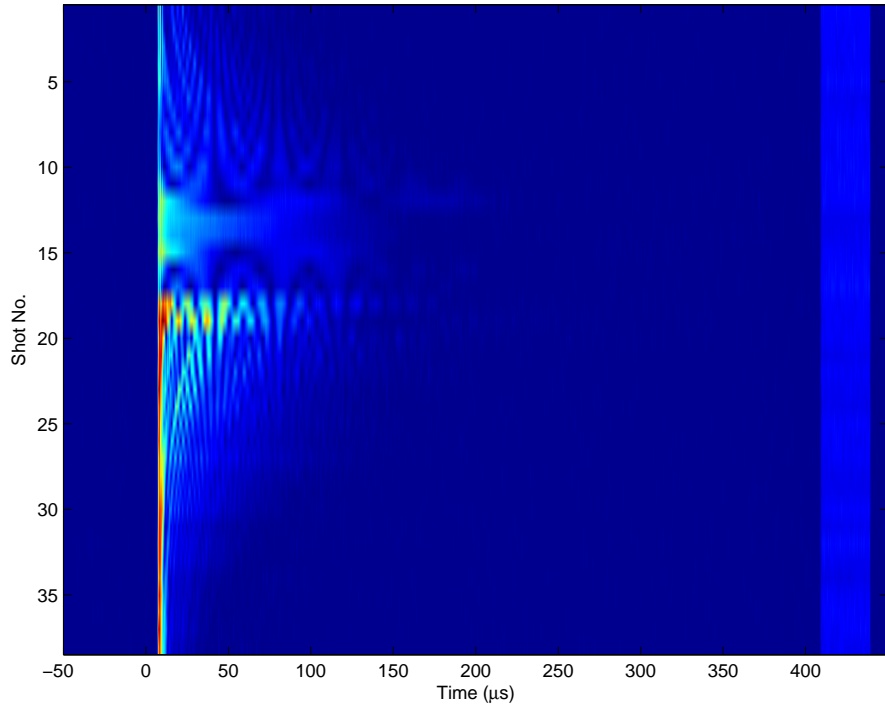
³Even though the crystallographic notation is used for the directions of the magnetic field, they are described here in terms of the ‘lab-frame’ defined by the XYZ coils rather than any axes of the crystal. The relationship between these two are described in the text.

Because of the stability of the laser and long coherence times of the optical transitions involved the spectral resolution achieved is impressive. However, the bandwidth of the technique is also small, being limited by the length of the readout pulse, which is in turn limited by the laser power. Further to this, when compared to the hyperfine splittings the resolution of the technique is not so impressive. In many of the 13 directions for which the data was taken it was not possible to clearly see the spectral lines due to their finite width.

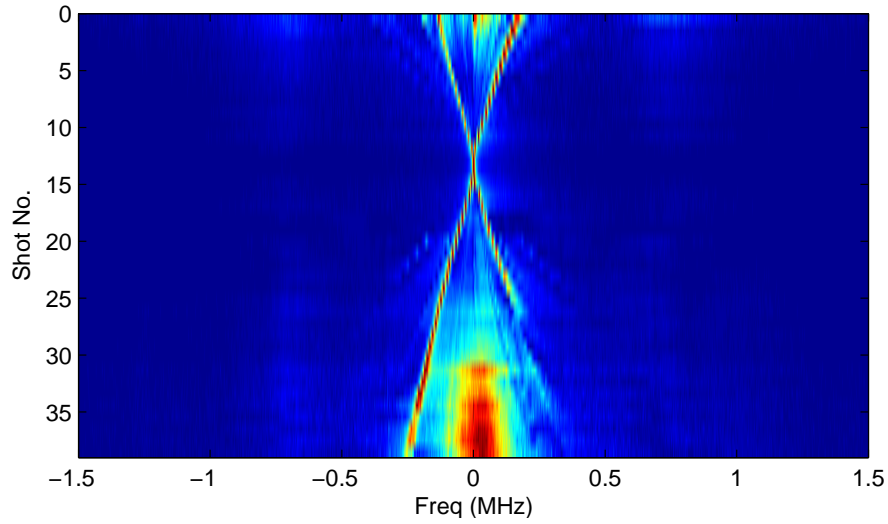
3.2.4 Conclusions

With the data obtained it has not been possible to extract the spin Hamiltonian parameters yet. The spectral lines weren't well resolved. In some cases the interpretation of the spectra was further complicated by weak overlapping peaks due to transitions of the system that we were not trying to measure.

From the data obtained the Zeeman splitting of the hyperfine transition is of the order of 1 kHz/G and the largest quadratic Zeeman splitting was of the order 4 Hz/G².



(a)



(b)

Figure 3.20: Spectra of the Zeeman split $\pm 5/2 \rightarrow \pm 5/2$ transition as the field is increased along the C_2 axis. (a) Each horizontal slice is the amplitude of the delayed free induction decay (FID) signal from hitting the hole with the $0.6 \mu s$ readout pulse. Both phases of the free induction decay signal were recorded. The light blue band to the right of the figure is made of the weak phase reference pulses applied after each FID had finished. (b) The spectra of split hole as a function of magnetic field obtained by Fourier transform of FID signal.

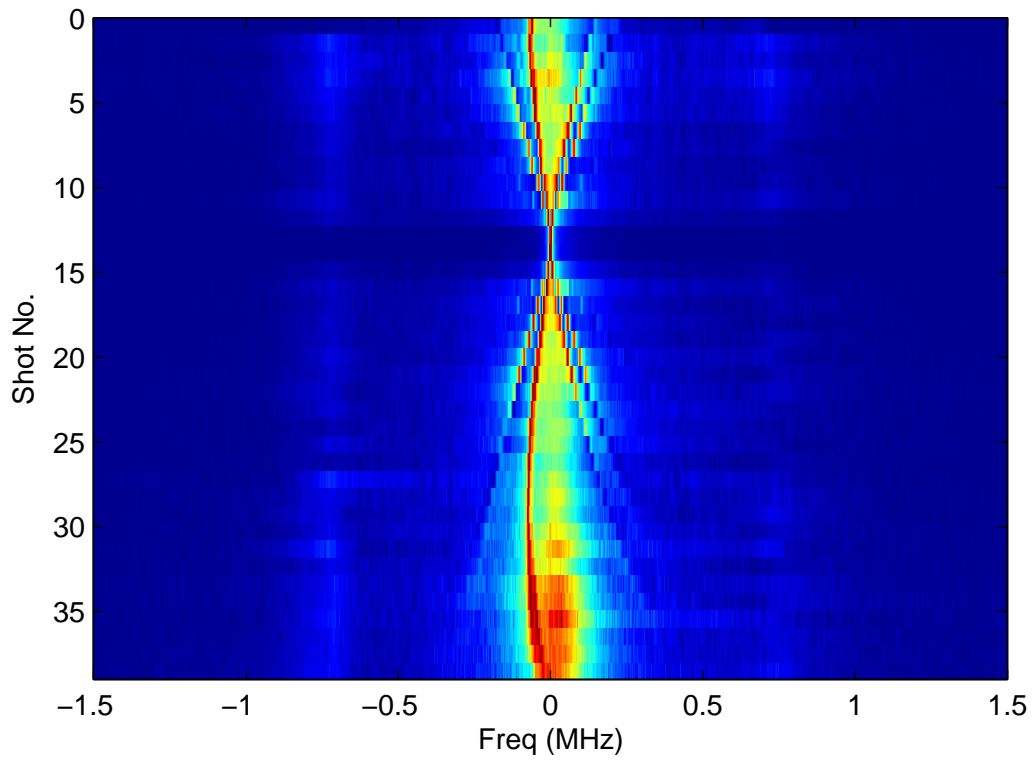


Figure 3.21: Spectra of the Zeeman split $\pm 5/2 \rightarrow \pm 5/2$ transition as the field is increased along a field direction different to the C_2 axis (see text).

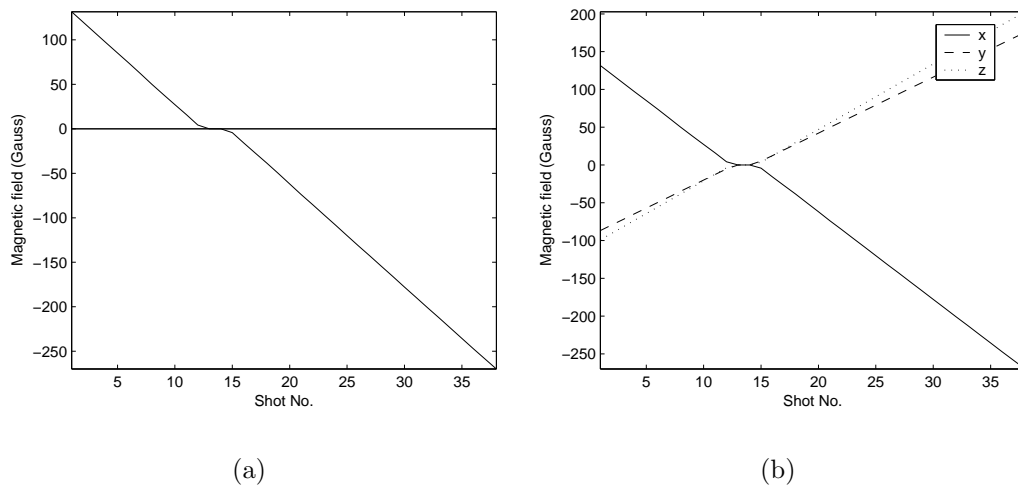


Figure 3.22: Magnetic field values used to obtain the spectra shown in (a) Fig. 3.20 and (b) Fig. 3.21. For (a) the magnetic field was applied along the crystal's C_2 axis (z in the lab frame). See the text for how the x , y and z axes of the lab frame correspond to the crystallographic axes.

Chapter 4

Optical Quantum Computing in Solids

In this chapter a review is made of the proposals for optical based quantum computation in solids. These are based on two types of systems, rare earth ion dopants and NV centres in diamond. After discussing the details of ion-ion interactions in rare earth ion dopants, each of the published schemes is evaluated critically. Then the direction pursued in this thesis is then laid out. The progress made in trying to implement this direction experimentally is described in Chapter 5.

While the most sophisticated quantum computing demonstrations to date have involved liquid state NMR, it is unlikely the problems involved in scaling such an approach to a large number of qubits can be overcome (see Sec. 1.4.1). The experiments must be carried out at close to room temperature. Consequently the thermal state is highly mixed. There are other, perhaps less important, problems in NMR quantum computation. Firstly, the interactions between the qubits are on all the time which leads to the need for rephasing sequences to stop the effects of interactions when they are not wanted. Secondly, the interactions between the nuclei are weak, ~ 100 Hz, making the operation of the computer slow.

Optical centres in solids provide a method of overcoming the problems of liquid state NMR computing, while retaining its two main strengths. These strengths are: (a) the storage of quantum information in long lived nuclear states and (b) the elegance of a scheme that doesn't require complex fabrication. It is desirable to avoid this fabrication for two reasons; the most immediate, but perhaps least important, is cost. A much bigger issue is that nano-fabrication will cause damage to the crystal structure and this is likely to affect coherence times. Importantly, this "damage" not only includes unintentional damage caused in the manufacture, but also includes the disruption

to the crystal that the fabricated structures represent. In rare earth systems, crystal imperfection has been shown to significantly increase dephasing rates [104].

The rare earth ions stand out as a group of optical centres for quantum computing. The lifetimes for the hyperfine levels can be very long (hours) [102]. Furthermore, the coherence times for the hyperfine transitions can also be long — 80 ms was recently measured [81] and it is thought that this could be increased significantly. The outstanding feature of rare earth ions is the narrowness of their optical transitions, an optical coherence time of 2.6 ms has been measured for $\text{Eu}^{3+}:\text{Y}_2\text{SiO}_5$ [66]. Furthermore there is a comparatively large distribution of transition frequencies within an ensemble of ions ($\sim\text{GHz}$). These two facts allow many different groups of ions to be addressed individually, based on their resonant frequencies. The ratio between the inhomogeneous and homogeneous broadening can be as large as 10^7 . The nuclear splittings are generally $\mathcal{O}(10\text{ MHz})$ in zero field. This is much bigger than the homogeneous linewidths of the transitions, which means the nuclear states of the ions can be manipulated optically. The fact that the hyperfine structure is resolvable optically means quantum information encoded in the nuclear transitions can be transferred to the optical transitions and vice versa.

Rare earth ions in non-centro-symmetric hosts also have large (as big as GHz) interactions involving their optical transitions and these provide the ion-ion interactions needed for multi-qubit gates. The advantage of these interactions is that quantum information is only sensitive to their action when it is encoded in the optical states. Putting the quantum information into the ground state hyperfine structure would free one from having to rephase the interaction when it is not wanted. This isolation was investigated in the recent work of Alexander [100].

One weakness of rare earth ions is the difficulties that will be encountered when reading out the states of single ions. In this the NV centre in diamond does much better. Single site spectroscopy has been demonstrated for the NV centre in diamond [105] and this has allowed it to be used as the basis of single photon sources [106]. A nitrogen-vacancy or NV centre is where two of the carbon atoms in the diamond lattice have been replaced by a nitrogen atom and a vacancy. The NV centre has an oscillator strength similar to that of an allowed transition in a free atom. The larger oscillator strength means higher Rabi frequencies are available and faster spontaneous emission, both of which help in single site detection. The problem with all the previous proposals for quantum computing using NV centres is in realising the interactions between ions. Previous proposals have used either cavities

that have difficult to realise parameters or the resonance interaction. Using the resonance interaction puts strict criteria on the optical frequencies of the centres — criteria that would be hard to meet in practice. With this in mind, the possibility that NV centres might interact using exactly the same mechanism as the rare earths is exciting. This is discussed in Sec. 4.1.1.

Several schemes for optical quantum computing in solids have been proposed [107, 108, 109]. The use of both ensembles [108] and single impurities [107, 108, 109] for the qubits has been proposed. In all such systems the long lived hyperfine levels of an impurity, be it a rare earth ion or a NV centre, are used to store the quantum information. Optical transitions are used to cause qubit-qubit interactions for multi-qubit gates. The inhomogeneous broadening in such transitions is used to selectively address the qubits.

The ability to apply accurate single qubits operations optically in a solid was first demonstrated by Pryde et al. [80]. The single qubits were absorptive features prepared in the inhomogeneous line that were narrow compared to the available Rabi frequencies. Further development of the techniques to create and characterise these ensembles was carried out in this work and the results are presented in Chapter 5.

These demonstrations of single qubit operations leave the following challenges of this type of quantum computing: effecting qubit-qubit interactions and detection of the qubit states. These are discussed below.

4.1 Interaction between rare earth ions' optical transitions

Here we discuss the various phenomena that might be exploited in order to effect two qubit-qubit operations, and in the case of phonon mediated interactions, those processes that might interfere with these. The treatment is focused on rare earth ions; however the applicability of the concepts to the NV centre is also discussed. The discussion of the use of high finesse cavities to effect ion-ion interactions is deferred until later in the chapter.

Rare earth ions at low temperatures can exhibit very narrow homogeneous linewidths. Because of this, very sensitive measurements of frequency shifts and the decoherence caused by various phenomena can be studied. Using photon echo techniques means one is not limited by the inhomogeneous linewidth and it is possible to probe for effects that are only limited by the homogeneous linewidths. Historically these effects have not been studied for academic interest alone, but also because of the application of these materials for time-domain optical memory (TDOM) [78]. The frequency shifts and

decoherence effects discussed here are of great importance in TDOM as they provide fundamental limits to the performance of a particular dopant/host system.

In all the experiments previous to this thesis, the random nature of the frequency shifts which were caused by otherwise coherent ion-ion interactions have always been observed as decohering effects, which increase with the size of perturbing pulses. In spite of this the mechanisms for these interactions could be put forward and a great deal of supporting evidence given. A good review of the ion-ion interactions and their role in causing photon echo attenuation is found in the work of Graf et al. [110].

4.1.1 Electric dipole-dipole interactions and excitation induced frequency shifts

The use of the electric dipole-dipole interaction that occurs in rare earth ion systems for quantum computation was first proposed by Sellars and Manson [111]. The environment surrounding a rare earth ion in most hosts is anisotropic, which leads to a permanent electric dipole moment associated with the dopant. This dipole moment depends on the electronic state of the ion. An ion will therefore experience a Stark shift that is conditional on the state of its neighbour. The interaction between the ions is given by [112]

$$\hbar\omega_{ij} = \frac{[\delta\boldsymbol{\mu}_i \cdot \delta\boldsymbol{\mu}_j - 3(\delta\boldsymbol{\mu}_i \cdot \hat{\mathbf{r}}_{ij})(\delta\boldsymbol{\mu}_j \cdot \hat{\mathbf{r}}_{ij})]}{4\pi\epsilon r_{ij}^3} \quad (4.1)$$

Here $\delta\boldsymbol{\mu}_i$ is the (vector valued) change in the electric dipole moment between the ground and excited state for ion i , and \mathbf{r}_{ij} is the vector describing the relative positions of ions i and j .

This interaction is the dominant ion-ion interaction for the Eu:Y₂SiO₅ and it is used in this thesis to effect the qubit-qubit interactions. The interaction is *diagonal* in the sense that the perturbation it causes only changes the energies of the existing eigenstates of the system. This is to be contrasted with off-diagonal interactions, such as the resonance interaction, which can cause an exchange of excitation. Diagonal interactions cause ‘instantaneous spectral diffusion’ or ‘excitation induced frequency shifts’, which are other phrases used to describe diagonal interactions. To the author’s knowledge, the electric dipole-dipole interaction is the only mechanism for such diagonal interactions that has been put forward.

Excitation induced frequency shifts for the optical transitions in solids first appeared in the literature in 1974 in the work of Taylor and Hessler [113].

They were attempting to explain the concentration dependence of photon echo decays in ruby [114]. While the mechanism was eventually discounted for ruby [115], it has turned out to be an important dephasing mechanism for rare earth ions, especially when there are few other perturbations in the lattice.

The effects of excitation induced frequency shifts were first demonstrated in $\text{Tb}^{3+}:\text{LiYF}_4$ by Liu et al. [116]. In this work they demonstrated that the effective dephasing times as measured using photon echoes were sensitive to the sizes of the perturbing pulses used. Furthermore the first pulse had a much smaller effect in shortening the coherence time than did the second. This can easily be understood in terms of excitation induced frequency shifts. If the first pulse excites a lot of ions it will cause a large random shift in the frequencies of the ions' transitions. Unless the time between pulses is long compared to the lifetime, however, the frequency shift will stay constant throughout the echo sequence and will be rephased along with the inhomogeneous broadening. If the middle pulse excites a lot of ions, then the ions which form the echo will experience a large random frequency shift that is only effective for half of the photon echo sequence. These frequency shifts will not get rephased and will cause a decoherence of the ensemble of ions that produce the echo, leading to smaller echoes.

Huang et al. followed this with more probing experiments on a $\text{Eu}^{3+}:\text{Y}_2\text{O}_3$ sample [117]. Their experiments used pulses from a gated CW laser and shorter more intense pulses made from the excimer-pumped dye amplification of the gated CW laser pulse.

The measurements reported by Huang et al. can be broken up into three groups.

First they did T_2 measurements using photon echoes where one of the driving pulses was a gated CW pulse and the other an amplified pulse. They found, as Liu had, that putting the large pulse second caused more echo demolition than having it first. Further when the intense pulse was first they noticed non-exponential decay in the echo heights as the time between the pulses was increased. This could be expected because the decay rate of the coherence changes as the ions which were excited by the first pulse relax back to the ground state.

Next, Huang et al. performed photon echo experiments where both the pulses of the echo sequence were produced by gated CW pulses. A third, amplified pulse was applied at some time during the echo sequence. The time when this perturbing pulse was applied was varied and its effect on the echo height observed. They found the echo height showed a 'U' shaped de-

pendence with the position of the perturbing pulse. With perturbing pulses near either the first pulse or the echo, the height of the echo was not strongly affected. However, for the perturbing pulse applied close to the second pulse of the photon echo sequence the reduction in the echo amplitude was significant. This can be explained using a simple extension of ideas given above to describe the increased sensitivity of the echo height to the amplitude of the second pulse compared to that of the first. From their measurements and estimates of the number of ions excited by the perturbing pulses, an electric dipole change of $\mathcal{O}(10^{-32} \text{ Cm})$ was inferred.

Thirdly, Huang et al. showed that the mechanism causing the reduction in the echo height was due to the number of ions that the pulses excited, rather than the energy of the pulses. To do this, they measured the decay in echo amplitude as a function of length of the echo sequences. They did this twice, each time using pulses that approximated the ideal $\pi/2$ and π areas for resonant ions. The second time the intensities of the pulses were reduced by a factor of ten and the lengths increased by a factor of ten. A longer effective T_2 was observed for the long weak pulses. This was explained using the fact that the longer weaker pulses excited less ions due to their narrower spectral width.

Further insight was provided by Mitsunaga et al. in 1992 [118] using three pulse echo techniques. They showed that the excitation of ions in one of the two sites of $\text{Eu:Y}_2\text{SiO}_5$ produced an instantaneous ($< 1 \mu\text{s}$) frequency shift in the ions of the other site. Furthermore this shift lasted for a time ($\sim 2 \text{ ms}$) similar to that required for these ions to decay. A three pulse echo experiment is similar to a normal photon echo experiment except that the second (π) driving pulse is replaced with two pulses of half the length. The first two pulses cause a spectral grating to be written into the population of the ions in a manner similar to Ramsey fringes [119]. When hit with the third pulse, an echo is formed from the combined free induction decay signals of the ions in this spectral grating. The advantage of the three pulse echo techniques to these experiments is that the dephasing and rephasing time intervals are separated by the length of time between the second and third pulses. This length of time can be made very long because, due to spectral holeburning, the grating is still present after the decay of the population in the excited state. The time the resulting grating exists is governed then by the population lifetimes for the ground state spin structure. These lifetimes can be as long as hours [102].

In Chapter 5 experiments which further characterise these ion-ion interactions are described. In particular, Rabi oscillations are seen in the size

of a photon echo as the duration of the perturbing pulse, which was hitting another group of ions, was varied.

In 1992, both Meixner et al. [120] and Wang et al. [121] published direct measurements of the Stark shifts of Rare Earth Ions. In both cases the methods employed were essentially the same — a photon echo sequence was used where an electric field was applied for half of the time. In both cases YAlO_3 was used as the host,¹ Meixner investigated europium dopants and Wang erbium. The use of YAlO_3 was crucial for the technique. In YAlO_3 the dopants are in two equal groups each with their dipole moments in opposite directions. These two groups of ions see equal and opposite frequency shifts. The beating of these two frequency shifts results in an oscillation in the height of the photon echoes as the time delay is varied. In this manner the phase shifts caused by the Stark shift could be observed without requiring a high resolution laser. A Stark coefficient of $33.7 \text{ kHz cm V}^{-1}$ was reported for europium and $141 \text{ kHz cm V}^{-1}$ for erbium.

Because the expression of Eq. 4.1 only depends on the change in the electric dipole moment between the ground and excited states, these measurements of the change in dipole moment together with the relative positions of two ions, completely describe their interaction.

The Stark shift value measured in [120] was used in Eq. 4.1 by Ohlsson et al. to estimate interaction strengths of 1 GHz, 1 MHz and 1 kHz for separations of 1, 10 and 100 nm respectively.

The NV centre in diamond consists of a nitrogen sitting next to a vacancy and as such it is obviously an anisotropic system. Because of this a Stark shift can be expected. To the author's knowledge no values of the Stark shifts have been reported. However, the effect of electric field perturbations on optical centres in diamond was investigated in 1980 by Davies and Manson [122]. They were more interested at that stage in determining what the optical centres were, rather than making quantitative measurements. The measurements were made by applying an oscillating electric field to the sample and looking for a change in the absorption as the shape of the inhomogeneous line was varied.

In their experiments, electric fields of the order of 10 kV/mm were used. For the sake of argument, we shall assume that this causes a Stark shift comparable to the inhomogeneous line width. This is an incorrect assumption — the splittings were less than the linewidth. This assumption will result

¹Wang also did measurements for the chromium ions in alexandrite ($\text{Cr}^{3+}:\text{BeAl}_2\text{O}_4$ (0.05%)) which have shorter coherence times, but apart from a slightly more complicated geometric arrangements of dopants, modulating heights of the echo signal were produced in much the same way.

in a upper bound for the Stark shift. Using 10 kV/mm and a value for the inhomogeneous linewidth of ~ 1000 GHz this leads to a value of the Stark coefficient of the order of 10^9 Hz cm V $^{-1}$. This is of the order of 10^4 times greater than for rare earth systems and so the interaction strengths will be of the order of 10^8 times larger. This should be compared to the shorter coherence times; coherence times for NV centres in diamond are of the order of 10^6 larger than typical rare earth values. Assuming the separations between the centres involved are the same, we get an 100 fold increase in the ratio of interaction strength to dephasing rates with the NV centre compared to rare earths. Of course, this should be seen as an absolute best case scenario. However, it can still be concluded that the implications of the possibility of a sizable electric dipole-dipole interaction for the NV centre justifies further investigation. Interaction between the centres is the weakest part in current quantum computing proposals for the NV centre.

4.1.2 The resonance interaction

As well as the diagonal interactions mentioned above, the possibility of off-diagonal interactions in rare earths has also been investigated. Their possible role in causing excess dephasing was investigated theoretically by Root and Skinner [123] and a method for using this interaction to effect controlled atom-atom interactions has been put forward by Lukin and Hemmer [124]. These off-diagonal or exchange interactions occur when two resonant ions are placed in each other's near field. Without the interaction, the two of the four eigenstates of the system, namely $|ge\rangle$ and $|eg\rangle$, would be degenerate². The resonance interaction which comes from the exchange of virtual photons between the two ions will cause this degeneracy to be broken. This interaction and its R^{-3} dependence was first noted by Eisenshitz and London in investigations of the first excited states of H₂ [125]. The new eigenstates are the symmetric and anti-symmetric linear combinations of the two states mentioned above

$$|p_{\pm}\rangle = \frac{|ge\rangle \pm |eg\rangle}{\sqrt{2}} \quad (4.2)$$

The energy difference between these two states for distances close compared to the wavelength of the transitions takes the form³ [126]

$$V(R) = 3\hbar\gamma \left(\frac{\lambda}{R}\right)^3 \quad (4.3)$$

²Here the state $|ge\rangle$ is the one where ion 1 is in the ground state and ion 2 is in the excited state.

³Here $\lambda = \lambda/(2\pi)$.

There is some disagreement about the behaviour of the interaction for distances larger than the wavelength. The commonly accepted result is that of McLone and Power [127] which predicts long range oscillatory behaviour. Boström et al. [128] showed the same result is achieved using a semi-classical method, if the usual approximation is made where the atom-field coupling constant is assumed to be constant. This approximation is invariably made when dealing with optical resonances in atoms as the linewidth is always a very small percentage of the transition frequency. When Boström et al. didn't make this approximation a R^{-4} dependence was found. This disagreement has little importance to quantum computing because it only occurs in the regime $R > \lambda$. In this regime the interaction strength is weak compared to the spontaneous emission rate, making it useless for effecting qubit-qubit interactions.

For rare earth systems, using Eq. 4.3, it can be seen that the resonance interaction has the same R^{-3} dependence and a similar size to the diagonal electric dipole-dipole interactions mentioned above. At a distance of one wavelength, the size of the interaction is comparable to the spontaneous emission rate in both cases. However, the resonance interaction does not contribute significantly to ion-ion interactions because of inhomogeneous broadening. Off diagonal interactions, such as the resonance interaction, are significant only when the detuning between the two systems is small compared to the interaction strength.

This requirement for resonance has important implications for quantum computation in solids. Ideally, one might expect that it could be useful because the interactions would be more selective. In the medium term, however, it is hard to see how this would outweigh the extra complication arising from strict requirements on the optical transition frequencies.

4.1.3 Dephasing by non-equilibrium phonons

Instantaneous spectral diffusion is most commonly invoked to explain the intensity dependent relaxation rates in rare earth systems. However it is also possible that incoherent effects cause excess dephasing. It is important to be aware of this when using such systems for quantum computing. Bai and Kachru [129] provided an example of such an effect. Their work followed a previous investigation [130] that showed that the sensitivity of a photon echo in $\text{Pr}^{3+}:\text{YAlO}_3$ to the size of the first pulse was too high to be explained by an excitation induced frequency shift. By varying the laser focus Bai and Kachru were able to show that for such a system the excess dephasing was dependent “on both the density of the excited ions *and the size of the excitation volume*”.

For this to happen, they concluded, the “perturbers” caused by the excitation must be mobile. In their mechanism the reduction in the size of the echoes was due to a cloud of resonant phonons caused by the non-radiative decay of the praseodymium ions interacting with other praseodymium ions. The praseodymium ions in YAlO_3 are particularly sensitive to phonons because of another member of the ${}^3\text{H}_4$ crystal field split manifold close to the ground state ($\sim 51 \text{ cm}^{-1}$). The ground state for trivalent europium is a singlet. Therefore there is no possibility of other low lying levels in the ground state manifold. This means that this mechanism shouldn’t be important for the quantum computing experiments carried out in $\text{Eu}^{3+}:\text{Y}_2\text{SiO}_5$ for this thesis.

4.2 Previous schemes for optical quantum computation in solids

Of the three previously published schemes for all optical quantum computation in solids, two [107, 109] overcome the problems of qubit-qubit interactions and readout using high finesse optical cavities. They are in many ways similar to an earlier work of Pellizzari et al. [131] for trapped atoms but use either rare earth ions [107] or NV-centres [109].

In order for the cavity to be useful, the strong coupling regime is required. This is where the coupling strength between the colour centres and the cavity field (the *single photon Rabi frequency*) is much larger than the decay times for both the cavity and the coherence of the colour centres. This requires the use of very small cavities in order to achieve a coupling strength that is large compared to the spontaneous emission rate of the impurity. The requirement for small cavities means that the finesse must be very large in order to achieve the required cavity decay rates.

It is possible, if difficult, to achieve this regime for free atoms [47] but it has not yet been possible for optically active colour centres in the solid state. The difficulty lies in making the cavity decay smaller than the single photon Rabi frequency. The oscillator strength of the NV centre, suggested by Shahriar et al. [109], is comparable to that of an allowed transition in a free atom; however, the losses caused by having a solid material in the cavity are significant. The production of better cavities using photonic-band gap materials and surface plasmon modes is under active investigation [132] and for the NV centre it is possible that the strong coupling regime will be achievable in the medium term. The oscillator strengths for $f-f$ transitions in rare earth ions, suggested by Ichimura [107], are three orders of magnitude smaller than the NV centre and it’s unlikely that for such systems the strong

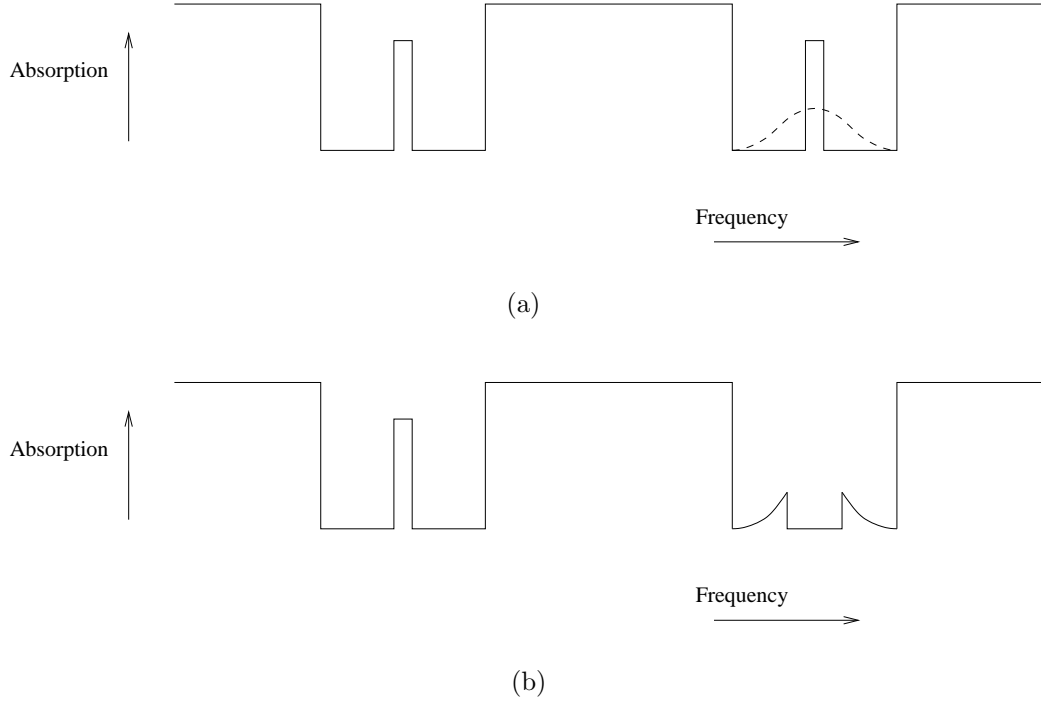


Figure 4.1: Sketches of absorption versus frequency for two different steps when carrying out the instance identification for the scheme of Ohlsson et al.

coupling regime will be achieved without radically new techniques for making optical cavities.

4.2.1 Ensembles and instance identification

The electric dipole-dipole interactions explained in Sec. 4.1.1, together with the single qubit ensembles of Pryde et al. [80], would suffice for quantum computing if it were not for one problem — the inhomogeneity of the interactions strengths. Fortunately, this problem can be solved to some extent using holeburning techniques.

The scheme would be as follows. First a number of the Pryde single qubits would be prepared in the inhomogeneous line and then all the ions in these ensembles that didn't have the correct interaction strength would be optically pumped into an auxiliary hyperfine level and removed from consideration. The process has been called *instance identification* [133].

The method that has appeared in the literature for achieving this instance identification is that of Ohlsson et al. [108], which appeared in 2002. Their procedure for two qubits was as follows. First one (the left in Fig. 4.1) qubit is excited with a π pulse. Because of the interaction between the two qubits this causes a spread in the resonant frequencies of the ions of the second qubit

(see dotted line in Fig. 4.1(a)). Then the ions with resonant frequency which haven't shifted by a sufficient amount are then burnt away (Fig. 4.1(b)). The left qubit is then brought back down to the ground state. The process is then repeated with the roles of the two qubits reversed. What remains are two qubits, one of which can be switched out of resonance by the excitation of the other. In the description of the scheme of Ohlsson et al. the interaction between the ions within one qubit was disregarded, but perhaps this flaw could presumably be overcome with only slight complication.

One problem with this approach is that the mean frequency shift in the ions of a target qubit when a control qubit is excited is generally a small fraction of the spectral width of the control [134]. Put another way, the dotted peak in Fig. 4.1(b) should have a width that is only a few percent wider than the unbroadened peak. It has been estimated in a subsequent paper by the same group that in order to achieve two qubits in such a system 99.7% of the ions in each qubit would have to be pumped into the auxiliary hyperfine state, leaving only 0.3% of the ions [135]. This puts severe limits on the allowable background level of ions in the holeburning process. The reason that so many ions must be thrown away is that the Ohlsson technique requires the controlled frequency shift of the ions to be larger than the inhomogeneous linewidths of each anti-hole.

Wesenberg and Mølmer [133] recently proposed the use of composite pulses for the single qubit rotations in the Ohlsson scheme. Using these pulse sequences, it may be possible to get closer to the value of 0.3% of the ions than would have otherwise been the case. Still, the requirement that the interaction must be larger than the inhomogeneous linewidth of each anti-hole would mean that you have to burn away the vast majority of the ions in each qubit. In Section 4.5 it is shown that there is nothing fundamental in this restriction and provides an alternative method for instance identification requirements. The introduced technique only requires the interactions to be larger than the homogeneous linewidth. It also naturally deals with the problem of interaction between ions within the same qubit.

A second problem with the ensemble approach of Ohlsson is the difficulty in scaling it to a large number of qubits. Initialisation of the Ohlsson quantum computer consists of starting with a very large number of ions and throwing away (by optically pumping to the auxiliary hyperfine state) all those that don't have the correct interactions. As the number of qubits increase, the number of 'instances' of a suitable collection of ions will decrease exponentially. Using the techniques of Section 4.5, the number of ions may not need to decrease as quickly as 0.003^N , as in the Ohlsson scheme, but the

decrease would still be exponential. Wesenberg and Mølmer [133] suggest a “bus architecture”, where each of the qubits is only coupled to one “bus” qubit. Such an architecture they argue would require less ions to be thrown away. From the author’s reading such a system would still require working with exponentially smaller groups of ions as the number of qubits increases. No definitive statements are made in the paper.

4.3 The direction pursued in this thesis

Developing a practical quantum computer is a very considerable undertaking, and as such it is useful to have both shorter and longer term goals. This work, due to its limited timespan and the infancy of rare earth quantum computation, has been primarily involved in achieving shorter term goals. These include characterisation of the physical systems and processes that might be used and also simple demonstrations. Longer term goals, such as overcoming obstacles to scalability were not actively pursued experimentally, although some thoughts about these are presented toward the end of this chapter.

All the experimental work in this thesis was carried out using ensembles. Narrow anti-holes were used as single qubits and the states of these qubits were detected by monitoring coherent optical emission. In order to achieve the demonstration of two qubit operations the electric dipole-dipole interactions were used. Using a method of instance identification, an ensemble was selected from the ions that made up two qubits where the interaction between the two qubits was no longer random. As discussed above, the method presented by Ohlsson et al. is totally inadequate for achieving this in practice because the mean interactions between the ions in each ensemble are a small percentage of their spectral width. To overcome this problem a technique was developed that required the interactions be large compared to the homogeneous linewidth only and this required a lot less ions to be thrown out when distilling the ensemble.

While this improved method for the instance identification allows demonstrations to be carried out for a small number of qubits the approach is not scalable to a large number of qubits. It still requires throwing away all the ions except those with particular interactions. Just as for the Ohlsson et al. method, the requirements on what groups of ions are allowed to stay in the qubits get rapidly more severe as the number of qubits increases. Starting with a randomly doped material you would be dealing with qubits that contained on average less than one ion before you got past a handful of qubits.

In order to achieve the long term goal of a scalable computer, a better way for overcoming this inhomogeneity in interaction strength would be required. Options are discussed at the end of this chapter.

4.4 NMR-like measurements for ensembles

When dealing with spontaneous emission especially in atomic systems, the atoms⁴ are usually treated independently, and the resulting spontaneously emitted radiation is isotropic and incoherent.

Theoretical investigation beyond this *independent atom* approximation were first carried out by Dicke [136]. In his paper there were two predictions. Firstly, if the *atomic states* have particular phase inter-relationships then the resulting spontaneous emission from the atoms can interfere and the result can be both directional and coherent. This effect, which we shall call *coherent spontaneous emission*, produces the free induction and photon echo signals discussed in Chapter 2 and provides measurements completely analogous to those available in NMR quantum computing. Coherent spontaneous emission is sometimes used to explain the signals produced in magnetic resonance. However that situation is complicated by the presence of the detector in the near field of the nuclear spins [137].

The second of Dicke's predictions was the possibility that the spontaneous emission from a collection of atoms could be greatly larger or smaller than if the atoms were independent. Because of the dilute nature of the samples used and the random spatial distribution of dopants, such *super-radiant* phenomena wasn't important in the work supporting this thesis.

In what follows we shall give a brief outline of the theory of coherent spontaneous emission. A more full description is given in [138].

In the rotating wave approximation, the Hamiltonian describing N atoms coupled to a bath of radiation modes can be written

$$H = H_{\text{atoms}} + H_{\text{rad}} + H_{\text{int}} \quad (4.4)$$

⁴From here on in this section the word 'atom' will be used to describe a system that spontaneously emits and therefore includes atoms, ions, colour centres etc.

where

$$H_{\text{atoms}} = \sum_{i=1}^N \hbar \omega_i \sigma_i^z \quad (4.5)$$

$$H_{\text{rad}} = \sum_k \hbar \omega_k b_k^\dagger b_k \quad (4.6)$$

$$H_{\text{int}} = G \sum_{i=1}^N \sum_k \left(e^{i\mathbf{k} \cdot \mathbf{r}_i} b_k \sigma_i^+ + e^{-i\mathbf{k} \cdot \mathbf{r}_i} b_k^\dagger \sigma_i^- \right) \quad (4.7)$$

The menagerie of constants such as the transition dipole moment, quantisation volume etc. have all been put into G .

Here we shall assume the laser is a plane wave, with wavevector \mathbf{k}_0 and frequency ω_0 . Moving into the interaction picture spinning at ω_0 we introduce the two new operators

$$S_i^- = e^{-i(\omega_0 - \omega_i)t} e^{-i\mathbf{k}_0 \cdot \mathbf{r}_i} \sigma_i^- \quad (4.8)$$

$$a_0 = b_0 e^{-i\omega_0 t} \quad (4.9)$$

Also included in the S_i^- is the term $e^{-i\mathbf{k}_0 \cdot \mathbf{r}_i}$ which is equivalent to changing the phases of the atomic basis states so that the plane wave with wave vector \mathbf{k}_0 addresses all the ions with the same phase.

Moving into the interaction picture where all the evolution due to H_{rad} and H_{atoms} have been put into the states we arrive at the following equation of motion for a_{k_0}

$$\frac{d}{dt} a_{k_0} = \sum_{i=1}^N S_i^- \quad (4.10)$$

which leads to

$$\frac{d}{dt} \langle a_{k_0} \rangle = \sum_{i=1}^N \langle X \rangle - i \langle Y \rangle \quad (4.11)$$

In other words, the sample radiates coherently into the same mode as the driving laser, and the amplitudes of the two quadratures are given by $\langle X \rangle$ and $\langle Y \rangle$. Thus, by measuring the amplitude of the coherent emission in a phase sensitive manner, direct measurements of the ensemble averages of $\langle X \rangle$ and $\langle Y \rangle$ can be obtained.

The coherent emission is generated at a well defined frequency and in a well defined spatial mode. Very sensitive measurements of the echoes can be made because of the good discrimination and very high collection efficiency this enables. Very small ensembles can be measured in principle, perhaps with as few as thousands of ions. Photon echoes with as few as 400 photons

have been measured. In this work, the signal to noise ratio when detecting the coherent emission was not a limiting factor.

4.5 CNOT with refocusing

As mentioned above, the method of Ohlsson et al. selects out ions which shift a large amount compared to the inhomogeneous linewidth. Assuming the perturbing and target ensembles are the same size, no ions satisfy this criterion in practice. The situation is depicted in Fig. 4.2.

Coherent transient techniques [77] have been used extensively in rare earth systems to probe the rare earth ion system with greater resolution than what would be allowed by the inhomogeneous broadening using conventional techniques. Here we provide a method for achieving both the *instance identification* and the computation based on photon echo sequences.

In the appropriate interaction picture, the Hamiltonian for two ions in two separate anti-holes is

$$H = \frac{\delta_1}{2} Z_1 + \frac{\delta_2}{2} Z_2 + \frac{\eta}{2} Z_1 Z_2 \quad (4.12)$$

Here δ represents the detuning from the centre anti-hole and η the interaction strength. Z is the Pauli-Z operator ($Z = \begin{bmatrix} 1 & 0 \\ 0 & -1 \end{bmatrix}$).

The pulse sequence to achieve a CNOT operation between the two ions is illustrated in Fig. 4.3. The first pulse puts the target ion on the equator of the Bloch sphere where it then precesses around the equator at a rate given by its detuning from resonance. This detuning is given by the sum of δ_1 and the effect of the interaction. Without the π pulse on the control qubit at the middle of the gate operation the π pulse to the target gate would refocus this precession. This would lead to the target ion being at the same position on the equator of the Bloch sphere as if no interaction was present. The application of the π pulse to the control ions stops the re-phasing of the precession due to the interaction. If the waiting time is equal to an odd multiple of $\frac{\pi}{4\eta}$ then the two trajectories on the Bloch sphere corresponding to the control ion being initially in the states $|0\rangle$ and $|1\rangle$ end up separated by angle π . They can then easily be mapped to the ground and excited states with the appropriate $\pi/2$ pulse. Such a pulse sequence would be useful in liquid state NMR if you were limited by the inhomogeneity of your DC magnetic field.

The unitary evolution operator describing the gate's operation can be

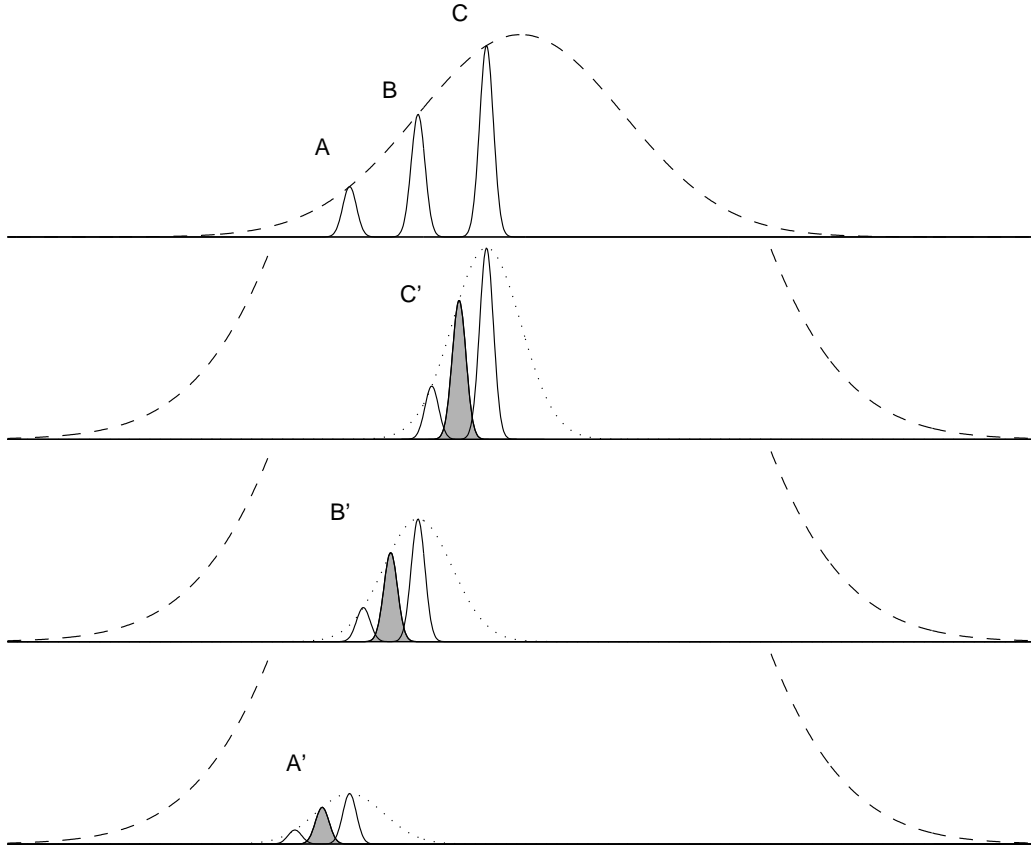


Figure 4.2: Shows the effect on the ions in one anti-hole when exciting another. Due to the electric dipole-dipole interactions, the frequencies of each of the ions will get a random shift. The top trace depicts the inhomogeneous profile of the anti-hole (dashed line) and three homogeneously broadened packets, labelled A, B, and C. The excitation of the perturbing anti-hole causes a random shift in the ions' frequencies. This causes the packets A, B and C to become inhomogeneously broadened, which is shown in the lower three traces. The vertical scale on the bottom three traces is different to the top, while the dashed line is the same in all four traces. The scheme of Ohlsson et al. selects ions that are shifted outside the original inhomogeneous linewidth. Because the mean frequency shifts caused by the interaction are much smaller than the initial homogeneous linewidth, no ions satisfy this criterion in practice. The refocusing based technique developed here selects out ions and achieves computation using shifts that occur within the inhomogeneous linewidth. The ions selected for in this case are the ones shaded in each of A', B' and C'.

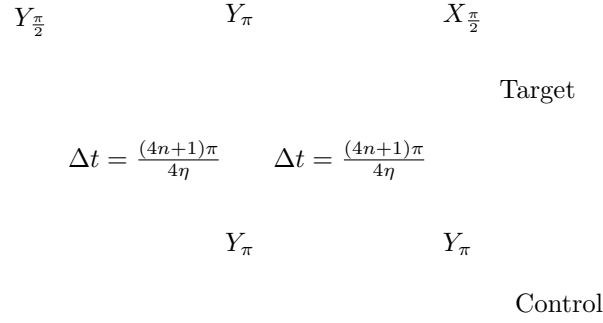


Figure 4.3: Pulse sequence to achieve a CNOT gate in the presence of inhomogeneous broadening. X_{π} is a pulse that causes a π rotation about the x axis on the Bloch sphere.

expressed as the product of seven elementary operations

$$U = U_7 U_6 U_5 U_4 U_3 U_2 U_1 \quad (4.13)$$

where

$$U_1 = \exp\left(\frac{-iY_1\frac{\pi}{2}}{2}\right) \quad (4.14)$$

$$U_2 = \exp(-iH\Delta t) \quad (4.15)$$

$$U_3 = \exp\left(\frac{-iY_1\pi}{2}\right) \quad (4.16)$$

$$U_4 = \exp\left(\frac{-iY_2\pi}{2}\right) \quad (4.17)$$

$$U_5 = \exp(-iH\Delta t) \quad (4.18)$$

$$U_6 = \exp\left(\frac{-iX_1\frac{\pi}{2}}{2}\right) \quad (4.19)$$

$$U_7 = \exp\left(\frac{-iY_2\pi}{2}\right) \quad (4.20)$$

This gives us, independent of $\delta_{1,2}$,

$$(-1)^{\frac{1}{4}} \begin{bmatrix} \sin(\theta) & -i \cos(\theta) & 0 & 0 \\ -\cos(\theta) & i \sin(\theta) & 0 & 0 \\ 0 & 0 & \cos(\theta) & -i \sin(\theta) \\ 0 & 0 & -\sin(\theta) & -i \cos(\theta) \end{bmatrix} \quad (4.21)$$

where $\theta = 2\eta\Delta t$. For $\Delta t = \frac{(4n+1)\pi}{4\eta}$ this becomes

$$(-1)^{(\frac{1}{4}+n)} \begin{bmatrix} -1 & 0 & 0 & 0 \\ 0 & i & 0 & 0 \\ 0 & 0 & 0 & i \\ 0 & 0 & 1 & 0 \end{bmatrix} \quad (4.22)$$

The difference between this and the evolution matrix describing the CNOT operation

$$\begin{bmatrix} 1 & 0 & 0 & 0 \\ 0 & 1 & 0 & 0 \\ 0 & 0 & 0 & 1 \\ 0 & 0 & 1 & 0 \end{bmatrix} \quad (4.23)$$

is simply rotations about the qubits Z axis. These need not be physical operations but can instead be changes in the definition of the phases for the qubits [139].

Initially, because of the random distribution of the ions throughout the crystal there will be a distribution of interaction strengths. In order to create an ensemble with interaction strengths given by $\eta\Delta t = (4n+1)\pi/4$ the gate operation can be applied repeatedly with both ensembles initially in their ground states and with a pause between the pulse sequences to allow the ions to relax. The target ions that see the correct interaction strengths will still be in the ground state at the end of the operation while the others will have some population in the excited state. Repeated application of such sequences, swapping the roles of target and control qubit will gradually optically pump all the ions that don't see the correct interaction strength into an auxiliary hyperfine level in an way analogous to spectral holeburning.

Results of modelling of the interaction-strength-holeburning process are shown in Fig. 4.4. The branching ratio for an atom to spontaneously emit back down into the state $|0\rangle$ versus another hyperfine level was taken to be one half.

One problem with this method is achieving high fidelity gate operation in the presence of what is still reasonably large inhomogeneity in the interaction strength. This problem can be overcome using the results of Jones' findings [140]. Jones pointed out that the problem of inhomogeneity in interaction strength for two qubit gates is exactly analogous to the problem of inhomogeneity in Rabi frequency for single qubit operations. This means that methods analogous to the "composite pulses" used to overcome these problems can be used. In the absence of other errors, using such techniques would enable a fidelity better than 10^{-6} in the presence of 10% inhomogeneity in

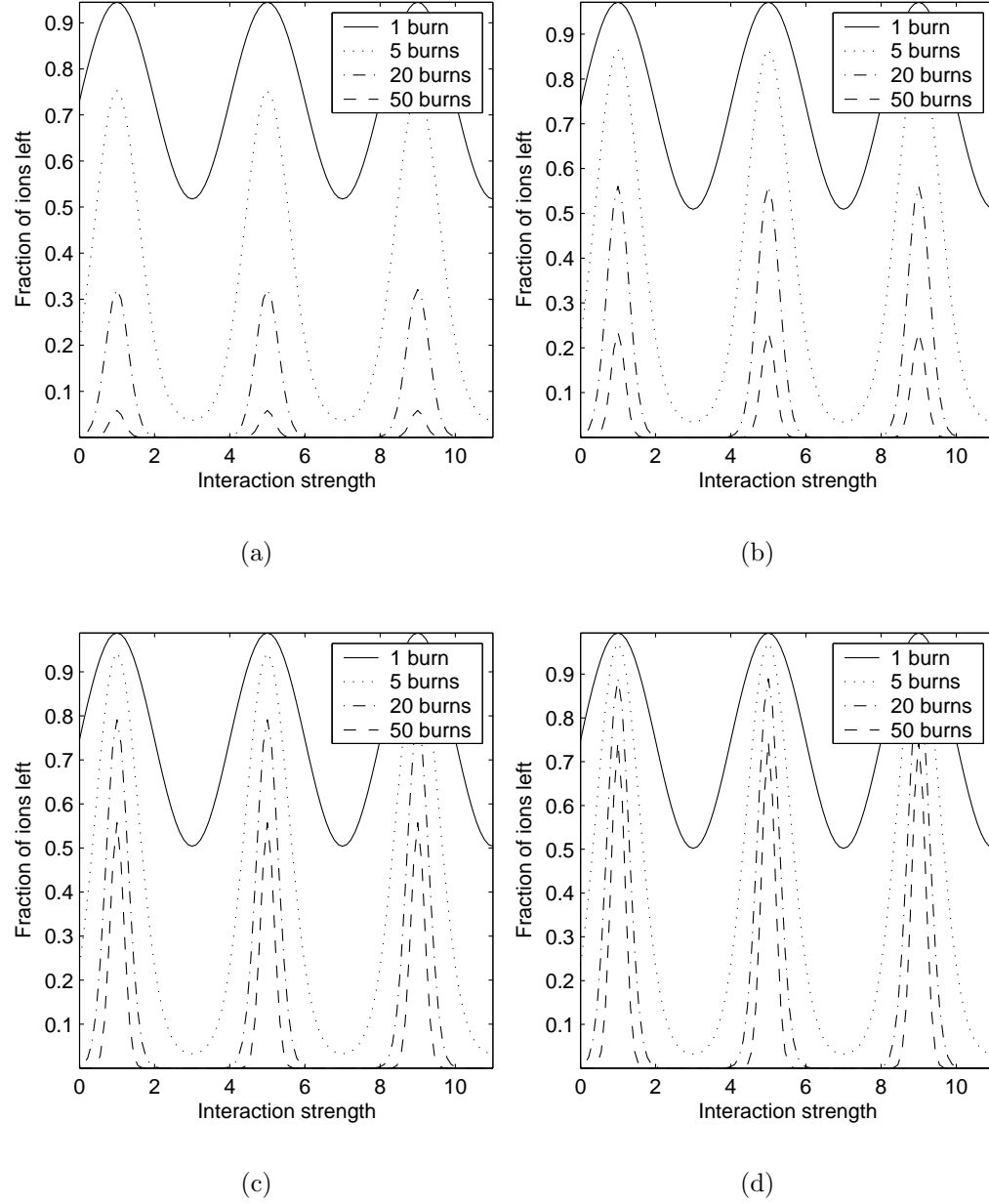


Figure 4.4: Selecting target ions with the desired interaction strength using repeated application of the CNOT gate. Each graph shows the fraction of ions left at a particular interaction strength after 1, 5, 20 and 50 gate operations. The holeburning efficiency is assumed to be 50%. The time for free evolution between pulses in the CNOT gate was $\Delta t = \pi/4$. The effect of spontaneous emission was included with the spontaneous emission rates being: (a) $\gamma = \frac{1}{10}$, (b) $\gamma = \frac{1}{20}$, (c) $\gamma = \frac{1}{50}$, (d) $\gamma = \frac{1}{100}$.

the interaction strengths.

This leads to the two conditions that must be satisfied in order to demonstrate the CNOT using this refocusing process.

Firstly, in order that the ensemble selection and gate operation sequences do not suffer too much dephasing, the chosen interaction strength must be large compared to the dephasing rate. In order for there to be a reasonable number of ions in the selected ensemble the chosen interactions strength must be comparable to the average interaction between the ions. These conditions are more easily satisfied when starting with wider anti-holes.

The second condition is that the spectral width of the ensembles must be small enough, when compared to the available laser power, that the pulses applied have the same effect on the whole ensemble.

For the example of $\text{Eu:Y}_2\text{SiO}_5$ if we prepare anti-holes of the order of 100 kHz wide then we expect to have appreciable numbers of ions with interaction strengths of the order of 10 kHz which is large compared to the ≈ 500 Hz spontaneous emission rate. With 500 mW of laser power focused with a 10 cm lens, Rabi frequencies of the order 1 MHz can be easily achieved. This suggests that the demonstration of such a two qubit gate is achievable with current technology.

The demonstration of something like a two qubit gate using this technique is described in Chapter 5. The remainder of this chapter discusses ways that rare earth quantum computation might be scaled.

4.6 Inhomogeneity in the interaction strength and scaling

In one sense, the problem of inhomogeneity is the only problem to overcome in rare earth quantum computation. The ions have experimentally verified long coherence times and large interaction strengths and, for ensembles, measurements akin to NMR are available.⁵ In the approach suggested above ions are selected from a macroscopic collection based on their resonant frequency and interactions strength. The criterion for determining which ion groups are acceptable to be part of the ensemble of quantum computers gets increasingly more stringent with the number of qubits. As mentioned above this will lead to exponentially fewer ions as the size increases.

⁵It was rightly pointed out by one of the referees that the ability to make projective measurements on one qubit while leaving others untouched is important for procedures such as error correction. It is possible that such projective measurements could be made using the large difference in decay times for different energy levels in rare earth ions.

In order to make rare earth quantum computing scalable a better way of overcoming this inhomogeneity is needed. The possibilities discussed here involve single ion spectroscopy, either directly or by coupling to other ions, and the use of “solid state molecules”.

4.6.1 Solid state “molecules”

In liquid state NMR based quantum computing you are dealing with an ensemble of “computers” just as for the rare earth scheme described above. The problems of inhomogeneity overcome because each computer is a molecule which is identical to all the others. It should be emphasised that rare earth quantum computing doesn’t share the initialisation problem that causes NMR quantum computing to become untenable for large numbers of qubits. A material can be imagined where there are large numbers of identical collections of rare earth dopants. The coherent detection method used in this thesis is sufficiently sensitive that perhaps ensembles with as few as a thousands of atoms could produce a measurable signal (see Sec. 4.4). With the huge research effort currently being brought to bear on problems involving nanotechnology, it may in the future be possible to make such ensembles. One advantage in trying to achieve this is that ‘defective’ members of the ensemble, for example where an atom is missing, would have a different set of optical resonant frequencies due to the huge interactions which would be achieved by having the ions so close. Indeed the situation is similar to selecting out the right ensemble from a bulk sample but with a more favourable starting position.

All the rare earths are strongly electro-positive with their bonding to other atoms essentially ionic in nature [71] and as such incorporating them in a molecular solid would be difficult. One possibility, put forward by Sellars [141], for realising something akin to “solid state molecules” is by adding defects to a stoichiometric sample. Crystals containing stoichiometric amounts of europium can still exhibit relatively long coherence times, as long as the inter-europium spacing is large within the crystal [142]. The europiums close to defects would provide an ensemble of a identical groups of europium ions. The defect would shift the resonant frequencies of the members of this group to differing amounts allowing them to be individually manipulated based on their optical frequencies. The fact that they are shifted out of resonance with the bulk europiums should also increase their coherence times.

4.6.2 Single dopant detection

One way of overcoming the inhomogeneity in interaction strength is by abandoning the use of ensembles. In such a situation the computer would consist of a single cluster of ions. Because the ions are selected based on their frequency rather than their precise positions and because the gate operations can be tailored to given interaction strengths no complex fabrication would be required. This leaves the problem of detection of single ions. Spectroscopic measurements of single NV centres in diamond have been demonstrated [105] and while the lower oscillator strengths for rare earth ions would push current detector technology, it may be possible to detect the approximately 1000 photons/sec produced when driving an optical transition strongly. The reason for such weak fluorescence is due to the long radiative lifetimes associated with rare earth ions. How long any emission lasts depends on what rate population gets optically pumped into other hyperfine levels. For free atoms/ions outside solids strong selection rules result in “cyclic transitions” where the optically excited state only decays into the ground state from which it is being driven. This means that the state of the hyperfine level can be read out to a high fidelity. If the atom is in the hyperfine state from which the atom is being driven from then a large amount of fluorescence is generated, whereas if it is in a different state no fluorescence will be generated.

Another option [141] is to use non-radiative transitions and detect the phonons produced. The qubit would be transferred to the optical transition and then a short lived non-radiative transition would be driven from the ground state. What would determine whether this would work would be if you detect the amount of phonons that could be produced within the (~ 2 ms) life time of the long lived optically excited state. Extremely sensitive calorimeters (bolometers) exist that operate on the edge of superconducting transitions [143]. These have been highly developed due to their application as detectors for astronomy. Their sensitivity has been demonstrated in their use as part of a single photon detector that operated down to a wavelength of $4\text{ }\mu\text{m}$ [144].

Other options involve coupling to other centres that can be read out more easily. A detailed theoretical examination of such a scheme using the NV centre to readout an nuclear spin has been carried out recently by Pulford et al. [145]. Another option is to treat rare earth quantum computing as something of a prototype and to move on to optical centres which are easier to read out. The centre that immediately comes to mind is the NV centre in diamond. If this has a reasonable Stark shift as speculated in Sec. 4.1.1 then the quantum computing operations could be envisioned that were completely

analogous to those carried out in this thesis in rare earths. Doing the operations in a time-domain manner would require much faster modulators than rare earths. The excited state lifetime is 8 ns, but very high bandwidth modulators have been realised for telecommunications applications and this may not be impossible. While these very fast operations may be possible, another alternative is to use EIT in a manner analogous to the current proposals for quantum computing in diamond that use different interactions [146, 109].

4.7 Cyclic transitions in rare earth systems

When compared to free atoms/ions cyclic transitions are harder in the solid state because of the reduced symmetry. One possible method for achieving something like a cyclic transition in the systems studied in this thesis uses a special characteristic of a pseudo-quadrupolar Hamiltonian. In zero magnetic field the effective spin Hamiltonian for the rare earth systems studied in this thesis is given by the Hamiltonian below. See Sec. 2.4.

$$H = D(I_z^2 - I^2/3) + E(I_x^2 - I_y^2) \quad (4.24)$$

This is called a pseudo-quadrupole Hamiltonian because although it has the same form as a nuclear quadrupole Hamiltonian, it has some contribution from second order electronic Zeeman effects. Using identities for angular momentum operators this can be rewritten

$$H = D(I_z^2 - I^2/3) + E(I_+^2 + I_-^2) \quad (4.25)$$

In the I_z basis and for a nuclear spin $I = 5/2$ the Hamiltonian will have a matrix representation of the form

$$H = \begin{matrix} & \begin{matrix} |-5/2\rangle & |-3/2\rangle & |-1/2\rangle & |+1/2\rangle & |+3/2\rangle & |+5/2\rangle \end{matrix} \\ \begin{matrix} |-5/2\rangle \\ |-3/2\rangle \\ |-1/2\rangle \\ |+1/2\rangle \\ |+3/2\rangle \\ |+5/2\rangle \end{matrix} & \begin{pmatrix} \frac{25}{4}D & 0 & 2\sqrt{10}E & 0 & 0 & 0 \\ 0 & \frac{9}{4}D & 0 & 6\sqrt{2}E & 0 & 0 \\ 2\sqrt{10}E & 0 & D/4 & 0 & 6\sqrt{2}E & 0 \\ 0 & 6\sqrt{2}E & 0 & D/4 & 0 & 2\sqrt{10}E \\ 0 & 0 & 6\sqrt{2}E & 0 & \frac{9}{4}D & 0 \\ 0 & 0 & 0 & 2\sqrt{10}E & 0 & \frac{25}{4}D \end{pmatrix} \end{matrix} \quad (4.26)$$

Because the terms I_\pm^2 always only add terms to the second upper and lower diagonals, the Hamiltonian will be of this tridiagonal form for all values of nuclear spin. Matrices of such a form can be made block diagonal by

changing the ordering of the I_z , in particular, if we take the normal ordering $(-I, -I+1, \dots, I)$ and replace it with all the odd members followed all the even members. For our example of nuclear spin $I = 5/2$ the Hamiltonian is

$$H = \begin{matrix} & \begin{matrix} |-5/2\rangle & |-1/2\rangle & |+3/2\rangle & |-3/2\rangle & |+1/2\rangle & |+5/2\rangle \end{matrix} \\ \begin{matrix} |-5/2\rangle \\ |-1/2\rangle \\ |+3/2\rangle \\ |-3/2\rangle \\ |+1/2\rangle \\ |+5/2\rangle \end{matrix} & \begin{pmatrix} \frac{25}{4}D & 2\sqrt{10}E & 0 & 0 & 0 & 0 \\ 2\sqrt{10}E & D/4 & 6\sqrt{2}E & 0 & 0 & 0 \\ 0 & 6\sqrt{2}E & \frac{9}{4}D & 0 & 0 & 0 \\ 0 & 0 & 0 & \frac{9}{4}D & 6\sqrt{2}E & 0 \\ 0 & 0 & 0 & 6\sqrt{2}E & D/4 & 2\sqrt{10}E \\ 0 & 0 & 0 & 0 & 2\sqrt{10}E & \frac{25}{4}D \end{pmatrix} \end{matrix} \quad (4.27)$$

The transition strength between a particular ground state hyperfine level and an optically excited hyperfine level is the product of two terms. The first is the transition strength for the optical transition ignoring the hyperfine interaction. The second term is the overlap between the nuclear states for the ground level and the excited state level. The eigenvalues for the above Hamiltonian can be broken into two groups one of which consists of linear combinations of the I_z states $\{|1/2\rangle, |-3/2\rangle, |5/2\rangle\}$ and the other linear combinations of the states $\{|-1/2\rangle, |3/2\rangle, |-5/2\rangle\}$. Thus, if the z axes for each electronic state overlapped, then these two groups are closed under the operations of driving and spontaneous emission leading to something akin to a cyclic transition. The states from the manifold $\{|1/2\rangle, |-3/2\rangle, |5/2\rangle\}$ will not spontaneously emit into the states $\{|-1/2\rangle, |3/2\rangle, |-5/2\rangle\}$. A energy level diagram showing how this could be used for single ion readout is shown in Fig. 4.5.

An example of a situation where the z axes for each electronic state will overlap is a system that contains an axis of symmetry, for example $\text{Pr}:\text{LaCl}_3$ where there is a C_2 axis through the Praseodymium impurities.

One complication is that the hyperfine states are two fold degenerate at zero field with each pair consisting of a member of each group. This degeneracy can be lifted without affecting the closed nature of the groups by applying a magnetic field along the z direction. Only a small field is needed to break the degeneracy of the multiplets and it is possible to work in a regime where the effect of the field can be treated as a first order perturbation to the pseudo-quadrupole Hamiltonian. In such a situation the effect would not be very sensitive to the alignment of the magnetic field along the z axis. This is because a magnetic field in any direction, while it would have a first order effect on the energies of the eigenstates, would only have a second order effect

on the eigenstates themselves.

4.8 Conclusion

The future for optical solid state quantum computation is exciting. It has many strengths. These include the possibility to avoiding complex fabrication and well characterised systems that have useful parameter regimes. Two qubit demonstrations have been carried out and currently the only known problem that stands in the way of scalable rare earth quantum computation is detecting the state of single dopants. Single site spectroscopy has been carried out for NV centres in diamond. Measurements of the NV centre suggest the same phenomena used in the rare earths demonstrations might be applicable in those cases also. A simple measurement of the Stark shift would be all that would be required to determine whether this was the case.

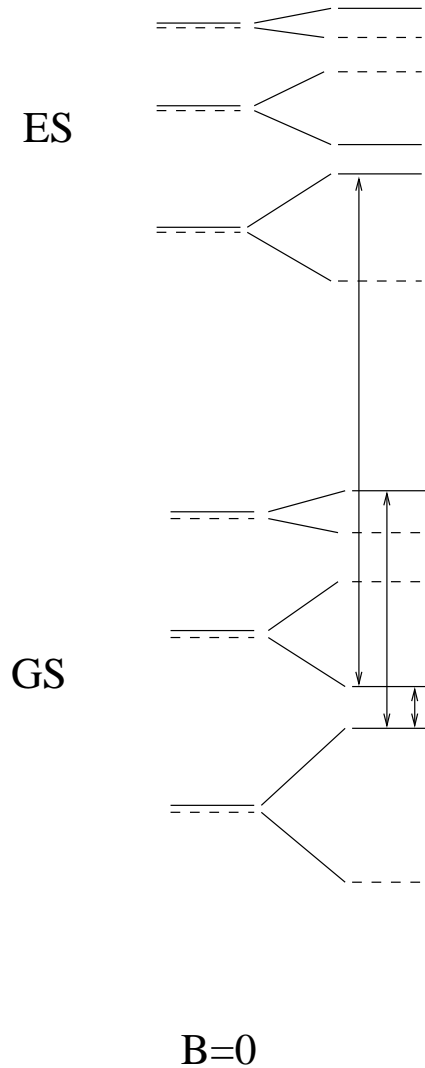


Figure 4.5: Energy levels diagram showing cyclic transition. ES denotes the optically excited state and GS denotes the ground state. A small magnetic field is needed to break the degeneracy of the two groups of eigenstates. The states represented by dashed lines don't spontaneously emit into the states represented by solid lines and vice-versa. If the ion is initially in one of the ground states represented by a solid line there will be continual fluorescence, whereas if the ion is in a dashed state, it will stay in that state, resulting in no fluorescence. For the example system of Pr:LaCl₃, GS is the lowest crystal field level in the 4H_4 multiplet and ES the lowest crystal field level in the 1D_2 .

Chapter 5

Quantum computing using rare earths — Experiment

This chapter describes the progress made in implementing quantum logic operations in rare earth ion dopants. The theoretical background to these investigations is discussed in Chapter 4. All the experiments described were carried out with ensembles. Spectral holeburning techniques were used to create ensembles of ions that had the wanted properties.

First existing techniques [80] for selecting spectrally narrow groups of ions were investigated and improved. Various experiments were carried out on these spectrally narrow packets, or “anti-holes”, to demonstrate their utility as qubits. Following this, the electric dipole-dipole interactions discussed in Section 4.1.1 were investigated. This not only confirmed the nature of and the size of the interactions in this system were suitable for quantum computing. The ability to apply the same single qubit operation to a group of ions enabled the nature of the interaction to be demonstrated in a more direct manner than previously possible.

Finally, ions were selected from one anti-hole (qubit) based on their interactions with the ions of another anti-hole. This enabled the demonstration of a conditional phase shift, the most rudimentary quantum logic operation.

5.1 The sample

Europium doped yttrium orthosilicate (Y_2SiO_5) was used for these experiments. The population lifetime for its ground state hyperfine structure is a number of hours [102], which for the purposes of these investigations is infinite. This means that the ions that one wishes to remove from interaction with the laser stay in their auxiliary hyperfine levels indefinitely, allowing

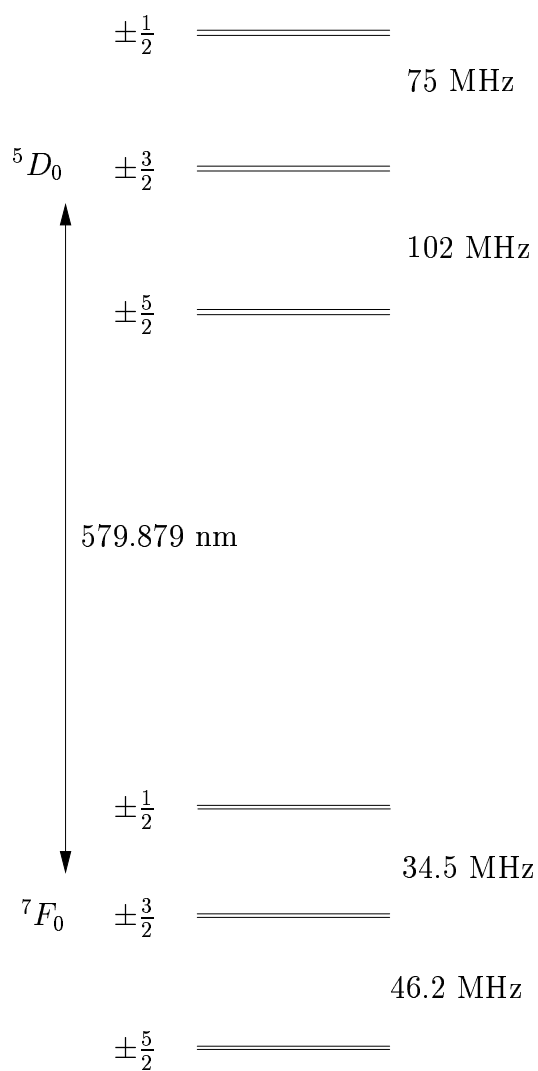


Figure 5.1: Energy level diagram of Yano et al. for ^{151}Eu at ‘site 1’.

		Ground state		
		$\pm\frac{1}{2}$	$\pm\frac{3}{2}$	$\pm\frac{5}{2}$
Excited state	$\pm\frac{1}{2}$	0.0	34.5	80.2
	$\pm\frac{3}{2}$	-75.0	-40.5	5.2
	$\pm\frac{5}{2}$	-177.0	-142.5	-96.2

Table 5.1: Frequencies (in MHz) of the optical transitions of $^{151}\text{Eu}:\text{Y}_2\text{SiO}_5$ at ‘site 1’ based on the measurements of Yano et al. The frequencies are relative to the $\pm\frac{1}{2} \rightarrow \pm\frac{1}{2}$ transition. The uncertainty is dominated by 1 MHz uncertainty for the excited state hyperfine splittings. This work gave a more precise measurement of the value for the $\pm\frac{5}{2} \rightarrow \pm\frac{5}{2}$ transition of -95.95 ± 0.05 MHz.

the ensembles to be prepared in a number of steps.

The coherence times for the optical transitions are also long (2.6 ms). In terms of the ratio of the linewidth to transition frequency, they are the narrowest spectral lines that have been observed in a solid [66]. While those measurements were made in a magnetic field, the field was moderate and similar coherence times can be achieved without such a field. In order that the coherence times weren’t affected by instantaneous spectral diffusion, very low laser powers and dilute samples were used. The instantaneous spectral diffusion was caused by the same interaction between the ions that we wished to utilise for the interactions between qubits. It was therefore heartening that instantaneous spectral diffusion was so easy to observe.

The sample used in these experiments was provided by Scientific Materials Corporation of Bozeman, Montana [147]. The europium concentration was 0.1 at. %.

The experiments were carried out on the $^7F_0 \rightarrow ^5D_0$ optical transition. As explained in the introduction to Chapter 3, there are two crystallographically distinct sites where europium can substitute for yttrium in the crystal. These experiments were carried out on the ions at ‘site 1’, which have the $^7F_0 \rightarrow ^5D_0$ occurring at approximately 589.879 nm. Europium has two naturally occurring isotopes that occur in approximately equal abundance, ^{151}Eu and ^{153}Eu , each of which leads to different hyperfine structure. For these experiments the isotope ^{151}Eu was used. The energy level diagram, as constructed by Yano et al. [102], for this system is shown in Fig. 5.1. The optical transition frequencies relative to the $\pm\frac{1}{2} \rightarrow \pm\frac{1}{2}$ transition are given in Table. 5.1. The $^7F_0 \rightarrow ^5D_0$ transition for ions at ‘site 1’ had an inhomogeneous linewidth of approximately 1.6 GHz in this sample.

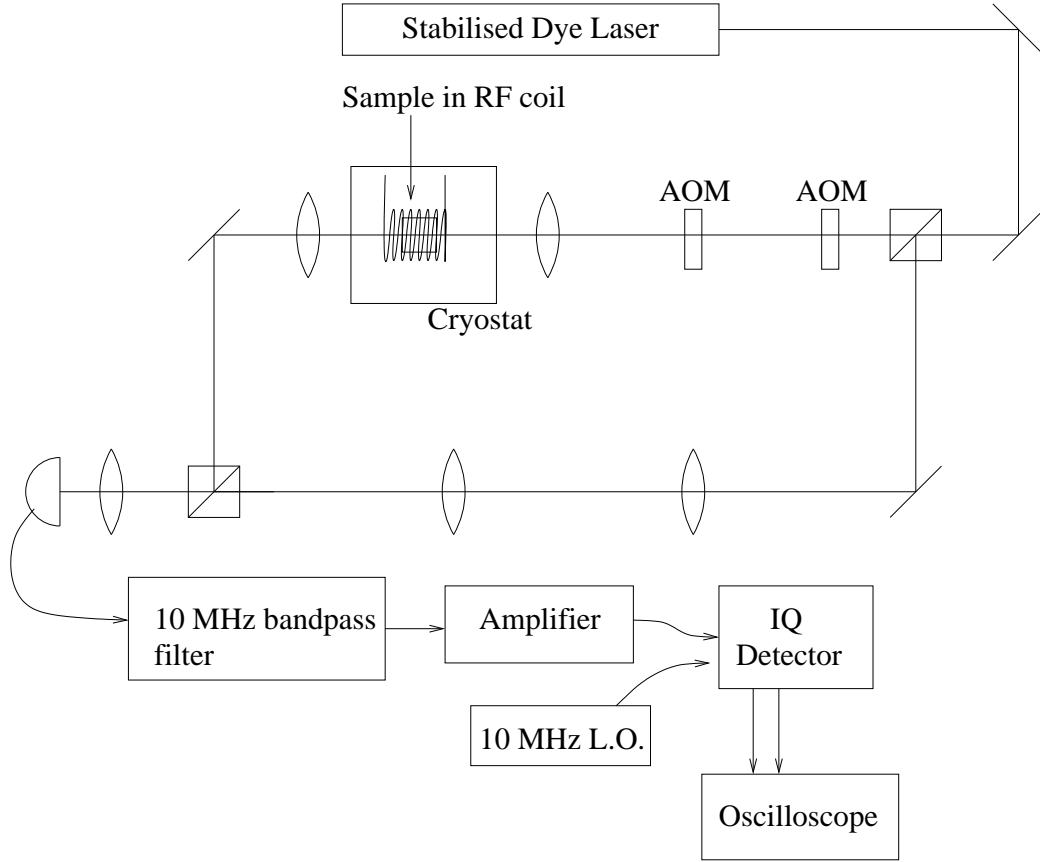


Figure 5.2: Experimental setup used for europium studies. An auxiliary beam is not shown. It was picked off the main beam, passed through an AOM and then steered toward the sample. This beam was used to apply light shifted from the laser frequency by ~ 100 MHz when ‘burning back’ the narrow features.

5.2 Experimental setup

The experimental setup used for the quantum computing related experiments is shown in Fig. 5.2. Light from a highly stabilised dye-laser was steered toward a Mach-Zehnder interferometer. The first beam-splitter in this interferometer is a piece of uncoated glass. This resulted in most of the light going into one particular arm. This arm, the ‘sample arm’, contained two acousto-optic modulators (AOMs) in series followed by the sample. The ‘reference arm’ was empty except for a polarisation rotator followed by a polariser. These two elements were used to provide continuous attenuation to the light in the reference arm and enabled the intensity of this reference arm to be reduced to a suitable level for the detector.

Not shown in Fig. 5.2 is the auxiliary optical beam. This was taken off one of the zeroth order beams of the first AOM in the sample beam, passed through an AOM. This auxiliary beam was then steered through into

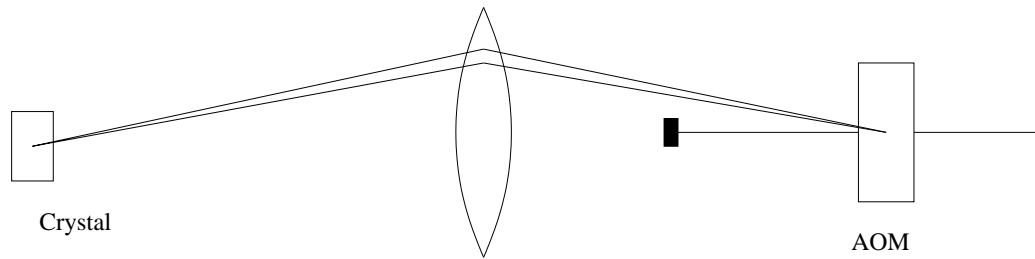


Figure 5.3: The different beams generated by the second AOM to address the *control* and *target* anti-holes deflected by differing amounts as they are deflected. The geometry shown was used to counteract this. The angle between the two beams has been exaggerated and without the lens, the two beams would only just be resolved by the time the light had propagated to the cryostat. Very good overlap between the beams could be achieved because of this.

the spare output port of the interferometer. Because of the layout of the experiment on the optical table this was the easiest way to assure that the auxiliary beam and the main experimental beam overlap in the sample. It was decided to make the auxiliary beam quite wide at the sample to make achieving this overlap easier.

The use of two acousto-optic modulators resulted in a total attenuation of the light of > 100 db when turned off. The first AOM was driven with a 90 MHz signal and the first order diffraction on the low frequency side left unblocked. For the experiments involving only one anti-hole, the second AOM was driven with a 80 MHz signal and the first order diffraction taken on the high frequency side. This resulted in the light reaching the sample being 10 MHz lower than that in the reference arm. When the two beams were combined on the exit beam-splitter of the interferometer, a 10 MHz beat on the light was produced. When the light from each arm is mode-matched and of the same intensity, the resulting amplitude modulation on the signal from the detector will have 100% depth. If care was taken adjusting the positions of the lenses and aligning the beams modulation depths of $> 95\%$ were obtained. Typically a modulation depth of $> 80\%$ was used.

As well as shifting the frequency, AOMs deflect the light an amount proportional to the modulating frequency. So that the beams that were used to address each anti-hole were well overlapped, the lens that focused the light on to the sample was arranged such that it imaged the second AOM. It was this AOM that was used to shift the frequency of the beam to address different anti-holes. The geometry is shown in Fig. 5.3. A 60 cm lens was placed upstream of the interferometer and this was used to alter the position of the beam waist relative to the AOM. This was used to vary the position of the beam waist relative to the sample.

While the interferometer was aligned for the target beam, the mode matching was sufficient to see beat signals at the detector due to the control beam.

The physics of how the detection scheme operates is described in Sec. 4.4. In summary, the amplitude and phase of the coherent emission produced in the same mode as the exciting laser beam provides a direct measurement of the ensemble average of the Pauli operators $\langle X \rangle$ and $\langle Y \rangle$. Generally measurements were made on the target anti-hole. The coherent emission from the target anti-hole produces a 10 MHz beat signal when combined with the light from the reference arm of the interferometer. This beat signal was passed through a 10 MHz band pass filter with a bandwidth of approximately 3 MHz. This filtered signal was then amplified and passed into a Mini-Circuits MIQA-10D detector [148]. This detector has two outputs which give the amplitude of the component of the input signal that is both in phase and in quadrature with a supplied 10 MHz local oscillator signal. A block diagram of the detector is shown in Fig. 5.4. Assuming the interferometer is rigid, the phase of the 10 MHz beat signal is given by the phase of the light in the sample arm. Thus, the output of the IQ detector gives the amplitude and phase of the light coming from the sample arm of the interferometer. The resulting system was shot noise limited and has previously enabled photon echoes containing as few as 400 photons [141] to be observed. The IQ detector could only operate at 10 MHz which meant that it could only monitor the target anti-hole easily. When measurements of the other anti-hole were required, the roles of the two anti-holes could be reversed. Both a simple amplitude detector and recording the beat signal raw were also used at times, but not for any of the results presented here.

Over the short timescales of an experimental shot (hundreds of microseconds) the phase noise from the interferometer was small $<5^\circ$ but in some cases significant. Over longer periods, such as the time between shots, the effect of the phase noise from the interferometer was total. As the pulses used to drive the atoms saturated the detection system, a weak phase reference pulse was applied after the experimental shot in situations where phases of the emission from the ions relative to the laser were required.

A photon echo obtained with this detection system is shown in Fig. 2.7 on page 44.

5.2.1 Ultra-high resolution laser

As has been mentioned above, the homogeneous linewidths of the optical transitions are extremely narrow. To make full use of these long coherence

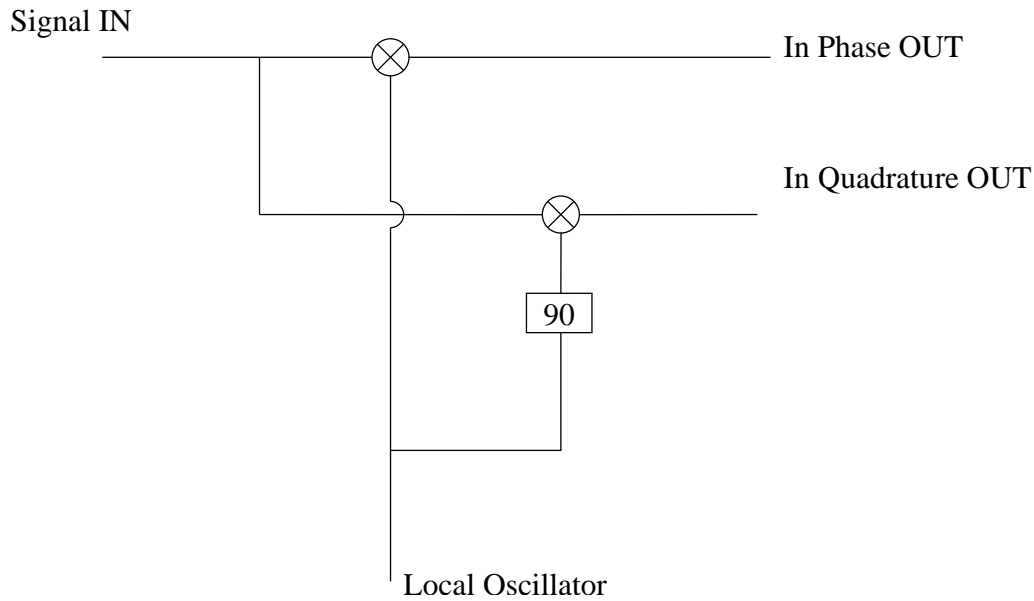


Figure 5.4: Block diagram showing the operation of the IQ detector.

times, a laser that is phase stable for at least a similar length of time is required. This is a very strict criterion and it was fortunate that such a laser was indeed available. The criterion of phase coherence times for the laser was not met by many of the labs RF sources (even some reputedly designed for NMR) even though the frequencies of oscillation were seven orders of magnitude smaller. Achieving such stability in a system that contains what is essentially a jet of antifreeze in the optical path is truly remarkable. The laser has been developed by Dr. Matthew Sellars and various co-workers at the Laser Physics Centre, at ANU.

This laser is discussed in detail elsewhere [149, 150], so only a brief description is given here.

The laser is a modified Coherent 699 ring dye laser. If the laser was perfectly mechanically stable it would have a linewidth of approximately 2 Hz [151]. However the motion of various parts of the laser, in particular the dye jet cause frequency jitter and active stabilisation is required to obtain a reasonable linewidth. In its unmodified form the frequency control elements used consist of a galvo-driven Brewster plate and cavity mirror mounted on a piezoelectric-electric stack. The Brewster plate is used to correct for slow fluctuations (DC up to around 100 Hz) and the piezoelectric-stack is used for faster fluctuations. The error signal for the commercial control system is generated from the side of a transmission peak of a low finesse near-confocal cavity. This cavity has a free spectral range of approximately 1 GHz. The laser linewidth achieved by the commercial stabilisation system

is approximately 2 MHz.

An investigation of the frequency noise of this laser showed significant frequency jitter over timescales much faster than the 2 kHz bandwidth of the commercial frequency stabilisation system [150].

The frequency reference for the improved stabilisation system was custom-made by the CSIRO. The spacer for the cavity 50 cm long tube of “zerodur”, was suspended by wires and surrounded by a heat-shield. The temperature of the heat-shield was actively stabilised at approximately 313 K. The whole assembly placed in a vacuum chamber to help this. The error signal for the laser frequency was generated by the Pound-Drever method [152].

The bandwidth of the stabilisation system was improved by improvements to the servo electronics. An electro-optic modulator was added to the laser cavity to provide frequency corrections over faster timescales than those possible using the piezoelectric-driven mirror.

When optimised the resulting stability was better than 200 Hz over timescales of 0.2 s [149].

5.3 Generating and characterising single qubits

In order to obtain the same single qubit rotations of an ensemble when applying pulsed driving fields, two criteria must be satisfied.

Firstly each ion in the ensemble must experience the same Rabi frequency. This is problematic because the intensity of light is not constant across the nominally Gaussian profile of a laser beam. The hyperfine structure also causes problems because the oscillator strength of an optical transition depends on which of the ground state hyperfine and excited state hyperfine levels are involved.

The second criterion for definite single qubit rotations involves the detuning of the ions within the ensemble. In order that the dephasing caused by the inhomogeneous spectral width of the ensemble not be significant during the pulse, it is necessary for the duration of the pulse to be short compared to the inverse of the spectral width of the feature. Thus, for a rotation about a substantial angle, the Rabi frequency must be large compared to the spectral width of the feature. The inhomogeneous linewidth of the whole ensemble is typically >1 GHz, which is, unfortunately, much larger than the Rabi frequencies available using CW lasers. With 200 mW of laser focused to $100\text{ }\mu\text{m}$, Rabi frequencies of the order of 500 kHz are achieved.

Fortunately, ensembles can be created using the spectral hole-burning mechanism of Section 2.6.1 which satisfy the two criteria. The ensembles are

created by taking all of the ions present in the crystal and optically pumping those which are unwanted into a different ground state hyperfine level. There the unwanted ions have no population in levels that have transitions close to resonance with the laser. As a result they no longer interact with the laser and can be removed from consideration. The lifetimes of the ground state hyperfine levels for $\text{Eu:Y}_2\text{SiO}_5$ are much longer than the timescale of the experiment [102]. This means that until, the application of either optical or RF perturbations, the features can be considered permanent.

The application of definite pulse areas to an optical transition in a solid was first demonstrated by Pryde, Sellars and Manson [80]. Their paper represented a significant milestone for optical spectroscopy of solids, as it was the first time that multiple definite area pulses from a phase coherent oscillator were used on an optical transition. In the Pryde experiment, the narrow absorptive feature was made by applying “zero area” pulses to a region of the inhomogeneous line. The problem of intensity variations in the resulting ensemble was then alleviated by applying a sequence of ‘ 2π ’ pulses. The pulses applied corresponded to 2π pulses only for ions that saw a particular intensity. These ions would be returned to the ground state after each pulse. The rest of the ions in the ensemble would be left with some population still remaining in the excited state after each pulse. In the time between the pulses these excited ions would relax and incrementally get optically pumped into other ground state hyperfine levels and thus removed from consideration.

For demonstrating the two qubit operations using ensembles, one would prefer ensembles with the largest possible spatial density of ions in order to get the largest mean interaction strength between two qubits. It is therefore important that when creating an ensemble to minimise the number of ions that are wanted for the ensemble, but are none the less removed. Further to this, the number of ions that are not wanted in the ensemble, but will still be excited by the control pulses should be minimised. The excitation of these ‘background’ ions will hinder the two qubit operations.

The anti-holes achieved by Pryde et al. do not stand up well to these criteria, so other techniques were investigated. The two techniques described here involved using more sophisticated zero-area pulses and ‘burning back’ a narrow anti-hole into a wide hole. In the early, single qubit, experiments a combination of these two methods were used. An anti-hole made by burning up was subsequently ‘cleaned up’ with zero area pulses. In later, two qubit, experiments the zero area pulses were dispensed with. The reasons for this were two fold. Firstly, it was discovered that it was possible using weak

burn-back optical beams with their frequencies carefully tuned, to burn back narrow anti-holes. The second reason was to combat the growing amount of equipment needed for the experiments — equipment which wasn't always immediately available¹.

5.3.1 Zero area pulses

The zero area pulses used by Pryde et al. are shown in Fig. 5.5. As can be seen from Fig. 5.5(v) as well as the anti-hole there is a significant background also. The width of this background feature is here limited by the spectral width of the pulses used to measure it. In working toward the goal of big anti-holes with small background levels, ‘double-sinc’ zero area pulses as shown in Fig. 5.6 were investigated. The sharp cornered frequency spectrum of these pulses allow more pulses to be applied, thus reducing the background levels without eroding the anti-hole. The flat spectrum of these pulses around zero frequency should make the process of creating the anti-hole more robust with respect to drifts in laser frequency.

The envelope of the double-sinc pulses was given by²

$$y(t) = A \exp\left(-\frac{t^2}{2u^2}\right) (w_1 \text{sinc}(w_1 t) - w_2 \text{sinc}(w_2 t)) \quad (5.1)$$

Here the width of the trench burnt is given by the larger of the w_i and the width of the anti-hole in the middle is given by the smaller w_i . A is a scaling factor and the Gaussian term is used to remove any ringing that would occur if a rectangular window was used. The sequence length of the pulse used determines u and, in turn, the maximum spectral resolution achievable. If the fast sinc function is much shorter than the slower sinc function, it will have to be much more intense in order to have the same area. Therefore, the ratio between the spectral widths of the sinc functions is limited by dynamic range concerns. In view of all these considerations the following parameters were chosen

$$w_1 = 50 \text{ kHz} \quad (5.2)$$

$$w_2 = 1 \text{ MHz} \quad (5.3)$$

$$u = 24 \mu s \quad (5.4)$$

The result of a photon echo sequence applied to an anti-hole prepared

¹This was in no small part due to RF switches inexplicably failing at the hands of the author.

²Here $\text{sinc}(x) \equiv \sin(\pi x)/(\pi x)$ for $x \neq 0$, and $\text{sinc}(0) \equiv 1$.

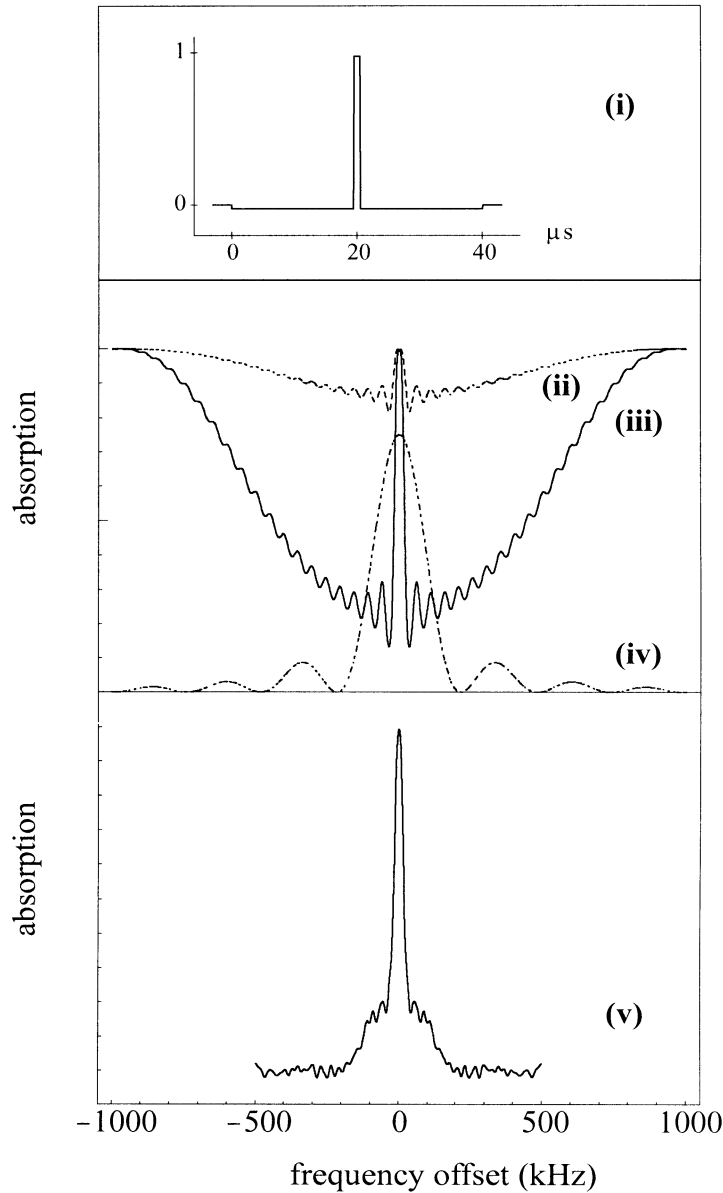


Figure 5.5: Graphs describing the anti-holes created by Pryde et al. [80]. The amplitude of the zero-area pulses used to generate the anti-hole is given as a function of time in (i). Here the combined areas of the long weak pulses is the same as that of the short intense pulse, leading to a zero area pulse. Traces (ii) and (iii) show numerical estimates of absorption profiles of the resulting anti-hole after 13 and 130 pulses (a hole-burning efficiency of 5% was assumed). Trace (iv) shows the spectra of the pulses used in their experiments. Trace (v) is a Fourier transform of the experimental echo shape. This is equal to the product of the ion density versus frequency and the spectrum of the exciting pulses. The shoulders on this peak indicate a significant number of background ions. This figure was scanned from [149].

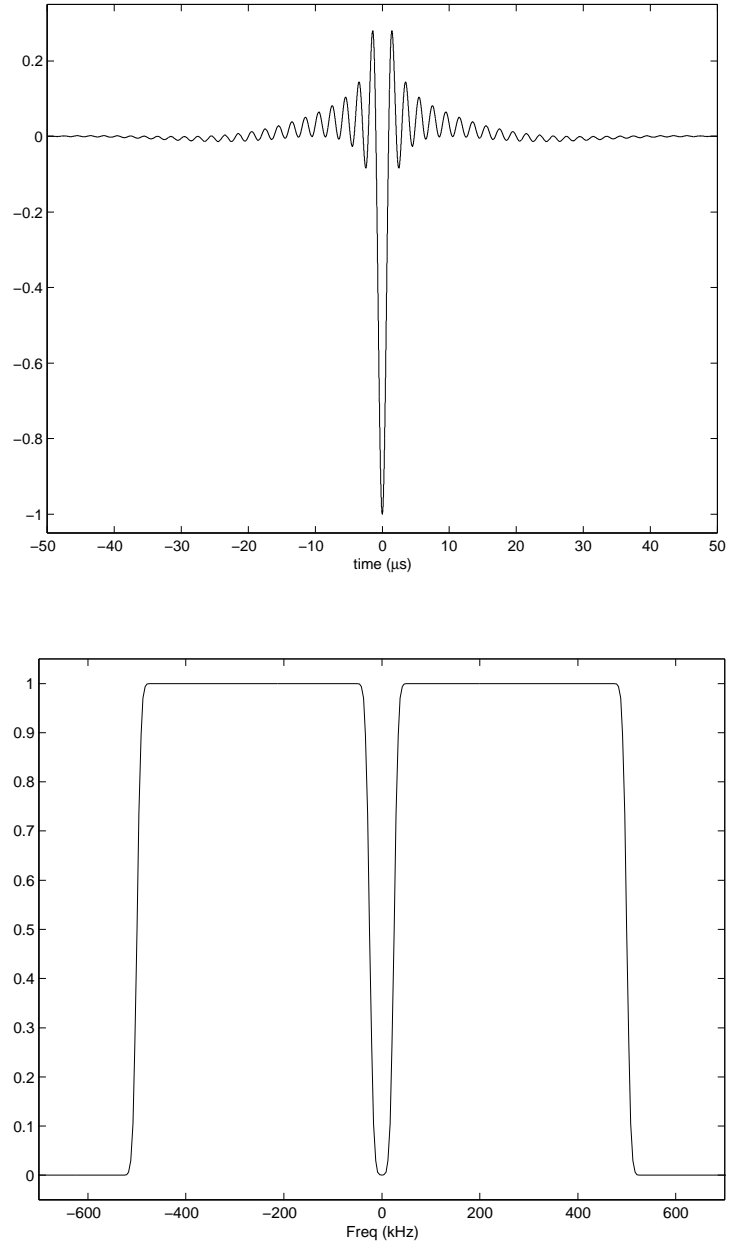


Figure 5.6: The envelope and spectra of the double-sinc pulses used for creating anti-holes. Because the pulses used had to be of a limited temporal extent, a Gaussian window was used. This caused the rounded edges in the spectrum of the pulses.

with these zero area pulses is shown in Fig. 5.7. To prepare the anti-hole, 300 double-sinc pulses were applied to a broad burn-back feature. (See next section.) The sinc-like shape of the echo and its square shaped spectrum correspond well with what would be expected from the preparation pulses applied. Compared with the earlier results of Pryde et al. a great improvement in the background level can be seen. For Fig. 5.7 the overall phase was chosen so the integrated echo signal was all in one quadrature. There is a slight dispersive nature to the echo, as can be seen from the other quadrature. This dispersion is due to a slight frequency mismatch between laser and the anti-hole. This also appears as the spectrum shown in (b) being slightly off centre.

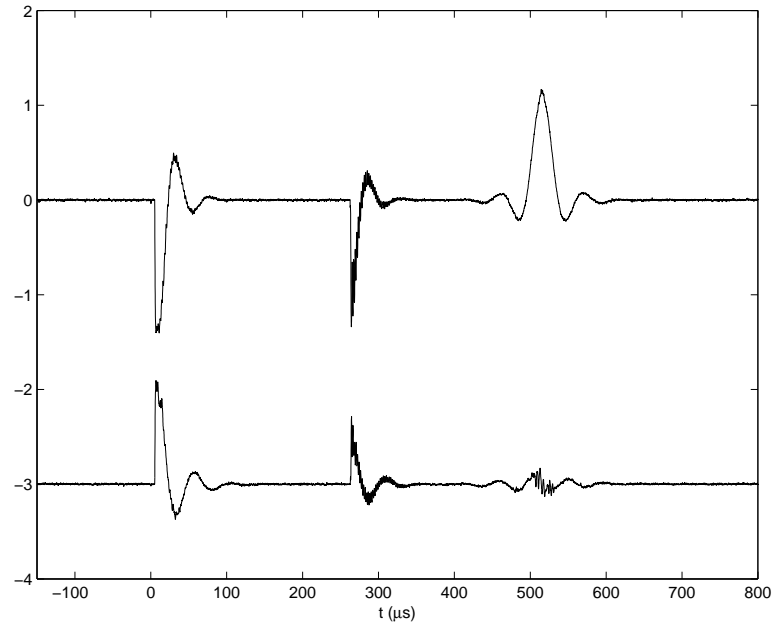
If the laser and the ions in the crystal were perfectly phase stable, the free induction decays from the two pulses would be exactly out of phase with the signal from the echo. This is not the case and it appears the phase between the laser and ions drifted approximately 30° during the 0.5 ms of the shot. The high frequency signal on the second FID is at 500 kHz and is due to the excitation of the edges of the trench in which the anti-hole lies (see spectrum in Fig. 5.6). These ions don't contribute much signal to the echo because they are only weakly excited by the applied laser pulses and therefore do not get rephased well.

The well defined frequency of the ringing suggests sharp spectral features. Very recent simulations [153] have shown that such sharp features can be expected if the driving sinc pulses are intense enough to drive the ions far from the ground state.

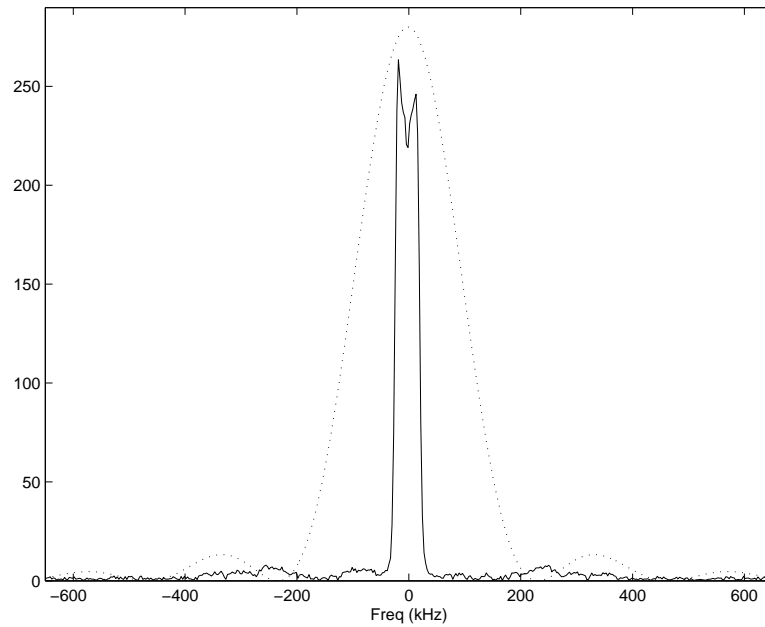
5.3.2 Burning back anti-holes

Another method of generating a sharp absorptive feature is by burning a spectral hole at another frequency. One advantage of such a technique is that it is possible to generate an anti-hole such that all the ions in the feature interact with the laser using the same transition. Thus, one of the reasons for inhomogeneity in the Rabi frequency can be removed.

While one doesn't have the same control over the sharpness of the resulting feature as when using zero area pulses, the simplicity of the technique is helpful when doing experiments with more than one anti-hole. Using very weak burn-back beams enabled features with sufficiently narrow widths. The limit of how narrow the features could be made was of the order of 30 kHz, which is comparable to what is likely for the inhomogeneous broadening in the hyperfine levels. No hard measurements of the level of this inhomogeneous broadening have been made.



(a) The two quadratures of the coherently emitted light as a function of time. The first pulse of the echo sequence was applied at $t = 0 \mu s$ and the rephasing pulse at $t = 250 \mu s$. The overall phase was chosen so the integrated echo signal was all in one quadrature.



(b) Shows the Fourier transform of the echo. The dotted line is the spectrum of the rephasing π pulse.

Figure 5.7: Photon echo on an anti-hole prepared with the double-sinc pulses. Three hundred double-sinc pulses were applied.

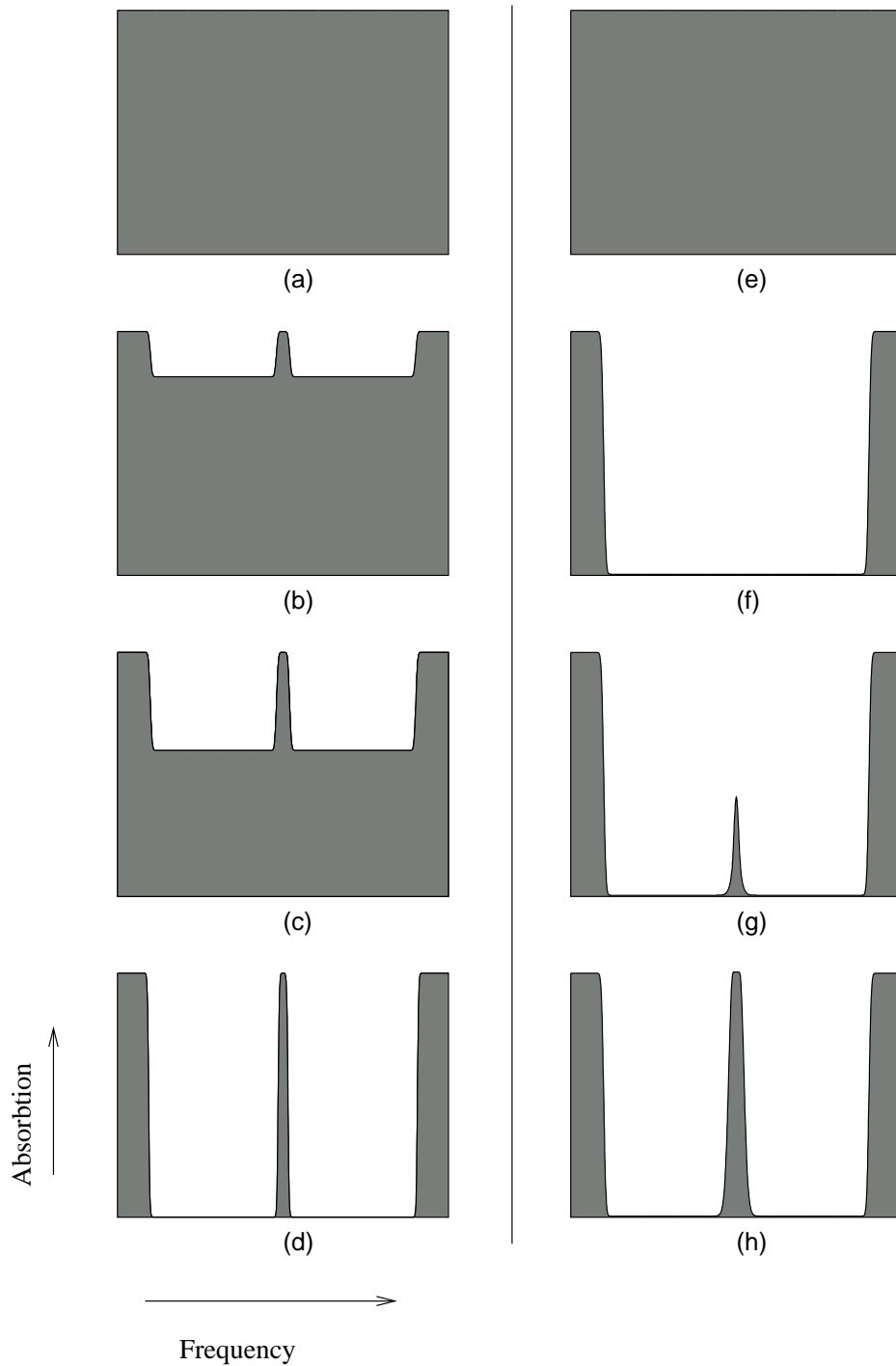


Figure 5.8: A diagram showing the two methods used to prepare sharp absorptive features to which accurate pulses could be applied. Plots (a)–(d) show the absorption versus frequency for various stages of the preparation using zero area pulses. The zero area pulses are repeatedly applied and the ions that are close to resonance with the laser but not wanted as part of the feature are burnt away. Plots (e)–(h) show the absorption versus frequency for various stages of the preparation using the burn back of ions. First, a broad hole is burned with a swept frequency beam (f) then by applying a different frequency, which is determined by the hyperfine splittings, an anti-hole can be burnt back in the middle of this trench.

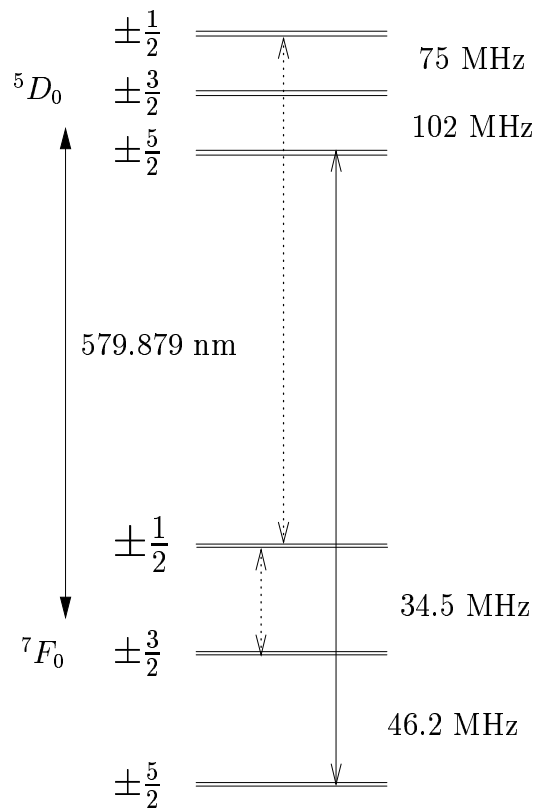


Figure 5.9: Energy level diagram showing the energy levels used when burning back anti-holes. The diagram also shows the effect of the burn back beams on an ion that will end up at the centre of the anti-hole. The transitions depicted with dotted lines were used to optically pump all the ions with the correct inhomogeneous splitting into the $\pm 5/2$ ground states. The trench in which the anti-hole lay was made by using a swept beam of a frequency close to that shown with the solid line. The difference between the frequency of the optical burn back beam and the frequency at which the anti-hole appears is a combination of the hyperfine splittings.

The transitions driven to create an anti-hole for an ion in the centre of the resulting anti-hole are shown in Fig. 5.9. The ions in the resulting anti-hole will interact with the laser due to the $\pm 5/2 \rightarrow \pm 5/2$ transition (shown as a solid line in Fig. 5.9).

The procedure for creating the anti-hole was as follows. First, the main laser beam and the RF signal at 34.5 MHz was applied to all the sample. The laser optically pumped all the ions that have a transition close to the laser into a hyperfine level where they no longer interact with the laser. The RF field ensured that no ions would get placed back into the hole if only a 34.5 MHz RF field is applied. In order to counteract the lack of precise knowledge of the $\pm 1/2 \leftrightarrow \pm 3/2$ transition frequency, the 34.5 MHz signal was swept approximately 200 kHz. For early experiments this wide trench was prepared using an intense laser beam. Power broadening and saturation of the hole, made the trench sufficiently wide. In later experiments, a less intense beam was used with its frequency swept; this reduced the number of ions left in the bottom of the trench. This improvement was attributed to the weak beam causing less off-resonant excitation of other hyperfine transitions.

The anti-hole was then placed in this trench by applying an auxiliary optical beam, to drive the $\pm 1/2 \rightarrow \pm 1/2$ transition. The RF field at 34.5 MHz was also applied in order to stop population accumulating in ground state $\pm 3/2$ hyperfine levels. The field was necessary because the branching ratio from the $\pm 1/2$ excited state to the $\pm 5/2$ ground state is low, due to the small degree of mixing of these two levels. It was decided to use these transitions primarily because of the ease with which the auxiliary beam could be generated. The frequency difference between the main and auxiliary beams was ≈ 96 MHz which allowed the auxiliary beam to be created easily with an acousto-optic modulator.

The degree to which the resulting anti-hole is centred at the laser frequency can be determined by looking at the shape of the photon echo that the anti-hole gives. The frequency difference can be determined from the phase ramp across the echo. In this way, the frequency difference between the two optical transitions was measured as 95.95 ± 0.05 MHz. This is more than an order of magnitude more precise than previous measurements and such techniques would be useful for characterising the hyperfine structure more generally.

5.3.3 Nutations

Using either one of or both of the techniques described in the last two sections, it was possible to produce ensembles such that the inhomogeneous width was

smaller than the available Rabi frequencies. If the ensemble was based around an anti-hole as described in Sec. 5.3.2 it was also possible to have all of the members of this ensemble resonant via the same transition. However due to the spread of laser intensity across the beam it is not possible to apply pulses of definite area with such ensembles. To overcome this problem a series of ‘ 2π ’ pulses were applied to the sample. These were separated by a time long compared to the lifetime of the optically excited state. For the ions in a particular part of the beam, this was a true 2π pulse and they were in the ground state at the end of the pulse. Ions in different parts of the beam that didn’t experience a 2π pulse would be left partially excited. As more pulses were applied, these ions were incrementally optically pumped into an auxiliary ground state and passed out of consideration. The resulting ensemble experienced a well defined Rabi frequency.

The effect of the application of 2π pulses is illustrated in the results shown in Figs. 5.10 and 5.11. The ensemble on which the measurements were made, was made by first burning back an anti-hole as described in Sec. 5.3.2. Because of the moderately intense power used for the burn-back beam this anti-hole had a width of approximately 300 kHz. The anti-hole was then ‘cleaned up’ using 300 of the double-sinc zero area pulses as described in Sec. 5.3.1.

From the decay of the nutation shown in Fig. 5.11, it can be concluded that the Rabi frequency spread over the ensemble was of the order of 10% after the application of 10 ‘ 2π ’ pulses.

5.4 Quantum state tomography

In order to demonstrate how well the narrow ensembles act as single qubits, quantum state tomography was demonstrated. The ensembles used were as described in the above section; that is a ≈ 300 kHz wide feature was burnt back into an empty trench. This anti-hole was then narrowed to a 50 kHz feature with a rectangular lineshape by applying ‘zero area pulses’ to the ions.

It should be mentioned that because of the tighter focus of the laser applied to the sample, the Rabi frequencies experienced by the ions were higher for the results in this section than in the previous one. In this case, $4\ \mu s$ long ‘ 2π ’ pulses were used to select which ions experienced Rabi frequencies close to 250 kHz. As above, ten 2π pulses were applied with an 8 ms delay between.

The pulse sequence used for the tomography consisted of three pulses,

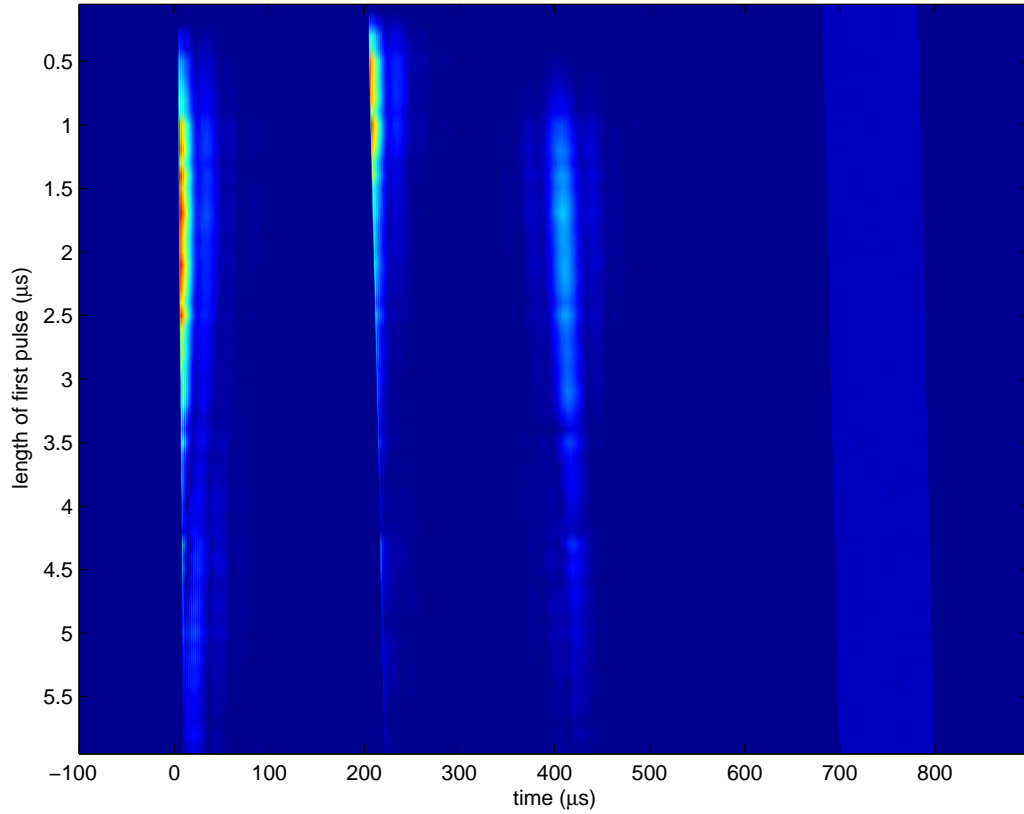
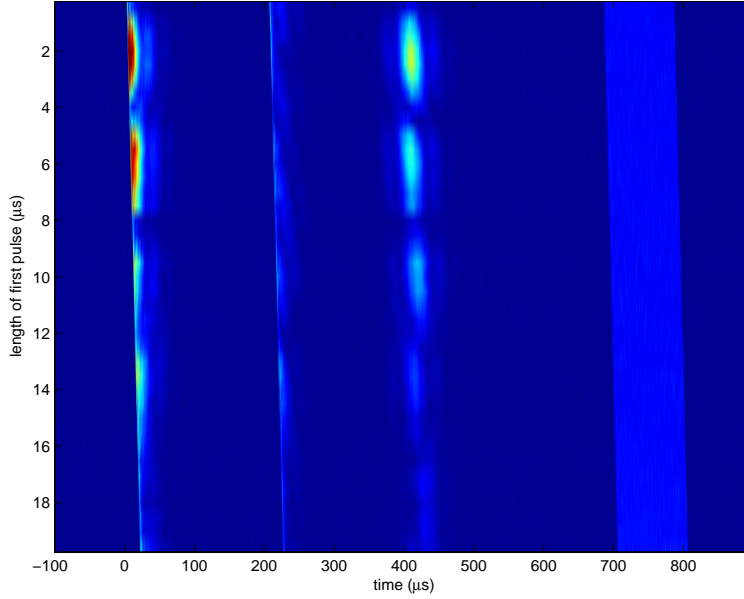
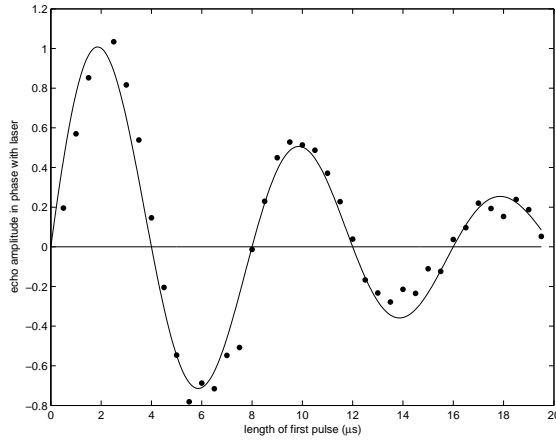


Figure 5.10: An anti-hole without 2π pulses applied. Each row of pixels in the image shows the amplitude of the coherent emission from the sample during a photon echo experiment. The first pulse was applied at $t = 0 \mu\text{s}$ and a length as indicated on the y axis. The second pulse was applied at approximately $t = 200 \mu\text{s}$ and had a length twice that of the first. Due to these two pulses an echo formed at about $t = 400 \mu\text{s}$. As can be seen from the echo and the FIDs from the two pulses, a $\pi/2$ pulse for the ions is around $2 \mu\text{s}$. A strong FID from the second pulse is seen when it has a length of approximately $2 \mu\text{s}$. A strong FID from the first pulse and a strong echo are seen when the lengths of the pulses are 2 and $4 \mu\text{s}$ respectively. The vertical blue stripe to the right of the figure is due to long, weak phase reference pulses being applied after the end of each shot. The sinc-like modulation of the echoes and FIDs is due to the square frequency profile of the anti-hole.



(a) As in Fig. 5.10 each horizontal line corresponds to one photon echo shot. Here the length of the first pulse was varied while the second one was held constant ($4 \mu s$). Before the photon echo sequence ten 2π pulses were applied to the anti-hole in order to remove ions which didn't experience Rabi frequencies close to $1/(8 \mu s) = 125 \text{ kHz}$. Nutations in the size of the echo and FID from the first pulse can be seen with the strongest emission occurring for pulses with areas $(n + 1/2)\pi$. Only small FID signals are seen after the rephasing π pulse, as is expected, because it should create no coherence.



(b) The amplitude of the component of the echo emission that is in phase with the laser. In all cases the component of the echo emission in quadrature with the laser was small. An initial $\pi/2$ ($2 \mu s$) pulse produces a FID out of phase with the laser and an echo in phase with the laser. Conversely a $3\pi/2$ pulse ($6 \mu s$) puts the states on the opposite side of the Bloch sphere resulting in a FID in phase with the laser and an echo out of phase with the laser.

Figure 5.11: An anti-hole with 2π pulses applied.

each separated by 70 μs . First a pulse of a particular length and phase was applied. This was followed by a 2 μs long π pulse unshifted in phase — to rephase the inhomogeneous broadening in the sample. At $t = 140 \mu\text{s}$, a 1 μs long $\pi/2$ pulse was applied that was also unshifted in phase. The axes for the Bloch vectors were chosen such that the ground state ($|0\rangle$) was along the negative z axis and laser pulses that were unshifted in phase caused rotations about the y axis.

The first pulse was used to create an arbitrary state, and the coherent emission resulting from this and the rest of the sequence constituted a measurement of this state. The first pulse was, therefore, viewed as causing a rotation of the state vector on the Bloch sphere and the following two pulses viewed as a rotation of the both the state vector and the Bloch sphere itself. At each point, the coherent emission measured the projection of the state onto the horizontal plane. Thus, the amplitude of the component of the emission after the first pulse that was in phase (in quadrature) with the laser was proportional to $\langle -X \rangle$ ($\langle Y \rangle$) for the initial state. This coherent emission decayed over $\sim 20 \mu\text{s}$ ($1/(50 \text{ kHz})$) due to the inhomogeneous linewidth of the ensemble. The ensemble rephased at 140 μs and, at that time, a 1 μs long $\pi/2$ pulse was applied. As the ensemble was rephasing before the $\pi/2$ pulse the amplitude of the emission in phase (in quadrature) with the laser was proportional to $\langle X \rangle$ ($\langle Y \rangle$) for the initial state. After the $\pi/2$ pulse the amplitude of the emission in phase (in quadrature) with the laser was proportional to $\langle -Z \rangle$ ($\langle Y \rangle$) for the initial state. These measurements over-determined the initial Bloch vector, and linear least squares was used to extract the measured Bloch vector. The length of the Bloch vector was calibrated using two particular input states: $(|0\rangle + |1\rangle)/\sqrt{2}$ prepared using a $\pi/2$ pulse unshifted in phase; and $|0\rangle$ prepared by not having a preparation pulse.

The fidelity is given by $\mathcal{F} = \langle \phi | \rho | \phi \rangle$ where $|\phi\rangle$ is the input state and ρ is the measured density matrix. A significant contribution to the error in the tomography process was the shot to shot variation in the number of ions to which the process was applied. The requirement of phase coherence for the 200 μs of the tomography sequence was easily satisfied by the laser. However, the preparation of the anti-hole took approximately 10 s, leading to the possibility that the laser drifts a significant fraction of the 50 kHz width of the anti-hole in this time. This caused a shot to shot variation in the number of ions to which the tomography was applied, which in turn had the effect of scaling the length of the measured Bloch vector. If a state that is being measured can be assumed to be pure, the measured Bloch vector

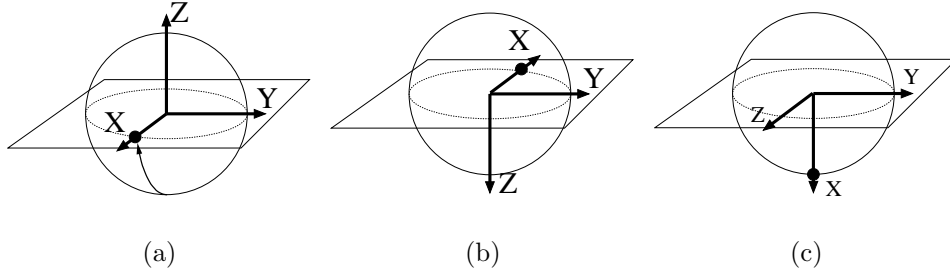


Figure 5.12: The effect of the tomography sequence on the Bloch sphere when the preparation pulse is a $\pi/2$ pulse. Experimental results for a shot of this type are shown in Fig. 5.13. (a) The state is moved to the equator by the first pulse in the sequence. This gives coherent emission out of phase with the laser. (b) Just before $t = 140\mu\text{s}$ the system rephases on the opposite side of the Bloch sphere, giving coherent emission in phase with the laser. (c) The final $\pi/2$ pulse rotates the state to the ground state, which results in no coherent emission.

should be normalised. This normalisation makes the tomography process insensitive to drifts in the number of ions to which the process is applied. This leaves the inhomogeneity in the Rabi frequencies as the main source of error in the process.

The fidelity of the combined state preparation and tomography for a number of different input states are shown in table 5.2.

The results of one particular experimental shot are shown in Fig. 5.13. Here the state to be measured is created at $t = 0 \mu\text{s}$ with a $\pi/2$ pulse unshifted in phase. This puts the Bloch vector along the x axis. This gave coherent emission out of phase with the laser and this emission decayed as the inhomogeneous broadening dephases the ensemble. At $t = 70 \mu\text{s}$ the π pulse was applied to rephase the inhomogeneous broadening. This should have caused no polarisation of the ions and thus produced no coherent emission. As the time $t = 140 \mu\text{s}$ was approached the ensemble rephased on the opposite side of the Bloch sphere, producing coherent emission in phase with the laser. At $t = 140 \mu\text{s}$ a $\pi/2$ pulse was applied, which took the ions down to the ground state, stopping the coherent emission. The high frequency ringing superimposed on the emission following the application of the pulses was due to the excitation of the edges of the trenches in which the anti-hole lay (see Sec. 5.3.1).

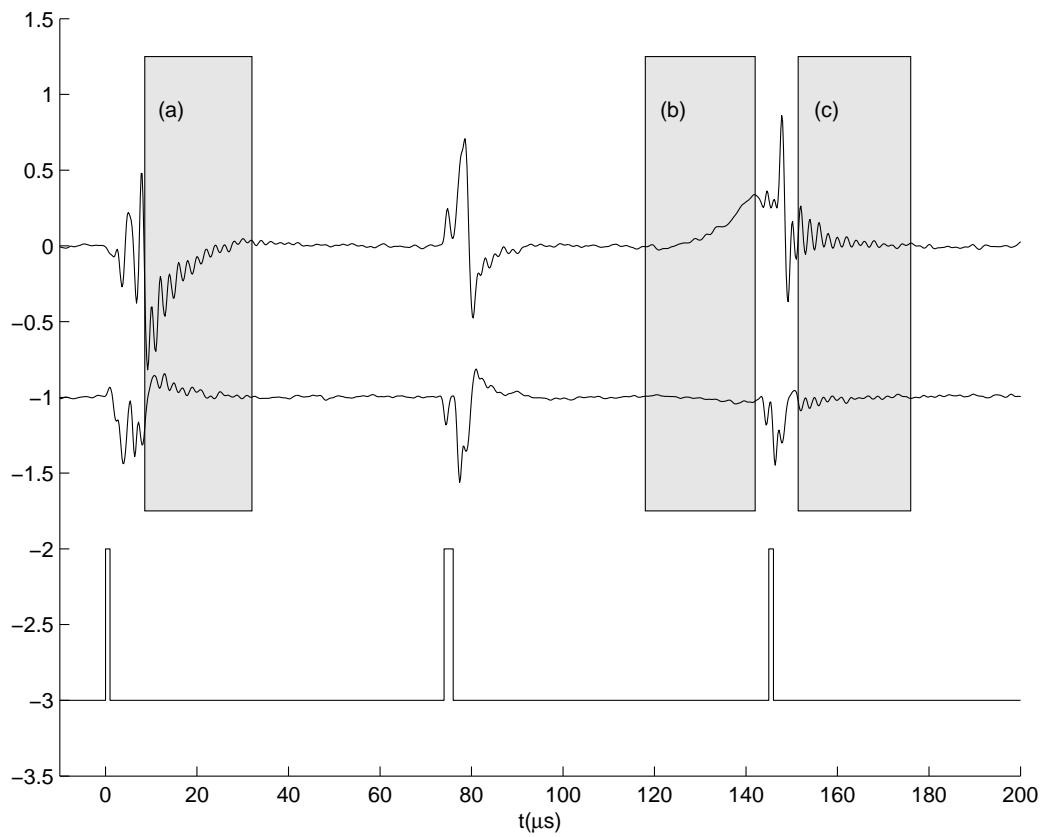


Figure 5.13: The results of a quantum state tomography sequence. In the top trace the amplitude of the coherent emission in phase with the applied light is plotted versus time. The second trace shows the component in quadrature with the applied light. The applied optical pulses saturate the detector which takes $\approx 10\mu\text{s}$ to recover. The positions of the applied light pulses are shown schematically in the third trace. The labels (a), (b) and (c) correspond the snapshots of the Bloch spheres shown in Fig. 5.12. The regions over which the signal was integrated to arrive at measurements are shown in grey.

Input State	Fidelity	Fidelity assuming pure state
$(0\rangle + i 1\rangle)/\sqrt{2}$	0.95	0.95
$(0\rangle + 1\rangle)/\sqrt{2}$	0.95	0.95
$ 0\rangle$	0.96	0.97
$(0\rangle - 1\rangle)/\sqrt{2}$	0.96	0.97
$ 1\rangle$	0.88	0.89
$(0\rangle - i 1\rangle)/\sqrt{2}$	0.88	0.96
$\cos(0.960) 0\rangle + \sin(0.960)\exp(2.60i) 1\rangle$	0.81	0.99

Table 5.2: Fidelity of the combined state preparation and tomography for different input states. Each point was repeated three times and the fidelities reported are the worst of those repeats. The position of the last state on the Bloch sphere corresponds to the position of Canberra on the Earth.

5.5 A four level system for type-II quantum computing

perhaps the simplest way to extend the single qubit demonstrations described above to perform multi-qubit quantum computation is to use more than two levels of each ion. In particular, a four level system is required to encode two qubits. Such an approach doesn't scale very well, as you quickly run out of energy levels and the operations needed to apply simple gates quickly become complicated. However, it is one of the strengths of rare earth quantum computation that quantum information can be stored in the long lived ground state hyperfine levels. It would therefore be desirable to demonstrate this. Furthermore such a four state system would be ideal for the "Type-II" quantum computation described in Sec. 1.6. The large inhomogeneous broadening and the many spectrally resolvable spots in a given crystal provide a wealth of different ways in which the parallelisation required could be carried out. Rare earth ion dopants are competitive materials for classical data storage and signal processing [78] for the same reasons.

The four levels that were investigated are shown in Fig. 3.19. This four level system was chosen to simplify the experimental setup because the frequencies of all the transitions would be within the (a few MHz) bandwidth of an acousto-optic modulator.

Fig. 5.14 shows the spectra of an anti-hole that has been split by a magnetic field. The anti-hole consisted of ions resonant with the laser via the $\pm 5/2 \rightarrow \pm 5/2$ transition. The magnetic field was applied along the crystal's

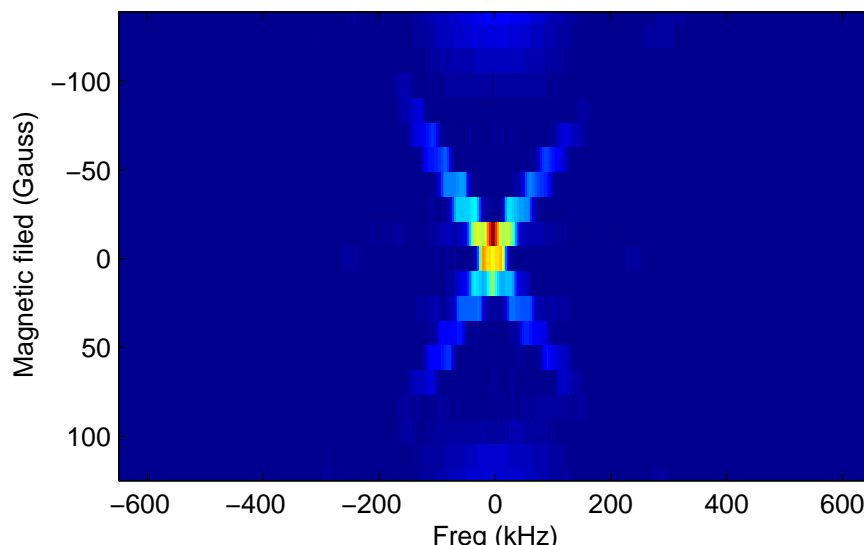


Figure 5.14: The splitting of a square anti-hole by the application of a magnetic field along the C_2 axis. Each horizontal line is from the Fourier transform of a photon echo produced from an anti-hole that had been split with a magnetic field.

C_2 axis and as such the two orientations of ‘site-1’ should behave the same. Four transitions are expected if all the transitions were allowed. However only two were observed. Following this failure to observe all four transitions, a systematic investigation of the hyperfine structure of the ions was carried out. This investigation is described in Sec. 3.2.

5.6 Characterisation of dipole-dipole interactions

Before the work for this thesis took place, a number of experiments had investigated the electric dipole-dipole interactions between rare-earth ions and their role in dephasing due to excitation induced frequency shifts. These experiments have been discussed in Sec. 4.1.1. In this section we report on further experiments to characterise these interactions. These experiments add weight to the conclusions of an already considerable amount of work characterising the ion-ion interactions. Furthermore, the ability to apply accurate pulses enables more direct demonstrations of the phenomena involved than has been possible previously. These include Rabi nutations in the size of the echo produced by one set of ions as the area of a pulse applied to another set of ions is varied. This shows directly that the mechanism causing the echo demolitions is related to the excitation of another group of ions and is the first time in such experiments that a bigger perturbing pulse has led

to a smaller effect on the echo.

The other reason for these investigations was to characterise the ion-ion interactions for this sample and the type of ensembles used. Simple estimates of the interaction strengths based on the expected change in dipole moment and the density of the ions were confirmed. This approach also provided a step-by-step path for approaching the two qubit operations discussed in Sec. 5.7

5.6.1 Instantaneous spectral diffusion on an anti-hole

The first experiments that were carried out in the pursuit of two qubit operations were to measure the coherence times using photon echoes and study how the results varied with the number of ions excited. In order to vary the number of ions excited, the intensities and lengths of the exciting pulses were varied. In all cases the combination of intensities and length were chosen so that the pulse areas for resonant ions were constant. These pulse areas were chosen to be close to the ideal case of $\pi/2$ and π pulses.

Similar measurements have previously been made by Huang et al. [117]. However, in the present case, the measurements were made on an anti-hole rather than a broad part of the inhomogeneous line. Furthermore the use of a highly stabilised laser allowed much longer and weaker pulses to be applied than in previous experiments.

The results are shown in Fig. 5.15. The measurements show the echo amplitude decays fastest (blue) for an unattenuated beam (~ 150 mW) and pulse lengths of $0.6 \mu\text{s}$ and $1.2 \mu\text{s}$. For the other four cases shown the driving beam was attenuated by 10 db, 20 db, 30 db and 40 db. The first pulses were correspondingly $1.8 \mu\text{s}$, $6 \mu\text{s}$, $18 \mu\text{s}$ and $60 \mu\text{s}$. The amplitude of each coloured set of data was scaled so that the fit lines all went through the origin. This early data had a significant noise level in the echo height; this was later improved by grounding the set of XYZ coils in which the sample was mounted. The stark shift makes the transition sensitive to electric field fluctuations and mounting the sample in a copper box proved useful to get the longest coherence times that have been measured [66]. It should be noted that each dot in Fig. 5.15 represents one experimental shot — no averaging was performed.

The slopes for the different length pulses are generally as expected. As the pulses got longer and weaker they excited fewer ions, and this causes less instantaneous spectral diffusion. For the most intense and shortest pulses, the effective T_2 was $375 \mu\text{s}$. The T_2 values were longer for -10 db pulses but then changed little over the next two orders of magnitude. The effective T_2 values

for -10 db, -20 db and -30 db were 940 μs , 780 μs and 1.36 ms respectively. The effective T_2 then jumped significantly between -30 db and -40 db pulses. For the -40 db pulses the decay rate in the echo height was too small to be measured with any sort of accuracy and the slope of the fit was very small and positive. In summary, the excess dephasing rate dropped rapidly, then stayed constant and then finally dropped rapidly again as the pulses were lengthened. This behaviour was attributed to the fact that the measurements were made on an anti-hole and not just part of the inhomogeneous line. The most intense pulses were attributed with exciting both the ions in the anti-hole and the edge of the trenches in which the anti-holes sat. Because of the large number of ions excited there was significant excess dephasing. For the -10 db, -20 db and -30 db pulses, the excess dephasing was relatively constant in spite of the large changes in the spectral width of the exciting pulses. This was because the pulses applied had sufficient spectral width to excite all the ions in the anti-hole but not enough to excite the edges of the trench. The spectral width of the -40 db (60 μs) pulses was ~ 16 kHz, which, because it had reached a size narrower than the width of the feature, means the dephasing rate started decreasing again with the length of the pulses.

5.6.2 Dependence of the first pulse length

As discussed in Sec. 4.1.1, the first pulse in a photon echo sequence doesn't alter the amount of excess dephasing because the frequency shifts caused by the excitation of the ions are rephased. Investigations were carried out to see if this was the case when pulses of definite area were applied. Coherence decay measurements were made for an x - π -echo sequence.

The motivation for this was that with an initial $\pi/2$ pulse the rephasing π pulse causes no change in the populations. Whereas for a smaller initial pulse the rephasing π pulse would cause significant change in the populations. Because of this one might expect faster decay for say $\pi/4$ - π -echo sequences than for $\pi/2$ - π -echo sequences but this belief proved to be erroneous as is discussed below.

The echo height as a function of time for the x - π -echo sequences with $x \in \{\pi/4, \pi/2\}$ are shown in Fig. 5.16. As can be seen from that graph, there is no difference in the behaviour of the two cases except for the obvious constant difference in the size of the echoes.

To see how this is still consistent with the excess dephasing being due to the electric dipole interactions we shall consider the simple case of two ions

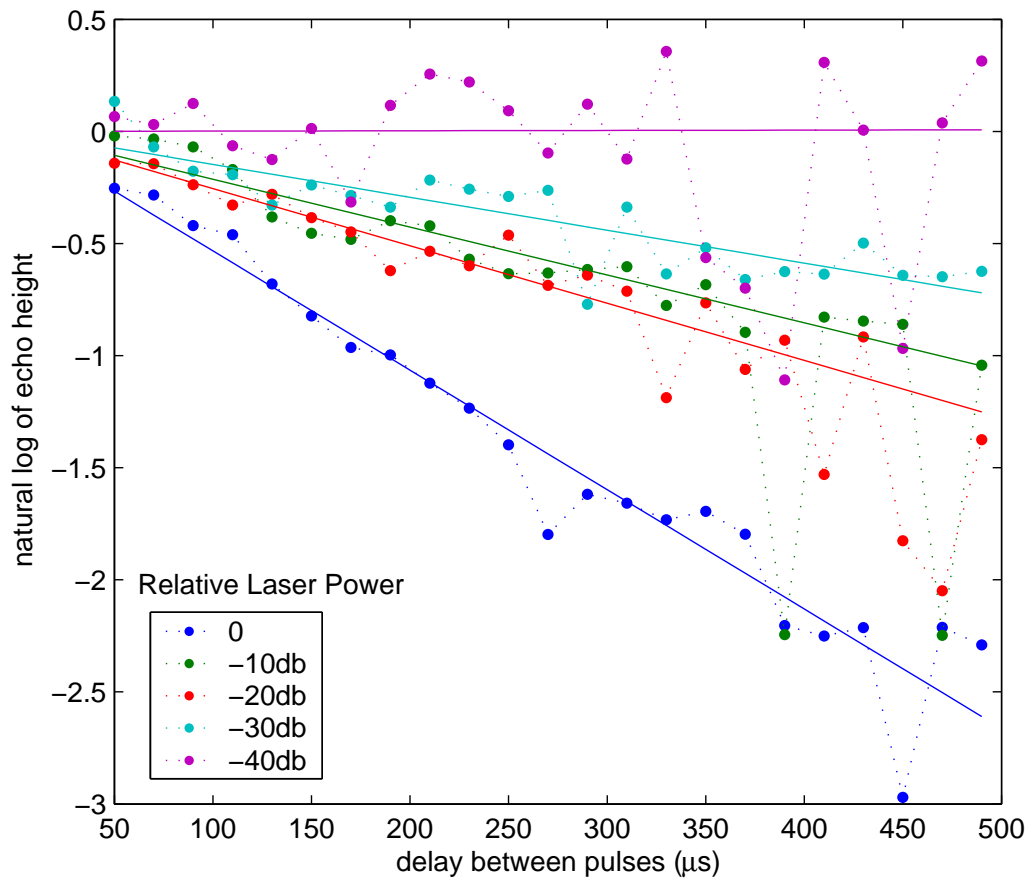


Figure 5.15: Instantaneous spectral diffusion on an anti-hole. The decay in photon echo amplitude as a function of delay time for various intensity pulses is shown. In each case the length of the pulses was chosen so that the areas of the pulses, for resonant ions, were the same.

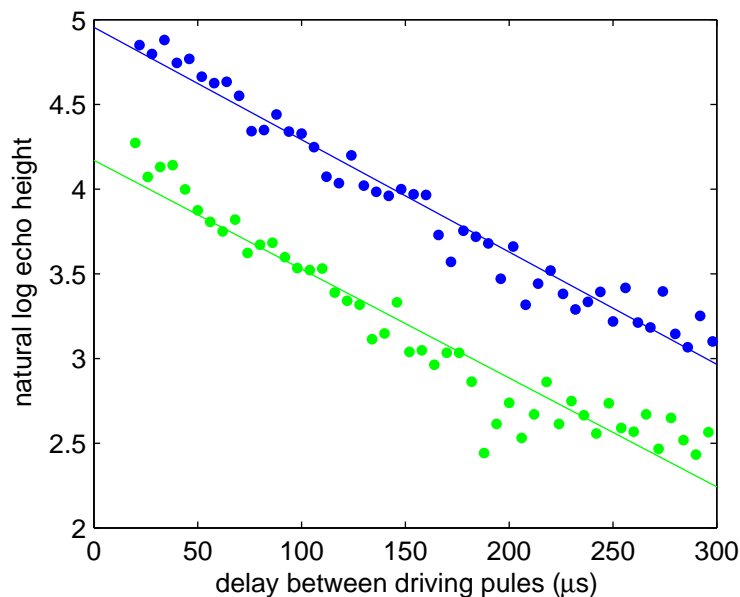


Figure 5.16: The echo decay behaviour for an ensemble to which accurate pulse areas could be applied. The upper (blue) points are for a $\pi/2$ - π -echo sequence and the lower (green) for a $\pi/4$ - π -echo sequence.

in the ensemble that interact with one another with the Hamiltonian

$$H_{\text{int}} = \delta |ee\rangle \langle ee| \quad (5.5)$$

This is equivalent to Eq. 4.12, except that a different interaction picture has been chosen and we have neglected inhomogeneous broadening. Inhomogeneous broadening is important of course, with slight complication it could be added to this treatment. The final result would remain unchanged. After the application of the initial pulse, with area θ the state of the system is

$$\left(\cos \frac{\theta}{2} |g\rangle + \sin \frac{\theta}{2} |e\rangle \right) \otimes \left(\cos \frac{\theta}{2} |g\rangle + \sin \frac{\theta}{2} |e\rangle \right) \quad (5.6)$$

$$= \cos^2 \frac{\theta}{2} |gg\rangle + \cos \frac{\theta}{2} \sin \frac{\theta}{2} (|ge\rangle + |eg\rangle) + \sin^2 \frac{\theta}{2} |ee\rangle \quad (5.7)$$

After a wait of Δt the interaction has caused a rotation of the $|ee\rangle$ component of the state. Thus just before the application of the rephasing π pulse the state is

$$\cos^2 \frac{\theta}{2} |gg\rangle + \cos \frac{\theta}{2} \sin \frac{\theta}{2} (|ge\rangle + |eg\rangle) + e^{-i\delta\Delta t} \sin^2 \frac{\theta}{2} |ee\rangle \quad (5.8)$$

The π pulse just swaps the roles of $|g\rangle$ and $|e\rangle$ leading to the state after

the π pulse of

$$\cos^2 \frac{\theta}{2} |ee\rangle + \cos \frac{\theta}{2} \sin \frac{\theta}{2} (|ge\rangle + |eg\rangle) + e^{-i\delta\Delta t} \sin^2 \frac{\theta}{2} |gg\rangle \quad (5.9)$$

There is then another period of Δt before the echo forms as the ensemble rephases, this leads to the state of the two ions at the time of the echo being

$$e^{-i\delta\Delta t} \cos^2 \frac{\theta}{2} |ee\rangle + \cos \frac{\theta}{2} \sin \frac{\theta}{2} (|ge\rangle + |eg\rangle) + e^{-i\delta\Delta t} \sin^2 \frac{\theta}{2} |gg\rangle \quad (5.10)$$

In order to calculate the complex valued echo amplitude we take the expectation value of $\sigma_1^+ = (X_1 + iY_1)/2$. As the roles of the two ions are symmetric the same result is gained for σ_2^+ . The expectation value gives

$$\langle X \rangle + i \langle Y \rangle = \sin(\theta) \exp(-i\delta\Delta t) \quad (5.11)$$

Integrating this result over the range of interactions strengths δ we find two things. Firstly, as expected, the echo decays with increasing Δt . Secondly, the size of the first pulse, θ , in no way influences the nature of this decay. It simply scales the size of the echo in a manner independent of delay, as was observed.

5.6.3 Echo demolition

The rest of the results discussed in this chapter concern experiments that used two anti-holes. In the rest of this section the experiments which investigated the electric dipole-dipole interaction between two anti-holes are described.

In these experiments, the inter-anti-hole interactions were of random strength. Because of this, the effect of shifts caused by the interactions only cause a dephasing of the ensembles. This was observed by applying a photon echo sequence to one anti-hole (the target) and recording how the height of the echo was affected by manipulating the second anti-hole (the control).

The anti-holes were made using the CW process described in Sec 5.3.2. The zero area pulses described in Sec 5.3.1 weren't used, primarily to reduce the level of complexity. The burn back beam was on for 3 seconds and the spectral width of the resulting anti-hole was controlled by varying the intensity of this beam. Narrow (~ 50 kHz) control ensembles were used in order to minimise the effect of interactions between the ions in the target anti-hole. In order that the interactions between the control and the target be as large as possible, the width of the control was chosen to be as large as the available Rabi frequency allowed. Generally anti-holes of the order of

200 kHz wide were used.

There are a number of factors to consider when deciding how far apart in frequency the two anti-holes should be. Obviously they should be far enough apart that the pulses intended to address one anti-hole do not excite the other. However if the anti-holes are too far apart then problems of beam overlap become significant. Taking into account these concerns, a separation of 5 MHz was initially used. However, this precise value was problematic because of a coincidence in the hyperfine transition frequencies. The difference in frequencies between the $\pm 5/2(\text{gs}) \rightarrow \pm 3/2(\text{es})$ transition and the $\pm 1/2(\text{gs}) \rightarrow \pm 1/2(\text{es})$ transition was approximately 5 MHz (see Table 5.1). This means that applying the beam to “burn back” ions into the lower frequency anti-hole drives the transition $\pm 5/2(\text{gs}) \rightarrow \pm 3/2(\text{es})$ on the higher frequency anti-hole. To avoid this problem a frequency separation of 3 MHz was used. This separation was many times the 210 kHz Rabi frequencies used.

5.6.4 Perturbing pulse position dependence

The first two anti-hole experiments carried out investigated the effects of exciting the control at either the beginning of the pulse sequence, exciting the control at the middle of the pulse sequence or not exciting the control anti-hole at all. The results of these measurements are shown as the delay between the pulses was varied. Figure 5.17 shows the results of these measurements as the delay between the photon echo driving pulses was varied.

It is characteristic of instantaneous spectral diffusion that the echo height is much less sensitive to the size of the first pulse of a photon echo sequence than the second. The explanation in terms of electric dipole-dipole interactions is that exciting an ion causes a random frequency shift in its neighbours. So long as population decay for the perturbing ions is not important, the frequency shifts that are induced by the first pulse are rephased. The frequency shifts induced by the second pulse break the symmetry between the two time periods in the photon echo sequence and therefore can significantly affect the size of the echo.

In this experiment the perturbing pulses were applied at a different frequency and to a different ensemble of ions than those creating the echo. However, exactly the same argument applies and Fig. 5.17 shows that perturbing at the start of the pulse sequence had no effect except for times significant when compared to the excited state lifetime. However, just as in the previous case, exciting the control at the middle of the pulse sequence causes a significant reduction in the echo amplitude because the frequency

shifts induced are in place for only half of the photon echo sequence. The fact that a reduction of $1/e$ in the echo heights is caused by the interaction being on for $\sim 500 \mu\text{s}$ indicates that $1/(500 \mu\text{s}) = 2 \text{ kHz}$ is some sort of representative value for the interaction between the ions of the control and the target. Assuming the control ensemble contains 10^{-6} of the total ion density, then the mean separation between the ions in the control ensemble would be of the order of

$$\begin{aligned} \text{mean inter-particle distance} &= (\text{separation for nearest neighbours}) \\ &\quad \times (\text{fraction of dopant ions})^{-\frac{1}{3}} \end{aligned} \quad (5.12)$$

$$\sim 1 \text{ \AA} \times \left(\frac{0.1\%}{100\%} \times 10^{-6} \right)^{-\frac{1}{3}} \quad (5.13)$$

$$= 100 \text{ nm} \quad (5.14)$$

This interaction strength is therefore similar to what one would expect theoretically if the stark shift in this material was the same as for Eu:YAlO_3 (see Sec. 4.1.1).

5.6.5 Perturbing pulse length dependence

Here we describe experiments in which a photon echo sequence was applied to the target anti-hole and the length of the perturbing pulse applied to the control anti-hole pulse was varied. The pulse sequence that was used is shown in Fig. 5.18. Because accurate area pulses could be applied, it was possible to observe Rabi nutations of the control anti-hole in the amplitude of the echo produced by the target ions. This is only one step away from quantum logic operations. If there was just one particular interaction strength between the ions in the control and the target. In particular one would see a phase shift in the echo rather than its demolition.

Figure 5.19 shows the echo decay versus delay between the pulses for the cases of no perturbation, perturbation with a π pulse and perturbation with a 2π . If the perturbation pulses were ideal, one would expect that the perturbation by a 2π pulse to have no measurable effect on the size of the echo. By the end of the pulse the ions would all be placed in the ground state. The frequencies of the target ions would only be affected during the length of the perturbing pulse which is too short for any appreciable dephasing to occur. This effect is seen in Fig. 5.19 with the 2π pulses having a much smaller effect on the echo amplitude than the π pulses. The modulation in the echo height as the delay increased was tentatively attributed to a background magnetic field slightly lifting the $\pm x/2$ degeneracies in the hyperfine levels.

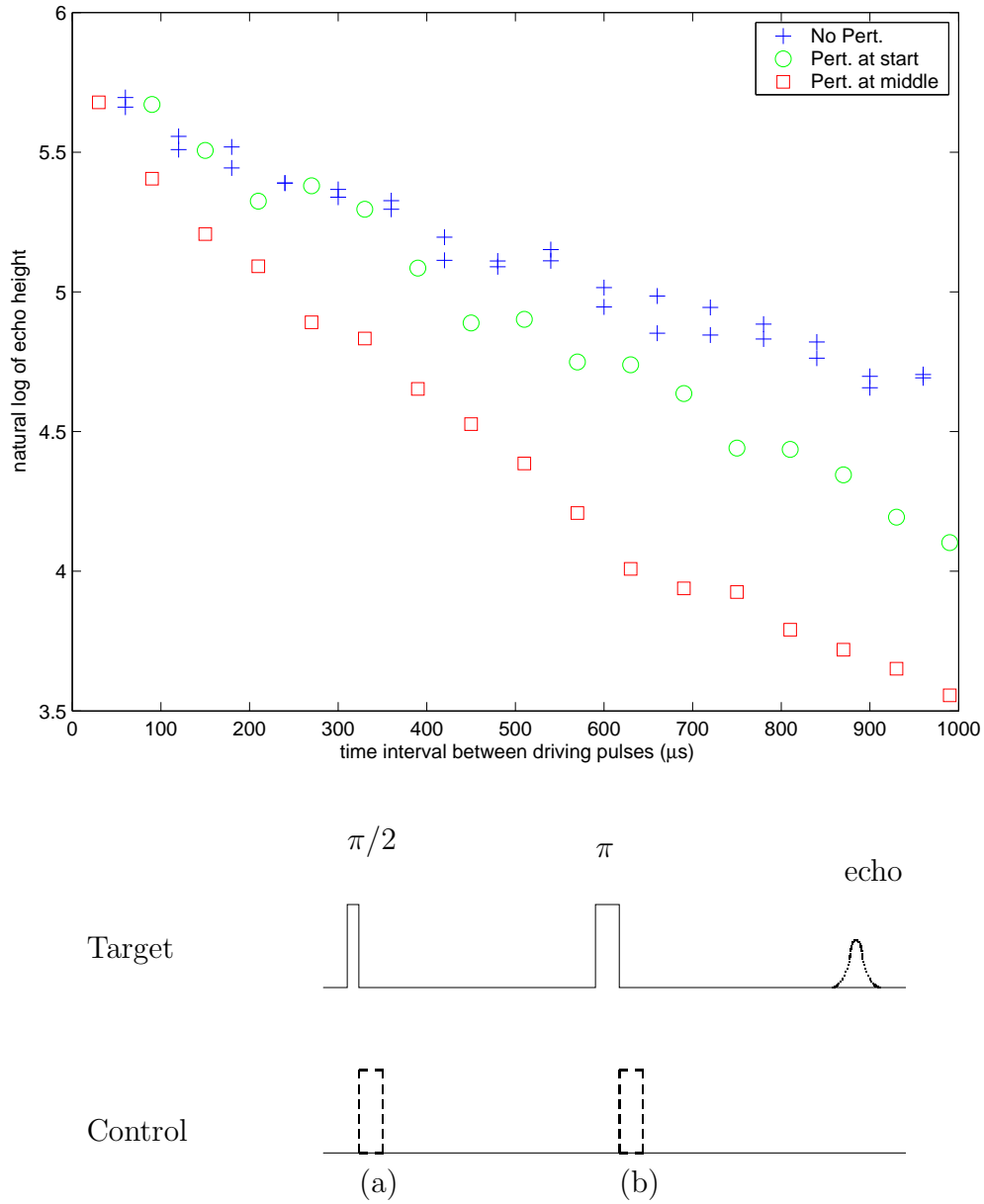


Figure 5.17: The effect on the size of the echo produced by the target anti-hole by exciting the control anti-hole at various positions. A photon echo sequence is applied to the target anti-hole. The control anti-hole is excited either (a) at the beginning of the sequence, (b) at the middle, or not excited at all. Each point corresponds to one experimental shot.

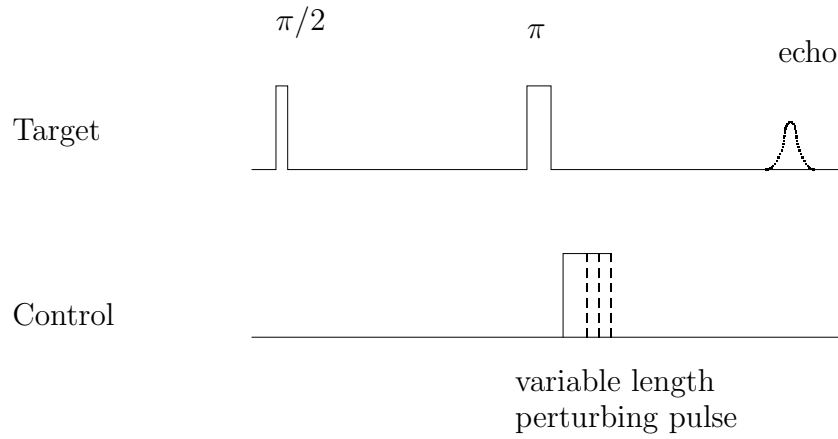


Figure 5.18: Pulse sequence used to collect the results shown in Figs. 5.19 and 5.20. A photon echo sequence was applied to the target ions. Immediately after the π pulse of this sequence, a perturbing pulse of varying length was applied to the control anti-hole.

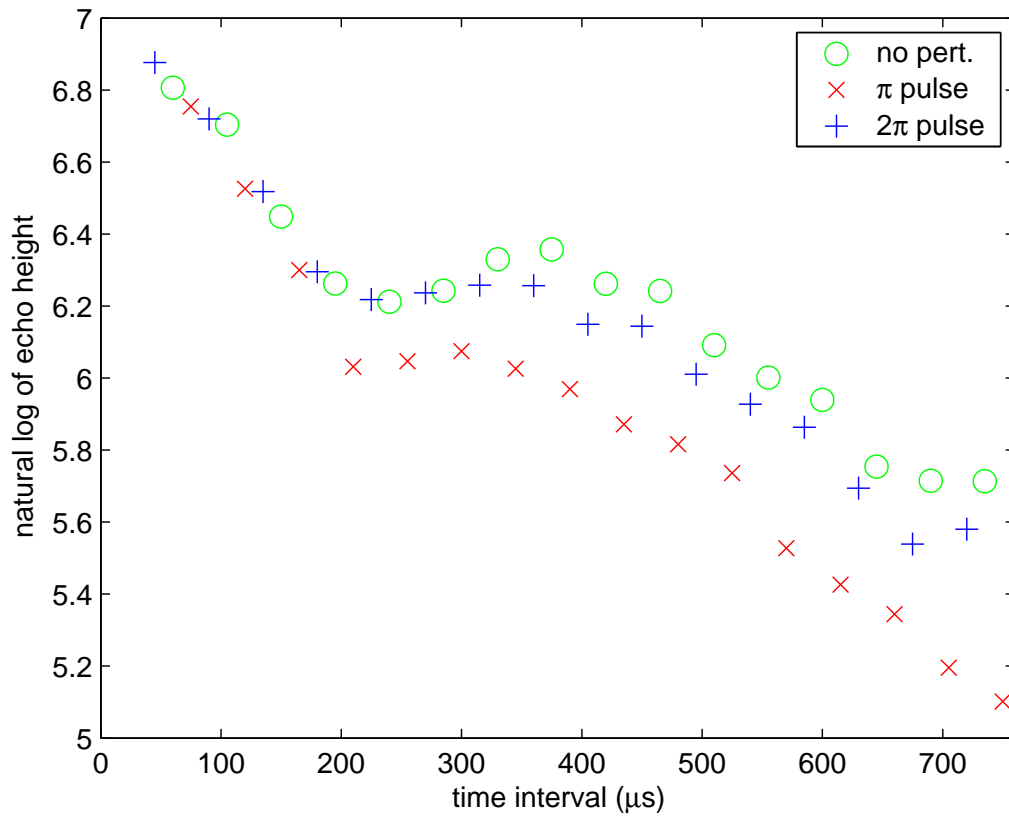


Figure 5.19: Echo amplitude as a function of delay between the two pulses. Three cases are shown. These are where the target ions were perturbed with a π pulse applied to the control, perturbed with a 2π pulse and not perturbed. Rabi frequency spread for the control anti-hole had been reduced with 10 2π pulses. The modulation in the echo height as the delay increased was attributed to a background magnetic field slightly lifting the $\pm x/2$ degeneracies in the hyperfine levels.

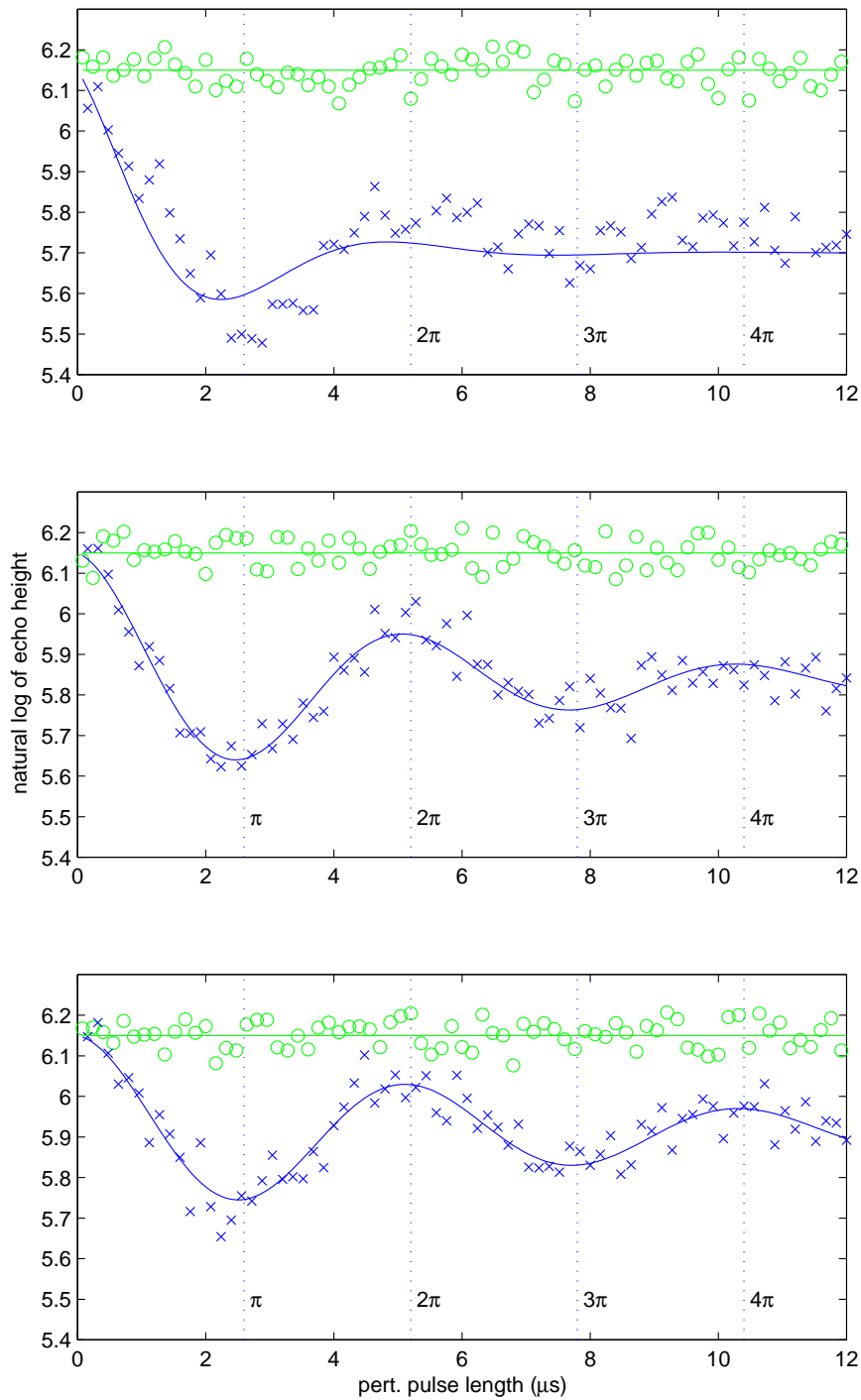


Figure 5.20: Nutation in the size of the echo produced by the target anti-hole as the length of the perturbing pulse applied to the control is varied. The measurements were made alternating between the blue crosses, which represent where the perturbation was applied and the green circles where the perturbing pulse was not applied. In the top graph nothing was done to the anti-hole to select ions with a particular Rabi frequency. In the middle and bottom graphs 4 and 10 ' 2π ' pulses were used respectively.

The application of a small magnetic field changed the rate of the modulation.

To obtain the results presented in Fig. 5.20, the delay between the photon echo pulses was fixed at $500 \mu\text{s}$ and the length of the perturbing pulse varied. It is instructive to compare the Rabi nutation measured in this indirect manner with the more direct measurements for a single anti-hole of Sec. 5.3.3. It should be noted in this case the measurement being made of the control anti-hole is the degree of excitation — this is maximum for pulse areas of $(2n + 1)\pi$. In Sec. 5.3.3, the coherence was measured. This attains its maximum absolute values for pulse areas of $(n + \frac{1}{2})\pi$. It should be noted that for the measurements of Sec. 5.3.3 the beam size at the sample and the laser power were different and therefore the Rabi frequencies were different also.

In the case depicted in the top graph of Fig. 5.20 no 2π pulses were applied in the preparation of the control anti-hole. Due to the variation in intensity across the beam, the distribution of Rabi frequencies was therefore large. A small hint of a nutation can be seen, but the effect is washed out much beyond a π pulse. This is similar to the sort of nutations seen in Fig. 5.10. In that figure one can see the outcomes of direct measurements made on an anti-hole that was prepared without 2π pulses. In Fig. 5.20 the results are shown with the exponentially damped cosine wave that best fits the data. For the top graph, the distribution of Rabi frequencies is such that there is not a particularly good fit.

In the cases depicted by the lower two graphs of Fig. 5.20, 4 (middle) and 10 (bottom) 2π pulses were applied to the control. As the number of these pulses applied to the control ensemble increased the nutation became more pronounced. The recovery of the echo for a 2π perturbing pulse was significantly larger in the case of an anti-hole prepared with ten 2π pulses than one prepared with four. The more 2π pulses that are applied to the control anti-hole, the less ions it will contain. As a result the magnitude of the echo demolition for a perturbing π pulse decreased as the number of 2π pulses applied increased.

5.6.6 Rephasing of the interaction induced decoherence

If the accumulated phase shifts due to the interactions are the same in both periods of free evolution of the photon echo sequence then the effect of the interaction should be rephased. This is illustrated by the experiments where the perturbing pulse was applied at either the middle or the end of a photon

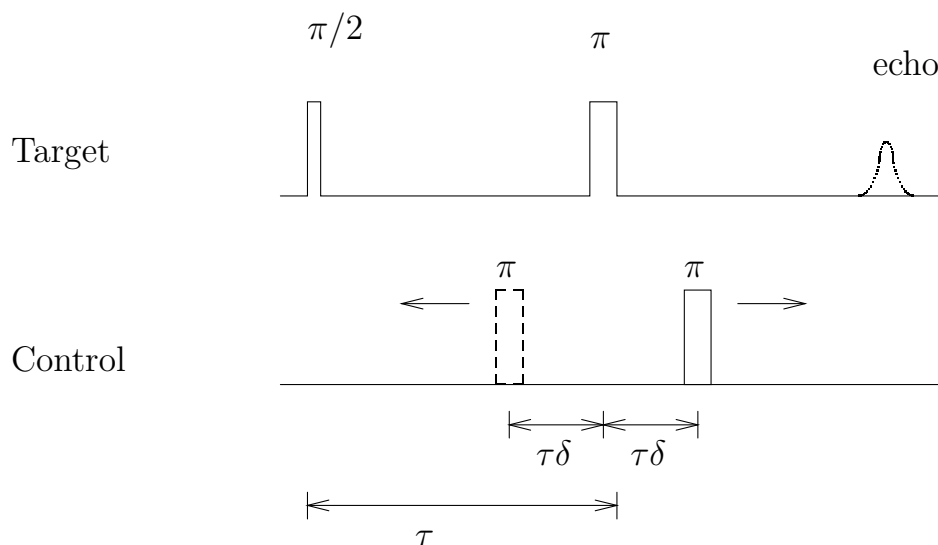


Figure 5.21: Pulse sequence used to demonstrate the recovery of the photon echoes when the two periods of free evolution in the photon echo sequence are equivalent. A series of shots were taken as the value of δ was increased from zero to one. The shots alternated between having no perturbing pulses applied, having just the later perturbing pulse applied and having both perturbing pulses applied. The delay between the two driving pulses of the photon echo, τ , was $400 \mu\text{s}$. The results are presented in Fig. 5.22.

echo sequence (see Fig. 5.17). With the command that we had over the state of the control anti-hole it was possible to demonstrate this rephasing when the effect of the interaction wasn't constant during the entire pulse sequence. These experiments were useful because they provided a measure of how well the single qubit operations could be applied to the wide control anti-hole. Furthermore they were arrived at by looking at the effect on the target anti-hole. Thus, the measurements were sensitive to the imperfections in the control pulses in a manner similar to potential quantum computation demonstrations.

Experiments with a similar theme have been carried out by Altner and Mitsunaga [154] but instead of coherent control over the perturbing ensemble they used a co-doped sample. Ions with long coherence times were used for the target ions and ions with a much shorter lifetime were used for the control. The symmetry between the two periods of free evolution of the photon echo was achieved by having the lifetime of the perturbing ions short compared to the length of these periods of evolution.

The pulse sequence that was used is shown in Fig. 5.21 and the results in Fig. 5.22.

In the case of one perturbing pulse (red dots of Fig. 5.22) the behaviour is easy to understand. As δ is increased the length of time for which the control ions are excited reduces. The interaction therefore causes less

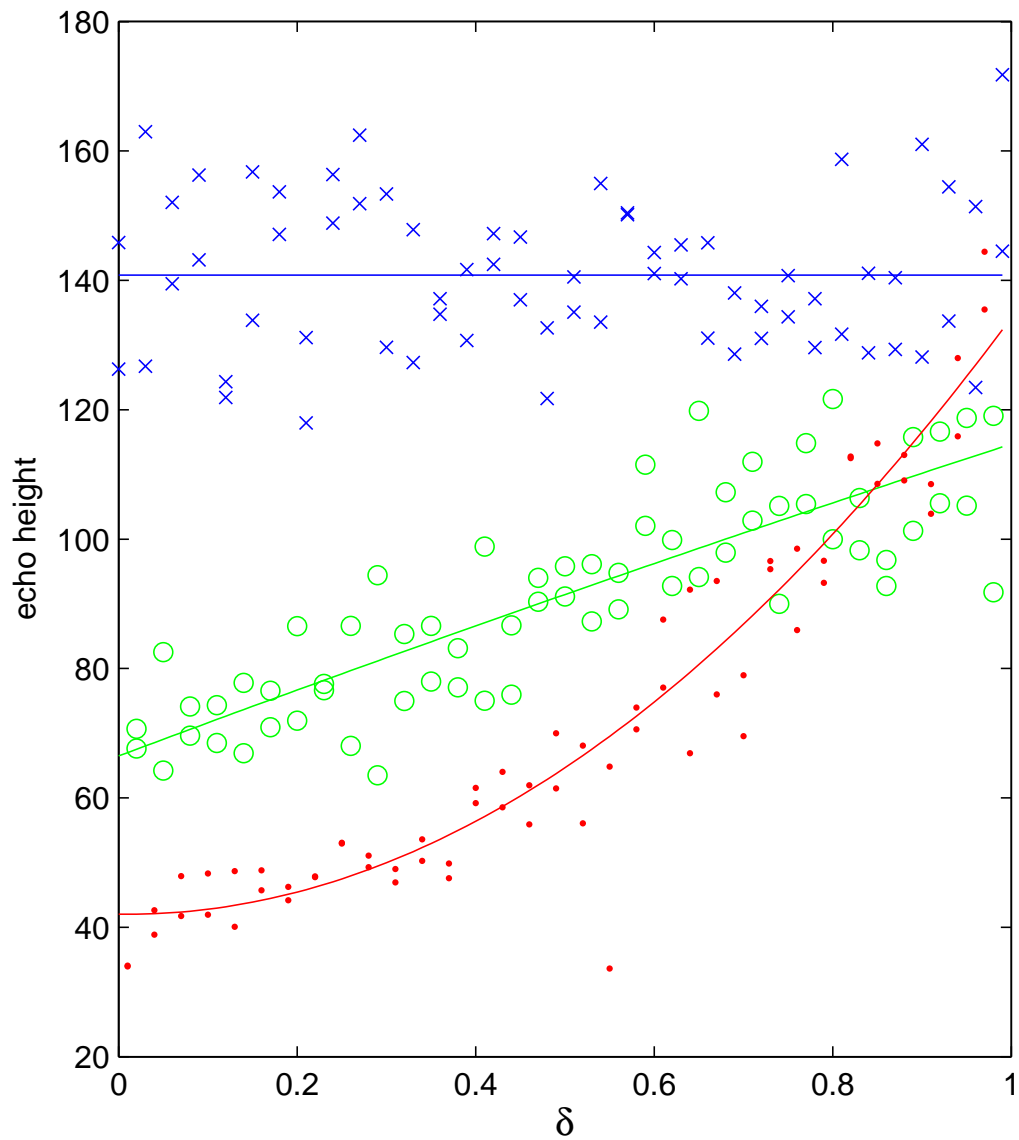


Figure 5.22: Echo recovery. The results obtained using the pulse sequence of Fig. 5.21. The dots (red) correspond to applying only the latter perturbing pulse and the open circles (green) to applying both perturbing pulses. The blue crosses correspond to when no perturbing pulses were applied. The blue line shows the mean echo height in the absence of perturbing pulses. The other two lines are least squares fits of an arbitrary quadratic to the data.

decoherence.

The experimental points represented by open circles (green) in Fig. 5.22 correspond to the application of both of the perturbation pulses, depicted in Fig. 5.21.

If the first perturbing pulses were an ideal π pulse for all of the control ensemble, then the first pulse would put all of the control ensemble into the excited state, then the second would put them all back in the ground state. As a result, each of the free evolution periods in the photon echo sequence would have the control ensemble excited for a fraction δ of the time. This should result in no echo demolition because the effect of the interactions should be rephased. The phase shift due to the interaction accumulated by the target ions during each half of the photon echo sequence would be the same.

In practice, the echoes from the target ions when the control ions had been addressed twice (open circles Fig. 5.22) were smaller than those when the control ions were left untouched (blue crosses). The main contribution to the asymmetry that caused the reduction in the echo heights was the imperfection in the π pulses. The 210 kHz Rabi frequency used was about the same as the spectral width of the control anti-hole, rather than being much bigger.

For the smaller values of delta, the primary reason for this asymmetry was the fact that all control ions were not placed perfectly into the ground state by the second pulse. As delta was increased, the length of time after the second pulse decreased and this resulted in the echo heights represented by open circles (green) getting larger. Neglecting population decay, the periods of each photon echo sequence during which the ions were excited were the same even with imperfect π pulses on the control.

However for larger values of delta, when the fraction of time spent with the excited control ions excited was largest, population decay became more important. This means that at $\delta = 1$, the echo heights represented by open circles (green) do not reach those of the unperturbed echoes unlike the singly perturbed echoes, which are shown as dots (red).

How much closer the open circles (green) in Fig. 5.22 are to the crosses (blue) than to the dots (red) is a measure of the echo recovery. In this case, the echo recovery was much smaller than in the experiments depicted in the lower graph in Fig. 5.20 (Sec. 5.6.5). In those experiments, a perturbing π pulse caused significant echo demolition whereas the echo height after a 2π perturbation was almost the same as the unperturbed height. This is primarily a consequence of how the ensembles were prepared. The ' 2π ' pulses

that were applied to the anti-holes are intended to select out ions based on their Rabi frequencies. For ensembles with spectral width small compared to the Rabi frequency this would occur. However, for ensembles where the spectral width of the ensemble was comparable to the Rabi frequency one must remember that the selection of ions was based on their *generalised* Rabi frequency. Keeping this in mind it is easy to see why the 2π pulses did a better job of putting ions back in the ground state than two separated π pulses did. We chose our ensembles so they would consist of ions that ended up back in the ground state at the end of a ' 2π ' pulse. Another contributing factor to the smaller recovery in Fig. 5.22 was the use of ensembles for the control anti-hole that were wider in frequency. This can be seen in the larger amount of echo demolition that occurred when a π pulse was applied to the control ensemble half way through an echo sequence on the control.

5.7 Conditional phase shifts

The experiments discussed in the previous section demonstrate that the interaction between the ions is coherent, although inhomogeneous. The experiments also show that the control ensembles used above had a (spatial) ion density large enough for the average interaction with the ions of the target ensembles to be observable over the homogeneous linewidth.

The only problem left to overcome in order to carry out quantum logic operations concerns the inhomogeneity in the interaction strength. This inhomogeneity was tackled using spectral holeburning techniques. Pryde et al. were the first to use spectral holeburning to select for something other than frequency with the use of ' 2π ' pulses to select for the Rabi frequency experienced by ions. Here we extend spectral holeburning further to select ions based on their interactions with other ions. The pulse sequence used for selecting the ions is shown in Fig. 4.3 on page 101 and the method for this selection process is discussed in Sec. 4.5.

Composite pulses [30] were used for the pulses applied to the control ensemble in order to make better use of the limited Rabi frequency available. With composite pulses, a number of pulses of various amplitudes and phases are applied one after another. The result is intended to better approximate the intended pulse over a range of detunings and driving strengths. The use of composite pulse sequences in quantum computing generally has been investigated by Jones and co-workers [140]. To the author's knowledge the present work is the first time that composite pulses have been used on an optical transition. The composite pulses were used in place of the π pulses

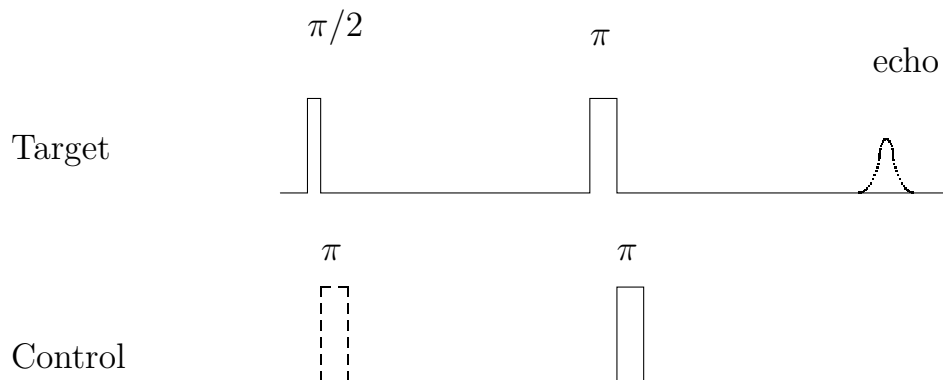


Figure 5.23: Pulse sequence used to demonstrate conditional phase shifts once the target ions had been selected based on the interaction strength. The delay between the driving pulses for the target ions was $60 \mu\text{s}$. The phase difference in the echo conditional on whether the first π is applied to the control ions is shown in Fig. 5.24. Composite pulses were used for the operations on the control ensemble (see text).

to the control anti-hole. It consisted of a conventional π pulse that was split into two $\pi/2$ pulses, and a π pulse that was shifted by 90° was inserted in the middle. No systematic investigations of the benefits of using composite pulses were conducted but quick checks, similar to the $\delta = 0$ case for the experiments of Sec. 5.6.6, were made. These showed that the use of composite pulses resulted in a measurable, if not a substantial, improvement.

The two anti-holes used for the results presented in this section were prepared in the same manner as described in Sec. 5.6.3. Five $4.8 \mu\text{s}$ long ‘ 2π ’ pulses were applied to both the control and the target anti-holes in order to select out ions with a particular Rabi frequency. This was followed by five applications of the pulse sequence shown in Fig. 4.3 to select ions from the target anti-hole that only experienced a particular interaction with those of the control anti-hole. As mentioned above, composite pulses were used for the control anti-hole. It was not possible in practice to drive both anti-holes at the same time so when the pulse sequence required pulses to be applied to both anti-holes at the same time, the pulses to the control anti-hole were applied directly after those to the target. The timing error introduced was small compared to the periods of time over which the interaction was significant.

The value of Δt (see Fig. 4.3) chosen was $60 \mu\text{s}$ and the delay between the application of successive pulse sequences was 10 ms.

The pulse sequence used to demonstrate the conditional phase shift is shown in Fig. 5.23. This is very similar to the CNOT sequence of Fig. 4.3 except the pulses at the end of the sequence were not applied. The state of the control ions was not measured so it was of little value to apply a

single qubit operation to them at the end of the sequence. Also, the laser pulse required to achieve this would have interfered with the measurements of the target ensemble. The measurements of the ions which could be made were of coherence so there was little to be gained by applying a $\pi/2$ pulse to convert the accumulated phase shift into a population difference, because the application of a subsequent $\pi/2$ pulse would be required to measure such a difference. As with the pulse sequences used for selecting the ions based on their interaction strength, composite π pulses were used on the control ions.

The pulse sequence used — if we ignore the pulse represented with a dotted line for a moment — can be interpreted as a CNOT gate minus single qubit operations at the end of the sequence. Alternatively, if the first $\pi/2$ pulse applied to the target ions is viewed as state preparation performed prior to the gate operation, the pulse sequence can be viewed as carrying out a phase-gate operation. The difference between a phase-gate and a CNOT is, of course, a Hadamard gate ($\pi/2$ pulse) applied to the target qubit on either end [31]. The first π in the pulse sequence for the control qubit (represented with a dotted line) was applied when it was desired to investigate the effect of the gate with an initially excited control qubit.

To obtain the results shown in Fig. 5.24 the gate operation was carried out 26 times and on alternate shots the gate was carried out with the control ions initially excited. The echoes were averaged in a phase coherent manner and the envelope and phases for the two cases (control initially excited or not) are shown. When each of the echoes measured was integrated, the mean phase shift between the two cases was 17.9° . From the scatter in the phases of the echoes an uncertainty in this phase shift of $\pm 2.3^\circ$ was inferred. Control experiments were carried out where the control ions were burnt away before readout and where no pulses were applied to the control ions during the readout. In both cases no phase shift was observed. The phase of the echo signal changed across the echo because of the spectral profile of the target. The imperfections of the pulses used in the pulse sequence for interaction strength burning meant that target ions were selected on their resonant frequency as well as their interaction with the control ions. The phase varied across the echo in the same manner as in the control experiments where no pulses were applied to the control ions.

5.7.1 Limiting factors

A conditional phase shift of 180° would be required for gate operation with high fidelity rather than the 20° that was observed in the experiments. This poor fidelity is due to purely technical reasons and significant improvement

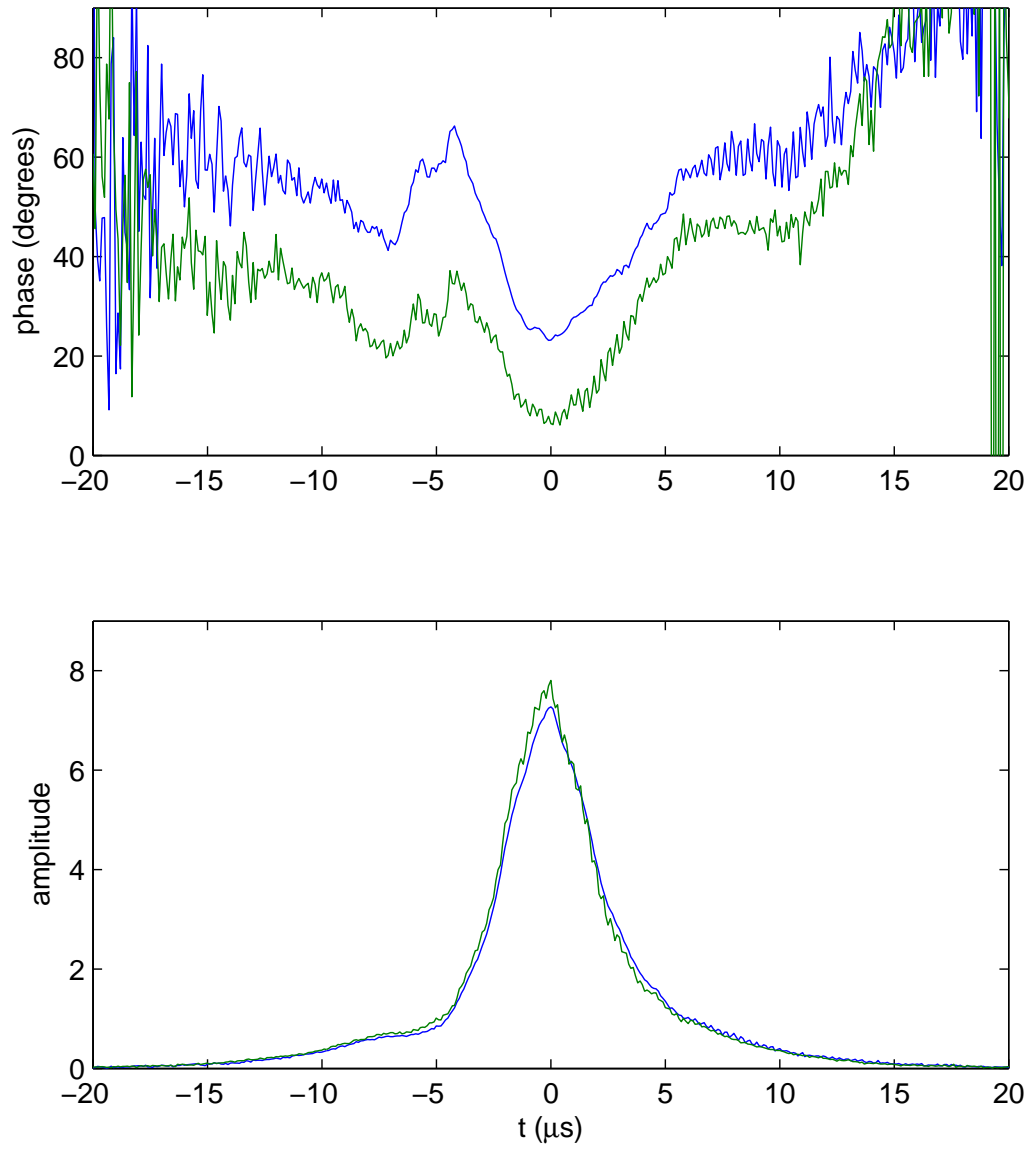


Figure 5.24: The amplitude and phase for the echoes produced by the target ions when the control ions were initially in the excited state (green) or the ground state (blue).

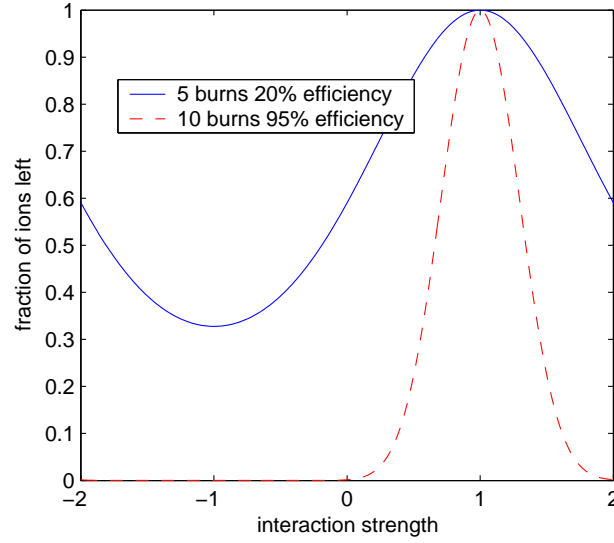


Figure 5.25: The fraction of ions left in a target anti-hole as a function of their interaction strength with the ions of the control. Five interaction strength burns and 20% holeburning efficiency are similar parameters to those used for the observation of the conditional phase shift. In order to obtain an ensemble with a better defined interaction strength with the control ions, either more interaction strength burns or a larger holeburning efficiency is required.

should be possible.

The small phase shift was attributed to the small number of interaction strength selecting pulse sequences that were applied. If a large number of interaction strength selecting pulse sequences were used, then a very particular interaction strength would result. With the small number of interaction strength burns applied and the low ($\sim 20\%$) holeburning efficiency, the interaction strength was not particularly well defined. The problem restricting the number of interaction strength selecting pulse sequences was the fidelity of the single qubit operation. An estimate of the resulting distribution of interaction strengths, for perfect single qubit operations, is shown in Fig. 5.25. In order to obtain an ensemble with a better defined interaction strength, more interaction strength selecting pulse sequences and/or a higher holeburning efficiency would be required. There are a number of simple measures which should result in significant improvement in both of these areas.

5.7.2 Realising larger conditional phase shifts

As discussed above, the small conditional phase shift was the result of the experiments being restricted to a small number of interaction strength selecting pulse sequences and the low holeburning efficiency. The experiment was carried out using the $\pm 5/2$ levels in both the ground and excited states. The

holeburning efficiency was low because ions that were left in the $\pm 5/2$ excited states at the end of an operation spontaneously emitted — into the $\pm 5/2$ ground states predominantly rather than into the other hyperfine levels. One possibility for improving this situation is to use, for example, the $\pm 1/2$ hyperfine levels for the excited state. While the holeburning efficiency would be higher, the oscillator strength for the $\pm 5/2 \rightarrow \pm 1/2$ transition would be correspondingly lower. This lower oscillator strength would result in lower Rabi frequencies which is undesirable as is discussed below. One way to improve the holeburning efficiency without introducing this problem would be to drive an excited state hyperfine transition with a RF π after the unwanted ions had been left to decay. For this to be useful the Rabi frequencies obtainable would need to be higher than the optical decay rates. Using 1 kHz/G (see Sec. 3.2) for the Zeeman splitting, one can estimate that a RF amplitude of 10 G would be required to obtain a 10 kHz Rabi frequency. With a big amplifier and a resonant coil such amplitudes are available experimentally.

The problem restricting the number of interaction strength selecting pulse sequences was the accuracy to which single qubit operations could be applied to the spectrally wide anti-holes.

Wide spectral features are required for the spatial ion density to be high, which is in turn required so the mean interaction between ions in such features is high. In order to apply pulses which achieve the same operation for all the ions of an inhomogeneously broadened ensemble, the pulse length must be short compared to the inverse of the spectral width. The Rabi frequencies provided by the laser only enabled this criterion to be achieved approximately. The two ways to increase the Rabi frequency are to either increase the laser power or reduce the spot size. Laser powers greater than the ~ 200 mW used in these experiments have been generated from dye lasers. However, the easiest way to increase the intensity at the sample would be to use a smaller spot size. For the experiments described in this section the laser was focused onto the sample with a 15 cm lens; Rabi frequencies of ~ 210 kHz resulted. Initially experiments were attempted with a 10 cm lens which resulted in Rabi frequencies of ~ 400 kHz. However the resulting higher intensities were incorrectly considered responsible for the “5 MHz problem” discussed in Sec. 5.6.3. The ability to apply definite area pulses would be helped by the square features provided by the zero area pulses mentioned in Sec. 5.3.1. The fact that the use of composite pulses only slightly increased the ability to perform the single qubit operations suggests possible problems with the background level of ions, or the presence of long tails on the anti-holes, or both. The zero area pulses are good at getting rid of such problems.

There is nothing that stopped these being used in these experiments other than the desire to keep the setup as simple as possible coupled with the lack of a small amount of extra equipment.

Composite pulse sequences can be very useful in magnetic resonance experiments when there is inhomogeneity in the transition frequency and driving strengths. The composite pulses used in this experiment were added in an ad hoc fashion and were retained because they improved the performance slightly. A more systematic look at the use of composite pulses than was carried out here would no doubt be useful.

Another way to increase the spatial density of the ions in the anti-holes is to increase the total concentration of dopant ions. It should be noted, however, that increasing the concentration of the ions would also increase strain in the crystal and thus the inhomogeneous broadening. A packet of the same spectral width would, therefore, contain a smaller fraction of the total number of ions than in a sample with a smaller concentration. Further investigation is warranted.

Ideally, the interaction strength burning process should be only limited by the homogeneous line width optical transitions but it is also sensitive to laser jitter. For these experiments the linewidth of the laser was of the order of 200 Hz which is larger than the ~ 100 Hz homogeneous linewidth. A more stable laser would allow smaller interaction strengths to be selected by using longer interaction strength selecting pulse sequences. This would then in turn reduce the spatial ion density required and, as a result, the spectral width of the control anti-hole as well. This would allow more accurate single qubit operations to be applied to the control anti-hole and higher two qubit fidelities would result. However, the benefit of improving the laser frequency stability would diminish quickly as the laser's linewidth approached the homogeneous linewidth of the optical transition.

5.7.3 Tomography

The use of quantum state and process tomographies (see Chapter 1) provide a powerful framework for the description of quantum operations. The application of such two qubit quantum tomographies was considered to characterise our two qubit system. Quantum process tomography on the conditional phase shifts and quantum state tomography on an entangled state made using these phase shifts was considered. However, these experiments were not performed, it was decided that higher fidelities for the conditional phase shift operations should be sought before such work was attempted.

It was initially thought that state tomography along the lines of that

described by Chuang et al. [155] for an NMR system could be used. For the purposes of the tomography the NMR system and our two qubit system are analogous. However, it was realised when investigating the implementation of the tomography that the method did not provide what it advertised. In the paper of Chuang et al., the state was determined by making measurements of the free inductions signals after a number of different combinations of single qubit operations had been applied to the two qubits. They used XI to represent a rotation of $\pi/2$ about the x axis for the first qubit and nothing (the identity) for the second. Chuang's method involved measuring the free induction signals after II , IX , IY , XI , XX , XY , YI , YX and YY . This didn't provide full characterisation of the density matrix as can easily be seen by considering the maximally entangled state $\frac{1}{2}(|0\rangle + |1\rangle) \otimes (|0\rangle + |1\rangle)$. Such a state will give no coherent emission regardless of what single qubit operations are applied to it and is thus indistinguishable from the $T \rightarrow \infty$ thermal state. The least squares means that in the presence of a number of states that fit the data equally well the one with the lowest $\text{Tr}(\rho^2)$ (purity) is used. Chuang's method in effect simply does single qubit tomography for each of the two qubits and then takes the product state. It should be remembered that the state that was being reconstructed by Chuang et al. was a product state so the procedure was accurate for their situation. However it was never stated that this was partial state tomography rather than full state tomography as could be inferred. The paper has been cited widely and the error has been repeated in other works (e.g. [156]).

The difficulty with tomography highlights the physical principal that without either making correlated measurements on the two qubits or using an interaction between them, it is impossible to distinguish entanglement from classical noise. Thus, to carry out full quantum state tomography for the system considered in this chapter, where correlated measurements are impossible, it would be necessary to use the interaction between the qubits. Because the ensemble still contained a relatively broad range of interaction strengths, using these interactions to characterise the system will be problematic until the fidelity is improved.

5.8 The future

Above we have described experiments in which a 17.9° conditional phase shift was observed for two independent qubits (anti-holes). The interaction used was the electric dipole-dipole interaction that usually causes instantaneous spectral diffusion in such systems. A pulse sequence that was developed in

Chapter 4 was used to select ions based on their interactions strength. The limitation in the fidelity of the two qubit operations was how well defined the interactions were for the resulting ensemble. This was in turn related to the holeburning efficiency and how many times the selecting pulse sequence could be applied. There are simple steps that could be taken to substantially improve both of these aspects. With such steps taken fidelities approaching the $\sim 90\%$ achieved in liquid state NMR [157] should be possible.

In order to increase the number of qubits beyond two, the ions' hyperfine structure could be used. The differing timescales for the decoherence could be used to demonstrate teleportation in a similar fashion to NMR [158], in this case the teleportation would be over 10–100 nm rather than between nuclei within the same molecule.

As discussed in Chapter 4 the selecting of sub-ensembles pursued here is not scalable to a large number of qubits. The conditional phase shift is nonetheless an important demonstration, it is the first time that such a conditional phase shift has been observed between independent qubits in a solid. Also discussed in Chapter 4 are a number of exciting possibilities for scalability, in particular the detection of single dopants.

Chapter 6

Summary

This thesis explores and demonstrates the utility of rare earth ion dopants for quantum computing. The experiments performed were broken into two sets. The first are presented in Chapter 3 and relate to the characterisation of the hyperfine structures of rare earth ion dopants. The aim of this work was to provide the information about oscillator strengths and transition frequencies required for the optical manipulation of hyperfine states. The characterisation of $\text{Pr}^{3+}:\text{Y}_2\text{SiO}_5$ was the first time that such information had been gathered in such a low symmetry site. The knowledge gained has enabled an increase in the coherence times of hyperfine transitions by over two orders of magnitude.

The second set of experiments relate to quantum computation demonstrations with optical states. The ability to perform state initialisation and single qubit operations had already been demonstrated in this laboratory when this research began. This left the problems of readout and two qubit operations. Solutions to these two problems were discussed. A discussion of ion interactions in optical centres with emphasis on rare earth ions was presented. Following this and a review of previous schemes, the direction that was pursued in this thesis was given. Included was a practical method for realising demonstrations of quantum computation, using ensembles, for a small number of qubits. Also included are discussions of how the method might be scaled, in particular the readout of single rare earth ions.

Experiments were performed with the aim of quantum computing demonstrations. These included methods for improving the “single qubit” ensembles that had been realised earlier and demonstrations of their utility as qubits using single qubit quantum state tomography. Also included were experiments that characterised the ion-ion interactions which culminated in the observation of conditional phase shifts between two qubits.

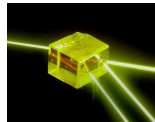
This is the first time that such conditional phase shifts have been observed

between two independent solid state qubits. The only previous two qubit demonstration in a solid used charge based superconducting qubits. These qubits had such short coherence times that the control needed to demonstrate conditional phase shifts was not available.

It is a commonly held belief that extensive nano-fabrication will be required for scalable solid-state spin based quantum computation. However, following the results of this thesis, everything required for scalable quantum computation has been demonstrated for rare earth ion dopants except for the detection of the states of single dopants.

The state detection for rare earth ion dopants will be difficult. However, there are measurements which suggest that the interaction between rare earth ions used in this thesis will also be significant for the NV-centre in diamond. Single site spectroscopy on these centres is now almost routine and the prospects for the detection of the spin states of single centres are promising.

This thesis shows the future of solid state all-optical quantum computing is exciting. It will no doubt continue to benefit from the advantages that come from the use of easy to characterise simple systems. It is hoped that this thesis will help convince the rest of the quantum computing community that the future of quantum computing might not lie with bunny suits but instead with something that looks like a small piece of glass.



Appendices

Appendix A

Rotation conventions used in creating M and Q tensors

The description used for the tensors describing the hyperfine parameters in this thesis is based on Euler angles (see Sec. 3.1.4). Euler angles are used to specify an arbitrary rotation in terms of three rotations about particular axes. There are many conventions in use. The one used in this thesis is called the *y*-convention by Goldstein [96]. Starting with the axis set (x, y, z) , first there is a rotation of α about the z axis producing a new system (x', y', z') (note $z = z'$). This is followed by a rotation of β about the y' axes to form the axis set (x'', y'', z'') , and then a rotation of γ about z'' to form (x''', y''', z''') . Explicitly we have

$$R(\alpha, \beta, \gamma) = R_3(\gamma)R_2(\beta)R_1(\alpha) \tag{A.1}$$

$$\begin{aligned} &= \begin{bmatrix} \cos(\gamma) & \sin(\gamma) & 0 \\ \cos(\gamma) & -\sin(\gamma) & 0 \\ 0 & 0 & 1 \end{bmatrix} \\ &\times \begin{bmatrix} \cos(\beta) & 0 & -\sin(\beta) \\ 0 & 1 & 0 \\ \sin(\beta) & 0 & \cos(\beta) \end{bmatrix} \\ &\times \begin{bmatrix} \cos(\alpha) & \sin(\alpha) & 0 \\ \cos(\alpha) & -\sin(\alpha) & 0 \\ 0 & 0 & 1 \end{bmatrix} \tag{A.2} \end{aligned}$$

$$= \begin{bmatrix} c(\gamma)c(\beta)c(\alpha) - s(\gamma)s(\alpha) & c(\gamma)c(\beta)s(\alpha) + s(\gamma)c(\alpha) & -c(\gamma)s(\beta) \\ -s(\gamma)c(\beta)c(\alpha) - c(\gamma)s(\alpha) & -s(\gamma)c(\beta)s(\alpha) + c(\gamma)c(\alpha) & s(\gamma)s(\beta) \\ s(\beta)c(\alpha) & s(\beta)s(\alpha) & c(\beta) \end{bmatrix} \quad (\text{A.3})$$

In the last line ‘cos’ has been replaced with ‘c’ and ‘sin’ with ‘s’.

The first two operations rotate the z axis to a point where its azimuthal angle is given by α and its elevation by $\pi/2 - \beta$. The third operation provides a rotation about this new z axis. From this it can easily be seen that the ranges $\alpha \in [0, 2\pi)$, $\beta \in [0, \pi]$ and $\gamma \in [0, 2\pi)$ cover all the possible rotations once.

The definition of the C_2 axis is less likely to cause confusion. The position of the C_2 axis was described by an azimuthal angle (ϕ) and an elevation (θ). Explicitly, the unit vector about which the rotation is applied is given by

$$\hat{\mathbf{r}} = (\cos \theta \cos \phi, \cos \theta \sin \phi, \sin \theta) \quad (\text{A.4})$$

Rodrigues’ formula is helpful when constructing the matrix describing a rotation of t (for our case $t = \pi$) about a particular axis [96].

$$\mathbf{x}' = \mathbf{x} \cos(t) + \sin(t)(\hat{\mathbf{r}} \times \mathbf{x}) + (1 - \cos(t))(\hat{\mathbf{r}} \cdot \mathbf{x})\hat{\mathbf{r}} \quad (\text{A.5})$$

Here, the rotation about $\hat{\mathbf{r}}$ maps $\mathbf{x} \rightarrow \mathbf{x}'$.

Appendix B

Algorithm for assigning observed spectral lines.

Below is the C file for determining the value of the misfit (see Sec. 3.1.4) if given a set of theoretical and observed spectral lines. The function `assign_lines` on line 98 takes two arrays containing the frequencies of the `nobs` observed transitions and the frequencies of the `ntheo` theoretical transitions and returns the misfit. The algorithm is based on each observed peak claiming the nearest theoretical as its own. When more than one observed peak claims the same theoretical peak “dispute sets” are created each of which contain a group of observed peaks and the group of theoretical peaks they want. These dispute sets are merged together until they no longer have any theoretical peaks in common. These disputes are resolved by recursively searching through all the combinations for the minimum misfit.

After declaring variables the first thing done in `assign_lines` is to make a table `distance_table` of size `nobs`×`ntheo` table containing all the frequency differences between the observed and theoretical spectral lines. Next a table of the same size called `nearest_table` is initialised, each column in this table contains, in order of increasing distance from the observed peaks, the indices of each of the theoretical peaks. In the same loop (starting at line 136) the “dispute sets” are initialised. The array `peaks` contains a bitmask of all the peaks claimed by a particular dispute set. The array `dispute_size` contains the number of peaks in a given dispute set and is initialised to 1. The array `worry` represents how far down its list of preference an observed peak might have to settle.

Initially there is one dispute set for each observed line and each of these dispute sets only claims the nearest theoretical line to its founding member.

The ‘do’ loop that starts on line 153 continually loops through the dispute sets merging those which lay claim to the same theoretical peak. It continues

until none of the dispute sets overlap.

Then in line 184 the algorithm loops through the dispute sets finding the best mapping of experimental to theoretical peaks through an exhaustive search. Because the numbers of peaks in the dispute sets vary, this search was implemented recursively (`recursively_resolve_dispute`).

```

#include <math.h>

int min_peak(int num){
    int k;
    for(k=0;k<30;k++){
        if(num&1) break;
        num=num>>1;
    }
    return k;
}
10

int max_peak(int num){
    int k;
    for(k=30;k>=0;k--){
        if(num&1073741824) break; //1073741824=2^30
        num=num<<1;
    }
    return k;
}
20

void recursively_resolve_dispute(int pos, //current obs_peak to loop over position possibilities
                                int last_pos, // the last obs peak in this dispute set
                                int* start_peak, //array, where to start looping for each peak
                                int* finish_peak, //array, where to stop looping for each peak
                                double current_error, //error at this level
                                double* best_error, //pointer to the best error the answer
                                double* distance_table, //distance lookup table
                                int ntheo)
{
    int k;
    if(pos==last_pos){ //if at highest level of recursion
        for(k=start_peak[pos];k<=finish_peak[pos];k++){
            if(current_error+distance_table[pos*ntheo+k]<*best_error){
                *best_error=current_error+distance_table[pos*ntheo+k];
            }
        }
    }
    else{ //other wise recurse some more
        for(k=start_peak[pos];k<=finish_peak[pos];k++){
            start_peak[pos+1]=k+1;
            recursively_resolve_dispute (pos+1,
20
                                        last_pos,
                                        start_peak,
                                        finish_peak,
                                        current_error+distance_table[pos*ntheo+k],
                                        best_error,
                                        distance_table,
                                        ntheo)
            k++;
        }
    }
}
30
40

```

```

                                ntheo);
        }
    }
}
50

void jsort(int* nearest_table, double* distance_table, int ntheo){
    int k,min_index=-1,max_index;
    double min =HUGE_VAL;
    for(k=0;k<ntheo;k++){
        if(distance_table[k]<min){
            min = distance_table[k];
            min_index = k;
        }
    }
    60

    if(min_index==-1){
        printf("error");
        exit(1);
    }

    max_index=nearest_table[0]=min_index;

    for(k=1;k<ntheo;k++){
    70
        if(min_index==0)
            nearest_table[k]=++max_index;
        else {
            if(max_index==ntheo-1)
                nearest_table[k]=--min_index;
            else {
                if(distance_table[max_index+1]>distance_table[min_index-1])
                    nearest_table[k] = --min_index;
                else
                    nearest_table[k] = ++max_index;
            }
        }
    }
}

//auxillary function for sorting
int compare_double_pointers(const void *p1,const void *p2)
{
    const double *da = *(const double **)p1;
    const double *db = *(const double **)p2;
    90
    if(fabs(*da-*db)<1e-4)
        return (da > db) - (da < db);
    else
        return (*da > *db) - (*da < *db);
}

double assign_lines(double* obs, //freq of observed
                    //spectral lines

```

```

        int nobs, // num observed lines
        double* theo, //freq of theoretical lines
        int ntheo) //no theo lines
{
    //temporary vairables
    double temp_dbl;
    int temp_int;
    int k,l,no_merges;
    double error_out=0;
    double dispute_set_error;

    // member (i,j) will be the ith closest theoretical peak to the observed peak j
    int nearest_table[nobs*ntheo];
    //lookup table containing the distances between
    //the observed and theoretical frequencies
    double distance_table[nobs*ntheo];
    //used for looping over all combinations within a dispute set
    int start_peak[nobs],finish_peak[nobs];
    int worry[nobs]; //used in merging of dispute sets
    //each member bitwise mask of which peaks are in each dispute set
    int peaks[nobs+1];
    int dispute_size[nobs+1]; //num of members in each dispute set

    // initialise distance table
    for(k=0;k<(nobs);k++){
        for(l=0;l<ntheo;l++){
            temp_dbl = (obs[k]-theo[l]);
            distance_table[k*ntheo+l] = temp_dbl*temp_dbl;
        }
    }

    //loop over all observed peaks
    for(k=0;k<nobs;k++){
        //initialise nearest table
        jsort(&nearest_table[k*ntheo],&distance_table[k*ntheo],ntheo);

        //Initialise each dispute set to contain a observed peak
        worry[k] = 0;
        dispute_size[k] = 1;
        peaks[k] = 1<<(nearest_table[k*ntheo]);
    }

    //used to terminate loops
    dispute_size[nobs]=0;
    peaks[nobs]=0;

    //make dispute sets by merging sets which claim common peaks

```

```

do {
    no_merges=0;
    for(k=0;k<(nobs-1);){
        //if the set of peaks in this dispute set and that of the
        //next dispute set intersect
        if(peaks[k]&peaks[k+dispute_size[k]]){
            //merge the two dispute sets
            no_merges++;
            peaks[k]=peaks[k]|peaks[k+dispute_size[k]];
            temp_int = dispute_size[k+dispute_size[k]];

            dispute_size[k+dispute_size[k]]=0;
            dispute_size[k]+=temp_int;

            for(l=k;l<k+dispute_size[k];l++){
                while(worry[l]<dispute_size[k]-1){
                    worry[l]++;
                    peaks[k]=peaks[k]|(1<<(nearest_table[l*ntheo+(worry[l])]));
                }
            }
        }else{
            //go onto the next dispute set
            k+=dispute_size[k];
        }
    }

}while(no_merges!=0); //loop until the peaks want by each dispute set dont intersect

//for each dispute set recursively try all combinations looking for the best

for(k=0;k<nobs;k+=dispute_size[k]){
    if(dispute_size[k]==1){
        error_out+=distance_table[k*ntheo+nearest_table[k*ntheo]];
    }else{
        //find start and end pos for each peak for each dispute
        temp_int = k+dispute_size[k]-1; //end of this dispute set

        finish_peak[temp_int] = max_peak(peaks[k]);
        for(l=temp_int-1;l>=k;l--){
            finish_peak[l]=finish_peak[l+1]-1;

            start_peak[k]=min_peak(peaks[k]);
            for(l=k+1;l<=temp_int;l++){
                start_peak[l] = start_peak[l-1]+1;
            }

            dispute_set_error=HUGE_VAL;
            //recursively resolve dispute
            recursively_resolve_dispute(k,
                temp_int, //last obs peak in this dispute set
                start_peak,
                finish_peak,

```

```
                                0, //error at this level of recursion
                                &dispute_set_error, //where to put the answer
                                distance_table, //so we dont have to calc it again
                                ntheo);
    error_out+=dispute_set_error;
}
}
if(error_out==HUGE_VAL){
    printf("error");
    exit(1);
}
return error_out;
}
```

Appendix C

Publications

Accepted Papers

- (i) J. J. Longdell, M. J. Sellars, and N. B. Manson. *Hyperfine interaction in ground and excited states of praseodymium-doped yttrium orthosilicate*. Phys. Rev. B, 66:035101, 2002
- (ii) M. Boström, J. J. Longdell, and B. W. Ninham. *Molecular resonance interaction in channels*. Europhys. Lett., 59(1):21–27, 2002.
- (iii) M. Boström, J. J. Longdell, D. J. Mitchell, and B. W. Ninham. *Resonance interaction between one excited and one ground state atom*. Accepted for Euro. Phys. D.
- (iv) M. Boström, J. J. Longdell, and B. W. Ninham. *Atom-atom interactions at and between metal surfaces at nonzero temperature*. Phys. Rev. A, 64:062702, 2001
- (v) S. T. Hyde, S. Ramsden, T. D. Matteo, and J. J. Longdell. *Ab-initio construction of some crystalline 3d euclidean networks*. Accepted for Solid State Sciences, 2002.

Not yet published

- (vi) J. J. Longdell and M. J. Sellars. *Experimental demonstration of quantum state tomography applied to dopant ions in a solid*. quant-ph/0208182
- (vii) E. Fraval, M. J. Sellars and J. J. Longdell. *Method of extending hyperfine coherence times in Pr:YSO*. In preparation
- (viii) J. J. Longdell and M. J. Sellars. *Rare earth quantum computation with ensembles*. In preparation
- (ix) M. J. Sellars and J. J. Longdell. *Observation of conditional phase shifts between two solid state qubits*. In preparation

Conference talks and posters

- (x) J. J. Longdell and S. T. Hyde. *New space partitioners and a possible mesostructure of the $Pm-3n$ cubic mesophase*. European Meeting on Lipid Lipase Interaction, 2000. (talk)
- (xi) J. J. Longdell, M. J. Sellars, and N. B. Manson. *Improving EIT in praseodymium doped YSO*. ACOLS 2001. (poster)

Bibliography

- [1] A. M. Turing, *On computable numbers, with an application to the Entscheidungs problem*, Proc. Lond. Math. Soc. **42**, 230 (1936).
- [2] A. Church, *An unsolvable problem of elementary number theory*, Am. J. Math. **58**, 345 (1936).
- [3] G. E. Moore, *Cramming More Components onto Integrated Circuits*, Electronics, 1965, currently also at:
<http://www.intel.com/research/silicon/moorespaper.pdf>.
- [4] M. D. Davis, *The Undecidable* (Raven Press, New York, 1965).
- [5] D. Deutsch, *Quantum theory, the Church-Turing Principle and the universal quantum computer*, Proc. R. Soc. London A. **400**, 97 (1985).
- [6] D. Deutsch and R. Jozsa, *Rapid solution of problems by quantum computation*, Proc. R. Soc. London A. **439**, 553 (1992).
- [7] R. P. Feynman, *Simulating Physics with Computers*, Int. J. Theor. Phys. **21**, 467 (1982).
- [8] D. S. Abrams and S. Lloyd, *Simulation of Many-Body Fermi Systems on a Universal Quantum Computer*, Phys. Rev. Lett. **79**, 2586 (1999).
- [9] A. Y. Kitaev, *Quantum computations: algorithms and error correction*, Russ. Math. Surv **52**, 1191 (1997).
- [10] R. Cleve, A. Ekert, C. Macciavello, and M. Mosca, *Quantum algorithms revisited*, Proc. Roy. Soc. A **454**, 339 (1998).
- [11] P. Shor, in *35th Annual Symposium on Foundations of Computer Science* (IEEE Press, Los Alamos, 1994).
- [12] R. L. Rivest, A. Shamir, and L. M. Aldeman, *A method of obtaining digital signatures and public-key cryptosystems*, Comm. ACM **21**, 120 (1978).

- [13] L. Grover, in *Proceedings of the 28th Annual ACM Symposium on Theory of Computing* (ACM Press, New York, 1996).
- [14] D. P. DiVincenzo, The Physical Implementation of Quantum Computation, 2000. [arXiv:quant-ph/0002077](#)
- [15] A. Barenco *et al.*, *Elementary gates for quantum computation*, Phys. Rev. A **52**, 2457 (1995). [arXiv:quant-ph/9503016](#)
- [16] S. Lloyd, *Almost any Quantum Logic Gate is Universal*, Phys. Rev. Lett. **75**, 346 (1995).
- [17] D. Deutsch, A. Barenco, and A. Ekert, *Universality in quantum computation*, Proc. Roy. Soc. London A **449**, 669 (1995).
- [18] J. L. Brylinski and R. Brylinski, in *Universal quantum gates*, Chap. II in [20]. [arXiv:quant-ph/0108062](#)
- [19] M. J. Bremner *et al.*, *A practical scheme for quantum computation with any two-qubit entangling gate*, Phys. Rev. Lett. **89**, 247902 (2002). [arXiv:quant-ph/0207072](#)
- [20] *Mathematics of Quantum Computation*, edited by R. K. Brylinski and G. Chen (Chapman & Hall / CRC Press, New York, 2002).
- [21] A. Messiah, *Quantum Mechanics* (North Holland Pub. Co., Amsterdam, 1961).
- [22] G. E. Pake and T. L. Estle, *The Physical Principles of Electron Paramagnetic Resonance* (W. A. Benjamin, Inc., Reading, Mass., 1973).
- [23] M. O. Scully and M. S. Zubairy, *Quantum Optics* (Cambridge Univ. Press, Cambridge, UK, 1997).
- [24] F. Bloch, *Nuclear induction*, Phys. Rev. **70**, 460 (1946).
- [25] C. W. Gardiner, *Quantum Noise* (Springer-Verlag, Berlin, 1991).
- [26] D. F. Walls and G. J. Milburn, *Quantum Optics* (Springer-Verlag, Berlin, 1994).
- [27] B. E. Kane, Nature **393**, 133 (1998).
- [28] P. M. Platzman and M. I. Dykman, *Quantum Computing with Electrons Floating on Liquid Helium*, Science **284**, 1967 (1999).

- [29] L. M. K. Vandersypen *et al.*, *Experimental Realization of an Order Finding Algorithm with an NMR Quantum Computer*, Phys. Rev. Lett. **85**, 5452 (2000).
- [30] R. R. Ernst, G. Bodenhausen, and A. Wokaun, *Principles of Nuclear Magnetic Resonance in One and Two Dimensions* (Oxford University Press, Oxford, U.K., 1990).
- [31] M. A. Nielsen and I. L. Chuang, *Quantum Computation and Quantum Information* (Cambridge Univ. Press, Cambridge, 2000).
- [32] L. J. Shulman and U. Vazirani, *Molecular scale heat engines and scalable quantum computation*, Proc. 31st Ann. ACM Symp. on Theory of Computing (STOC '99) 332 (1999).
- [33] D. W. Leung, I. L. Chuang, F. Yamaguchi, and Y. Yamamoto, *Efficient implementation of coupled logic gates for quantum computation*, Phys. Rev. A **61**, 042310 (2000).
- [34] D. V. Averin and K. K. Likharev, in *Mesoscopic Phenomena in Solids*, edited by B. L. Alsthuler, P. A. Lee, and R. A. Webb, p. 71.
- [35] T. A. Fulton and G. J. Dolan, *Observation of single-electron charging effects in small tunnel junctions*, Phys. Rev. Lett. **59**, 109 (1987).
- [36] K. K. Likharev, IEEE Trans. Magn. **23**, 1142 (1987).
- [37] Y. Nakamura, Y. A. Pashkin, and J. S. Tsai, *Coherent control of macroscopic quantum states in single-Cooper-pair box*, Nature **398**, 786 (1999).
- [38] B. H. Bransden and C. J. Joachain, *Introduction to Quantum Mechanics* (Longman Scientific and Technical, London, 1989).
- [39] Y. A. Pashkin *et al.*, *Quantum oscillations in two coupled charge qubits*, Nature **421**, 823 (2003).
- [40] P. T. H. Fisk *et al.*, *Very high Q microwave spectroscopy on trapped $^{171}\text{Yb}^+$ ions: Application as a frequency standard*, IEEE Trans. Instrum. Measurement **44**, 113 (1995).
- [41] J. I. Cirac and P. Zoller, *Quantum Computations with Cold Trapped Ions*, Phys. Rev. Lett. **74**, 4091 (1995).

- [42] D. M. Meekhof *et al.*, *Experimental Issues in Coherent Quantum-State Manipulation of Trapped Atomic Ions*, J. Res. Natl. Inst. Stand. Technol. **103**, 259 (1998), currently at <http://nvl.nist.gov/pub/nistpubs/jres/103/3/j33win.pdf>.
- [43] C. A. Sackett *et al.*, *Experimental entanglement of four particles*, Nature **404**, 256 (2000).
- [44] D. F. V. James, P. G. Kwait, W. J. Munroe, and A. G. White, *Measurement of qubits*, Phys. Rev. A **64**05, 2312 (2001).
- [45] G. J. Milburn, *Quantum optical Fredkin gate*, Phys. Rev. Lett. **62**, 2127 (1988).
- [46] Y. Yamamoto, M. Kitagawa, and K. Igeta, in *Proc. 3rd Asia-Pacific Phys. Conf.* (World Scientific, Singapore, 1988).
- [47] Q. A. Turchette *et al.*, *Measurement of condition phaseshifts for quantum logic*, Phys. Rev. Lett. **75**, 4710 (1995).
- [48] E. Knill, R. Laflamme, and G. J. Milburn, *A scheme for efficient quantum computation with linear optics*, Nature **409**, 46 (2001).
- [49] J. Kim, O. Benson, H. Kan, and Y. Yamamoto, *A single photon turnstile device*, Nature **397**, 500 (1999).
- [50] C. L. Foden *et al.*, *High frequency acousto-electric single photon source*, Phys. Rev. A **62**, 011803 (2000).
- [51] W. W. Peterson and E. J. Weldon, *Error-correcting codes*, 2nd ed. (MIT Press, Cambridge, Mass., 1972).
- [52] J. von Neumann, in *Automata Studies*, Chap. Probabilistic logics and the synthesis of reliable organisms from unreliable components, pp. 329–278.
- [53] S. Winograd and J. D. Cowan, *Reliable computation in the Presence of Noise* (MIT Press, Cambridge, Mass., 1967).
- [54] W. K. Wootters and W. H. Zurek, *A single quantum cannot be cloned*, Nature **299**, 802 (1982).
- [55] D. Dieks, *Communication by EPR Devices*, Physics Letters A **92**(6), 271 (1982).

- [56] J. Yepez, *Type-II Quantum Computers*, Int. J. Mod. Phys. C **12**, 1273 (2001).
- [57] J. Yepez, *Quantum lattice-gas model for the diffusion equation*, Int. J. Mod. Phys. C **12**, 1285 (2001).
- [58] G. P. Berman, A. A. Ezhov, D. I. Kamenev, and J. Yepez, *Simulation of the diffusion equation on a type-II quantum computer*, Phys. Rev. A **66**, 012310 (2002).
- [59] K. Vogel and H. Risken, *Determination of quasiprobability distributions in terms of probability distributions for the rotated quadrature phase*, Phys. Rev. A **40**, 2847 (1989).
- [60] D. S. Bridges, *Foundations of Real and Abstract Analysis* (Springer-Verlag, Heidelberg-Berlin-New York, 1998).
- [61] A. Kirsch, *An Introduction to the Mathematical Theory of Inverse Problems* (Springer Verlag, Heidelberg-Berlin-New York, 1996).
- [62] J. F. Poyatos, J. I. Cirac, and P. Zoller, *Complete characterization of a quantum process: the two-bit quantum gate*, Phys. Rev. Lett. **78**, 390 (1997).
- [63] I. L. Chuang and M. A. Nielsen, *Prescription for experimental determination of the dynamics of a quantum black box*, J. Mod. Opt. **44**, 2455 (1997). [arXiv:quant-ph/9610001](#)
- [64] A. J. Freeman and R. E. Watson, *Theoretical Investigation of Some Magnetic and Spectroscopic Properties of Rare-Earth Ions*, Phys. Rev. **127**, 2058 (1962).
- [65] R. M. Macfarlane, *High-resolution laser spectroscopy of rare-earth doped insulators: a personal perspective*, J. Lumin. **100**, 1 (2002).
- [66] R. W. Equall, Y. Sun, R. L. Cone, and R. M. Macfarlane, *Ultralow Optical Dephasing in $\text{Eu}^{3+}:\text{Y}_2\text{SiO}_5$* , Phys. Rev. Lett. **72**, 2179 (1997).
- [67] Y. Sun *et al.*, *Recent progress in developing new rare earth materials for hole burning and coherent transient applications*, J. Lumin **98**, 281 (2002).
- [68] W. B. Jensen, J. Chem. Educ. **59**, 634 (1982).
- [69] M. Attrep and P. K. Koroda, J. Inorg. Nuclear Chem. **30**, 669 (1968).

- [70] D. F. Shriver, P. W. Atkins, and C. H. Langford, *Inorganic Chemistry* (Oxford University Press, Oxford, 1994).
- [71] F. A. Cotton and G. Wilkinson, *Advanced Inorganic Chemistry*, 5th ed. (Wiley-Interscience, New York, 1988).
- [72] G. H. Dieke and H. M. Crosswhite, *Appl. Opt.* **2**, 681 (1963).
- [73] W. T. Carnall, H. Crosswhite, and H. M. Crosswhite, Technical Report No. 60439, Argonne Natl. Lab. (unpublished).
- [74] *Laser Spectroscopy of Solids*, edited by W. M. Yen and P. N. Sekzer (Springer-Verlag, Berlin, 1981).
- [75] M. A. Teplov, *Magnetic resonance on Pr^{141} nuclei in a $Pr_2(SO_4)_3 \cdot 8H_2O$ single crystal*, Soviet Physics JETP **26**, 872 (1968).
- [76] J. M. Baker and B. Bleaney, *Proc. R. Soc. London Ser. A* **245**, 156 (1958).
- [77] R. M. Shelby and R. M. Macfarlane, in *Spectroscopy of Solids Containing Rare Earth Ions*, edited by A. A. Kaplyanskii and R. M. Macfarlane, Chap. 1, p. 51.
- [78] M. Mitsunaga, *Time domain optical data storage by photon echo*, *Optical and quantum electronics* **24**, 1137 (1992).
- [79] E. L. Hahn, *Phys. Rev.* **80**, 580 (1950).
- [80] G. J. Pryde, M. J. Sellars, and N. Manson, *Solid state coherent transient measurements using hard optical pulses*, *Phys. Rev. Lett.* **84**, 1152 (2000).
- [81] Elliot Fraval, Personal Communication.
- [82] A. V. Turukhin *et al.*, *Observation of Ultraslow and Stored Light Pulses in a Solid*, *Phys. Rev. Lett.* **88**, 023602 (2002).
- [83] M. Aparicio and A. Duran, *Yttrium silicate coatings for oxidation protection of carbon-silicon carbide composites*, *J. Am. Ceram. Soc.* **83**, 1351 (2000).
- [84] *International Tables for X-Ray Crystallography*, 3rd ed., edited by N. F. M. Henry and K. Lonsdale (The Kynoch Press, Birmingham, 1969), Vol. I.

- [85] C. Michel, G. Buisson, and E. F. Bertaut, *Structure de Y_2SiO_5* , C. R. Acad. Sc. Paris, Series B **264**, 397 (1967).
- [86] B. A. Maximov, Y. A. Charitonov, V. V. Ilyikhin, and N. B. Belov, Dokl. Acad. Nauk SSSR Ser. Mat. Phys **183**, 1072 (1968).
- [87] B. S. Ham, M. S. Shahriar, M. K. Kim, and P. R. Hemmer, *Frequency-selective time-domain optical data storage by electromagnetically induced transparency*, Optics Letters **22**, 1849 (1997).
- [88] B. S. Ham, M. S. Shahriar, and P. R. Hemmer, *RF induced optical gain in $Pr^{3+}Y_2SiO_5$* , J. Opt. Soc. Am. **15**, 1541 (1998).
- [89] B. S. Ham, P. R. Hemmer, and M. S. Shahriar, *Efficient electromagnetically induced transparency in a rare-earth doped crystal*, Optics Communications **144**, 227 (1997).
- [90] Data sheet available at <http://www.allegromicro.com/datafile/3515.pdf>.
- [91] J. Mlynek *et al.*, *Raman Heterodyne Detection of Nuclear Magnetic Resonance*, Phys. Rev. Lett. **50**, 993 (1983).
- [92] N. C. Wong *et al.*, *Raman heterodyne detection of nuclear magnetic resonance*, Phys. Rev. B **28**, 2993 (1983).
- [93] N. Metropolis *et al.*, J. Chem. Phys **21**, 1087 (1953).
- [94] W. K. Hastings, *Monte Carlo sampling methods using Markov chains and their applications*, Biometrika **57**, 97 (1970).
- [95] S. Kirkpatrick, C. D. Gelatt, and M. P. Vecchi, Science **220**, 671 (1983).
- [96] H. Goldstein, *Classical Mechanics* (Addison-Wesley Pub. Co., Reading, Mass., 1980).
- [97] K. Holliday, M. Croci, E. Vauthey, and U. P. Wild, Phys. Rev. B **47**, 14741 (1993).
- [98] L. E. Erickson, Phys. Rev. B **16**, 4731 (1977).
- [99] M. Mitsuanga, E. S. Kintzer, and R. G. Brewer, , Phys. Rev. B **31**, 6947 (1985).

- [100] A. L. Alexander, Honours Thesis, Australian National University, <http://eprints.anu.edu.au/archive/00000761/> (unpublished).
- [101] B. S. Ham, M. S. Shahriar, and P. R. Hemmer, Phys. Rev. B **58**, R11825 (1998).
- [102] R. Yano, M. Mitsuanga, and N. Uesugi, Opt. Lett **16**, 1884 (1991).
- [103] A. J. Silversmith, *High resolution laser spectroscopy of trivalent europium centres in crystals*, Ph.D. thesis, Australian National University, 1985.
- [104] G. P. Flinn *et al.*, *Sample-dependent optical dephasing in bulk crystalline samples of $Y_2O_3:Eu^{3+}$* , Phys. Rev. B **49**, 5821 (1994).
- [105] A. Gruber *et al.*, *Scanning Confocal Optical Microscopy on Single Defect Centers*, Science **276**, 2012 (1997).
- [106] A. Beveratos *et al.*, *Single photon quantum cryptography*, Phys. Rev. Lett **89**, 187901 (2002).
- [107] K. Ichimura, *A simple frequency-domain quantum computer with ions in a crystal coupled to a cavity mode*, Optics Comm. **196**, 119 (2001).
- [108] N. Ohlsson, R. K. Mohan, and S. Kröll, *Quantum computer hardware based on rare-earth-ion-doped inorganic crystals*, Optics Comm. **201**, 71 (2002).
- [109] M. S. Shahriar *et al.*, *Solid-state quantum computing using spectral holes*, Phys. Rev. A **66**, 032301 (2002).
- [110] F. R. Graf, A. Renn, G. Zumofen, and U. P. Wild, *Photon-echo attenuation by dynamical processes in rare-earth-ion-doped crystals*, Phys. Rev. B **58**, 5462 (1998).
- [111] M. J. Sellars and N. B. Manson, talk given at *Workshop on Quantum Coherence and Information Processing*, University of Adelaide, 1997.
- [112] J. D. Jackson, *Classical Electrodynamics*, 3rd ed. (John Wiley & Sons, New York, 1999).
- [113] D. R. Taylor and J. P. Hessler, Phys. Lett. A **50**, 205 (1974).
- [114] P. F. Liao and S. R. Hartmann, Opt. Commun **8**, 310 (1973).

- [115] S. Meth and S. Hartmann, *The effect of instantaneous diffusion on the relaxation of photon echoes in ruby*, Phys. Lett. A **58**, 192 (1976).
- [116] G. K. Liu, M. F. Joubert, R. L. Cone, and B. Jacquier, J. Lumin. **38**, 34 (1987).
- [117] J. Huang, J. M. Zhang, A. Lezama, and T. W. Mossberg, *Excess Dephasing in Photon-Echo Experiments Arising from Excitation Induced Electronic Level Shifts*, Phys. Rev. Lett. **63**, 78 (1989).
- [118] M. Mitsunaga, T. Takagahara, R. Yano, and N. Uesugi, *Excitation-induced frequency shift probed by stimulated photon echoes*, Phys. Rev. Lett. **68**, 3126 (1992).
- [119] N. F. Ramsey, *Molecular Beam Resonance Method with Separated Oscillating Fields*, Phys. Rev. **78**, 695 (1950).
- [120] A. J. Meixner, C. M. Jefferson, and R. M. Macfarlane, *Measurement of the Stark effect with subhomogeneous linewidth resolution in Eu:YAlO₃ with the use of photon-echo modulation*, Phys. Rev. B **46**, 5912 (1992).
- [121] Y. P. Wang and R. S. Meltzer, Phys. Rev. B **45**, 10119 (1992).
- [122] G. Davies and N. B. Manson, *Electric field perturbation of optical centres in diamond*, Industrial Diamond Review (Feb 1980), ISSN 0019-8145.
- [123] L. Root and J. L. Skinner, *Frequency-dependent optical dephasing and the nature of inhomogeneous broadening in crystals*, Phys. Rev. B **32**, 4111 (1985).
- [124] M. D. Lukin and P. R. Hemmer, *Quantum entanglement via optical control of atom-atom interactions*, Phys. Rev. Lett. **84**, 2818 (2000).
- [125] R. E. Eisenschitz and F. London, Zeits. f. Physik **60**, 491 (1930).
- [126] G. W. King and J. H. Van Vleck, *Dipole-dipole resonance forces*, Phys. Rev. **55**, 1937 (1939).
- [127] McLone and E. A. Power, Mathematika **11**, 91 (1964).
- [128] M. Boström, J. J. Longdell, D. J. Mitchell, and B. W. Ninham, *Resonance interaction between an excited and one ground state atom*, Eur. Phys. J. D **22**, 47 (2003).

- [129] Y. S. Bai and R. Kachru, *Nonequilibrium resonant-phonon-induced excess photon-echo dephasing*, Phys. Rev. B **46**, 13735 (1992).
- [130] S. Kröll, E. Y. Xu, and R. Kachru, *Influence of excited-state Pr^{3+} on the relaxation of the $Pr^{3+}:YAlO_3$ 3H_4 - 1D_2 transition*, Phys. Rev. B **44**, 30 (1990).
- [131] T. Pellizzari, S. A. Gardiner, J. I. Cirac, and P. Zoller, *Decoherence, Continuous Observation and Quantum Computing: A Cavity QED Model*, Phys. Rev. Lett. **75**, 3788 (1995).
- [132] Phil Hemmer, Personal Communication.
- [133] J. Wesenberg and K. Mølmer, Robust quantum gates and a bus architecture for quantum computing with rare-earth-ion doped crystals, 2003. [arXiv:quant-ph/0301036](#)
- [134] J. J. Longdell and M. J. Sellars, Experimental demonstration of quantum state tomography applied to dopant ions in a solid, 2002. [arXiv:quant-ph/0208182](#)
- [135] M. Nilsson *et al.*, Physica Scripta **T102**, 178 (2002). [arXiv:quant-ph/0201141](#)
- [136] R. H. Dicke, *Coherence in Spontaneous Radiation Processes*, Phys. Rev. **93**, 99 (1954).
- [137] D. I. Hoult and N. S. Ginsberg, *The quantum origins of the free induction decay signal and spin noise*, J. of Mag. Res. **148**, 182 (2001).
- [138] L. Allen and J. H. Eberly, *Optical Resonance and Two-Level Atoms* (John-Wiley & Sons, New York, 1975).
- [139] R. Laflamme *et al.*, Introduction to NMR Quantum Information Processing, 2002. [arXiv:quant-ph/0207172](#)
- [140] J. A. Jones, Robust quantum information processing with techniques from liquid state NMR, 2003. [arXiv:quant-ph/0301019](#)
- [141] Matthew Sellars, Personal Communication.
- [142] M. J. Sellars and N. B. Manson, *Direct observation of radiation locking in using phase sensitive detection*, J. Lumin **76–77**, 137 (1998).

- [143] R. J. Schoelkopf *et al.*, *A concept for a submillimeter-wave single-photon counter*, IEEE Trans. Appl. Supercond. **9**, 2935 (1999).
- [144] B. Cabrera *et al.*, *Detection of single infrared, optical, and ultraviolet photons using superconducting transition edge sensors*, Appl. Phys. Lett. **73**, 735 (1998).
- [145] David Pulford, Personal Communication.
- [146] M. D. Lukin, S. F. Yelin, and M. Fleischhauer, *Entanglement of Atomic Ensembles by Trapping Correlated Photon States*, Phys. Rev. Lett. **84**, 4232 (2000).
- [147] Company homepage <http://www.scientificmaterials.com>.
- [148] Data sheet available at <http://www.minicircuits.com/dg03-212.pdf>.
- [149] G. J. Pryde, *Ultrahigh resolution spectroscopic studies of optical dephasing in solids*, Ph.D. thesis, Australian National University, 1999.
- [150] M. J. Sellars, *Ultra-High Resolution Laser Spectroscopy of Rare Earth Doped Solids*, Ph.D. thesis, Australian National University, 1995.
- [151] *Operators Manual, CR-699 Ring Dye Laser*, Coherent, Inc., Palo Alto, CA.
- [152] R. W. P. Drever *et al.*, Appl. Phys. B **31**, 97 (1983).
- [153] Darren Freeman, Personal Communication.
- [154] S. B. Altner, M. Mitsunaga, G. Zumofen, and U. P. Wild, *Dephasing-rephasing balancing in photon echoes by excitation induced frequency shifts*, Phys. Rev. Lett. **76**, 1747 (1996).
- [155] I. L. Chuang, N. Gershenfeld, M. G. Kubinec, and D. W. Leung, *Bulk quantum computation with nuclear magnetic resonance: theory and experiment*, Proc. R. Soc. Lond. A **454**, 447 (1998).
- [156] G. L. Long, H. Y. Yan, and Y. Sun, *Analysis of Density Matrix reconstruction in NMR Quantum Computing*, J. Opt. B **3**, 376 (2001). [arXiv:quantph/0012047](https://arxiv.org/abs/quantph/0012047)
- [157] A. M. Childs, I. L. Chuang, and D. W. Leung, *Realization of quantum process tomography in NMR*, Phys. Rev. A **64**, 012314 (2001). [arXiv:quant-ph/0012032](https://arxiv.org/abs/quant-ph/0012032)

- [158] M. A. Nielsen, E. Knill, and R. Laflamme, *Complete quantum teleportation using nuclear magnetic resonance*, *Nature* **396**, 52 (1998).